The University of Nottingham

Department of Civil Engineering,
Faculty of Engineering

NUMERICAL MODELLING OF ARCHING IN PILED EMBANKMENTS INCLUDING THE EFFECTS OF REINFORCEMENT AND SUBSOIL

Yan Zhuang, BEng, MSc.

Thesis submitted to the University of Nottingham

for the degree of Doctor of Philosophy

September 2009

ABSTRACT

Piled embankments provide an economic and effective solution to the problem of constructing embankments over soft soils. This method can reduce settlements, construction time and cost.

The performance of piled embankments relies upon the ability of the granular embankment material to arch over the 'gaps' between the pile caps. Geogrid or geotextile reinforcement at the base of the embankment is often used to promote this action, although its role in this respect is not completely understood.

Design methods which are routinely used in the UK (e.g. BS8006, 1995; Hewlett & Randolph, 1988; the 'Guido' method, 1987) estimate the stress which acts on the underlying soft ground completely independently of the properties of the soft ground. This stress is then generally used to design the amount of geogrid or geotextile reinforcement required. However, estimation of this load can vary quite considerably for the various methods.

Using finite element modelling the 2D and 3D arching mechanisms in the embankment granular fill has been studied. The results show that the ratio of the embankment height to the centre-to-centre pile spacing is a key parameter, and generic understanding of variation of the behaviour with embankment height has been improved.

These analyses are then extended to include single and multiple layers of reinforcement to establish the amount of vertical load which is carried and the resulting tension, both in 2D and 3D. The contribution to equilibrium of the subsoil beneath the embankment is also considered.

Finally the concept of an interaction diagram (and corresponding equation) for use in design is advanced based on the findings.

ACKNOWLEDGEMENTS

Firstly, I would like to thanks my supervisor Dr Ed Ellis, who always provided excellent guidance and patience throughout my research. I have been extremely fortunate to have had a supervisor who always made the time and effort to respond to my queries. He has been more than just a superb supervisor. Not only has he motivated me to become an independent geotechnical engineer but also taught me how to consider my future both in my career and in my life. Secondly I wish to acknowledge the support provided by Professor Hai-Sui Yu. He has always made great efforts to give me help whenever I had difficulties in my work. He has also provided me with great opportunities to extend my knowledge and experience.

The opportunity to work with Dr Ed Ellis and Professor Hai-Sui Yu has been the highlight of my professional career and personal experience in my life.

I would also like to thank my parents for their continuous encouragement and support. A special thank you to Zhibao Mian for his useful suggestions, help and company.

Finally, I am greatly indebted to the financial support provided by a Dorothy Hodgkin Postgraduate Award. This great support enabled me concentrate on the research and provided me with many opportunities to

extend my knowledge and experience, such as conferences and useful short courses.

CONTENTS

CHAPTER 9

DISCUSSION OF RESULTS

CHAPTER 10

CONCLUSIONS

LIST OF FIGURES

Chapter 1

Chapter 2

Chapter 3

Chapter 4

Chapter 5

Chapter 6

Chapter 7

Chapter 8

Chapter 9

LIST OF TABLES

Chapter 9

NOTATION

Dimensions

a = the pile cap width (m)

h = the height of embankment (m)

h_s = the thickness of subsoil (m)

h_w = the thickness of working platform (piling mat) (m)

l = the length of the span (m)

s = the centre-to-centre spacing of pile caps (m)

Vertical stress

σ_a = the stress at the base of the embankment due to the action of arching alone (i.e. from the Ground Reaction Curve) (kN/m^2)

σ_g = the stress carried by geogrid (where this exists) (kN/m^2)

σ_s = the vertical stress in the subsoil beneath the embankment (kN/m^2)

σ_u = the vertical stress supporting the embankment (reinforced piled embankment with subsoil) (kN/m^2)

σ_w = the stress acting on the subsoil due to the working platform (any imported material below the pile cap level, which is hence not affected by arching) (kN/m^2)

Settlements

δ = the compatible settlement in the interaction diagram (m)

δ_{ec} = the settlement at the top of the embankment at the centreline above the pile cap (plane strain) (m)

δ_{ec} = the settlement at the top of the embankment at the centre above the pile cap (3D) (m)

δ_{em} = the settlement at the top of the embankment at the midpoint between piles (plane strain) (m)

δ_{em} = the settlement at the top of the embankment at the midpoint of the diagonal between piles (3D) (m)

δ_{i} = the interface friction angle between the embankment fill and geogrid (m)

δ_{s} = the maximum settlement of the subsoil at the midpoint between piles (plane strain) (m)

δ_{s} = the maximum settlement of the subsoil at the midpoint of the diagonal between piles (3D) (m)

Material parameters

k = the stiffness of the geogrid (kN/m)

E_0 = the one-dimensional stiffness of the subsoil (kN/m^2)

E_s = the Young's Modulus of subsoil (MN/m^2)

γ = the unit weight of the soil (kN/m^3)

ν = the Poisson's Ratio

ϕ = the angle of internal friction of the soil (degrees)

ψ = the kinematic dilation angle (degrees)

Others

c = the cohesion intercept (kN/m^2)

w = the uniform stress acting on the geogrid (kN/m^2)

K = the earth pressure coefficient (dimensionless parameter)

K_a = the active earth pressure coefficient (dimensionless parameter)

K_p = the passive earth pressure coefficient (dimensionless parameter)

T = the constant horizontal component of tension in the geogrid (kN/m ‘into the page’)

ε = the average strain based on the total extension in the geogrid

CHAPTER 1

INTRODUCTION

It is becoming necessary to construct projects on sites that may once have been considered unacceptable in terms of geotechnical issues. This is typified by the need to construct embankments over soft clay foundations. However the construction of embankments on soft soils has two potential problems:

- Low strength significantly limits the load (embankment height) that it is possible to apply with adequate safety for short term stability;
- High deformability and low permeability cause large settlements that develop slowly as pore water flows and excess pore pressure dissipates (consolidation).

1.1 Piled embankment

One of the most promising solutions to these problems is to use piled embankments (see Figure 1.1). In many cases, this method appears to be the most practical, efficient (low long term cost and short construction time) and an environmentally-friendly solution for construction on soft soil. The field applications are mainly highways, railways and construction of areas of fill for industrial or residential purposes.

Piles are installed through the soft subsoil and transfer load to a more competent stratum at greater depth. The majority of the load from the

embankment is carried by the piles and thus there is relatively little load on the soft subsoil. By using a piled embankment, the construction can be undertaken in a single stage without having to wait for the soft clay to consolidate. Settlements and differential settlements are also significantly reduced when the technique is used successfully.

Piles are typically arranged in square or triangular patterns in practice. However, only the square pattern has been selected in this research with the centre-to-centre spacing s and single pile cap is considered as square with the width a. The Figure 1.1 also shows the notation for geometry and settlement used in the thesis.

- a is the width of pile cap (m)
- s is the centre-to-centre spacing (m)
- h is the height of embankment (m)
- δ_s is the settlement of the subsoil at the midpoint between piles (m)
- δ_{ec} is the settlement at the top of the embankment at the centreline above the pile cap (m)
- δ_{em} is the settlement at the top of the embankment at the midpoint between piles (m)

This notation may also be extended to three dimensions. For instance, for square pile caps on a square grid in plan the pile cap is a square with side length a. The inclusion of a single or multiple layers of geogrid or geotextile reinforcement at the base of embankment is also considered in the thesis.

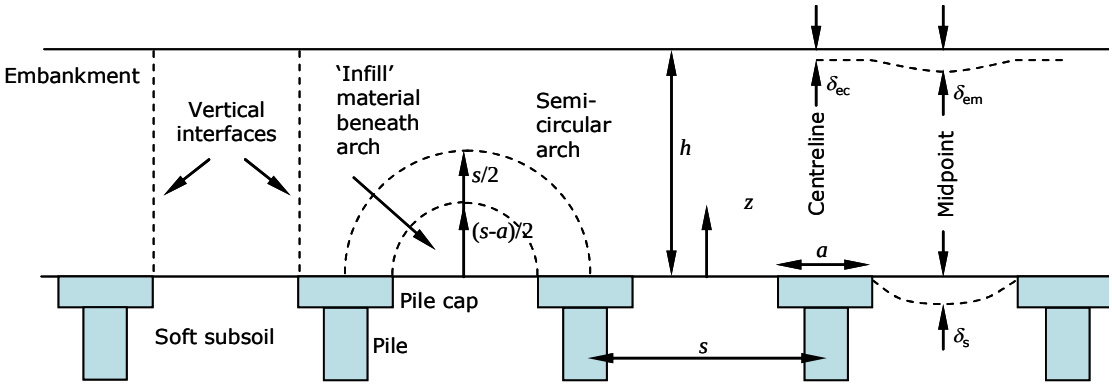

Figure 1.1. Piled embankment showing potential arching mechanisms, and notation for geometry and settlement (δ) used in this thesis

1.2 Soil arching

Differential settlement tends to occur between the relatively rigid piles and the soft foundation material. This causes the embankment fill material above the soft subsoil to settle more than the material above the piles.

The differential settlement in the embankment fill will cause corresponding shear strain or shear planes so that vertical stress is redistributed from the embankment over the soft subsoil to the pile caps, hence reducing the load on the subsoil. The embankment is normally constructed from well-compacted granular material to maximise this arching effect.

A number of conceptual and analytical models of arching have been proposed, either in a general context or specifically for a piled embankment. As shown in Figure 1.1, Terzgahi (1943) initially proposed

vertical shear planes at either side of a 'trapdoor'. Hewlett & Randolph (1988) proposed a semicircular arch for piled embankments, whilst BS8006 (1995) is based on analogy between the pile caps and a buried pipe.

1.3 Tensile reinforcement

In order to allow piles to be placed further apart, a reinforcing material can be included in the embankment fill between the piles. The vertical load carried by the reinforcement is transferred to the piles by tension as the reinforcement sags. The reinforcement can be 'geogrid' (with apertures) or 'geotextile'. The former term is used most widely in this thesis although generally any generic tensile reinforcement is implied.

There are two classes of geogrid reinforcements, uniaxial geogrids, which develop tensile stiffness and strength primarily in one direction, and biaxial geogrids which develop tensile stiffness and strength in two orthogonal directions. Moreover, biaxial geogrids can be divided into anisotropic biaxial geogrids and isotropic biaxial geogrids. For simplicity, only isotropic biaxial geogrid reinforcement, which exhibits the same stiffness and strengths in two orthogonal directions, has been used in the research.

A single layer of reinforcement may be used at or near the base of the embankment. Generally it is not placed directly on the pile caps due to the risk of damage. In this thesis it is assumed that a single layer of reinforcement is placed 100 mm above the pile cap.

Alternatively multiple layers of lower strength reinforcement may be distributed near the base of the embankment. This is often referred to as a 'Load Transfer Platform' (LTP). The premise is that this forms a zone of improved soil which enhances arching, particularly where geogrid which 'interacts' with the surrounding soil is used. Design of LTPs therefore often relies upon a contribution from the reinforcement beyond simple catenary action (sag). The geometry of LTP used in this thesis is shown in Figure 1.2.

Whatever reinforcement is used, care is required that it is 'taut' during construction and filling so that tension will result immediately from subsequent sag. For LTPs careful compaction of the fill within the LTP is also sometimes considered to be of particular importance to further enhance interaction with the geogrid reinforcement.

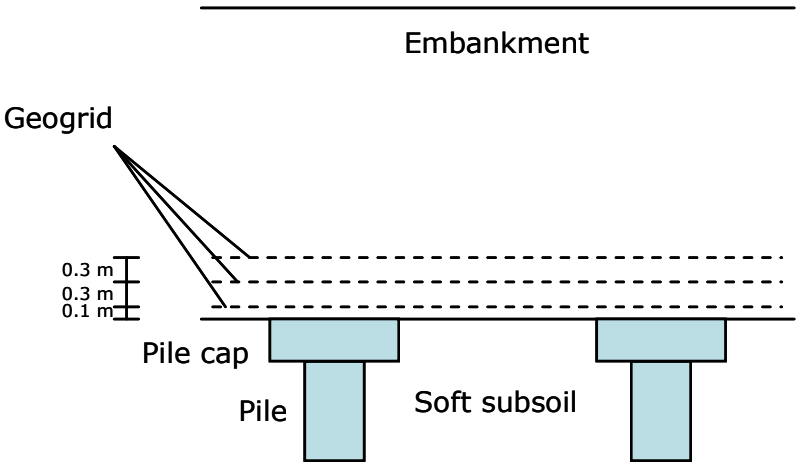

Figure 1.2. Layout of geogrid in a piled embankment Load Transfer Platform as considered in this thesis

1.4 Vertical stress in soft subsoil

Before loading by the embankment, the soft foundation is in equilibrium, probably with hydrostatic pore water pressures. As embankment construction proceeds the soft subsoil will actually be virtually incompressible (it is likely to contain a significant fraction of clay and will therefore have low permeability). Thus, the vertical effective stress does not change and the increased stress is totally supported by an increase in pore water pressure. This excess pore water pressure causes water to flow out of the soil eventually, with accompanying settlement. In the absence of significant tendency for bearing failure the associated strain may be assumed to be one-dimensional.

1.5 Aims and objectives

The aim of the research is to investigate the principles underlying the behaviour of piled embankments, including the effects of tensile reinforcement and the underlying subsoil. This ultimately aims to give additional guidance to designers on issues such as distribution of load and differential settlement.

The principal aims are as follows:

- To examine various aspects of arching behaviour in a piled embankment, first in plane strain and then in three-dimensions.
- To examine the effect of geometrical parameters, particularly pile spacing and systematic variation with embankment height.
- To establish the additional contribution of tensile reinforcement and subsoil.

1.6 Methodology

These aims and objectives are fulfilled by modelling unreinforced and reinforced piled embankments using the finite element program ABAQUS Version 6.6. Initially the subsoil is not explicitly modelled, but this is ultimately included.

1.7 Layout of the thesis

This thesis has ten Chapters.

Chapter 2 summarises existing theories and research related to piled embankments. A brief review of the finite element method is also given, and relevant features of ABAQUS are introduced.

Chapters 3–8 each introduce a particular series of analyses and present the corresponding results, building logically in complexity. Chapters 6-8 essentially repeat Chapters 3-5 in 3D rather than plane strain. Table 1.1 summarises the content. Where the subsoil is denoted 'N', the effect of stress representing the subsoil is modelled, but not the subsoil itself.

Table 1.1. Summary of analyses reported in different Chapters

Chapter	PS or 3D	Tensile reinforcement	Subsoil
3	Plane strain	N	N
4		Y	N
5		Y	Y
6	3D	N	N
7		Y	N
8		Y	Y

Chapter 9 summarises the key results and compares them with other recent research. A new method of analysis is also applied to some case studies of actual piled embankments.

Chapter 10 gives final conclusions.

CHAPTER 2
LITERATURE REVIEW

2.1 Introduction

Embankments constructed on soft ground (e.g. for road or rail transport) in the UK and throughout the world frequently use piles or similar long slender foundations to transmit loads through the compressible soil to a stronger stratum beneath. The foundations generally cover only a few percent of the total plan area, and economy dictates that they should be separated as widely as possible. However, normally provision of a structural 'raft' or similar at the base of the embankment to ensure that its weight is transferred to the piles would be too expensive and otherwise undesirable.

Rather it is normally assumed that natural 'arches' will form in the embankment over the soft soil between the foundations, and prevent differential settlement at the embankment surface. Polymer 'geogrids' which act in tension at the base of the embankment are also often used to justify increased pile spacing.

However, as evidenced by a number of recent conference and journal publications (e.g. Love & Milligan, 2003; Naughton et al., 2008; Ellis & Aslam, 2009a), there is continuing debate in the European and international geotechnical communities regarding the suitability of a

number of potential design methods for piled embankments. This is particularly the case for low embankments over very soft soil, as evidenced by the failure of a 'load transfer platform' for a housing development in Enniskillen, Northern Ireland (the subject of a presentation at the UK Institution of Civil Engineers in September 2006).

2.2 Arching concept

The concept of 'arching' of granular soil over an area where there is partial loss of support from an underlying stratum has long been recognised in the study of soil mechanics (e.g. Terzaghi, 1943). Its effect is widely observed, for instance in piled embankments. However, although this effect has been acknowledged for many decades, it remains quite poorly understood. There are a number of different models from different theoretical mechanisms and/or experimental data, but there does not yet exist a single method that can be agreed by the international geotechnical community.

The following theoretical models of arching often consider plane strain conditions. The embankment fill is assumed to be a dry homogenous material. Thus, the total and effective stresses are equal.

2.2.1 Rectangular prism: Terzaghi (1943) and McKelvey (1994)

Terzaghi was among the first theoreticians to define soil arching in his text "Theoretical Soil Mechanics" in 1943. Initially the vertical pressure at the base of the soil layer is everywhere equal to the nominal overburden stress. Terzaghi argued that gradually lowering a strip of support beneath the layer can cause yielding of the overlying material. The yielding material tends to settle, and this movement is opposed by shearing resistance along the boundaries between the moving and the stationary

mass of sand. As a consequence the total pressure on the yielding strip is reduced whilst the load on the adjacent supports increases by the same amount (in terms of force).

When the strip has yielded sufficiently, a shear failure occurs along two surface of sliding (between the moving and stationary masses of sand) which rise from the outer boundaries of the strip potentially to the surface of the sand.

Terzaghi (1943) considers the equilibrium of a differential element and then integrates this through the depth (z) of the moving soil mass. See Figure 2.1 where a rectangular soil element, having a thickness (dh) and weight (dw) is shown. The vertical stress applied to its upper surface is:

$$\sigma_v = \gamma H + q \quad (2.1)$$

Where:

σ_v = the vertical stress (kN/m^2)

γ = the unit weight of the soil (kN/m^3)

H = the thickness of soil above the point (m)

q = the surcharge acting at the surface of the soil (kN/m^2)

The corresponding normal stress on the vertical surface of sliding (σ_h) is given by:

$$\sigma_h = K \sigma_v \quad (2.2)$$

Where:

σ_h = the horizontal stress (kN/m^2)

K = the earth pressure coefficient (dimensionless parameter)

The shear strength of the soil is determined by (assuming the soil to be cohesionless):

$$\tau = \sigma_h \tan\phi \quad (2.3)$$

Where:

τ = the shear strength (kN/m^2)

ϕ = the angle of internal friction of the soil (degrees)

Resisting the movement of the soil element due to the applied stress and the weight of the element itself is the soil layer underlying this element ($\sigma_v + d\sigma_v$) and the shear strength of the soil adjacent to the element (τ) acting on both sides of the element. When the element is in equilibrium, the summation of the vertical forces must equal zero. Therefore, the vertical equilibrium can be expressed as:

$$\frac{d\sigma_v}{dz} = \gamma - K\sigma_v \frac{\tan\phi}{B} \quad (2.4)$$

Where:

$2B$ = the width of the strip (m)

z = the thickness of the soil overlying the element (m)

Using the boundary condition that $\sigma_v = q$ for $z = 0$, the partial differential equation can be solved as follows (Terzaghi 1943 and later McKelvey 1994):

$$\sigma_v = \frac{\gamma B}{K\tan\varphi}\left(1 - e^{-K\tan\varphi\, z/B}\right) + qe^{-K\tan\varphi\, z/B} \quad (2.5)$$

If q = 0,

$$\sigma_v = \frac{\gamma B}{K \tan\varphi}\left(1 - e^{-K\tan\varphi\, z/B}\right) \quad (2.6)$$

The main problem with this method is that the coefficient of earth pressures K is not known and may vary through the depth of the sliding surface. Handy (1985) describes Terzaghi's approach as a 'lintel' rather than an arch. He also points out that there is a fundamental assumption behind Terzaghi's approach: that the vertical and horizontal stress σ_v and σ_h equate to principal stresses σ_1 and σ_3. However, Krynine (1945) showed that the vertical and horizontal stresses could not be principal stresses if there is a plane of friction present. Krynine (1945) derived the following expression (Equation (2.7)) for the earth pressure coefficient K.

$$K = \frac{1-\sin^2\phi}{1+\sin^2\phi} \quad (2.7)$$

Handy (1985) proposed that the shape of the arched soil is a catenary and suggested the use of the coefficient K_w instead of K, by considering an arch of minor principal stress. K_w is derived as:

$$K_w = 1.06\left(\cos^2\theta + K_a \sin^2\theta\right) \quad (2.8)$$

Where:

$$\theta = 45^\circ + \phi/2$$

Russell et al. (2003) proposed that K could be conservatively taken as 0.5. More recently Potts & Zdravkovic (2008b) proposed that K = 1.0 gave good correspondence with the results of plane strain finite element

analyses of arching over a void. This does not seem to be consistent with frictional failure on a vertical plane. However, the assumption of failure on vertical planes is probably an oversimplification, particularly at the bottom of the soil layer near the void.

Figure 2.2(a) shows other work for an underground opening by McKelvey (1994) and Thigpen (1984). The width of the underground opening (a-b) is $2B$. The soil boundary (a-b) is assumed to have settlement Δ, and the remaining part is rigid. The base a-b is considered to be smooth so that τ = 0 at y = 0.

The elasticity solution to this problem was obtained by Finn (Thigpen, 1984) by using the slip line method and considering a plane strain condition. The vertical stress compared to the nominal overburden stress γH from Finn's analyses is plotted in Figure 2.2(c). It is noted that the stress approaches infinity at the edge of the base from the elasticity solution of Finn. However, plastic flow would occur before this happened (Thigpen, 1984).

Thigpen (1984) described that as the base (a-b) in Figure 2.2(a) yields, the compressive stress at the edge is steadily reduced (based on the elasticity solution of Finn, it changes to tensile). McKelvey (1994) proposed that momentarily just after the base yields, the soil remains its original position, forming a 'true arch', the soil directly over the underground opening is in tension. The soil tension arch can only last a finite period of time, which depends on the shear strength of the soil as

well as other variables. McKelvey (1994) then states that the soil element in tension will ultimately fail as portions of the soil element begin to drop, leaving a small gap in the tension arch, ultimately forming the inverted arch as shown in Figure 2.2(b).

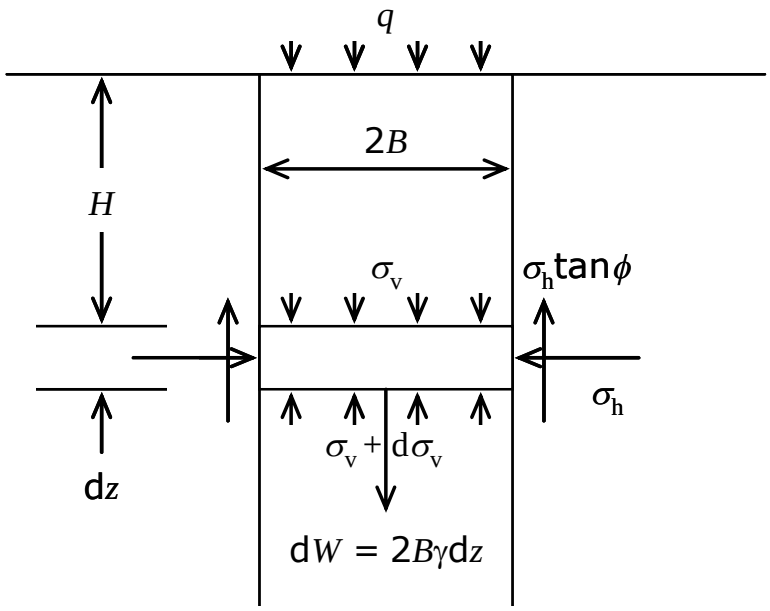

Figure 2.1. Stress state of a differential element (Terzaghi 1943 and Mckelvey 1994)

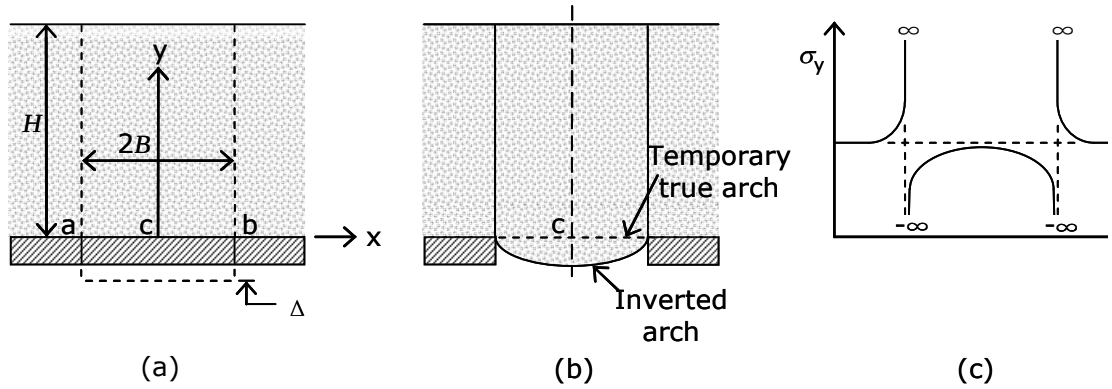

Figure 2.2. Cross-section of a soil mass; (a) overlying the underground opening, (b) True soil arch collapses and the soil immediately above the void takes the shape of an inverted arch or catenary, (c) vertical stress distribution ((a) and (b) McKelvey, 1994 (c) Thigpen 1984)

2.2.2 Semicircular arch: Hewlett & Randolph (1988)

Hewlett & Randolph (1988) derived theoretical solutions based on observations from experimental tests of arching in a granular soil. Their analysis attempts to consider actual arches in the soil, as shown in Figure 2.3 (rather than vertical boundaries as considered by Terzaghi). The 'arches of sand' transmit the majority of the embankment load onto the pile caps, with the subsoil carrying load predominantly from the 'infill' material below the arches. The arches are assumed to be semi-circular (in 2D) and of uniform thickness, with no overlap. The method also assumes that the pressure acting the subsoil is uniform.

The analysis considers equilibrium of an element at the 'crown' of the soil arch (see Figure 2.4(a)). Here the tangential (horizontal) direction is the direction of major principal stress and the radial (vertical) direction is the direction of minor principal stress, related by the passive earth pressure coefficient, K_p. Yielding is in the 'passive' condition since the horizontal stress is the major principal stress.

Considering vertical equilibrium of this element, and using the boundary condition that the stress at the top of the arching layer is equal to the weight of material above acting on the outer radius of the arch gives a solution for the radial (vertical) stress acting immediately beneath the crown of the arch (σ_i). The vertical stress acting on the subsoil is then

obtained by adding the stress due to the infilling material beneath the arch, based on the maximum height of infill (s-a)/2:

$$\sigma_s = \sigma_i + \gamma(s-a)/2 \qquad (2.9)$$

The vertical stress (σ_s) is considered uniform here. In a refinement proposed by Low et al. (1994), a parameter is introduced to allow a possible non uniform vertical stress on the soft ground.

At the pile cap (see Figure 2.4(b)), the tangential (vertical) stress is the major principal stress, and the radial (horizontal) stress is the minor principal stress (the reverse of the situation at the crown). Again, equilibrium of an element of soil is considered, and in conjunction with overall vertical equilibrium of the embankment a value of σ_s is obtained in the limit when the ratio of the major and minor principal stresses is K_p. In fact yielding occurs in an 'active' condition, since the vertical stress is the major principal stress.

The initial solutions developed by Hewlett & Randolph (1988) are for a plane strain situation (see Figure 2.3). However, equivalent 3-dimensional solutions for domes are also developed. It can be seen in Figure 2.5 that different geometry is considered in the three-dimensional situation. For the crown of the arch, the maximum height of infill is now (s-a)/$\sqrt{2}$, thus the vertical stress acting on the subsoil (σ_s) is (see Figure 2.5):

$$\sigma_s = \sigma_i + \gamma(s-a)/\sqrt{2} \qquad (2.10)$$

Overall equilibrium of the embankment and 'active' yielding in the soil above the pile cap is used to obtain the value of σ_s in a similar manner to the plane strain analysis. This corresponds to the pile caps 'punching' into the underside of the embankment.

Hewlett & Randolph (1988) proved that for a 2-dimensional case, the critical point of the arch is always at the crown or at the pile cap. However, it is necessary to consider the value of σ_s resulting from failure of the arch either at the crown or pile caps – the largest value will be critical.

Hewlett & Randolph (1988) suggest that the pile spacing (s) should probably not exceed about 3 times the width of the pile caps (a) and not be greater than about half the embankment height (H). The embankment fill should be chosen such that K_p is at least 3 (a friction angle of greater than 30°). In addition, in order to make optimum use of the piles, the spacing (s) should also be chosen such that the critical condition occurs at pile cap level, rather than at the crown of the arch (Hewlett & Randolph, 1988).

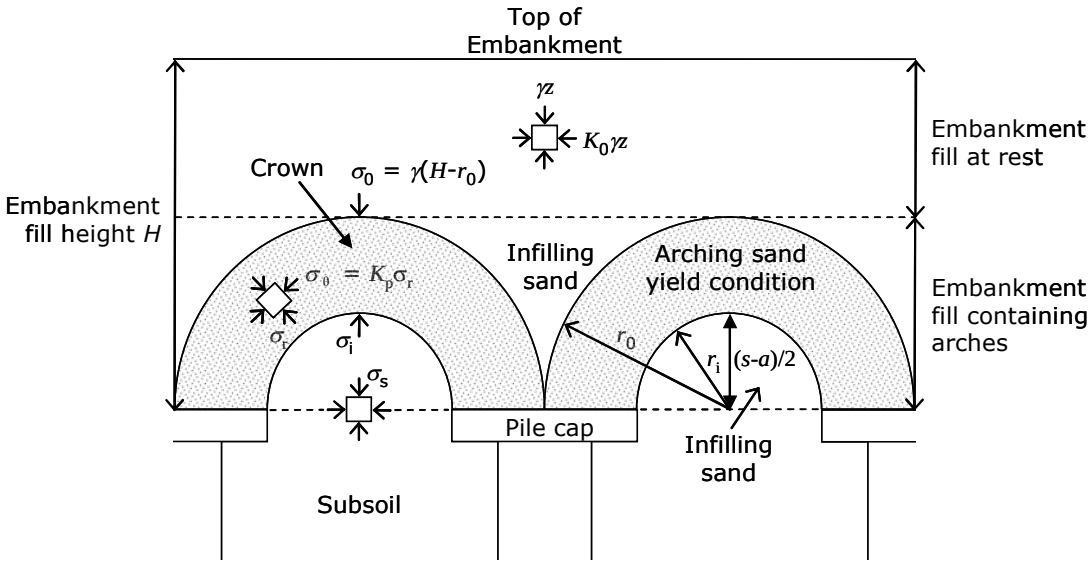

Figure 2.3. Section through a piled embankment (Hewlett & Randolph, 1988)

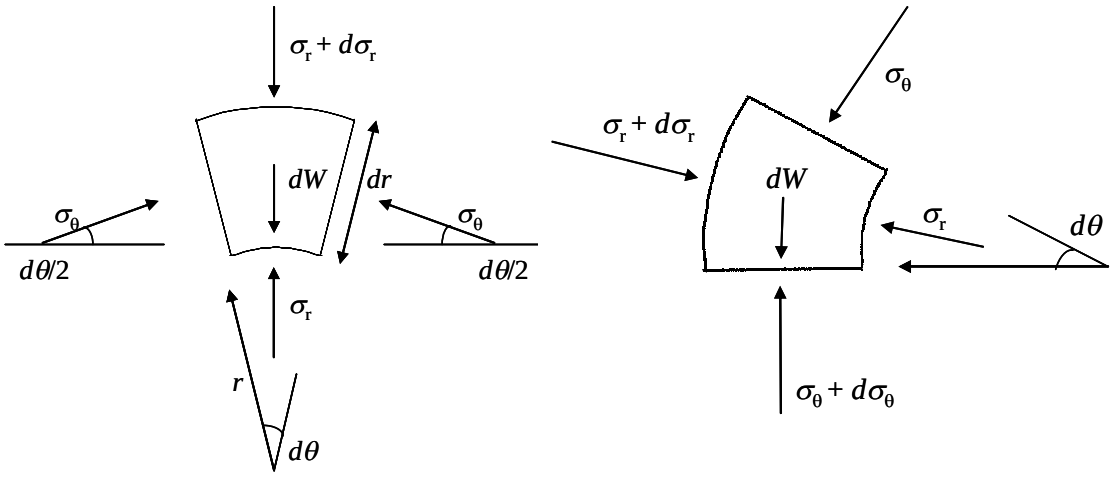

(a) An element of sand at the crown of an arch

(b) An element of sand above the pile cap

Figure 2.4. Stresses on an element of soil arch

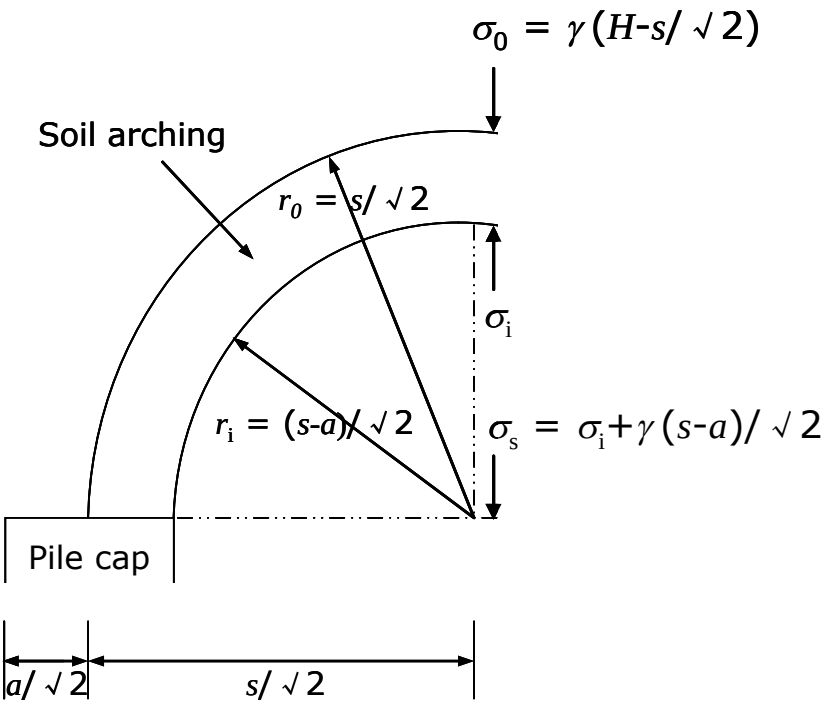

Figure 2.5. Analysis of arching at the crown of a dome in a three-dimensional situation

2.2.3 Positive projecting subsurface conduits: BS8006 (1995) and Marston's equation

The method used in the British Standard for strengthened/reinforced soils and other fills (1995) to design geosynthetics over piles was initially developed by Jones et al. (1990). A 2-dimensional geometry was assumed, which implies 'walls' in the soil rather than piles.

The British Standard differs from other methods by initially calculating the average stress on the pile cap itself rather that on the subsoil. BS8006 uses a modified form of Marston's equation for positive projecting subsurface conduits to obtain the ratio of the vertical stress acting on top of the pile caps to the average vertical stress at the base of the embankment ($\sigma_s = \gamma H$), using an equation normally used to calculate the reduced loads on buried pipes. The equation proposed by Marston was derived from field tests at the Engineering Experiment Station at Iowa State College in 1913.

For the 3-dimensional situation, and application to a piled embankment rather than a buried pipe, the result has been modified to give:

$$\frac{\sigma_c}{\gamma H} = \left(\frac{C_c a}{H}\right)^2 \qquad (2.11)$$

Where:

a = the size (or diameter) of the pile cap (m)

C_c = the arching coefficient, which depends on H and a

H = the height of the embankment (m)

γ = the unit weight of the embankment fill (kN/m^3)

γH = the nominal vertical stress at the base of the embankment (kN/m^2)

σ_c = the vertical stress on the pile cap (kN/m^2)

It can be seen from Equation (2.11) that the properties of the fill material have no effect on σ_c. It seems likely that the fill strength (which is accounted for in most methods) will have some impact, and it is likely that the result from BS8006 is only applicable to well compacted granular fill, with quite high frictional strength.

Vertical equilibrium requires that the combination of vertical stress on the pile caps (σ_c) and the subsoil (σ_s) must carry the embankment load. Thus, the overall vertical equilibrium is (for a 3D situation with pile caps with dimension a and spacing s):

$$\gamma H s^2 = \sigma_c a^2 + \sigma_s (s^2 - a^2) \quad (2.12)$$

This can be re-arranged to give:

$$\sigma_s = \frac{\gamma H s^2 - \sigma_c a^2}{s^2 - a^2} \quad (2.13)$$

so that σ_s can be derived from σ_c.

Like many approaches BS8006 actually assumes that the 'subsoil' stress is carried by a geogrid at the base of the embankment. The distributed load W_T carried by the reinforcement between adjacent pile caps (see later Section 2.4) can be expressed as follows:

For $H > 1.4(s-a)$

$$W_T = \frac{1.4s\gamma(s-a)}{s^2-a^2}\left[s^2 - a^2\left(\frac{\sigma_c}{\gamma H}\right)\right] \quad (2.14)$$

For $0.7(s-a) \le H \le 1.4(s-a)$

$$W_T = \frac{s\gamma H}{s^2-a^2}\left[s^2 - a^2\left(\frac{\sigma_c}{\gamma H}\right)\right] \quad (2.15)$$

These equations can be re-written as (substituting for σ_s from Equation (2.13)):

For $H > 1.4(s-a)$

$$W_T = \frac{1.4(s-a)}{H} s\left[\frac{\gamma H s^2 - \sigma_c a^2}{s^2-a^2}\right] = \frac{1.4(s-a)}{H} s\ \sigma_s \quad (2.16)$$

For $0.7(s-a) \le H \le 1.4(s-a)$

$$W_T = s\left[\frac{\gamma H s^2 - \sigma_c a^2}{s^2-a^2}\right] = s\ \sigma_s \quad (2.17)$$

It has been proposed (e.g. Love & Milligan 2003) that W_T can be calculated as $\sigma_s s$. These expressions are the same as this except that the first equation (for higher embankments) contains the factor $1.4(s\text{-}a)/H$. This effectively limits the height from the embankment considered to act on the subsoil to $1.4(s\text{-}a)$, instead of H. Thus, Love & Milligan (2003) concluded that the method does not satisfy vertical equilibrium, and also that it does not consider the condition at the crown of the arch.

In this method, a critical height $H_c = 1.4(s\text{-}a)$ is defined. If the embankment height is below the critical height, arching is not fully

developed and all loads have to be supported by the geosynthetic membrane. Otherwise, it is assumed that all loads above the critical height are transferred directly to the piles as a result of arching in the embankment fill, and the soil weight below the critical height has to be supported by the geosynthetic membrane.

This method does not allow $H_c < 0.7(s\text{-}a)$ to ensure that differential settlement does not occur at the surface of the embankment top.

2.2.4 Rectangular pyramid shaped arching: Guido method (1987)

This method is quite different from other methods of analysis for soil arching. The so-called 'Guido' design method is based on empirical evidence from model tests carried out with geogrid reinforced granular soil beneath a footing confined in a rigid box (see Figure 2.6). The results suggest that multiple layers of geogrid reinforcement increase the bearing capacity, which could be interpreted as an improved angle of friction (or otherwise enhanced strength) for the composite soil/ geogrid material (Slocombe & Bell, 1998). The 'load spread' angle in the reinforced soil beneath the footing was proposed to be 45^{o} (Bell et al., 1994).

A piled embankment situation can be envisaged whereby the embankment soil is loading the pile caps, effectively inverting the arrangement above (Jenner et al., 1998). Thus, the load spread from the caps into the embankment is as shown in Figure 2.7. The arch is a triangle with 45° angle in plane strain, and a similar pyramid in the three-dimensional case. Bell et al. (1994) applied this finding to evaluate an embankment with two layers of geosynthetic reinforcement supported on vibro-concrete columns (Stewart & Filz, 2005).

When this method has been employed in construction, numerous layers of relatively low strength geogrids at specific intervals are normally used, with significant compaction between each layer, so as to achieve the maximum lateral transmission of forces.

The stress on the subsoil (σ_s) results from the self-weight of the unsupported soil mass. The value is equal to the volume of the right-triangle/pyramid multiplied by the soil unit weight, and then divided by the area over which the soil prism acts. For the two-dimensional situation, the stress acting on the subsoil is:

$$\sigma_s = \frac{\gamma(s-a)}{4} \quad (2.18)$$

For the three-dimensional situation, the equation is modified to:

$$\sigma_s = \frac{\gamma(s-a)}{3\sqrt{2}} \quad (2.19)$$

It can be seen from Equation (2.18) and (2.19), that the height of the embankment has no effect on the pressure acting on subsoil. Additionally, the friction angle of the fill material (ϕ) is not considered in this case. The load spread angle above is assumed to be justified for compacted granular fill reinforced with multiple layers of geogrid. The experiment was undertaken within a rigid box, and thus confining the granular material may have caused the material strength to be enhanced artificially.

This approach is similar to equations for arching at the crown of the embankment proposed by Hewlett & Randolph (1988) when an allowance for a thickness of infill material of (s-a)/2 (see Equation (2.9)) and (s-a)/$\sqrt{2}$ (see Equation (2.10)) was made in 2D and 3D cases respectively (based on the maximum thickness). However, in the Guido method, the average values of thickness are lower by factors of 2 and 3 respectively.

Additionally, the Guido method does not consider any additional stress from the arch itself (σ_i, see Equation (2.9) or Equation (2.10)).

Love & Milligan (2003) point out that gravity in the embankment is operating in the opposite sense to that in Guido et al's laboratory tests; and the self weight of the soil in the arch area therefore acts to reduce confinement. Additionally, the method requires the underlying subsoil and geogrid to have sufficient strength to completely carry the weight of the fill in the pyramid. Love & Milligan (2003) suggest that the Guido method may experience difficulties when dealing with situations where support from the exiting subsoil is very low or negligible. The Guido method concentrates more on reinforcement rather than on the actual physical arching process.

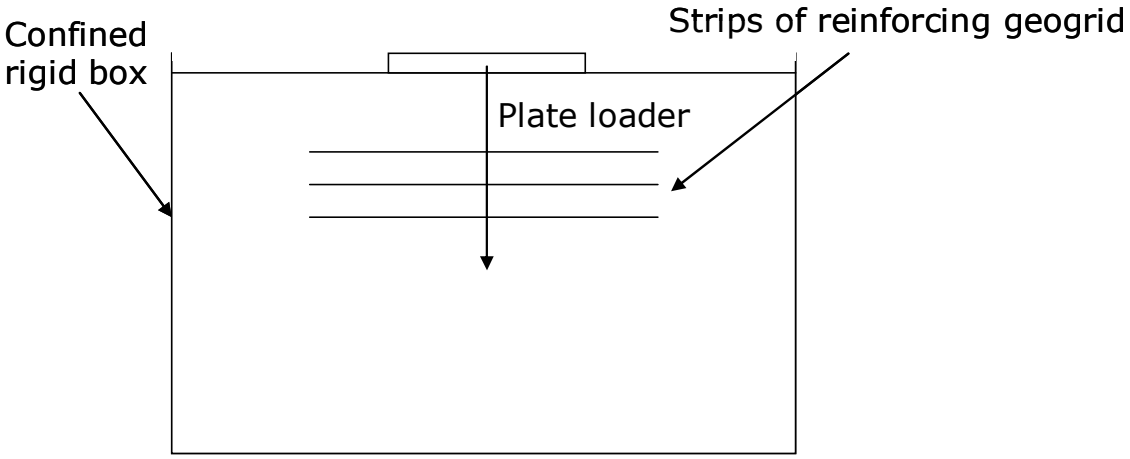

Figure 2.6. Guido's experimental set-up (geogrid-reinforced sand in a confined, rigid box, the geogrid is used to improve the bearing capacity of the foundation soil)

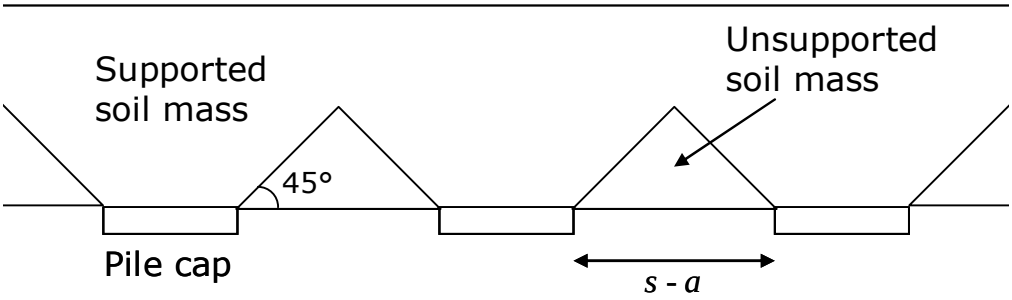

Figure 2.7. The mechanism of load spreading from the pile caps through an embankment which is geogrid-reinforced near the base (shown in 2D)

2.2.5 Other mechanisms

Carlsson (1987) and Han & Gabr (2002) assume a trapezoidal shape (which is in effect a truncated triangle or pyramid). The Carlsson reference is presented in Swedish, but it is discussed by Rogbeck et al. (1998) and Horgan & Sarsby (2002) in English. In a plane strain situation, a wedge of soil is assumed under the arching soil, where the internal angle at the apex of the wedge is equal to 30^{o} (see Figure 2.8). The Carlsson Method adopts a critical height approach, and thus the additional overburden above the top of the wedge is transferred directly to the piles. As presented by Van Eekelen et al. (2003), the critical height was 1.87(s-a) in two-dimensions. Ellis & Aslam (2009a) considered extending this theory to a 3-dimensional pyramid of the same height, the average height would be 1.87/3(s-a) = 0.62(s-a), and hence $\sigma_s/\gamma(s\text{-}a)$ = 0.62.

Comparing with the Guido method (see Section 2.2.4), an angle of 45^{o} to the horizontal is assumed for the edges of the pyramid. This is considerably lower than the Carlsson method, and thus gives relatively low results, as shown in Equation (2.19): $\sigma_s/\gamma(s\text{-}a)$ = 0.24. However, the Guido method does inherently assume that the soil is reinforced.

The German standard (EBGEO, 2004) is based on a three-dimensional arching model proposed by Kempfert et al. (1997), which appears similar to the Hewlett & Randolph (1988) approach. However, the average vertical pressure acing on the soft subsoil was obtained by considering the

equilibrium of dome shaped arches of varying size in the 'infill' material beneath a hemisphere (see Figure 2.9). EBGEO (2004) recommends the use of geosynthetic reinforcement but the arching effect and the membrane tension are dissociated.

Naughton (2007) proposed a new method for calculating the magnitude of arching, based on the 'critical height' for arching in the embankment. The critical height was calculated assuming that the extent of yielding in the embankment fill was delimited by a log spiral emanating from the edge of the pile caps (see Figure 2.10). An expression for the critical height (H_C) is then:

$$H_C = C(s-a) \quad (2.20)$$

Where:

$$C = 0.5e^{\frac{\pi}{2}\tan\phi} \quad (2.21)$$

Naughton noted that the effect of ϕ on the critical height of the embankment was significant. Figure 2.11 shows the critical height varying from 1.24(s-a) to 2.40(s-a), as ϕ increases from 30° to 45°. Naughton concluded that the critical height increases in proportion to the angle of friction.

Naughton suggests that the stress on the subsoil corresponds directly to the height of the zone of yielding so that

$$\sigma_s = \gamma H_C = \gamma C(s-a) \quad (2.22)$$

and hence

$$\frac{\sigma_s}{\gamma(s-a)} = C \qquad (2.23)$$

However, this implies that the stress on the subsoil increases as the soil strength increases, which is *not* the expected trend of behaviour.

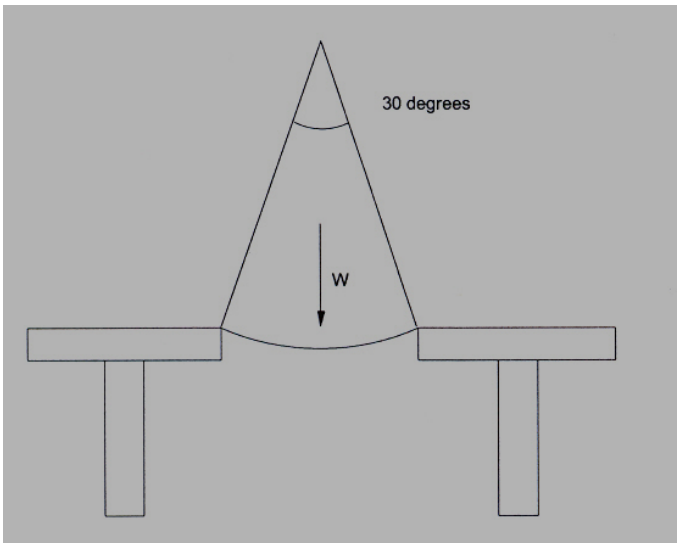

Figure 2.8. Soil wedge assumed by Carlsson (1987) and Han & Gabr (2002)

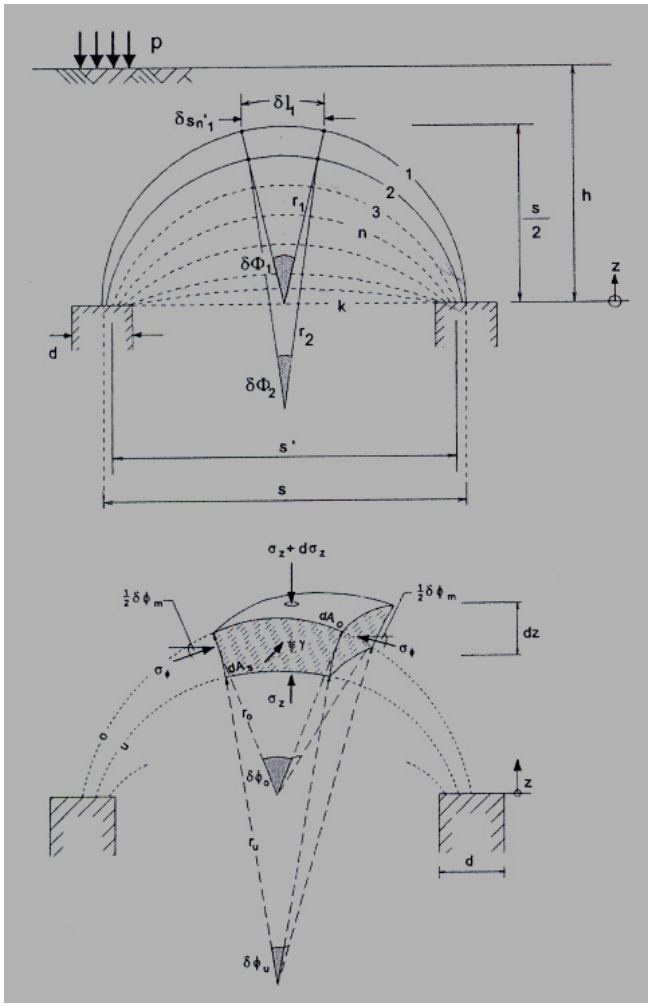

Figure 2.9. Geometry of arching and equilibrium of stresses, German standard (EBGEO, 2004)

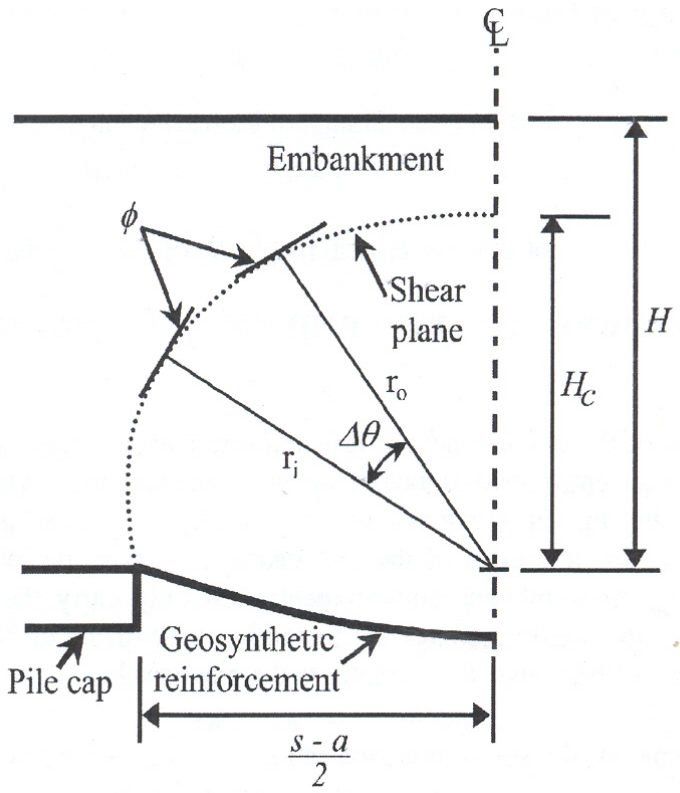

Figure 2.10. Geometry of assumed log spiral shaped yield zone (Naughton, 2007)

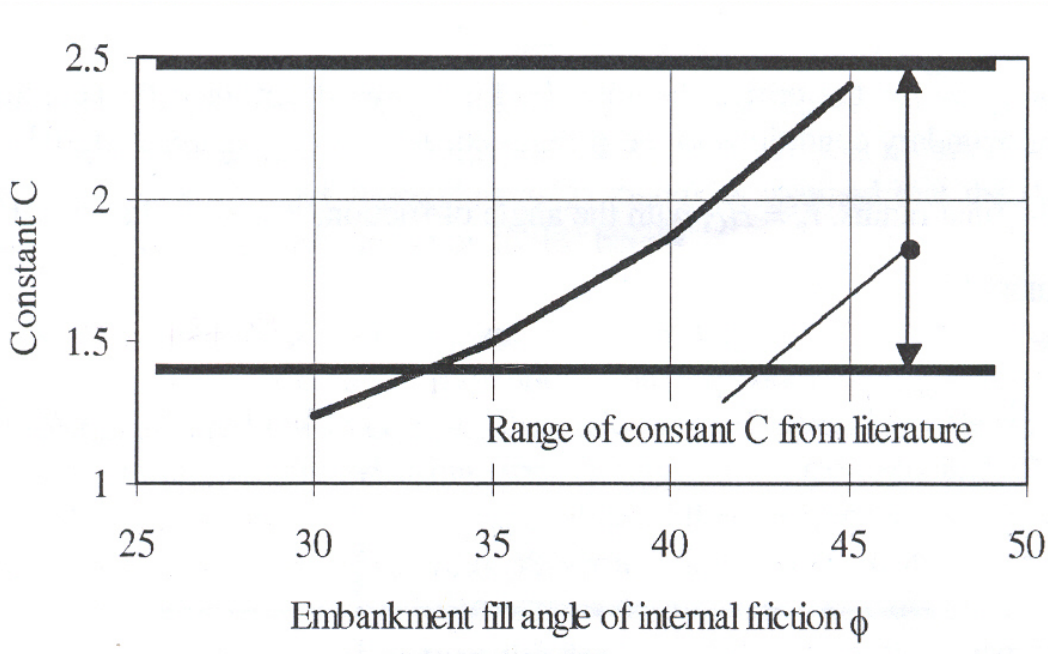

Figure 2.11. Influence of ϕ on the critical height H_C of the embankment (Naughton, 2007)

2.3 Introduction to the Ground Reaction Curve

The above methods consider that there is sufficient tendency for the soft subsoil to settle that arching of the embankment material will occur, but they do not specifically link arching with the amount of support from the subsoil. An interesting contrast to this is the concept of a 'Ground Reaction Curve' (GRC) used to determine the load on a plane strain underground structure such as a tunnel, Figure 2.12.

By combining experimental data from centrifuge 'trapdoor' tests with some theories on load redistribution due to arching, a novel approach for determining the vertical loading on underground structures in granular soils has been developed (Iglesia et al., 1999). This approach creates the ground reaction curve, which is a plot of load on an underground structure as the structure deforms causing the soil above it to arch over it.

As can be seen in Figure 2.13, it is proposed that as the trapdoor (or underground structure) is gradually lowered, the arch evolves from an initially curved shape (1) to a triangular one (2), before ultimately collapsing with the appearance of a prismatic sliding mass bounded by two vertical shear planes emanating from the sides of the trapdoor (3). Compared to analysis of a piled embankment the structure is analogous to the subsoil. It can be seen that the curved arch is similar to Hewlett & Randolph's semi-circular arch. The triangular arch is similar to Guido's triangular arch (although the angle is somewhat greater than 45°), and the prismatic sliding mass is similar to Terzaghi's sliding block.

A methodology has been proposed by Iglesia et al. (1999) not only for determining the vertical loading on the structure, but also for relating this to the movement of the roof of the underground structure. This is referred to as a 'Ground Reaction Curve' (GRC) for the overlying soil. In the GRC, a dimensionless plot of normalised loading (p^*) vs. normalized displacement (δ^*) is used:

$$p^* = \frac{p}{p_0} \quad (2.24)$$

$$\delta^* = \frac{\delta}{B} \quad (2.25)$$

Where:

p = the support pressure from the roof of the underground structure to the soil above (kN/m^2)

p_0 = the nominal overburden total stress at the elevation of the roof derived from the thickness of overlying soil (and any surcharge at the ground surface) (kN/m^2)

B = the width of the underground structure (m)

δ = the settlement of the roof (m)

It can be seen in Figure 2.14 that the GRC is divided into four parts – the initial arching phase, the maximum arching (minimum loading) condition, the loading recovery stage, and the ultimate state. These will be considered in turn below.

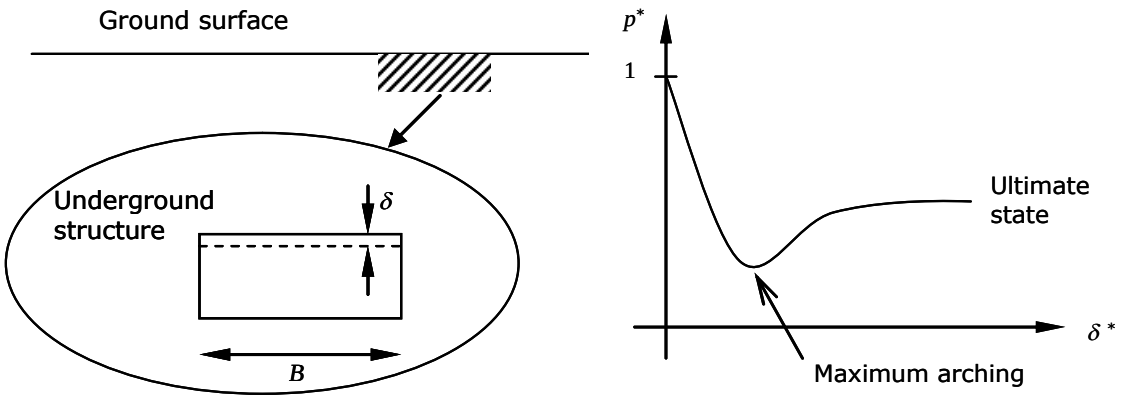

(a) Underground structure (b) Ground reaction curve (GRC)

Figure 2.12. Ground reaction curve for underground tunnel (Iglesia et. al., 1999)

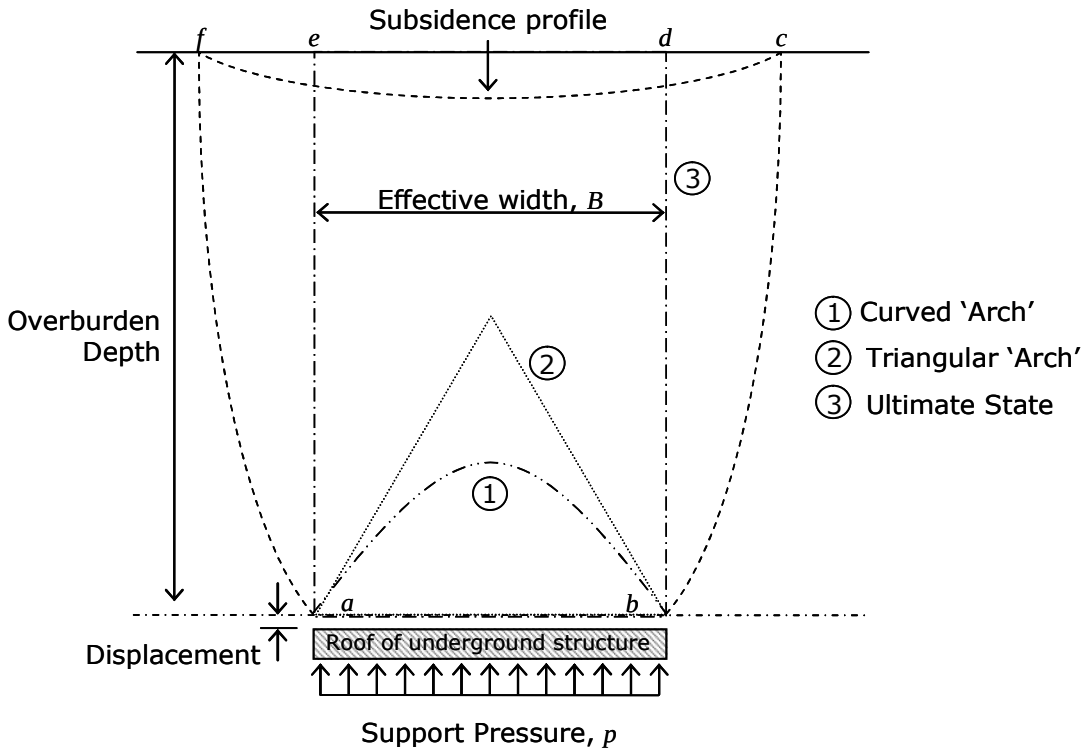

Figure 2.13. Arching evolution (Iglesia et al., 1999)

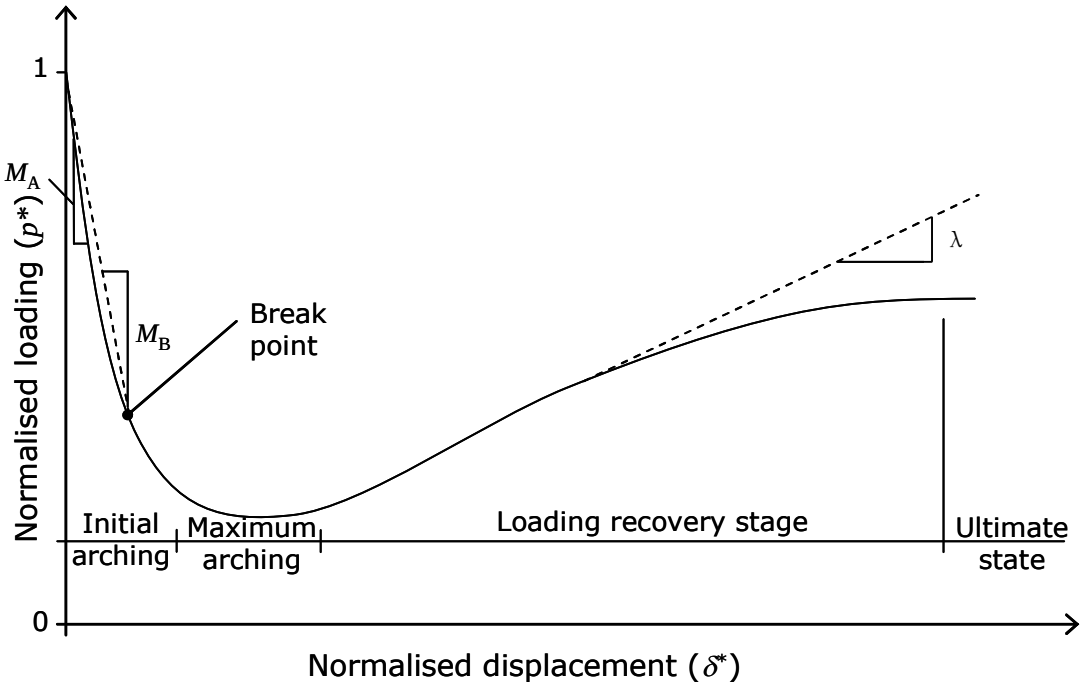

Figure 2.14. Generalized Ground Reaction Curve (GRC) (Iglesia et al., 1999)

Initial arching

As shown in Figure 2.14, the GRC starts with the geostatic condition ($p_0 = \gamma H$). The initial 'convergence' of the soil toward the underground structure causes a fairly abrupt reduction in load on the structure. In this phase, the arch starts to form. A modulus of arching (M_A) is defined as the rate of initial stress decrease in the normalised plot. Iglesia et al. (1999) propose that based on the centrifuge trapdoor experiments with granular media, the modulus of arching has a value of about 125. Thus p^* tends to zero (or its minimum value, when this approaches zero) when $\delta^* > 1$ %.

Break point and relative arching ratio

As the underground opening converges toward a state of maximum arching (minimum loading), the GRC changes from the initial linear line to a curve (since p^* can only approach zero and certainly cannot be negative). Iglesia et al. (1999) propose a method of determining the approximate shape of this part of the curve – the reader is referred to the original paper for further details.

Maximum arching

Maximum arching occurs when the vertical loading on the underground structure reaches a minimum. Iglesia et al. (1999) describe this corresponding to a condition in which a physical arch forms a parabolic shape just above the underground structure. In addition, this tends to occur when the relative displacement between the underground structure and the surrounding soil is about 2 to 6 % of the effective width of the structure (B).

Loading recovery stage

This stage is the transition from the maximum arching (minimum loading) condition to the ultimate state (where the arch has become a prism with vertical stress sides as proposed by Terzaghi). Iglesia et al. (1999) characterise this stage by the load recovery index (λ). Based on

centrifuge tests, they showed that the load recovery index increases with increasing B/D_{50} (D_{50} is the average particle size) and decreasing H/B. This aspect of behaviour is potentially of considerable significance, since it represents 'brittle' arching response.

Ultimate state

As the surrounding soil continually converges toward the underground structure, the arch will eventually collapse. Figure 2.13 shows the arching profile as presented by Finn's elasticity solution and Terzaghi. As the plane ab moves vertically the soil yields and the wedges aef and bdc move to the right and left respectively. As mentioned by Terzaghi, the real surfaces of sliding are curved and the real width of deformation at the surface of the soil layer may be considerably greater than the width of the yielding strip. Hence the surface of sliding must have a shape similar to that indicated in Figure 2.13 by the lines af and bc. However, Terzaghi pragmatically assumed a sliding prism but maintained that it is on the 'unsafe' side (the friction along the vertical sections cannot be fully mobilised).

Iglesia et al. (1999) use Equation (2.6) (Terzaghi's method for the plane strain situation) to determine the ultimate stress on the structure.

2.4 Reinforcement

2.4.1 Introduction

Geogrid reinforcement is commonly used in soils. By placing geogrid at the base of the embankment, it is possible to improve support to the embankment. The tension will provide support between the pile caps (Figure 2.15). At the edges of the embankment it also prevents lateral spreading (Hewlett & Randolph, 1988). However, these two functions are normally considered independently, and the former is of most interest in the context of this work.

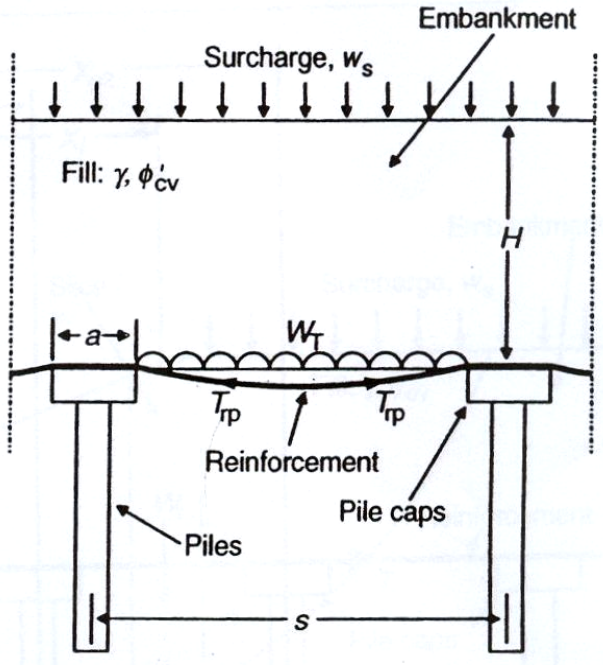

Figure 2.15. W_T is the vertical load acting on a reinforcement strip between two adjacent pile caps (from BS8006)

2.4.2 Methodology

As described by Ellis & Aslam (2009b), the effect of additional capacity to carry vertical load from geogrid layer(s) could be added based on purely tensile response (but not accounting for any other interaction). They proposed that assuming the geogrid was subjected to a uniform vertical load and deforms as a parabola, using a plane strain approach the constant horizontal component of tension can be linked to the load acting on it as follows (e.g. Russell et al., 2003):

$$T = \frac{wl^2}{8\delta_g} \quad (2.26)$$

Where:

T = the constant horizontal component of tension in the geogrid (kN/m 'into the page')

w = the uniform stress acting on the geogrid (kN/m^2)

l = the length of the span (m)

δ_g = the maximum sag (vertical deflection) of the geogrid (m)

The average strain based on the total extension in the geogrid (ε) can be expressed in terms of the maximum sag as follows:

$$\varepsilon = \frac{8}{3}\left(\frac{\delta_g}{l}\right)^2 \quad (2.27)$$

Note that ε increases as the square of δ_g.

The equation links tension and strain in the geogrid assuming linear response:

$$T = k\varepsilon \tag{2.28}$$

Where,

k = the stiffness of the geogrid (kN/m)

Substituting for T and ε from Equation (2.26) and Equation (2.27) respectively

$$\frac{wl^2}{8\delta_g} = \frac{8k}{3}\left(\frac{\delta_g}{l}\right)^2 \tag{2.29}$$

This can be re-arranged to express how the load which can be carried theoretically increases with the sag:

$$w = \frac{64k}{3l}\left(\frac{\delta_g}{l}\right)^3 \tag{2.30}$$

(Both side of the equation have units kN/m^2)

2.4.3 'Interaction diagram'

Ellis & Aslam (2009b) introduced an interaction diagram, which combined the Ground Reaction Curve (GRC) with the effect of subsoil and/or geogrid or geotextile reinforcement by considering the normalised load on the subsoil and corresponding normalised settlement (see Figure 2.16).

The settlement response of the subsoil to stress acting on it was determined from one-dimensional compression (the potential preconsolidation stress was also introduced; see Figure 2.16(a)):

$$\sigma_s = E_0' \frac{\delta_s}{h_s} \quad (2.31)$$

Where:

h_s = the thickness of the subsoil (m)

E_0' = the one-dimensional stiffness of the subsoil (kN/m^2)

δ_s = the settlement at the surface of the subsoil (m)

Figure 2.16(a) shows the combination of the GRC and the effect of the subsoil. Ellis & Aslam (2009b) argued that if the GRC and subsoil response meet, the subsoil is able to carry the 'remaining' embankment load accounting for arching at the given compatible settlement. Otherwise, there is not equilibrium.

Figure 2.16(b) shows the combination of GRC and the effect of subsoil and geogrid. Ellis & Aslam (2009b) concluded that if the stress from the

embankment GRC can be carried by the combined response of the subsoil and geogrid (adding the stresses for each component at a given settlement), the lines intersect, then stability should result.

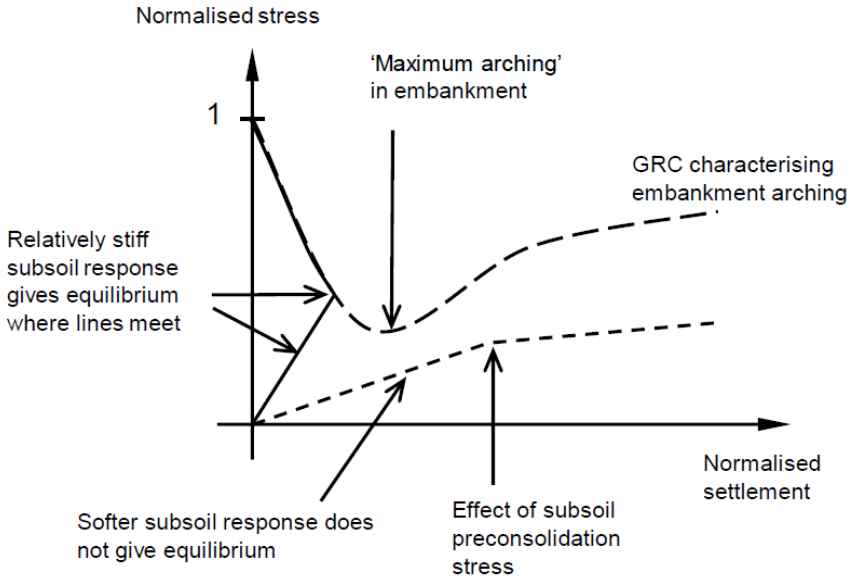

(a) Schematic illustration of embankment and subsoil response to give equilibrium

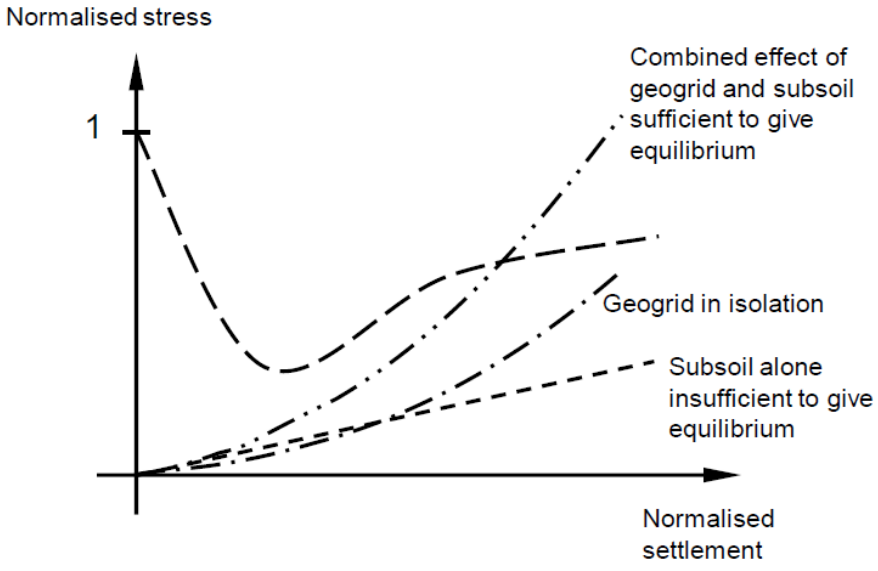

(b) Schematic illustration of combination of subsoil and geogrid response to potentially give equilibrium

Figure 2.16. Interaction diagrams for arching, subsoil and geogrid response (from Ellis & Aslam, 2009b)

2.5 Key studies

2.5.1 Numerical and analytical studies

A number of numerical analyses (e.g. Finite Element Modelling (FEM) and Fast Lagrangian Analysis of Continua (FLAC)) of piled embankments constructed on soft foundation have been undertaken. Models considered either plane strain, axisymmetric (this is potentially questionable) or full three-dimensional conditions. The numerical results are often compared with analytical studies, for instance by plotting

- the 'Stress Reduction Ratio' (SRR = the ratio of the average vertical stress remaining to be carried by the subsoil and/or reinforcement after arching has occurred to the nominal vertical stress due to the embankment fill). A SRR of 1.0 implies no arching, and the SRR reduces ultimately tending to zero as the effects of arching increase.
- the 'Efficacy' (the proportion of the embankment weight carried by the piles rather than the subsoil and/or reinforcement). Efficacy increases (tending towards 1.0) as the effect of arching increases.
- the 'Stress Concentration Ratio' (the ratio of the stress on the pile caps to that on the subsoil and/or reinforcement). This value also increases as the effect of arching increases.

Examples will be discussed below.

Russell & Pierpoint (1997) compared a number of design methods (BS8006, 1995; Terzaghi, 1943; Hewlett & Randolph, 1988 and Guido, 1987) for the assessment of SRR in a piled embankment. Two case studies were investigated: the A13 piled embankment and the Second Severn Crossing trial embankment. For the A13 piled embankment, the Terzaghi and Hewlett & Randolph methods gave the highest stress on the reinforcement, while BS8006 gave slightly lower value. However, the Guido method was significantly lower at only about 17 % of the Terzaghi and Hewlett & Randolph methods. The tension in the reinforcement also reflected these observations. For the Second Severn Crossing trial embankment, BS8006 gave the highest stress on the reinforcement. The Terzaghi and Hewlett & Randolph methods gave 60 % of the BS8006 value and the Guido method only 10 %. Again the tension in the reinforcement followed a similar pattern.

Russell & Pierpoint (1997) also present three-dimensional finite difference analyses by using the program FLAC-3D. Results from the numerical analyses were compared with existing design methods in order to understand the behaviour of the piled embankment. For the A13 piled embankment, the numerical result for stress on reinforcement gave approximately twice the value of the Terzaghi and Hewlett & Randolph methods. However, the tension in the reinforcement showed quite good correlation with the Terzaghi and Hewlett & Randolph methods. For the Second Severn Crossing trial embankment, the numerical study showed slightly less stress on the reinforcement than the Terzaghi and Hewlett &

Randolph methods. For the tension in the reinforcement, the numerical result was similar to Guido method.

Russell & Pierpoint (1997) concluded that the BS8006 method appeared inconsistent when compared with the numerical analyses: at the A13 the SRR was underpredicted whilst for the Second Severn Crossing trial embankment it was overpredicted. The design method following Guido's research appeared to consistently underpredict the numerical results. The Terzaghi and Hewlett & Randolph methods predict similar values and appear reasonably consistent although they do underpredict the stress on the reinforcement at the A13. They also noted that the maximum tension in the geogrid occurred at the edge of the pile cap.

Kempton et al. (1998) compared two- and three-dimensional numerical (FLAC) analyses for various piled embankment geometries. In both cases, the SRR reduced (i.e. the effects of arching increase) as a/s and h increases until a point of 'full arching' was reached after which the stress reduction ratio is virtually constant. The maximum displacement and tension in the geosynthetic increase with the SRR. The authors stated that the SRR is significantly higher in the 3D analyses than in 2D analyses for any given a/s ratio. Thus, the maximum displacement at the base of the embankment and the tension generated in the geosynthetic were underestimated in the 2D situation. Kempton et al. (1998) also compared 2D and 3D FLAC analysis with the BS8006 (1995) design method. They found that BS8006 overestimated the geosynthetic tension for all geometries in 2D and underestimated the tension in 3D. For a/s between

0.2 and 0.6 with H/s between 0.6 and 1.4, the BS8006 geosynthetic tensions were approximately 30 % lower than the 3D FLAC analysis. For the other geometries the difference was larger. However, if load factors were used in the BS8006 equations, BS8006 would overestimate the tension in the geogrid by 30 % in both cases.

Fakher & Jones (2001) argued that the bending stiffness of reinforcement should be considered in the design of earthworks over 'super soft' clay (the water content is higher than its liquid limit, with a very low yield stress). The analyses were performed using FLAC. Their results showed that the higher the bending stiffness of reinforcement the higher the bearing capacity of the soft clay. However, the effect of bending stiffness of reinforcement will not be as important when the underlying clay was not in a super soft state.

Han & Gabr (2002) performed a numerical study on reinforced piled embankments with subsoil using FLAC. In the numerical model, each single pile was considered as having an 'effective' equivalent circle. This allowed them to use an axisymmetric analysis. The legitimacy of this approach has however been questioned (Russell & Pierpoint, 1997), since the unit cell is actually square. They proposed that the 'soil arching ratio' (equivalent to the SRR) decreases with an increase in the height of embankment fill, an increase in the elastic modulus of the pile material, and a decrease in the tensile stiffness of geosynthetic. This seems reasonable since all these effects would tend to promote arching in the

embankment. Like Russell & Pierpoint (1997) the authors noted that the maximum tension in the geogrid occurred at the edge of the pile cap.

Rowe & Li (2002) investigated the time-dependent behaviour of embankments constructed over rate-sensitive foundation soils, using the finite element technique (AFENA). The authors stated that when embankments are constructed over rate-sensitive foundation soils at typical construction rates, the visco-plastic behaviour (i.e. creep and stress-relaxation) of foundation soils after the end of construction can have a significant effect on embankment performance, although this can be mitigated by the use of reinforcement. Their findings showed that the use of reinforcement can significantly reduce creep deformations of the foundation soils. The stiffer the reinforcement, the less the creep deformations that are developed (other things being equal).

Russell et al. (2003) presented a new design method for reinforced piled embankments based on Terzaghi's mechanism, supported by results from 3D FLAC analyses. The paper also considers the tension acting in geosynthetic reinforcement at the base of the embankment.

Naughton & Kempton (2005) compared a number of design methods: BS8006 (1995), Terzaghi (1943), Hewlett & Randolph (1988), Jenner et al. (1998) (the 'Guido' method), Russell et al. (2003) and Kempfert et al. (2004) using predictions of SRR and the tension in the reinforcement.

Stewart & Filz (2005) compared five existing methods: BS8006 (1995), Terzaghi (1943), Hewlett & Randolph (1988), Guido (1987) and the Carlsson (1987) design methods using SRR values. Like other authors they reported that the SRR decreases (i.e. arching is more effective) with increasing a/s and H/s. However, for a given geometry, the predicted SRR values vary greatly from one method to the next. They reported that the SRR value is more sensitive to variations in the a/s value for the BS8006 method than for any of the other methods (Ellis & Aslam, 2009a later noted that the SRR tends to zero for this method as a/s approaches a critical value). For many geometries, the Terzaghi, Hewlett & Randolph and Carlsson method gave similar values of SRR. As reported by other authors, the Guido method generally gave very low values of SRR compared to the other methods.

Stewart & Filz (2005) also investigated the impact of the compressibility of the soft clay between the piles on SRR by parametric numerical analyses of a piled embankment using 3D FLAC analyses. They found that as the clay compressibility increases, the SRR approaches values obtained from the Hewlett & Randolph method and the Carlsson method. The Guido method greatly underestimated the SRR.

Stewart & Filz (2005) proposed that the compressibility of the ground between the piles has a large impact on the vertical load applied by an embankment to geosynthetic reinforcement in piled embankments. For this reason, they suggested that the compressibility of the ground between the piles should be a factor in the design of piled embankments.

Cao et al. (2006) presented an analytical method for determining efficacy, which was based on the principle of minimum potential energy. A similar arrangement to the Han & Gabr (2002) axisymmetric 'unit cell' was used, with springs to model the pile and subsoil response. Their findings showed that the efficacy decreased with increasing pile spacing to embankment height ratio, and increased with increasing pile cap width. They also showed that the shear modulus of the embankment fill only slightly increased the efficacy of arching in the embankment. The usefulness of geotextile reinforcement was questioned since it reduced the differential settlement between the pile cap and subsoil, and therefore reduced the tendency for arching. However, the authors did note that reinforcement does have the beneficial effect of transferring load from the embankment onto the pile caps. The authors claim that overall geotexitile stiffness has little influence on efficacy. However, as noted previously Russell & Pierpoint (1997) have argued that assumptions of axisymmetry do not accurately reproduce the arching behaviour.

Chen et al. (2006b) and Chen et al. (2008) introduced an approximate closed-form solution, which considers soil arching in an embankment, the settlement of the substratum, and the corresponding negative skin friction acting on the piles. The method was compared with FEM analyses (using the package Plaxis), and the results showed reasonable agreement with the two examples considered, including variation of subsoil stiffness.

Chen & Yang (2006) derived analytical solutions for a reinforced piled embankment involving maximum deformation of the reinforcement and

the stress concentration ratio from the subsoil to the piles. They presented their results as the 'allowable' embankment height, which increased with pile diameter, the stress concentration ratio and maximum geogrid settlement. However, by the authors own admission the method has a significant drawback since the stress concentration ratio is required as an input to the analysis.

He et al. (2006) used FE analysis to model piled embankments which had lime fly ash and EPS (lightweight material with density of 20 kg/m^3) as part of the fill material. The authors compared numerical results with several theoretical methods (Terzaghi, 1943; BS8006, 1995; Hewlett & Randolph, 1988 and Low et al., 1994) using the soil arching efficacy.

Their findings showed that the height of fill has no influence on efficacy of embankment in Low et al.'s method. The efficacy increased slightly with the height of fill in the BS8006 method, and increased steadily in Terzaghi's method. For Hewlett & Randolph's method, efficacy either increased or (somewhat surprisingly) decreased with increase of the height of fill depending on the pile cap width. However, the results of the FEM analyses were different to all the design methods. The numerical analyses also showed that the vertical stress in the fill between the pile caps increased with embankment height to a maximum value then decreased. The authors suggested that the use of Expanded Polystyrene Styrofoam (EPS) increased the efficacy of the embankment. Moreover, unsurprisingly the efficacy increased with increase of the width of the pile cap.

Yan et al. (2006) modelled reinforced embankments on deep-mixed columns using FLAC in plane strain. The following factors were considered: the elastic modulus of the deep-mixed columns, the clear spacing between columns, the elastic modulus of the soft soil, and the tensile stiffness of geosynthetics. The results of the analyses were presented using maximum and differential settlement at the embankment crest. The findings showed that the inclusion of geosynthetics can increase the stress transfer to the deep-mixed columns, and reduce the maximum and differential settlements at the crest of the embankment. Unsurprisingly, increasing the stiffness of the soft subsoil also reduced settlement. The authors suggested that reinforcement with tensile stiffness of 3000 kN/m should use for pile spacing of 2.0 to 2.5 m.

Naughton et al. (2008) presented the historical development of analysis of piled embankments by discussing the developments in understanding of the arching mechanism, and how the geometry of piles and reinforcement strength requirements have changed over the past quarter of a century. The authors suggested that analysis of piled embankments should consider three-dimensional effects, and the support provided by the subsoil should also be considered in design. Finally, they concluded that the design of piled embankments was complex and was not yet fully understood.

Potts & Zdravkovic (2008a) investigated the behaviour of a geosynthetic reinforced fill Load Transfer Platform (LTP) over a void, as considered in BS 8006 (1995). Numerical analyses were conducted using the Imperial

College Finite Element Program (ICFEP), also comparing the output with results from 1g physical models of a 'trapdoor'. The authors considered the effects of void geometry, the properties of the reinforcement and the properties of the fill layer. Two types of void were considered: an infinitely long void (plane strain) and a circular void (axisymmetric). Their findings showed that BS8006 overestimated the tensile force acting in the reinforcement since the effect of arching in the LTP was not considered. They also demonstrated that the shape of the deformed reinforcement was more accurately described by a segment of a circle rather than a parabola (as assumed in BS8006). The paper also comments that BS8006 may be unconservative for the damage assessments of overlying infrastructure or buildings, since it predicts a wider settlement trough and hence lower slopes for a given maximum settlement.

Reporting other results from these analyses Potts & Zdravkovic (2008b) considered the suitability of the theories developed by Terzaghi (1943) and Hewlett & Randolph (1988) when applied to arching over a void. In the finite element analyses, arching behaviour was assessed by considering the orientation of major principal stress, profiles of vertical stress in the fill layer, and contours of stress level. Their findings showed that Terzaghi's method was more suitable in characterising stress changes in the fill overlying the void in both the plane strain and axisymmetric situations. However, the difficulty in applying Terzaghi's method to prediction of the stress in the soil over the void was determination of the earth pressure coefficient (K) along the assumed vertical shear surface

(see Figure 2.1). They concluded that a value of K = 1.0 gave good correspondence with the finite element analyses.

Taechakumthorn & Rowe (2008) provided a study of the combined effects of geosynthetic reinforcement and Prefabricated Vertical Drains on both the short-term and long-term behaviour of embankments on rate-sensitive soil. The analyses were performed using the finite element technique (AFENA). Their results indicated that reinforcement not only improves the stability of the embankment but also minimizes vertical and horizontal deformation in the foundation. Moreover, Prefabricated Vertical Drains work together with reinforcement to reduce differential settlement and increase the rate of excess pore water dissipation in the soil.

Van Eekelen & Bezuijen (2008) analysed BS8006 (1995) from the basic starting points, including Marston's equation for the load on the pile caps, the assumption of no support from the soft subsoil, and assumptions regarding the line load W_T on the reinforcement and the associated catenary equation. They concluded that BS8006 has some fundamental drawbacks. For instance the equations are plane strain rather than three-dimensional, vertical equilibrium was not satisfied (as also previously noted by Love & Milligan, 2003), and the embankment soil properties do not have any influence on the predictions. Finally, an adaptation of the equations was presented, addressing some of these points.

Abusharar et al. (2009) presented an analytical method for analysis of reinforced piled embankments. This method was based on Low et al.

(1994). The main refinements were: inclusion of a uniform surcharge, consideration of square pile caps (rather than considering a plane strain situation), and taking into account the 'skin friction mechanism' (soil-geosynthetic interface resistance). They suggested that further studies should be undertaken using full-scale or centrifuge prototypes to investigate the validity of their theoretical model. The analytical model presented will be considered further in Chapter 9.

2.5.2 Physical modelling

Physical modelling generally uses reduced scale models which are either tested in the laboratory at '1g', or in a geotechnical centrifuge at a g-level directly corresponding to the scale factor, so that stress level in the model corresponds to an equivalent full-scale prototype. Several 1-g tests are referred to below, but it should be remembered that the behaviour of these models may not be representative of a larger structure, and that scaling of geogrid stiffness etc will be questionable under these circumstances.

Low et al. (1994) investigated the arching in unreinforced and reinforced embankments supported by 'cap beams' on soft ground using 1g model tests and theoretical analysis. The 'cap beams' were placed along a row of piles, to promote arching in plane strain rather than three dimensions. Hence the authors used (and extended) the theory of 2D arching initially proposed by Hewlett & Randolph (1988) for comparison with their results. They found that the analytical solution showed reasonable agreement with the model test results for the case with no reinforcement, but the agreement was less satisfactory for cases with reinforcement. They suggested that further studies should use centrifuge or full-scale prototypes to investigate the validity of the analytical model at prototype conditions.

Van Eekelen et al. (2003) performed a plane strain 1g test, in which the soft subsoil between the piles was simulated with saturated foam plastic

blocks, inside watertight rubber bags, which were allowed to drain gradually via an outlet, mimicking consolidation of the subsoil. The authors considered states of both complete or full arching and incomplete arching in their studies. The test results were then compared with 2D calculation methods (Rogbeck, 1998; Carlsson, 1987; McKelvey, 1994 and BS8006, 1995). Their comparisons showed that results using the Rogbeck/Carlsson method (extended with incomplete arching) and the McKelvey method underestimated the load on the reinforcement. They also commented that BS8006 gave inconsistent results for increasing embankment thickness, and Rogbeck/Carlsson method gave inconsistent results for incomplete-arching-situations due to a limited embankment thickness.

Jenck et al. (2005) performed small scale 1-g physical plane strain models. The embankment was modelled using a 'Taylor-Schneebeli analogical material', which was an assembly of steel rods with diameter of 3, 4 and 5 mm. The subsoil was modelled by foam and the piles were modelled by metallic elements, which allow displacement to be readily determined from images. Their findings showed that the total and differential settlement of the embankment reduced with increasing pile cap size, and the efficacy increased with the embankment height. They also proposed that the arching effect was more efficient for greater rod size in comparison to the geometrical dimensions.

Jenck et al. (2005) also compared their physical results with design methods (e.g. Low et al., 1994; Terzaghi, 1943; BS8006, 1995 and

McKelvey, 1994). They commented that the test results showed good agreement with the method proposed by Low et al. (1994). They also stated that the different results between the Terzaghi and Mckelvey methods show their sensitivity to K (the earth pressure coefficient). They found that BS8006 was not intended to be applied to a plane strain situation, and it did not take into account the friction angle of the embankment fill.

In a further publication based on this work Jenck et al. (2006) presented the results of a parametric study which indicated that the amount of load transfer (arching) and settlement were significantly affected by the height of the embankment and the pile cap spacing ratio. The stiffness of the geogrid had some impact on these aspects of behaviour, whilst the stiffness of the subsoil had only limited impact on settlement.

As in the majority of studies increasing embankment height, pile cap area and geogrid stiffness improved arching, and hence reduced settlement. Increasing the subsoil stiffness reduced arching, but since the subsoil carried some of the embankment load settlement was reduced.

Britton & Naughton (2008) presented a 1:3 laboratory model of a small plan area of a piled embankment to investigate the influence of the 'critical height' in design. The base of the model essentially consisted of a trapdoor which could be lowered between pile caps set out on a square grid. Their results were compared with current design methods (BS8006, 1995; Kempfert et. al., 2004; Russell et al.,2003; Jenner et al., 1998;

Hewlett & Randolph, 1988; Terzaghi, 1943; Horgan & Sarsby, 2002 and Naughton, 2007) using the critical height and the SRR (stress reduction ratio). Their findings showed that for the value of the critical height, the model test results were in close agreement with Naughton's approach, and within the range given by Horgan & Sarsby. For the SRR, the model test results showed good agreement with Terzaghi and Naughton's methods.

Chen et al. (2008a) performed plane strain 1g laboratory tests to investigate soil arching in piled embankments with or without reinforcement. Two water bags were used to model the subsoil, and water was permitted to flow out gradually mimicking the consolidation of the foundation subsoil.

Their model results showed that stress concentration ratio and settlement are influenced significantly by the embankment height, the ratio of the capping beam width to clear spacing and reinforcement tensile strength. The author's findings showed that the stress concentration ratio increased with embankment height. A minimum embankment height of $1.6s$ (where s is the clear spacing between capping beams) was suggested necessary to ensure uniform settlement at the embankment surface. They also stated that the use of reinforcement to improve the stress concentration ratio was more effective as the embankment height increased.

Chen et al. (2008a) also compared their results with current design methods (Low et al.,1994; Terzaghi, 1943 and BS8006, 1995). The test

results showed good agreement with the method proposed by Low et al. (1994). The Terzaghi method gave good predictions of the maximum stress concentration ratio, whilst BS8006 underestimated this variable. The authors suggested that centrifuge or full-scale prototypes should be used in further studies to evaluate the validity of the current design methods to real structures.

Heitz et al. (2008) investigated differences in arching arising from use of a rectangular of triangular grid of piles in plan, using FEM analyses. They also carried out large scale model tests to examine the stress distribution in the soil above the pile heads, and the effect of cyclic loading (i.e. traffic on highway and railway embankments) on reinforcement. They found that cyclic loading lead to larger settlement and higher strains in the geogrid compared to static loading.

Ellis & Aslam (2009a and b) presented results from a series of centrifuge tests examining the performance of unreinforced piled embankments constructed over soft subsoil in terms of stress acting on the subsoil, and differential movement at the surface of the embankment. They compared the centrifuge test results with predictive methods (e.g. BS8006, 1995; Terzaghi, 1943; Hewlett & Randolph, 1988; and the 'German Recommendations', 2004) over a continuous range of embankment heights.

Their findings showed that most methods appear to give somewhat higher estimates of subsoil stress (σ_s) than the centrifuge tests for medium

embankment heights, where the centrifuge tests indicated $\sigma_s/\gamma(s\text{-}a) \approx 0.5$ (s is the centre-to-centre pile cap spacing, and a is the square pile cap dimension). For embankments higher than about $3(s\text{-}a)$ it was not possible to reliably determine σ_s in the centrifuge tests, since the efficacy was close to one, and relatively little load was carried by the subsoil.

Ellis & Aslam (2009a) pointed out that BS8006 tends to give relatively low predictions of σ_s for high embankments. Terzaghi's approach initially shows steady increase in $\sigma_s/\gamma(s\text{-}a)$ with embankment height, but ultimately tend to an asymptotic value of approximately 2-3 for high embankments for an earth pressure coefficient K less than 1.0 (e.g. using Equation (2.7)). More recent work by Potts & Zdravkovic (2008b) shows that K = 1.0 gives better correspondence with FE analyses. This value is at odds with Terzaghi's conceptual model of shearing on a vertical plane in a frictional soil, but this probably highlights the simplification of the conceptual model compared to reality. Using K = 1.0 gives lower $\sigma_s/\gamma(s\text{-}a) \approx 1.0$ for medium and high embankments.

In the Hewlett & Randolph method, for medium height embankments $\sigma_s/\gamma(s\text{-}a) \approx 1.0$ (failure at the crown of the arch), but for high embankment $\sigma_s/\gamma(s\text{-}a) \propto h$ (the embankment height, with failure at the pile cap), and values are approximately in the range 1 to 3 depending on the pile cap to spacing ratio (a/s) and the embankment fill frictional strength ϕ', which both have significant impact on the result. The 'German Recommendations' give results which are broadly similar to the Hewlett & Randolph method, but which are somewhat lower, particularly for high (a/s)

or ϕ. Ellis & Aslam (2009a) stated the method proposed by the Hewlett & Randolph seems most rational, particularly since the eventuality of pile caps 'punching' into the base of the embankment was specifically considered, which could be of particular concern for high embankments, or low (a/s). This feature of behaviour is not considered in either BS8006 or the Terzaghi approach. Unfortunately the centrifuge tests could not accurately verify predictions for high embankments.

The authors concluded from the centrifuge tests that the embankment height (h) normalised by the clear spacing between adjacent pile caps (s-a) appeared to be a critical parameter:

- $h/(s\text{-}a) < 0.5$: stress on the subsoil is not reduced by arching, and there is significant differential settlement at the surface of the embankment.
- $0.5 < h/(s\text{-}a) < 2.0$: there is increasing evidence of arching as h increases - the efficacy increases (tending towards 1.0), and differential settlement at the surface of the embankment reduces to a small value.
- $2.0 < h/(s\text{-}a)$: there is 'full' arching with efficacy close to 1.0 and little or no differential settlement at the surface of the embankment.

2.5.3 Field studies

Munfakh et al. (1984) presented a full scale field test to investigate the behaviour of a reinforced embankment supported on stone columns through the soft subsoil. The test site was located on the north bank of the Mississippi within the city of New Orleans, where the soil profile consisted of approximately 18 m of soft clay underlain by dense sands. The authors' findings indicated that stone columns can significantly improve the stability of embankments constructed on cohesive soils. They also concluded that installation of stone columns did not appear to cause serious disturbance to the adjacent in situ soil, and that use of stone columns increased the load carrying capacity of the underlying soil by approximately 50 percent, and reduced total settlement by about 40 percent.

Here the stone columns are regarded as a ground improvement technique for the subsoil. Throughout this thesis it will be assumed that the piles (or other inclusions in the subsoil) are effectively rigid, and arching onto the pile caps is the primary method of load transfer. Nevertheless, the role of the subsoil and/ or geogrid reinforcement in carrying remaining load will also be considered.

Jones et al. (1990) presented the use of a geotextile reinforced piled embankment technique at the Stansted Airport rail spur to limit the occurrence of long term differential settlements. A FEM parametric study was used to determine the tensile force in the reinforcement. They stated

that the use of reinforcement can enable reductions to be made in the size of the pile caps, and eliminate the need for raking piles along the extremities of the piled area. The authors also suggested that analytical procedures (such as Hewlett & Randolph and Marston's formula) were conservative inasmuch as they overestimated the tensile requirements of the reinforcement.

Jenner et al. (1998) presented the reinforced piled embankment used in the A525 Rhuddlan Bypass in North Wales (in fact Vibro concrete columns (VCCs) were used rather than piles). In the construction, biaxial geogrids with high stiffness at low strain were placed in two layers to interlock with the granular fill to create a stiff 'Load Transfer Platform' (LTP). In order to investigate the performance of the LTP, instrumentation was included in the platform construction to monitor settlement and geogrid strains and deflections. Their findings showed that the technique of a geogrid reinforced LTP were a cost effective solution to the problem of embankment construction over soft ground. They also concluded that there was no evidence of creep of the reinforcement due to the interlock of the geogrid with the fill forming a composite material. Hence the use of low strength, stiff biaxial geogrids was a viable alternative to the use of higher strength reinforcement.

Wood (2003) presented the reinforced piled embankment used in the A63 bypass to the south of Selby in North Yorkshire. The maximum allowable settlement in the project was 75 mm and a maximum differential settlement gradient along the carriageway was 1 in 500. The design

method adopted the principle of BS8006, considering both serviceability and ultimate limit states. However, the load on the reinforcement was calculated by estimating the efficacy of the embankment in supporting load arching naturally on to the piles as shown by Love & Milligan (2003) and Russell & Pierpoint (1997). The authors concluded that the embankment had been successfully constructed.

Almeida et al. (2007) presented data from the field monitoring of a piled embankment reinforced with bidirectional geogrid. The authors performed excavations under the geogrid in order to evaluate the effect of lack of support from the subsoil. They measured the embankment settlements and reinforcement strain in their studies. Their findings showed that the embankment settlement measured was in the range 0.1 up to 0.4 m (where excavation was undertaken). They also presented that the settlements between adjacent pile caps were about half the settlement at the centre of four pile caps. They proposed that the overall range of reinforcement strain was smaller than 2 % and the values of strain measured between piles were smaller than that near the pile caps.

Briancon et al. (2008) reports a full-scale trial of a piled embankment. Throughout various areas of the trial the presence and amount of reinforcement were varied. Their findings showed that the use of geogrid reinforcement can improve the efficacy and decrease settlement. The authors also presented results of stress acting on the pile caps and strain developed in reinforcement which showed that the behaviour of a single layer of reinforcement differed from that of two layers.

Raithel et al. (2008) reported the construction of a piled embankment on soft ground for a high speed railway in China. There were three different construction methods used in this project: reinforced concrete slab on top of the piles, horizontal geogrid reinforcement on top of the piles and cement stabilisation of the embankment fill. Their findings showed that a geosynthetic reinforcement as well as a cement stabilisation of the embankment material can be used instead of a concrete slab to guarantee sufficient load transfer and distribution. They also recommended that the center-to-center distance of the piles (s) and the pile diameter (a) (pile caps) should be chosen as follows:

- (s-a) ≤ 3.0 m: in the case of static loads;
- (s-a) ≤ 2.5 m: in the case of heavy live loads.

They also suggested that the distance between the reinforcement layer and the plane of the pile heads should be as small as possible, in order to achieve maximum efficacy of the geogrid membrane. The authors recommended a safe distance (z) between the lowest reinforcement and the pile heads in order to prevent a structural damage of the reinforcement because of shearing at the edge of the pile heads:

- z ≤ 0.15 m for single layer reinforcement;
- z ≤ 0.30 m for two layers reinforcement.

Van Eekelen et al. (2008) reported a comparison between 2 years of measurements in a full scale test of the 'Kyoto Road' (in Giessenburg in the Netherlands) with predictions by two design methods: BS8006 and the German Draft-Standard EBGEO. Their findings showed that EBGEO gave

better predictions of the load division/distribution in the piled embankment than BS8006. They also reported that EBGEO over predicted the loading on the piles, but showed the best prediction for the loads on the reinforcement.

2.6 Finite element analysis

2.6.1 Introduction

ABAQUS is the finite element (FE) software package used in this research, and the following section refers extensively to the associated manuals. This software has been used in many different engineering fields throughout the world. It can solve problems ranging from relatively simple linear analyses to the most challenging nonlinear simulations (Getting Started with ABAQUS, Version 6.6). The software contains an extensive library of elements that can model virtually any geometry, and the extensive material models enable it to simulate the behaviour of most typical engineering materials (e.g. metals, rubber, reinforced concrete and geotechnical materials such as soils and rock).

The ABAQUS finite element system includes (ABAQUS Analysis User's Manual, Version 6.6):

- ABAQUS/Standard, a general-purpose finite element program;
- ABAQUS/Explicit, an explicit dynamics finite element program;
- ABAQUS/CAE, and interactive environment used to create finite element models, submit ABAQUS analyses, monitor and diagnose jobs, and evaluate results;
- ABAQUS/Viewer, a subset of ABAQUS/CAE that contains only the postprocessing capabilities of the Visualization module.

Three of these are used in this study: ABAQUS/Standard, ABAQUS/CAE and ABAQUS/Viewer.

2.6.2 Finite element method

According to Becker (2004), the origins of the energy theorems used in modern Finite Element formulations can be dated back to the theoretical works of Gauss (1795), Galerkin (1815), Rayleigh (1870) and Castigliano (1879). Since then this method has been greatly developed. For instance, FE software was only used on large main-frame computers from the late 1960's to the early 1970's. However, since then there has been a transition to 'workstations' and then desktop PCs.

Ottosen & Petersson (1992) defined the finite element method as a numerical approach by which general differential equations can be solved in an approximate manner. In this method, the entire solution domain is divided into small finite segments, hence the name finite elements. For each element, the behaviour is described by the displacements of the elements and the material law. Then, all elements are assembled together and the requirements of continuity and equilibrium are satisfied between neighbouring elements. Finally, provided that the boundary conditions of the actual problem are satisfied, a unique solution can be obtained to the overall system of linear algebraic equations. The solution matrix is sparsely populated (i.e. with relatively few non-zero coefficients).

The FE method is very suitable for practical engineering problems of complex geometries. To obtain good accuracy in regions of rapidly changing variables, a large number of small elements must be used. The use of FE simulation has many benefits (Becker, 2004):

- Simulation of complex designs of engineering components and structures;
- Comprehensive information regarding the distribution of stresses and strains inside a structure;
- Better understanding of the effect of geometric features on the stress/strain state.

Although there are many benefits of using FE simulation, there are also risks (Becker, 2004):

- Incorrect data input;
- Errors in translating the real-life boundary conditions into FE input data;
- Incorrect use of the FE software;
- Using too few elements;
- Using badly shaped elements;
- Attempting to solve non-linear problems without knowing the background theory;
- Using the wrong type of elements (e.g. using shell elements when continuum elements would be best).

2.6.3 Basic theories according to ABAQUS/Standard

2.6.3.1 Mesh type

ABAQUS has an extensive element library to provide a powerful set of tools for solving many different problems (ABAQUS Analysis User's Manual, Version 6.6). There are several different element families, such as:

- continuum elements, such as solid elements and infinite elements;
- structural elements, such as membrane elements, truss elements, beam elements, frame elements and elbow elements;
- rigid elements, such as point masses;
- connector elements, such as springs and dashpots;
- special-purpose elements, such as cohesive elements and hydrostatic fluid elements;
- contact elements, such as gap contact elements, tube-to-tube contact elements.

In this research, three types of element are used:

- continuum elements, which are used to model the embankment fill and/or soft subsoil;
- truss elements, which are used to model geogrid or geotextile reinforcement in 2D;
- membrane elements, which are used to model reinforcement in 3D.

Continuum elements

According to the ABAQUS Analysis User's Manual, Version 6.6, solid (continuum) elements are the standard volume element of ABAQUS, which can be used for linear analysis and for complex nonlinear analyses involving contact, plasticity, and large deformations. The continuum elements can also be connected to other elements on any of their faces.

In ABAQUS, the continuum elements have names that begin with the letter "C". The next two letters usually indicate the dimensionality and the active degrees freedom in the element. For instance, the letter "3D" indicates a three-dimensional element; "AX", indicates an axisymmetric element; "PE", indicates a plane strain element; and "PS", indicates a plane stress element; "R", indicates a reduced integration element.

In ABAQUS/Standard, soil elements are provided with first-order (linear) and second-order (quadratic) interpolation, and the user must decide which approach is most appropriate for the application. The first-order elements are essentially constant strain elements. Second-order elements provide higher accuracy in ABAQUS/Standard than first-order elements for "smooth" problems that do not involve complex contact conditions, or severe element distortions. The second-order elements capture stress concentrations more effectively and are better for modelling geometric features: they can model a curved surface with fewer elements.

Moreover, the user also needs to choose between full- and reduced-integration elements. The expression "full integration" refers to the number of Gauss points required to integrate the polynomial terms in an element's stiffness matrix exactly when the element has a regular shape. As shown in Figure 2.17(a), fully integrated, linear elements have two integration points in each direction. Thus, the three-dimensional element C3D8 uses a 2×2×2 array of integration points in the element. Figure 2.17(b) shows that fully integrated, quadratic elements use three integration points in each direction. Reduced-integration elements use one fewer integration point in each direction than the fully integrated elements. As can be seen in Figure 2.18(a), reduced-integration linear elements have just a single integration point located at the element's centroid. The locations of the integration points for reduced-integration, quadrilateral elements are shown in Figure 2.18(b).

The ABAQUS Analysis User's Manual suggests that the second-order reduced-integration elements in ABAQUS/Standard generally yield more accurate results than the corresponding fully integrated elements. However, for first-order elements the accuracy achieved with full versus reduced integration is largely dependent on the nature of the problem.

In this research, the eight noded, reduced-integration, quadratic solid elements (CPE8R) are used to model the embankment fill and subsoil in plane strain conditions. The twenty noded, reduced-integration, quadratic brick solid elements (C3D20R) and eight noded, full-integration, linear

brick solid elements (C3D8) are used to model embankment fill and in three-dimensional models without and with contact respectively.

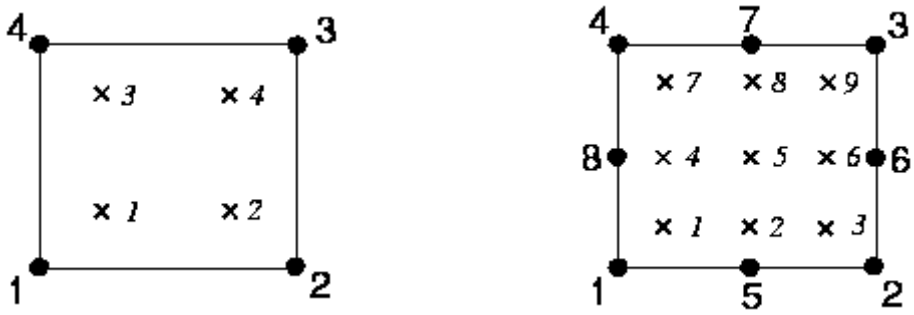

(a) Linear element (b) Quadratic element

Figure 2.17. Integration points in fully integrated, two-dimensional elements

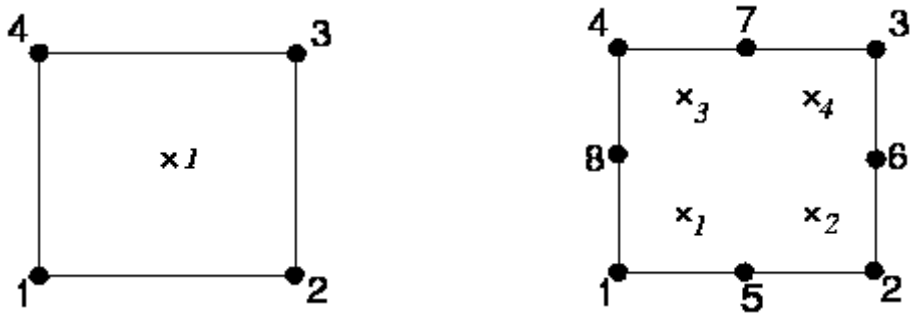

(a) Linear element (b) Quadratic element

Figure 2.18. Integration points in reduced integrated, two-dimensional elements

Truss element

The Truss element is defined in the ABAQUS Analysis User's Manual (Version 6.6) as a long, slender structural member that can transmit only axial force and does not transmit moments. This element can be used in two and three dimensions to model slender, line-like structures that support loading only along the axis or the centreline of the element, and no moments or forces perpendicular to the centreline.

ABAQUS provides 2-noded straight and 3-noded curved truss elements. As shown in Figure 2.19(a), the 2-noded truss element uses linear interpolation for position and displacement and has a constant stress, and using one integration point. Figure 2.19(b) shows the 3-noded truss element, which uses quadratic interpolation for position and displacement so that the strain varies linearly along the element, using two integration points.

In this research, three noded quadratic truss elements (T2D3) are used to model the geogrid or geotextile reinforcement in a two-dimensional situation.

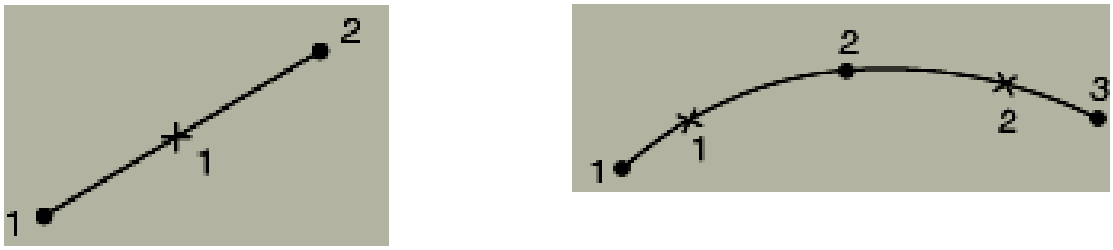

(a) 2-node element (b) 3-node element

Figure 2.19. Numbering of integration points for output in truss elements

Membrane element

The membrane element is defined in the ABAQUS Analysis User's Manual (Version 6.6) as a surface element that transmits in-plane forces only (no moments) and has no bending stiffness. This element is used to represent a thin surface in space that offers strength in the plane of the element but has no bending stiffness, for example, the thin rubber sheet that forms a balloon. In addition, it is often used to represent a thin stiffening component in solid structures, such as a reinforcing layer in a continuum.

ABAQUS provides three types of membrane elements: general membrane elements, cylindrical membrane elements and axisymmetric membrane elements. The general membrane elements are used in this research

In this research, the four noded, full-integration, three-dimensional membrane element (M3D4) are used to model the geogrid reinforcement in three-dimensional analyses.

2.6.3.2 Contact interaction

Choosing contact methods

The interface between two 'surfaces' is referred to as a 'contact'. In this study the contact corresponds to the interface between the geogrid or geosynthetic reinforcement and the adjacent soil.

There are two methods for modelling contact interaction in ABAQUS/Standard: using surfaces or using contact elements. Most contact problems are modelled using surface-based contact, such as

- contact between two deformable bodies. The structures can be either two- or three-dimensional, and they can undergo either small or finite sliding;
- contact between a rigid surface and a deformable body. The structures can be either two- or three-dimensional, and they can undergo either small or finite sliding;
- problems where two separate surfaces need to be "tied" together so that there is no relative motion between them;
- coupled thermal-mechanical interaction between deformable bodies with finite relative motion.

ABAQUS/Standard also provides a library of contact elements including:

- contact interaction between two pipelines or tubes modelled with pipe, beam, or truss elements where one pipe lies inside the other;
- contact between two nodes along a fixed direction in space;

- simulations using axisymmetric elements with asymmetric deformations;
- heat transfer analyses where the heat flow is one-dimensional.

This research considers contact between two deformable bodies: embankment fill with reinforcement and/or subsoil with reinforcement, in both two- and three-dimensional situations. Thus, surface-based contact is chosen to simulate the interaction between soil and reinforcement.

Defining surfaces

For surface-based contact simulations, surfaces are considered as part of the model definition, and thus all surfaces that will be used in the analysis must be defined at the beginning of the simulation. ABAQUS has three classifications of contact surfaces:

- element-based deformable and rigid surfaces;
- node-based surfaces;
- analytical rigid surfaces.

According to the ABAQUS Analysis User's Manual (Version 6.6), node-based surfaces have some limitations compared with element-based surfaces. Thus, only element-based surfaces are used as contact surfaces and double-sided surfaces are defined in this research. The embankment fill, subsoil and reinforcement are all defined as element-based surfaces at both their top and bottom surfaces.

Defining contact between surfaces

Once surfaces have been created, the user must specify which pairs of surfaces can interact with each other during the analysis by defining a "Contact Pair". At least one surface of the pair must be a non-node-based surface. There are three key factors which must be determined when creating a contact formulation: the contact discretisation, the tracking approach, and the assignment of "master" and "slave" roles to the respective surfaces.

ABAQUS/Standard offers two contact discretisation options: a traditional "node-to-surface" discretisation and a true "surface-to-surface" discretisation. For the "node-to-surface" discretisation, the contact conditions are established so that each "slave" node on one side of a contact interface effectively interacts with a point of projection on the "master" surface on the opposite side of the contact interface (see Figure 2.20). Thus, each contact condition involves a single slave node and a group of nearby master nodes from which values are interpolated to the projection point. Traditional node-to-surface discretisation has some characteristics. For instance, the slave nodes are constrained not to penetrate into the master surface; however, the nodes of the master surface can penetrate into the slave surface.

Surface-to-surface discretisation considers the shape of both the slave and master surfaces in the region of contact constraints in order to optimise stress accuracy. Figure 2.21 shows an example of improved

contact pressure accuracy with surface-to-surface contact as compared with node-to-surface contact. Surface-to-surface discretisation has some key characteristics. For instance, contact conditions are enforced in an average sense over the slave surface, rather than at discrete points (such as at slave nodes, as in the case of node-to-surface discretisation). Therefore, some penetration may be observed at individual nodes, but large undetected penetrations of master nodes into the slave surface do not occur with this discretisation.

The ABAQUS Analysis User's Manual states that surface-to-surface contact will generally resist penetrations of master nodes into a coarse slave surface; however, this formulation can add significant computational expense if the slave mesh is significantly coarser than the master mesh. In this work surface-to-surface contact has been used.

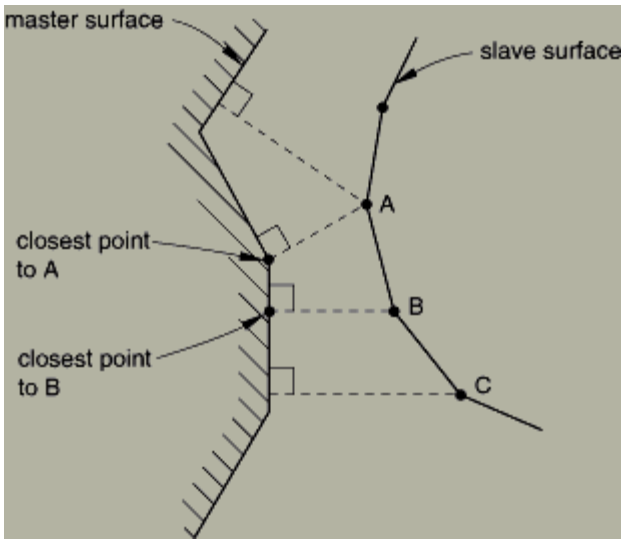

Figure 2.20. Node-to-surface contact discretisation

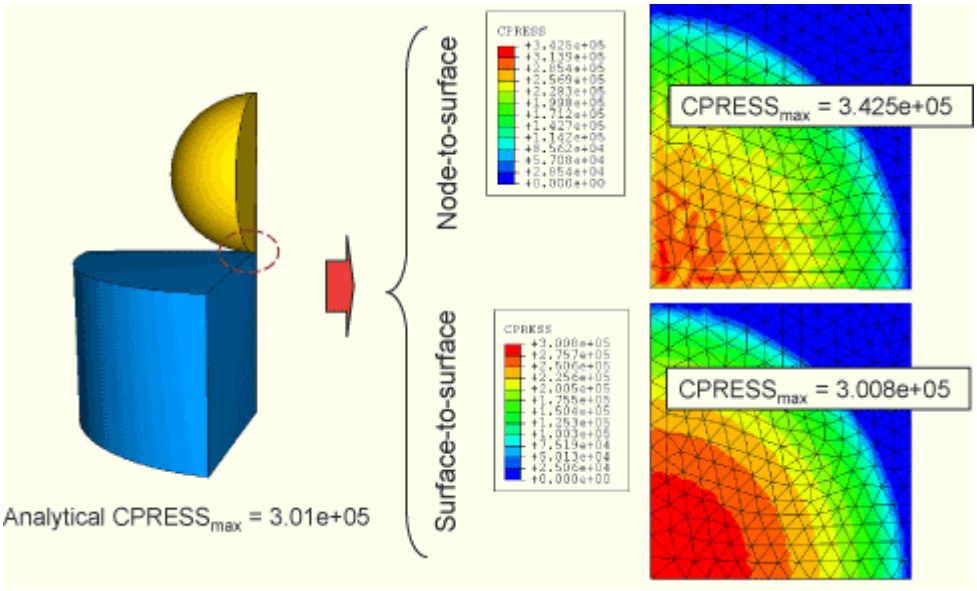

Figure 2.21. Comparison of contact pressure accuracy for node-to-surface and surface-to-surface contact discretization

In ABAQUS/Standard, there are two tracking approaches to account for the relative motion of the two surfaces forming a contact pair: finite-sliding and small-sliding. Finite-sliding contact is the most general tracking approach, which allows for arbitrary relative separation, sliding, and rotation of the contacting surface. However, the small-sliding contact assumes there will be relatively little sliding of one surface along the other and is based on linearised approximations of the master surface per constraint. The ABAQUS Analysis User's Manual suggests that the small-sliding contact should used when the approximations are reasonable, due to computational savings and added robustness, and this approach has been used in this research.

Regardless of whether node-to-surface or surface-to-surface contact, or whether finite or small-sliding contact is used, ABAQUS/Standard enforces the following rules related to the assignment of the master and slave roles:

- A rigid-element-based surface must always be the master surface;
- A node-based surface can act only as a slave surface and always uses node-to-surface contact.

When both surfaces in a contact pair are element-based and attached to either deformable bodies or deformable bodies defined as rigid, users have to choose which surface will be the slave surface and which will be the master surface. Generally, if a smaller surface contacts a larger surface, it is best to choose the smaller surface as the slave surface. If that distinction cannot be made, the master surface should be chosen as the surface of the stiffer body or as the surface with the coarser mesh if the two surfaces are on structures with comparable stiffness. However, compared with node-to-surface contact, the choice of master and slave surfaces for surface-to-surface contact typically has much less effect on the results.

In this research, the stiffness of the reinforcement is much higher than the embankment fill or subsoil. The denser mesh is at the contact surface of the soil (embankment fill or subsoil), whereas, the coarser mesh is at the contact surface of the reinforcement. Thus, the contact surfaces of the embankment fill and subsoil are defined as slave surfaces and the contact surfaces of reinforcement are defined as master surfaces.

Defining property models for contact simulation

Once the "Contact Pairs" have been defined, it is necessary to choose an appropriate Contact Property Model. There are four types of contact property models available in ABAQUS/Standard: Mechanical contact properties; Thermal contact properties; Electrical contact properties; and Pore fluid contact properties. Mechanical contact properties are used in the model. They may include:

- a constitutive model for the contact pressure-overclosure relationship that governs the motion of the surfaces;
- a damping model that defines forces resisting the relative motions of the contacting surfaces;
- a friction model that defines the force resisting the relative tangential motion of the surfaces.

In this research, the Coulomb friction model is used to simulate the interaction between the soil and reinforcement. In the basic form of the Coulomb friction model, the two contacting surfaces can carry shear stresses up to a certain magnitude across their interface before they start sliding relative to one another. The Coulomb friction model defines this critical shear stress, τ_{crit}, as a fraction of the contact pressure, p, between the surfaces ($\tau_{crit} = \mu p$).

Common difficulties associated with contact modelling

The ABAQUS Analysis User's Manual presents some difficulties that may be encountered when modelling contact interactions with ABAQUS/Standard. Problems may be related to factors such as mesh, element selection, and surface geometry. This can lead to nonconvergence and termination of an analysis.

Using poorly meshed surfaces

When a coarsely meshed surface is used as a slave surface for node-to-surface contact, the master surface nodes can grossly penetrate the slave surface without resistance. However, surface-to-surface contact will generally resist penetrations of master nodes into a coarse slave surface (this can add significant computational expense if the slave mesh is significantly coarser than the master mesh). To avoid this problem, surface-to-surface contact is used in this research. The slave surfaces (the contact surfaces of the embankment fill and subsoil) have denser mesh, and the master surfaces (the contact surfaces of reinforcement) have coarser mesh.

Three-dimensional surfaces with second-order faces

As mentioned before, the second-order elements not only provide higher accuracy but also capture stress concentrations more effectively and are better for modelling geometric features then first-order elements. However, some of the second-order elements may not be suited for

contact simulation with the default "hard" contact relationship or for analyses requiring large element distortions.

According to the theory of advanced non-linear finite element analysis (Becker, 2001), in three-dimensional problems, if the 20-node brick elements are used in the contact interfaces, an incorrect contact separation may be reported. This is caused by the fact that the kinematically equivalent nodal forces representing a uniform pressure on the face of a 20-node brick element contain positive and negative forces (tension forces) at the corner nodes, as shown in Figure 2.22(a). To overcome this problem, the 8-node brick element is used in the analysis, as shown in Figure 2.22(b). Abaqus also recommends using the first-order element as one of the best choice for problems involving contact in three dimensional analyses. In this research, the eight noded, full-integration, linear brick solid elements (C3D8) are used to model embankment fill and subsoil in 3D models with contact.

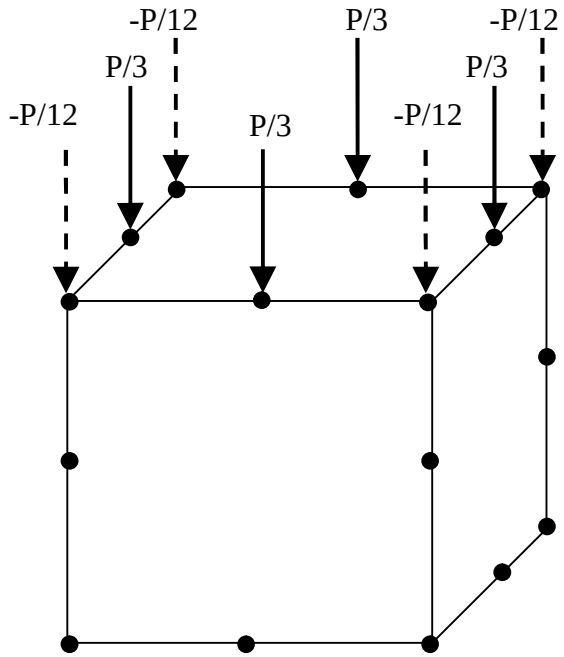

(a) Linear element (8-node brick, C3D8)

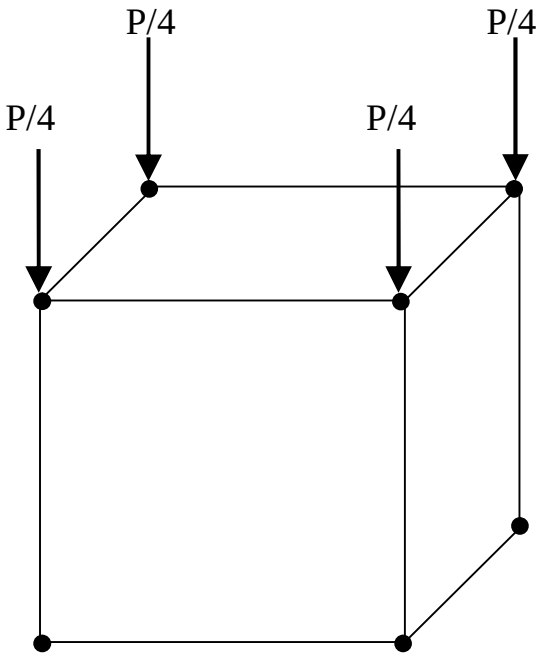

(b) Quadratic element (20-node brick, C3D20)

Figure 2.22. Uniform pressure kinematically equivalent nodal forces on element faces

2.6.3.3 Controls

There are two types of controls used in the simulations: commonly used controls and contact controls.

Commonly Used Controls

Solution control parameters can be used to control:

- nonlinear equation solution accuracy
- time increment adjustment.

The default values of these parameters are appropriate for most analyses. However, in difficult cases the solution procedure may not converge with the default controls or may use an excessive number of increments and iterations. After it has been established that such problems are not due to modelling errors, it may be useful to change certain control parameters.

The keyword "ANALYSIS = DISCONTINUOUS" have been used in the analyses. ABAQUS uses this keyword to set parameters that will usually improve efficiency for severely discontinuous behaviour, such as frictional sliding or concrete cracking, by allowing relatively much iteration prior to beginning any checks on the convergence rate.

Contact Controls

Contact controls in ABAQUS/Standard:

- should not be modified from the default settings for the majority of problems;

- can be used for problems where the standard contact controls do not provide cost-effective solutions; and
- can be used for problems where the standard controls do not effectively establish the desired contact conditions.

Problems that benefit from adjustments to the contact controls in ABAQUS/Standard are generally large models with complicated geometries and numerous contact interfaces.

Contact controls can be applied on a step-by-step basis to all of the contact pairs and contact elements that are active in the step or to individual contact pairs. This makes it possible to apply contact controls to a specific contact pair to take the simulation through a difficult phase. Contact controls remain in effect until they are either changed or reset to their default values. If in any given step the contact controls are declared for both the entire model and for a specific contact pair, the controls for the specific contact pair will override those for the entire model for that contact pair.

The "AUTOMATIC TOLERANCES" approach has been used in the analyses. This keyword is used to have ABAQUS/Standard automatically compute an overclosure tolerance and a separation pressure tolerance to prevent chattering in contact.

2.7 Summary

There are a number of theories to quantify arching in a piled embankment. Many authors have compared the methods for specific geometries and noted that they give differing results. However, they tend to focus on one or two specific geometries, or comparing the results with numerical analyses, but without commenting systematically on the generic features of various methods.

Any effect due to the subsoil is generally neglected. However, this influence could be a major effect on the overall embankment response.

CHAPTER 3
GROUND REACTION CURVE IN PLANE STRAIN

3.1 Introduction

The simplest starting point for analysis of arching is a two-dimensional (2D) plane strain model. Results from plane strain finite element analyses are presented in this chapter. The analyses focus on arching in the embankment, with the underlying pile cap assumed to be rigidly supported, and the effect of the subsoil represented by a uniform vertical stress. An alternative idealisation would be to impose a uniform settlement, but unsurprisingly this led to difficulties with high strain at the edge of the pile cap.

The results are presented in a form which can be compared with the 'Ground Reaction Curve' (GRC) proposed by Iglesia et al. (1999), Section 2.3 (Figure 2.14). This approach was originally proposed to consider arching over an underground structure. However, settlement of the subsoil beneath a piled embankment can be compared to deformation of the underground structure, since both tend to cause arching of the material above.

3.2 Analyses presented

The analyses reported here were undertaken in plane strain using Abaqus Version 6.6. Figure 3.1 shows a typical mesh for the embankment, with height h = 5.0 m and pile spacing s = 2.5 m. There are 1474 eight noded, reduced-integration, two-dimensional, quadratic solid elements (CPE8R). As described in Chapter 2, for reduced-integration elements, Abaqus evaluates the material response at each integration point in each element (Abaqus Analysis User's Manual, Version 6.6). Reduced-integration elements were chosen both for computational efficiency, and because second-order reduced-integration elements generally yield more accurate results than the corresponding fully integrated elements.

The vertical boundaries represent lines of symmetry at the centreline of a support (pile cap), and the midpoint between supports (see Section 1.1, Figure 1.1). Hence there is a restraint on horizontal (but not vertical) movement at these boundaries. No boundary conditions are imposed at the top (embankment) surface, and no surcharge is considered to act here.

The bottom boundary represents the base of the embankment, which is underlain by a half pile cap (width a/2) on the left, and subsoil (width (s-a)/2) at the right. The pile cap is assumed to provide rigid restraint to the embankment, both horizontally and vertically. The assumed uniform vertical stress in the subsoil beneath the embankment (σ_s) is used to

control the analysis – the subsoil itself was not actually modelled in this Chapter.

The pile cap width (a) was fixed at 1.0 m and the centre-to-centre spacing (s) was 2.0, 2.5 or 3.5 m. The embankment height (h) was varied using values in the range 1.0 to 10 m. Throughout the analyses minimum and maximum element sizes were approximately 0.002 and 0.012 m^3/m respectively. This corresponds to side lengths in the plane strain section of approximately 50 to 150 mm.

The embankment material was assumed to be granular (and hence with predominantly frictional strength), and modelled using the linear elastic and Mohr Coulomb (c', ϕ') parameters shown in Table 3.1. The embankment soil would be dense granular material which would initially exhibit a peak strength (i.e. friction angle ϕ' from 35° to 40°) and kinematic dilation. However, with ongoing yield there would be a brittle response and the strength would soften to critical state strength (i.e. friction angle ϕ' from 30° to 35°) with no dilation. Thus, for this reason the material parameters are more like a loose soil (with c' = 1kN/m^2, ϕ' = 30° and $\psi = 0^\circ$) which exhibits no peak strength or dilation, but goes straight to the critical state strength. This is pragmatic and would be slightly conservative. Moreover, in order to examine the 'ultimate state' of arching in the soil it is thought reasonable to assume a constant value of Young's Modulus (25 MN/m^2) with the depth.

For s =2.5 m the effect of increasing ϕ' to 40°, or increasing the kinematic dilation angle at yield (ψ) to 22° was also considered. This value of dilation angle is quite high, and did not reduce with ongoing deformation at yield (compared to actual soil where dilation is a transient effect). However, the aim of this analysis was to assess the sensitivity to dilation rather than to model the effect accurately, which would require a sophisticated constitutive model using complex and probably uncertain input parameters. The granular material was assumed to be dry and hence pore water pressures were not considered.

The sequence of analysis was straightforward. First the in-situ stresses were specified (based on a unit weight of 17 kN/m^3 and a K_0 value of 0.5) using the 'Geostatic' command in Abaqus. The K_0 value is based on a nominal 'at rest' value taken as (1-sinϕ'). Initially σ_s was specified as the nominal vertical stress at the base of the embankment to give equilibrium with the in situ stresses. This value was then reduced (generally allowing Abaqus to determine increment size automatically) to mimic loss of support from the subsoil. The subsoil in question is generally of low permeability, and thus this process has direct analogy with consolidation of the subsoil, which causes arching of the embankment material onto the pile caps.

All analyses presented in this Chapter are summarised in Table 3.2. Variations to the 'standard' parameters are highlighted in bold.

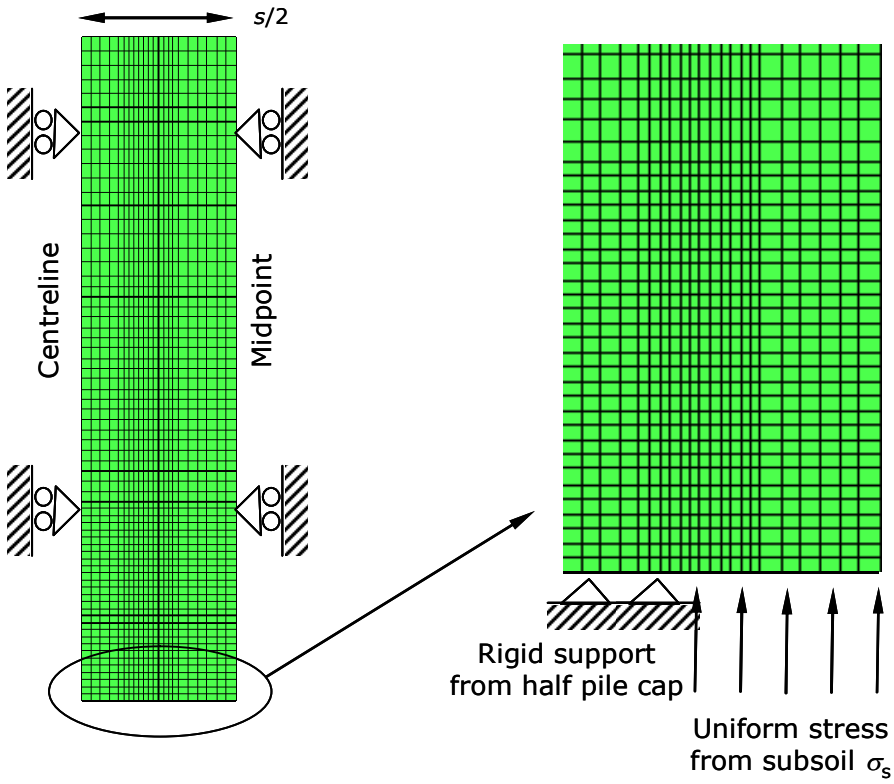

Figure 3.1. Typical finite element mesh (h = 5 m, s = 2.5 m) and boundary conditions

Table 3.1. Material parameters for granular embankment fill

Young's Modulus (MN/m^2)	Poisson's Ratio	c' (kN/m^2)	ϕ' (deg)	Kinematic dilation angle (ψ) (deg)
25	0.2	1	30 (or 40)	0 (or 22)

Table 3.2. Summary of analyses reported in this Chapter

h (m)	**s = 2 m**	s = 2.5 m	**s = 3.5 m**	s = 2.5 m	s = 2.5 m
	c' = 1kN/m^2 ϕ' = 30° ψ = 0°	c' = 1kN/m^2 ϕ' = 30° ψ = 0°	c' = 1kN/m^2 ϕ' = 30° ψ = 0°	c' = 1kN/m^2 **ϕ' = 40°** ψ = 0°	c' = 1kN/m^2 ϕ' = 30° **ψ = 22°**
sub-plot	(a)	(b)	(c)	(d)	(e)
1		√			
1.5	√	√	√		
2		√		√	√
2.5	√	√	√		
3.5	√	√		√	√
5		√	√	√	√
6.5		√	√		
8		√			
10	√	√	√	√	√

3.3 Results

3.3.1 Ground Reaction Curves

Figure 3.2 shows normalised ground reaction curves (GRC) broadly equivalent to the approach described in Section 2.3 (Figure 2.14) (Iglesia et al., 1999). The subsoil stress (σ_s) is normalised by the nominal overburden stress at the base of the embankment (γh), and therefore is initially one before there is any tendency for arching.

Because the analysis was controlled by reducing σ_s, corresponding settlement at the base of the embankment increased from zero at the edge of the pile cap to a maximum value at the midpoint between pile caps (see Section 1.1, Figure 1.1). The maximum value at the midpoint will now be referred to as δ_s (subsoil), and is thus slightly different to the definition in the ground reaction curve where δ be consistent with use of fonts is constant for the underground structure (see Section 2.3, Figure 2.12(a)). This settlement is normalised by the clear spacing between the pile caps (s-a), which is equivalent to the width of the structure. Data points are shown at the values of σ_s generated by automatic incrementation in Abaqus, and thus become more dense towards the end of the analysis as plasticity is more prevalent and there is more difficulty in achieving convergence.

The GRC curve is modelled up to the point of maximum arching. Using displacement (rather than stress) controlled analyses it was found that at

large displacements a constant value of σ_s was observed, rather than the subsequent increase exhibited in Figure 2.14 (in Section 2.3). It was concluded that the post-maximum stage of the GRC would only be observed in the finite element analyses if brittle soil behaviour (i.e. softening) was modelled, and it was decided not to introduce such complexity. Nevertheless, the analyses give the stress at maximum arching, and the displacement required to reach this point.

Figure 3.2(b) shows results for the standard soil parameters (Table 3.1), s = 2.5 m, and the most comprehensive variety of embankment heights (h). The highest embankment (10 m) requires the largest displacement to reach the point of maximum arching, but even here the normalised displacement is only slightly larger than 1 %. However, this value is directly related to the soil stiffness which has been chosen – as anticipated the value was doubled for an analysis with half the soil stiffness. The ultimate normalised stress is in the range 16 to 20 % for $h \geq$ 3.5 m, but tends to increase rapidly as h reduces below this value.

Subplots (a) and (c) (s = 2.0 and 3.5 m respectively) show trends of behaviour which are similar to (b). The normalised stress at the point of maximum arching for high embankments increases with s.

Subplots (d) and (e) show the effect of increased friction angle and non-zero dilation angle respectively for s = 2.5 m. The data again show similar trends. The normalised stresses at the point of maximum arching are slightly lower than for the standard soil parameters when s = 2.5 m. The

non-zero dilation angle seems to improve convergence of the solution towards the end of the analysis, allowing it to continue too much larger displacement at approximately constant subsoil stress. This is probably because the yielding behaviour is closer to an assumption of normality. However, the point of maximum arching is still initially reached at a normalised displacement of less than about 2 %. These results will be discussed further later in the Chapter.

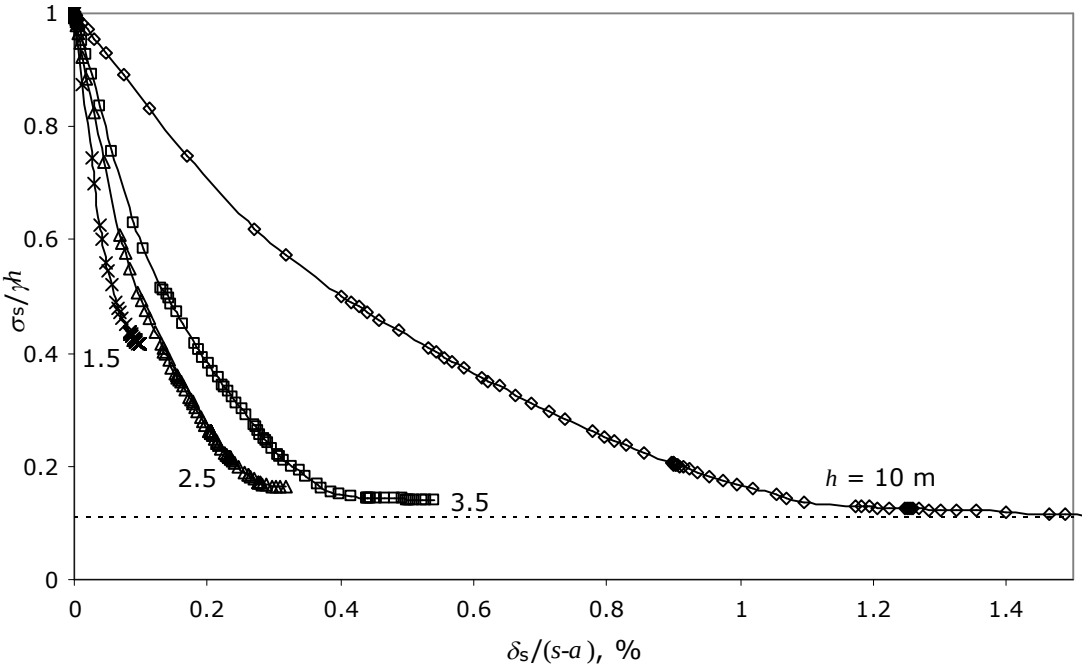

(a) s = 2.0 m

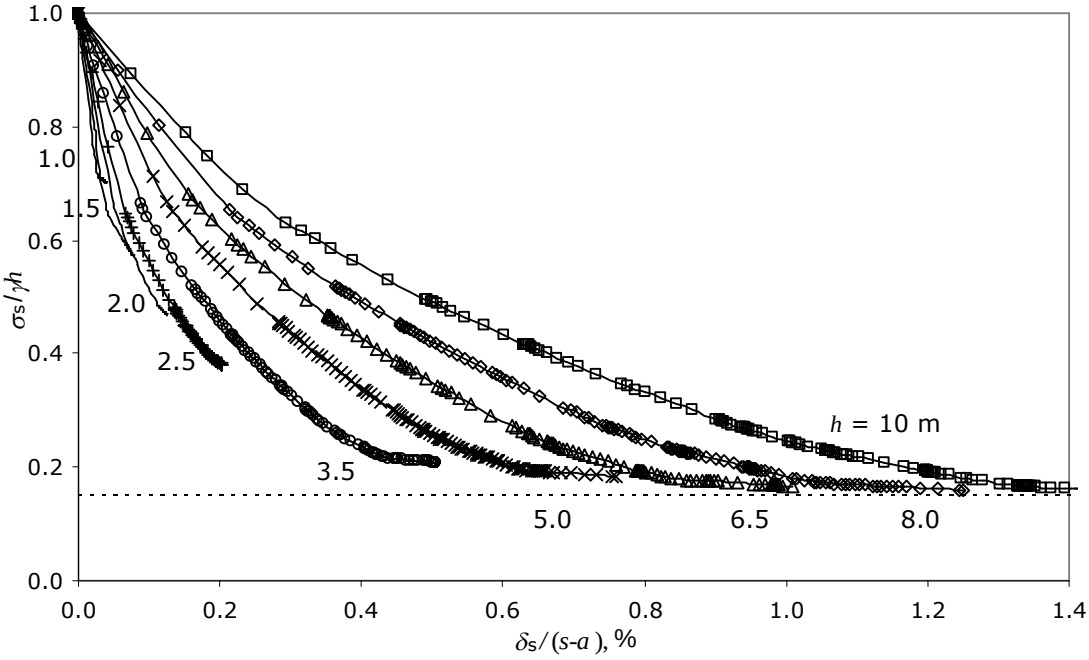

(b) s = 2.5 m

Figure 3.2 continued on following page

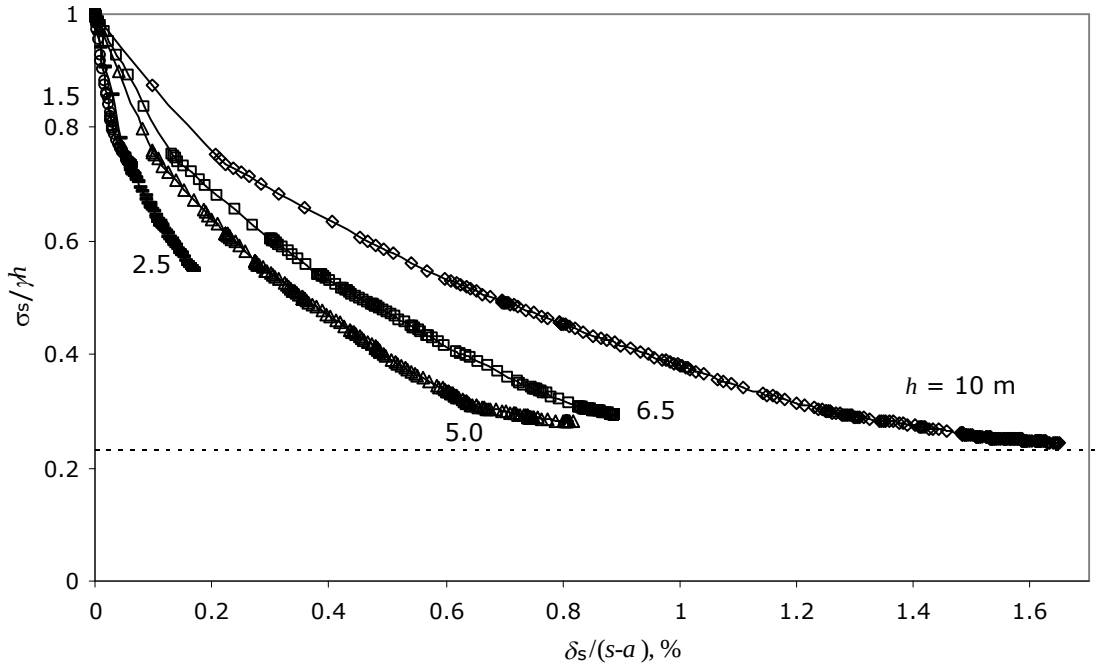

(c) s = 3.5 m

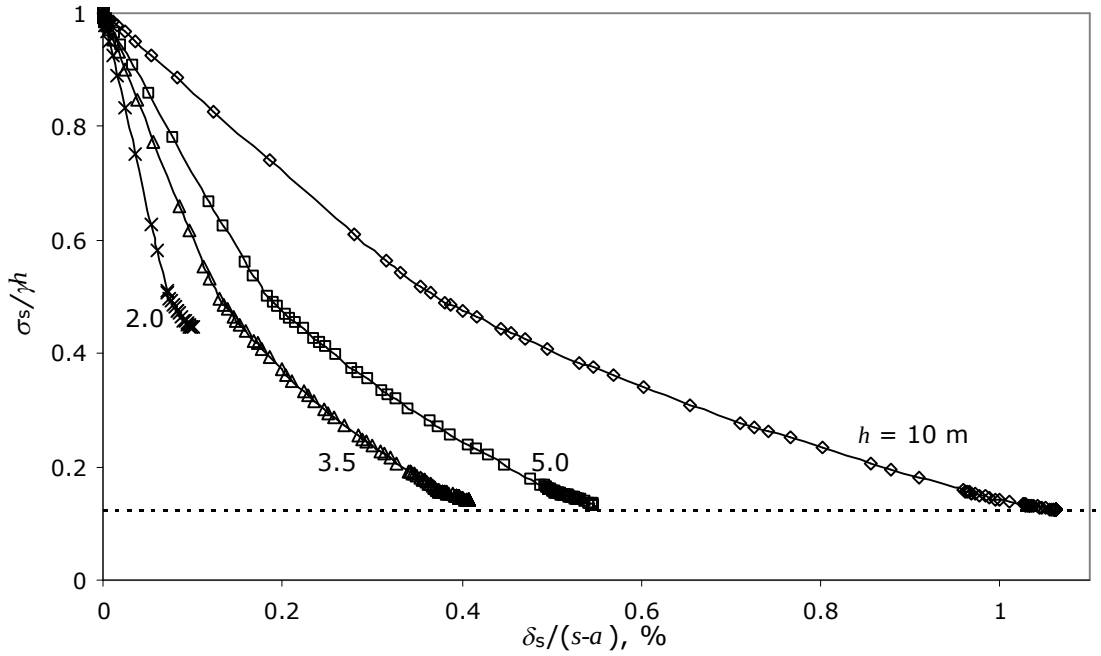

(d) s = 2.5 m, ϕ' = 40°

Figure 3.2 continued on following page

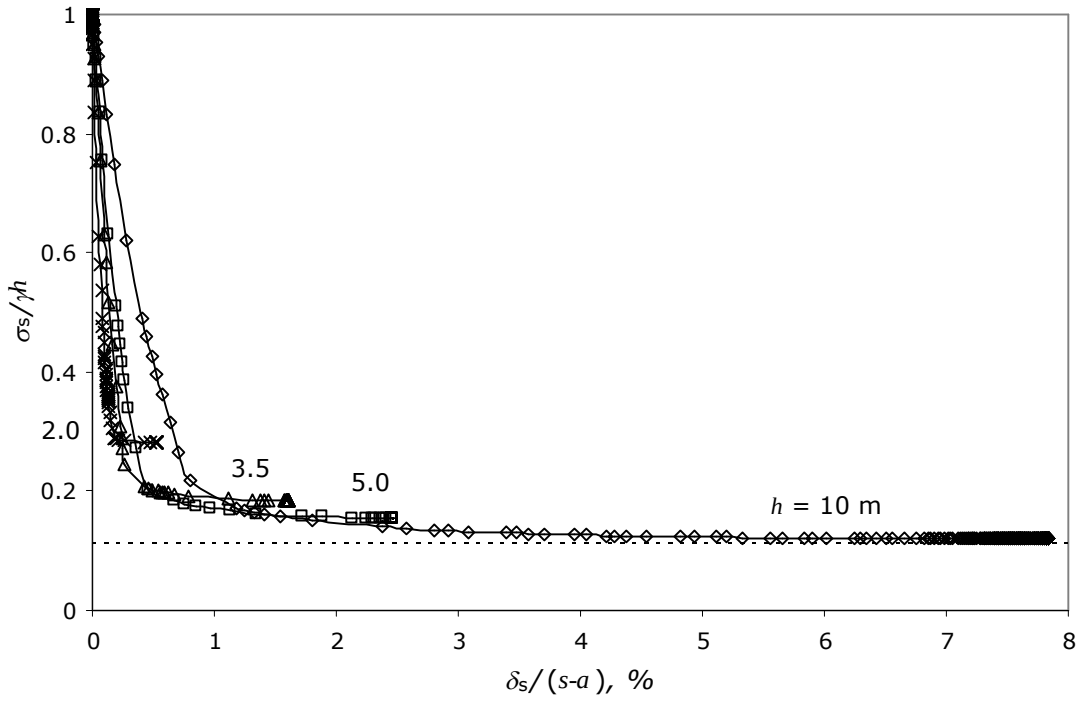

(e) s = 2.5 m, ψ = 22°

Figure 3.2. Ground Reaction Curves for a variety of embankment heights (h)

3.3.2 Midpoint profile of earth pressure coefficient

It was found that the earth pressure coefficient ($K = \sigma_h'/\sigma_v'$) plotted on a vertical profile at the midpoint between piles (the right-hand boundary of the mesh in Figure 3.1) gave a good 'illustration' of arching behaviour. Figure 3.3 shows the profiles plotted with z – vertical distance upwards from the base of the embankment (see Section 1.1, Figure 1.1), normalised by s. The profiles as plotted do not extend to the top of the embankment for the higher embankments. Values of 0.5(s-a), 0.5s and 1.5s are highlighted on the *z* axis; and $K = K_0$ and $K = K_p$ (the passive earth pressure coefficient, taking the standard Rankine value and ignoring the small cohesive element of strength) on the K axis. Subplots (a) to (c) again show variation of s whilst (d) and (e) show the effect of increased friction angle and non-zero dilation angle respectively.

Referring to Figure 3.3(b) for (z/s) > 1.5, $K = K_0$, and thus has not been modified by the formation of the arch. For embankments where (h/s) > 1.5, *K* increases with depth for z/s < 1.5, reaching K_p when $z \approx 0.5(s\text{-}a)$. Comparing this with a semicircular arch (see Section 1.1, Figure 1.1), the upper limit of the effect of arching is about 3 times higher, but the passive limit is only reached at the inner radius (and below) the arch, where the 'infill' material is evidently in a plastic state.

For embankments where (h/s) < 1.5 there is increasing tendency for the highest value of K to occur at the surface of the embankment, initially

giving an 'S-shaped' profile, and then monotonic reduction in K with depth in the embankment for the lowest h. In fact K_p as indicated on the plots neglects the small cohesion intercept, and thus can be exceeded, particularly when stress is small (e.g. near the surface of the embankment or immediately above the subsoil).

Subplots (a) and (c) (s = 2.0 and 3.5 m respectively) show trends of behaviour which are similar to (b). When s = 3.5 m there is some reduction in K at $z = 0.5(s\text{-}a)$ for the largest h, perhaps reflecting an increased tendency for failure of the arch at the pile cap rather than the 'crown' (top of arch) for large s (Hewlett & Randolph, 1988). This trend is supported for s = 2.0 m, where there would be increased tendency for passive failure at the crown, and where K is high at and below $z = 0.5(s\text{-}a)$. Subplots (d) and (e) show the effect of increased friction angle and non-zero dilation angle respectively. The data again show similar trends. The higher K_p for the increased friction angle is only fully mobilised when h is close to the 'critical value' of $1.5s$, and K is generally quite considerably less than K_p for $z = 0.5(s\text{-}a)$, particularly for the higher embankments. The non-zero dilation angle slightly promotes the tendency for K_p (for the standard friction angle) to be mobilised when $z > 0.5(s\text{-}a)$ compared to subplot (b), and the data shows less fluctuation with depth in the plastic infill zone for $z < 0.5(s\text{-}a)$. This probably again reflects improved numerical stability in the analysis when plastic strains show a greater degree of normality.

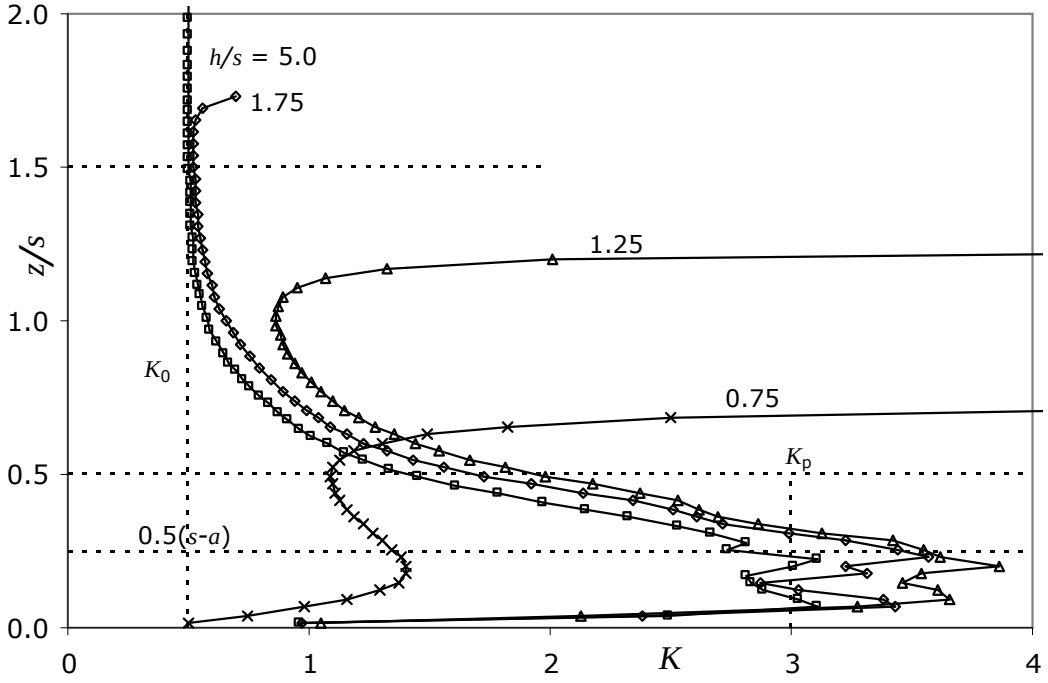

(a) s = 2 m

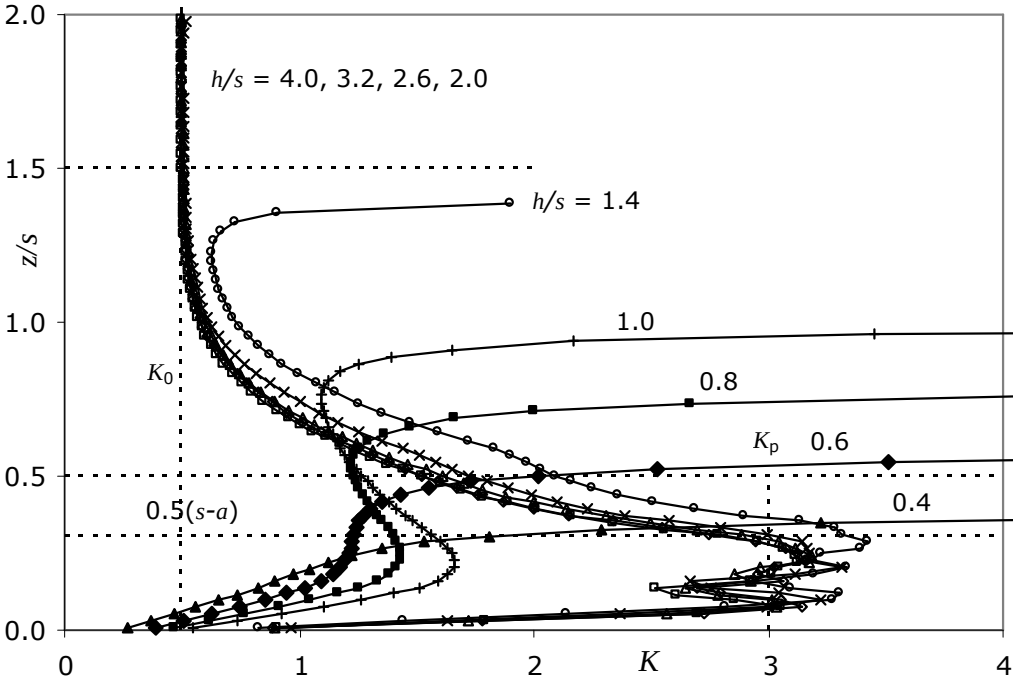

(b) s = 2.5 m

Figure 3.3 continued on following page

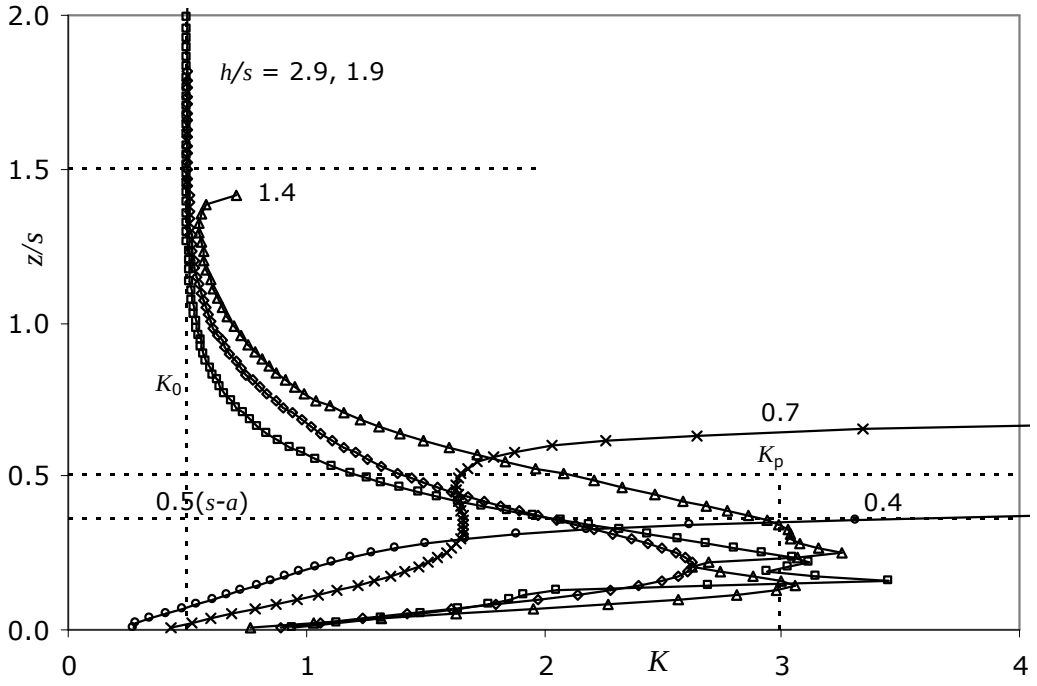

(c) s = 3.5 m

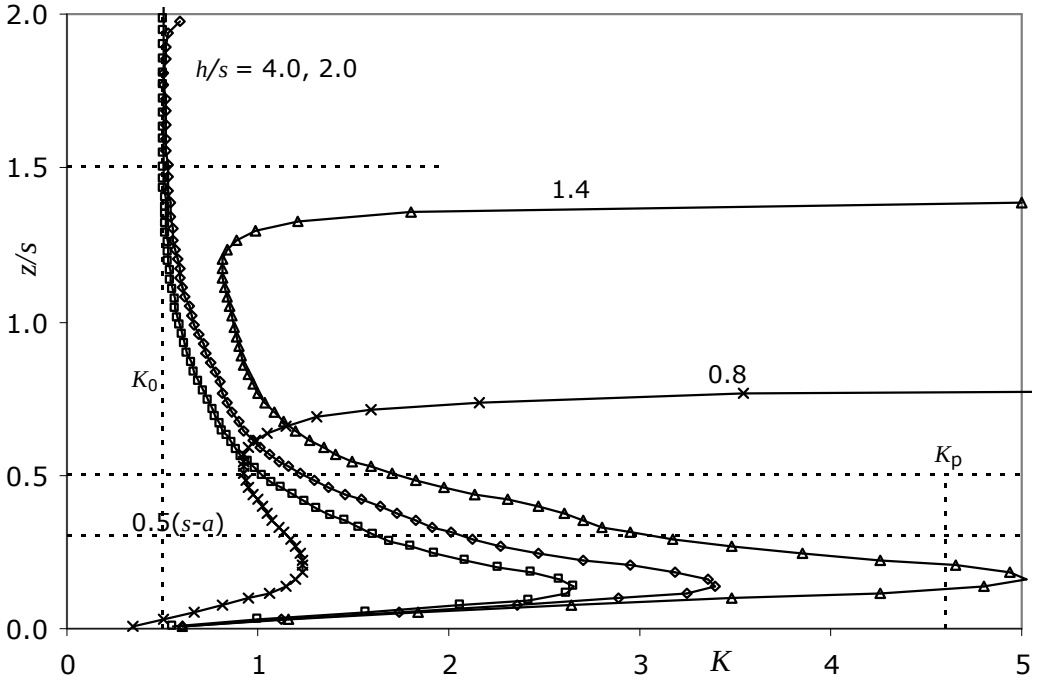

(d) s = 2.5 m, ϕ' = 40°

Figure 3.3 continued on following page

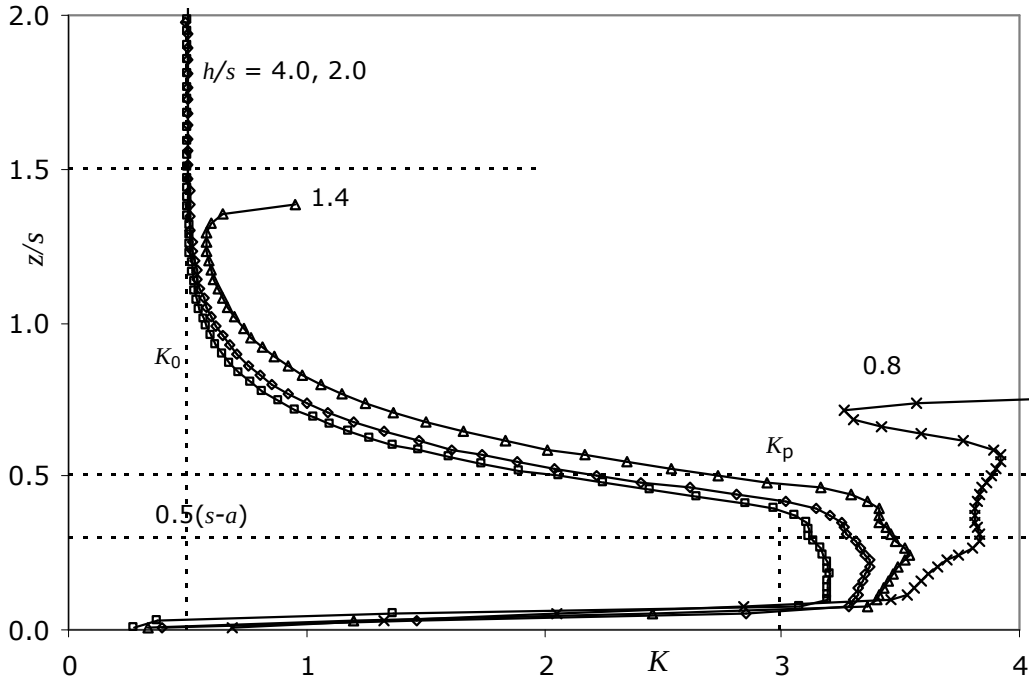

(e) s = 2.5 m, ψ = 22°

Figure 3.3. Profiles of earth pressure coefficient (K) on a vertical profile at the midpoint between piles (z measured upwards from base of embankment, see Section 1.1, Figure 1.1), showing variety of embankment heights (h)

3.3.3 Ultimate stress on the subsoil

Figure 3.4 shows the ultimate stress on the subsoil ($\sigma_{s,ult}$) at the point of maximum arching, illustrating variation with (h/s). Subplot (a) shows normalisation of $\sigma_{s,ult}$ by γh (as in the GRC), whilst (b) shows normalisation by γs.

Figure 3.4(a) shows that for (h/s) > 1.5, ($\sigma_{s,ult}/\gamma h$) reduces slowly as h increases, but when (h/s) < 1.5, ($\sigma_{s,ult}/\gamma h$) increases rapidly, tending towards 1.0. This behaviour was previously noted in Figure 3.2. Also as previously noted the minimum value of ($\sigma_{s,ult}/\gamma h$) tends to increase with s, and for s = 2.5 m is slightly reduced for increased friction angle or dilation angle.

Figure 3.4(b) shows lines $\sigma_s = \gamma h$ (i.e. 'no arching'), and $\sigma_{s,ult} = 0.5\gamma s$. Also shown is a simplified version of the condition for failure of the arch at the pile cap proposed by Hewlett & Radolph (1988). The equation of vertical equilibrium for the plane strain situation, assuming σ_s and σ_c (the vertical stress on the subsoil and pile cap respectively) to be constant is:

$$\sigma_c a + \sigma_s (s - a) = \gamma h s \qquad (3.1)$$

It is then assumed (from analogy with bearing capacity) that $\sigma_c = K_p^2 \sigma_s$, to give:

$$\frac{\sigma_s}{\gamma s} = \frac{h}{s} \frac{1}{(a/s)\left(K_p^2 - 1\right) + 1} \qquad (3.2)$$

This result is plotted for the 3 values of s.

For small (h/s), ($\sigma_{s,ult}/\gamma s$) is less than 0.5, and when (h/s) ≈ 0.5 the data converge with the 'no arching' line. At large h Equation (3.2) shows the correct trend of behaviour, but tends to overestimate $\sigma_{s,ult}$, particularly as s reduces.

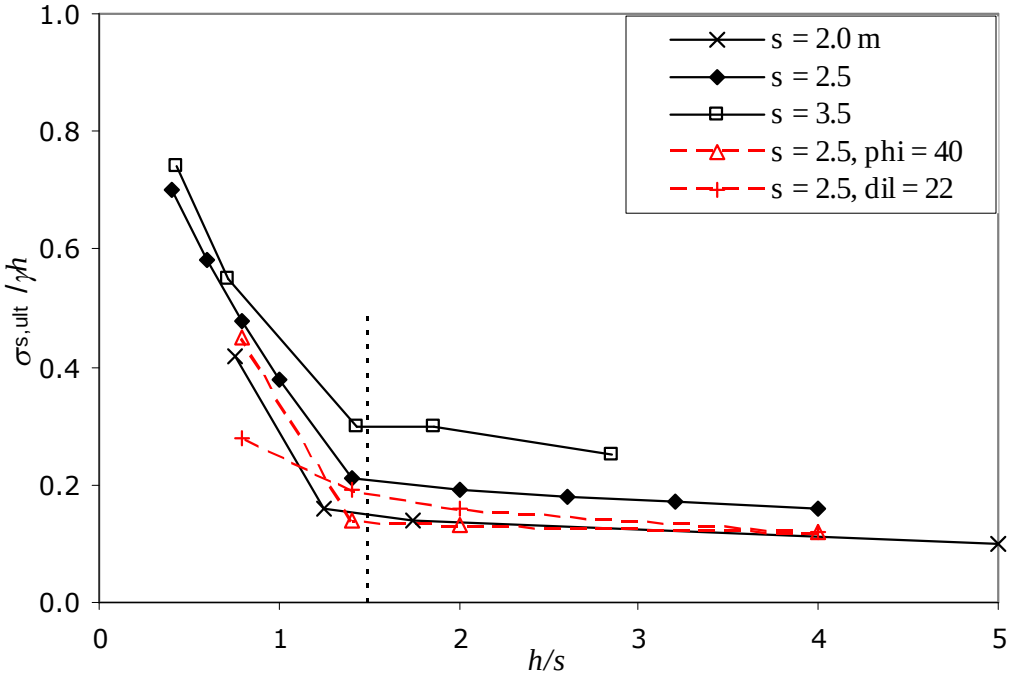

(a) Normalised by γh

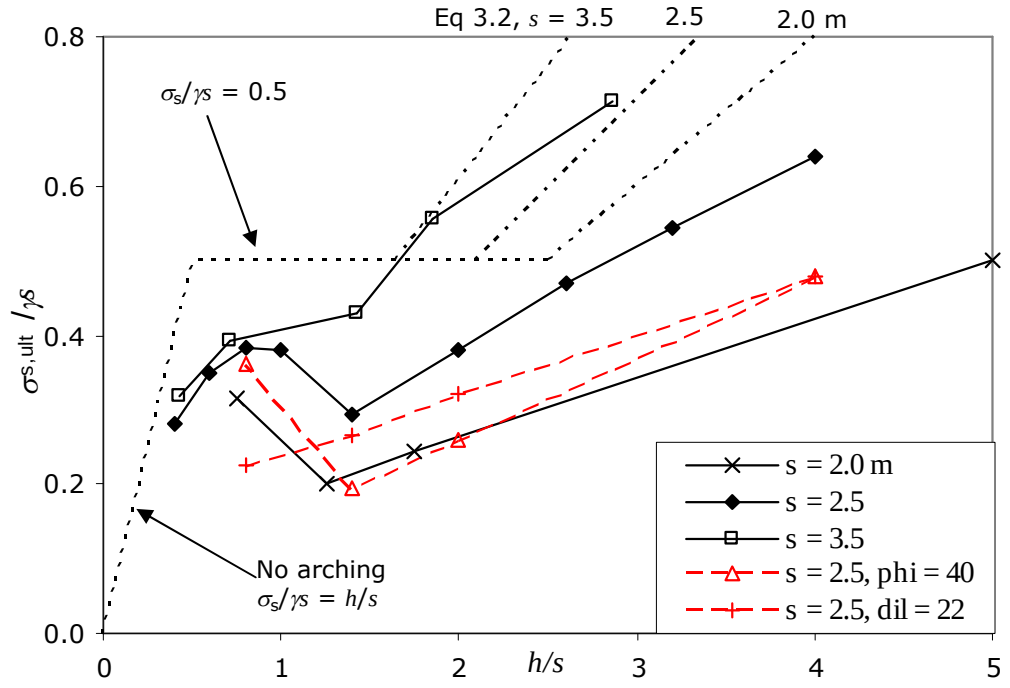

(b) Normalised by γs

Figure 3.4. Normalised stress on the subsoil at ultimate conditions ($\sigma_{s,ult}$) showing variation with (h/s)

3.3.4 Settlement at the subsoil and surface of the embankment

Figure 3.5(a) shows the maximum value of subsoil settlement at the midpoint between piles (see Section 1.1, Figure 1.1) required to reach ultimate conditions: $\delta_{s,ult}$. This value has been estimated 'by eye' from plots such as Figure 3.2, and thus is somewhat subjective. The value has been normalised by the clear gap between pile caps (s-a) so that it is analogous to δ^* for the GRC (see Section 2.3, Figure 2.14). Variation with (h/s) is shown.

The clearest trend is that the normalised displacement to reach ultimate conditions increases with (h/s), tending to zero when (h/s) ≈ 0.5, also corresponding to the point of convergence with the 'no arching' line in Figure 3.4(b). If there is no arching then no displacement is required to reach this 'ultimate' condition. This is also evident in Figure 3.2, where there is less tendency for an ultimate 'plateau' at lower h. As h increases arching occurs, and the amount of stress redistribution from the subsoil to the pile cap increases, thus it is not surprising that the amount of displacement required to achieve ultimate arching conditions also increases. This observation is also consistent with variation with s, which indicates more displacement as s increases (for a given h) since this also implies increased redistribution of load from the subsoil to the pile cap.

The absolute magnitude of $\delta_{s,ult}/(s\text{-}a)$ is somewhat smaller than the value of δ^* of 2 to 6 % quoted for 'maximum arching' by Iglesia et al. (1999),

which appears to be relevant to (h/s) ≈ 2 to 5 in the reference. However, the finite element analyses reported here are linear elastic, and the initial gradient of the GRC (Section 2.3) implies that the ultimate arching conditions would be reached at a lower value of about 1 %. Furthermore, the values shown in Figure 3.5(a) would vary directly in inverse proportion to the value of Young's Modulus used in these analyses. For instance, if the Young's modulus had been reduced by a factor of 2 to better simulate the secant modulus to failure the normalised displacement would be doubled.

As shown in Figure 3.5(b) the ratio of settlement at the top of the embankment at the midpoint between piles (δ_{em}, see Section 1.1, Figure 1.1) to the equivalent value in the subsoil (δ_s) at the point where ultimate conditions are reached: $(\delta_{em}/\delta_s)_{ult}$, was typically in the range 0.45 - 0.75. These values seem reasonable: the settlement at the surface of the embankment is less than beneath the arch, but the ratio tends to increase with s.

Figure 3.5(c) shows the ratio of δ_{em} to the equivalent value at the centreline above the pile cap (δ_{ec}, see Section 1.1, Figure 1.1) at the point where ultimate conditions are reached: $(\delta_{em}/\delta_{ec})_{ult}$, showing variation with (h/s). This is a measure of differential settlement at the surface of the embankment, which is of considerable practical importance in terms of piled embankments. For (h/s) > 1.5 the value is 1.0, indicating no

differential settlement. As h reduces below this value, differential settlement increases, dramatically so for (h/s) less than about 0.75.

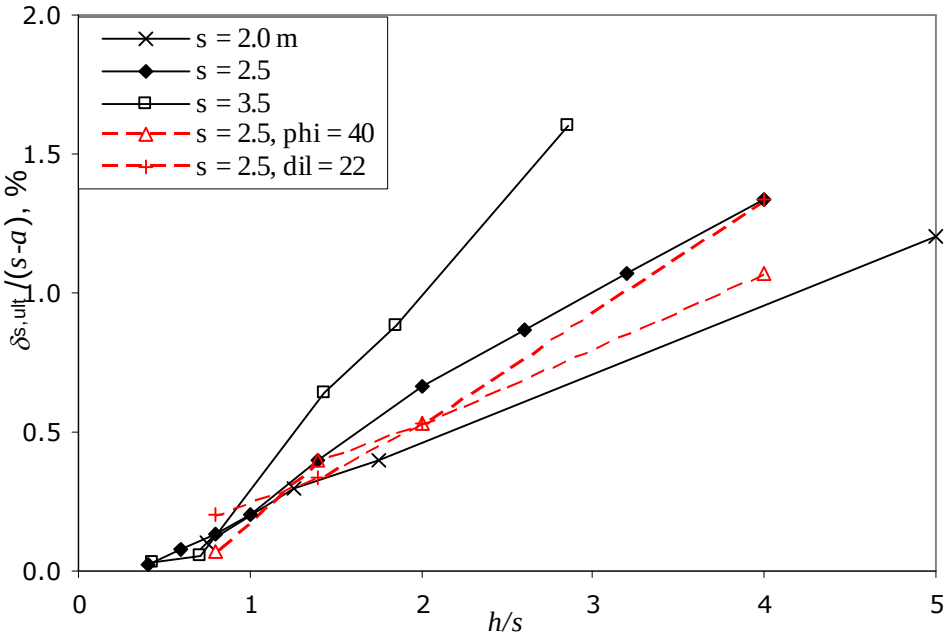

(a) Ultimate settlement of the subsoil at the midpoint between piles ($\delta_{s,ult}$) normalised by the clear gap between pile caps (s-a)

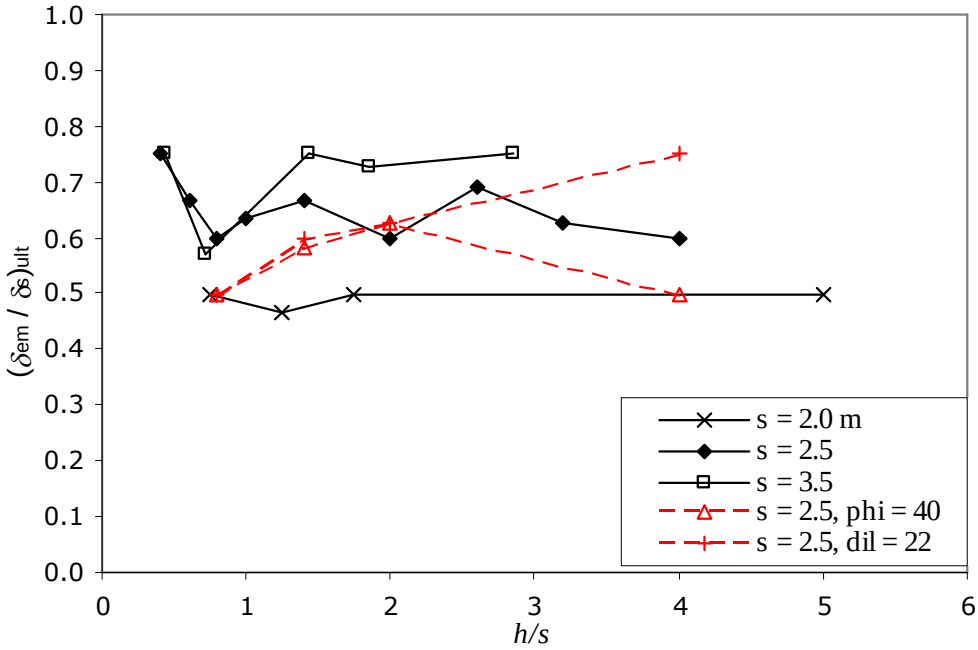

(b) Ratio of the settlement at the top of the embankment at midpoint between piles (δ_{em}) to the equivalent value in the subsoil (δ_s)

Figure 3.5 continued on following page

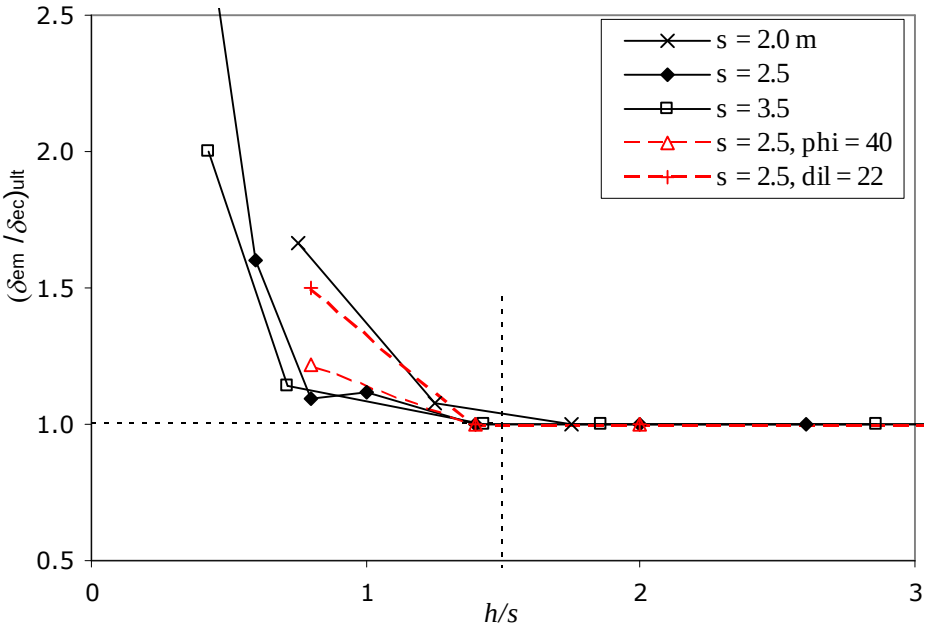

(c) Ratio of the settlement at the top of the embankment at midpoint between piles (δ_{em}) to the equivalent value at the centreline above the pile cap (δ_{ec})

Figure 3.5. Settlement results at the subsoil and surface of the embankment

3.4 Summary

The results of a series of linearly elastic-perfectly plastic plane strain finite element analyses to investigate the arching of a granular embankment supported by pile caps over a soft subsoil have been presented. The analyses demonstrate that the ratio of the embankment height to the centre-to-centre pile spacing (h/s) is a key parameter:

- (h/s) ≤ 0.5 there is virtually no effect of arching: 'ultimate' conditions are reached almost immediately (with very small displacement) in the analysis, relative differential settlement at the surface of the embankment is very large, and the stress acting on the subsoil is virtually unmodified from the nominal overburden stress.
- 0.5 ≤ (h/s) ≤ 1.5 there is increasing evidence of arching: as (h/s) increases the displacement required to reach 'ultimate' conditions increases, relative differential displacement at the surface of the embankment reduces, and the stress acting on the subsoil reduces compared to the nominal overburden stress.
- 1.5 ≤ (h/s) 'full' arching is observed: the displacement required to reach ultimate conditions continues to increase and a clearly defined ultimate state is maintained at large displacement. There is no differential displacement at the surface of the embankment, and the stress acting on the subsoil is considerably reduced compared to the nominal overburden stress. For a high embankment the

stress state is not significantly affected above a height of 1.5 s in the embankment.

Furthermore, it has been shown (Figure 3.4(b)) that up to a critical value of (h/s) the stress on the subsoil is less than $0.5\gamma s$, approximately representing the effect of the infill material below the arch. At higher values of (h/s) conditions at the pile cap are critical and Equation (3.2) can be used to conservatively estimate the stress on the subsoil in plane strain.

CHAPTER 4

GEOGRID REINFORCED PILED EMBANKMENT IN PLANE STRAIN

4.1 Introduction

This chapter considers piled embankments where one or more layers of geotextile or geogrid reinforcement are used at the base of the embankment. Again a plane strain model is used at this stage, forming a logical extension of the analyses presented in the previous chapter.

4.2 Analyses presented

The series of plane strain analyses presented here were again performed using the finite element program Abaqus Version 6.6. Figure 4.1 shows a typical mesh for the reinforced embankment, with height h = 3.5 m and pile spacing s = 2.5 m. There are 1566 eight noded, reduced-integration, two-dimensional, quadratic solid elements (CPE8R) for the embankment. The geogrid is modelled using 16 three noded quadratic truss elements (T2D3). As discussed in Chapter 2, Truss elements are used to model slender, line-like structures that carry loading only along the axis or the centreline of the element, and no moments or forces perpendicular to the centreline (Abaqus Analysis User's manual, Version 6.6). Hence the tensile action of the reinforcement is modelled with no bending stiffness.

A contact model is required to 'join' the 'solid' elements used for the soil and the 'truss' elements used for the geogrid. A 'surface to surface' contact type has been used (see Section 2.6.3.2). As in the previous Chapter the vertical boundaries represent lines of symmetry at the centreline of a support (pile cap), and the midpoint between supports (see Section 1.1, Figure 1.1) with corresponding restraint on horizontal movement. The reinforcement is positioned 0.1 m above the base of the embankment, and there is likewise restraint on horizontal movement at both ends. In some analyses three layers of reinforcement were used at 0.1, 0.4 and 0.7 m above the base of the embankment, in an attempt to simulate a 'Load Transfer Platform' (LTP).

Again there are no boundary conditions imposed at the top embankment surface, and no surcharge is considered to act here. The bottom boundary represents the base of the embankment, with the same boundary conditions as used in the previous chapter. The vertical stress in the subsoil supporting the embankment (σ_s) is again used to control the analysis - the subsoil itself was not actually modelled. As the subsoil stress (σ_s) reduces, arching will occur as studied in the previous Chapter, but tension will also be generated in the geogrid.

The pile cap width (a) was again fixed at 1 m and the centre-to-centre spacing (s) was 2.0, 2.5 or 3.5 m. The embankment height (h) was 1, 3.5 or 10 m. Throughout the analyses the minimum and maximum element sizes of the embankment were approximately 0.0006 and 0.00738 m^3/m.

This corresponds to side lengths of approximately 30 to 150 mm. The truss element lengths were 20 to 100 mm.

The embankment material was again assumed to be granular, and modelled using the standard linear elastic and Mohr Coulomb yield criterion parameters as the previous Chapter, as shown in Table 4.1.

The parameters used for the reinforcement are shown in Table 4.2. The tensile stiffness k was 6 or 12 MN/m for a single layer of reinforcement, or 2 MN/m for each of the layers where 3 layers were modelled. This is effectively specified using the product of the Young's Modulus of the material and the cross sectional area per metre width. Here the latter was taken as a nominal 1 mm thickness, and corresponding values of Young's Modulus were assigned to give the required value of k. The Poisson's Ratio of zero means that axial strain does not affect the plane strain direction. The interface friction angle (δ_i) between the embankment fill and geogrid was 0° or 20°, corresponding to a nominally 'smooth' or 'rough' interface.

All analyses reported in this Chapter are summarised in Table 4.3. Variations to the 'standard' parameters are highlighted in bold. In the first three analyses, for s = 2.5 m and k = 6 MN/m with δ_i = 0, the effect of increasing h from 1 to 10 m was considered. Then for h = 3.5 m, the influence of increasing s from 2.0 to 3.5 m was considered.

The remaining analyses considered the effect k, δ_i and the number of geogrid layers (N). Where three layers of geogrid were used, it was assumed that each grid would have a relatively low stiffness of 2 MN/m, thus giving a 'total' stiffness of 3×2 = 6 MN/m, as previously used for a single grid.

The sequence of analysis was the same as the previous chapter. First the in-situ stresses were specified (again based on a unit weight of 17 kN/m^3 and a K_0 value of 0.5). σ_s then reduced from the nominal vertical stress at the base of the embankment to mimic the loss of support from the subsoil.

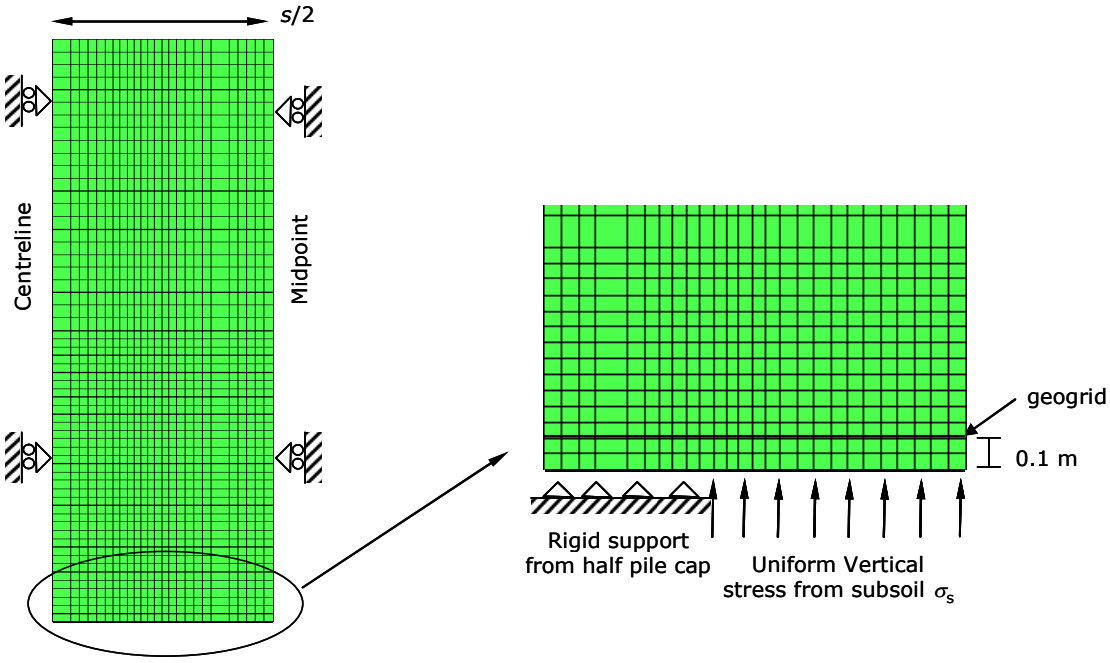

Figure 4.1. Typical finite element mesh (h = 3.5 m, s = 2.5 m, one layer of reinforcement) and boundary conditions for reinforced embankment

Table 4.1. Material parameters for granular embankment fill

Young's Modulus (MN/m^2)	Poisson's Ratio	c' (kN/m^2)	ϕ' (deg)	Kinematic dilation angle (ψ) (deg)
25	0.2	1	30	0

Table 4.2. Material parameters for geogrid

Young's Modulus (MN/m^2)	Poisson's Ratio	Cross-section area (m^2/m)
6,000 (or 12,000 or 2,000 with three layers of geogrid)	0.0	0.001

Table 4.3. Summary of analyses reported in this Chapter

	h (m)	s (m)	k (MN/m)	δ_i	subplot
Effect of h	**1**	2.5	6	0	(a)
	3.5	2.5	6	0	(b)
	10	2.5	6	0	(c)
Effect of s	3.5	**2**	6	0	(d)
	3.5	**3.5**	6	0	(e)
Effect of geogrid: k	3.5	2.5	**12**	0	(f)
Effect of geogrid: δ_i	3.5	2.5	6	**20**	(g)
Effect of geogrid: N	3.5	2.5	**3×2**	0	(h)
Effect of geogrid: N and δ_i	3.5	2.5	**3×2**	**20**	(i)

4.3 Results

4.3.1 Behaviour of reinforced piled embankment

Figure 4.2 shows the maximum displacement at the midpoint between pile caps (δ_s), which increases with a reduction in the stress on the subsoil (σ_s). There are three lines:

- 'Ground Reaction Curve' (GRC)
- 'Embankment with geogrid'
- 'GRC + effect of geogrid' (a theoretical comparison line)

The first part of the GRC line comes from the analyses reported in Chapter 3, for an unreinforced piled embankment. These results were previously presented in Figure 3.2 in a normalised form. The value of σ_s at the point of maximum arching has been 'extrapolated' to large δ_s.

The 'embankment with geogrid' line shows results from the analyses summarised in Table 4.3 as separate sub-plots. Note that 'geogrid' could equally refer to geosynthetic reinforcement.

The 'GRC + effect of geogrid' line, has been derived from the ground reaction curve (GRC) combined with Equation (2.30):

$$w = \frac{64k}{3l}\left(\frac{\delta_g}{l}\right)^3. \qquad (2.30)$$

Where:

w = the assumed uniform stress acting on the geogrid (kN/m^2)

δ_g = the maximum sag of the geogrid (m)

l = the span of the geogrid (m)

If the GRC data from Chapter 3 is σ_s(GRC), and $w(\delta_g = \delta_s)$ is the reduction in stress on the subsoil due to the vertical stress carried by the geogrid for a sag equal to the subsoil settlement, then

σ_s(GRC + effect of geogrid) = σ_s(GRC) – $w(\delta_g = \delta_s)$

Here, the length of span (l) is assumed to be ($s - a/2$) – the origin of this value will be explained later. This expression can then be evaluated for any value of δ_s where GRC data is available, and is hence plotted in Figure 4.2 as a 'theoretical comparison' line.

In general the response from an analysis of the 'Embankment with geogrid' is similar to the comparison ('GRC + effect of geogrid') line. However, in some cases (subplots (a) and (e)) the embankment with geogrid analysis performs 'better' than anticipated based on the comparison line (i.e. σ_s is less than predicted for a given δ_s). Generally the data points on the 'Embankment with geogrid' line are so densely positioned (corresponding to increments in the analysis) that they cannot be clearly identified. However, the extrapolated 'GRC' and 'GRC + effect of geogrid' are clearly identified and thus it can be established that the 'Embankment with geogrid' line is the remaining line.

For the GRC, the stress at the base of the embankment (σ_s) never reaches zero. However, if the geogrid carries the remaining stress at the point of

maximum arching, σ_s can reach zero, and approaches this value at the end of the analyses. However, significant sag of the geogrid is required for this to happen.

Subplots (a), (b) and (c) show the effect of increasing embankment height (h). The subsoil settlement at the midpoint between piles (δ_s) when $\sigma_s \approx 0$, increases with increasing embankment height. This is because σ_s at the point of maximum arching for the GRC increases with the height of the embankment (see Figure 3.4(b) in Chapter 3), and hence the geogrid has to carry more load and deforms more.

Subplots (d), (b) and (e) show the effect of increasing centre-to-centre pile cap spacing (s). The largest settlement of the subsoil is observed at the largest s, corresponding to very strong dependency on l in Equation (2.30).

For subplot (f), comparing with subplot (b) there is relatively little change, corresponding to relatively limited dependency on geogrid stiffness (k) in Equation (2.30).

Subplot (g) shows the effect of increased interface friction angle (δ_i) between the geogrid and embankment soil. Compared to subplot (b) the data show the settlement of the subsoil when $\sigma_s \approx 0$ is slightly reduced, but there is not a major impact.

Subplot (h) considers three layers of geogrid (k = 2 MN/m) with a frictionless interface. This causes the point of maximum arching in the analysis for the full embankment with geogrid to have slightly higher σ_s than the GRC. This can be attributed to the presence of the three layers of geogrid with frictionless interfaces, which weakens the mass properties of the soil near the base of the embankment. The results at larger displacement are closer to a comparison line based on k = 2 MN/m (for a single geogrid). This implies that the geogrids are less effective than a single geogrid with 3 times the stiffness. The tension in the geogrids will be considered further below.

Subplot (i) shows the result for three layers of geogrid with k = 2 MN/m, where the interface friction angle between the geogrid and the surrounding soil (δ_i) is 20°. This improves comparison with the GRC at the point of maximum arching, and the data are close to the comparison line for k = 6 MN/m, which reflecting the total stiffness of the 3 grids.

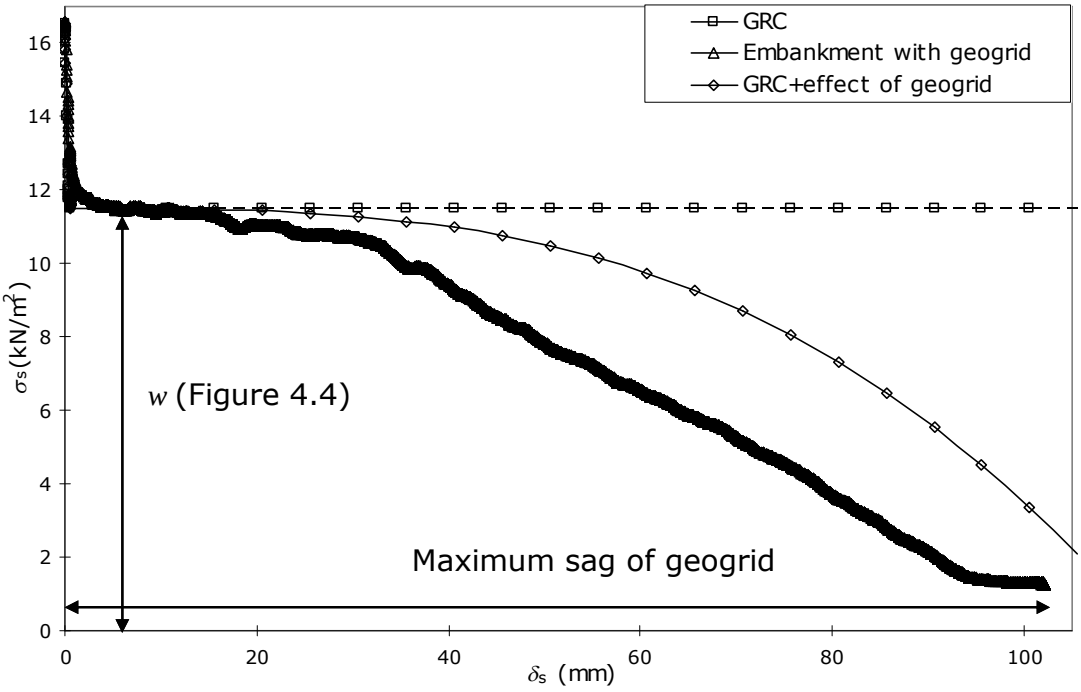

(a) h = 1 m, s = 2.5 m, k = 6 MN/m, δ_i = 0

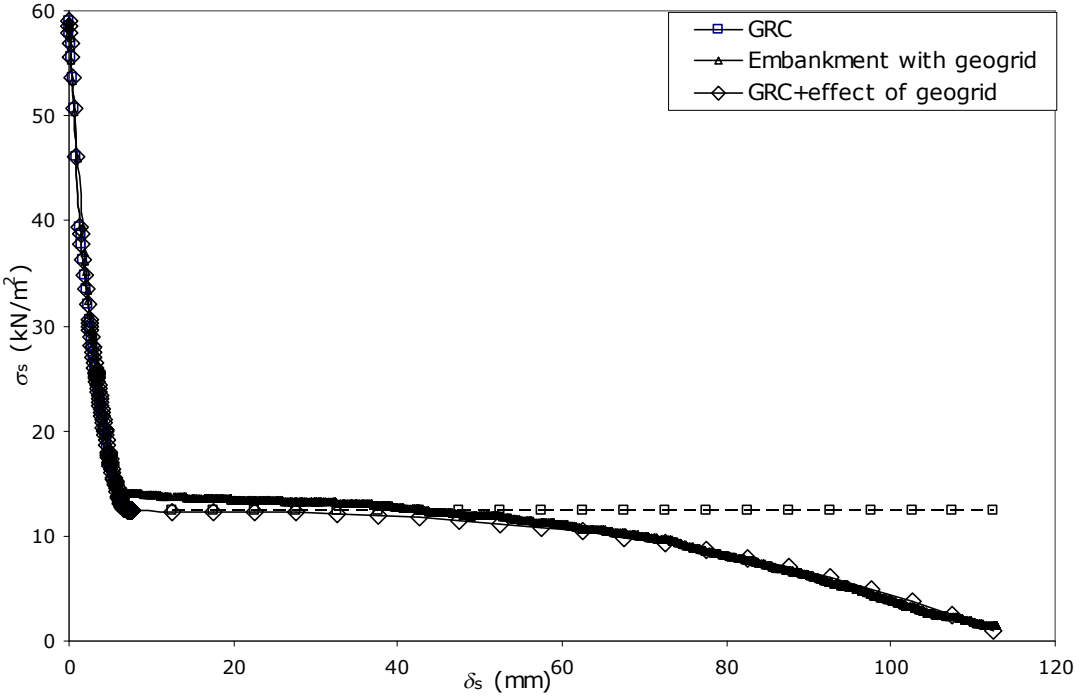

(b) h = 3.5 m, s = 2.5 m, k = 6 MN/m, δ_i = 0

Figure 4.2 continued on following page

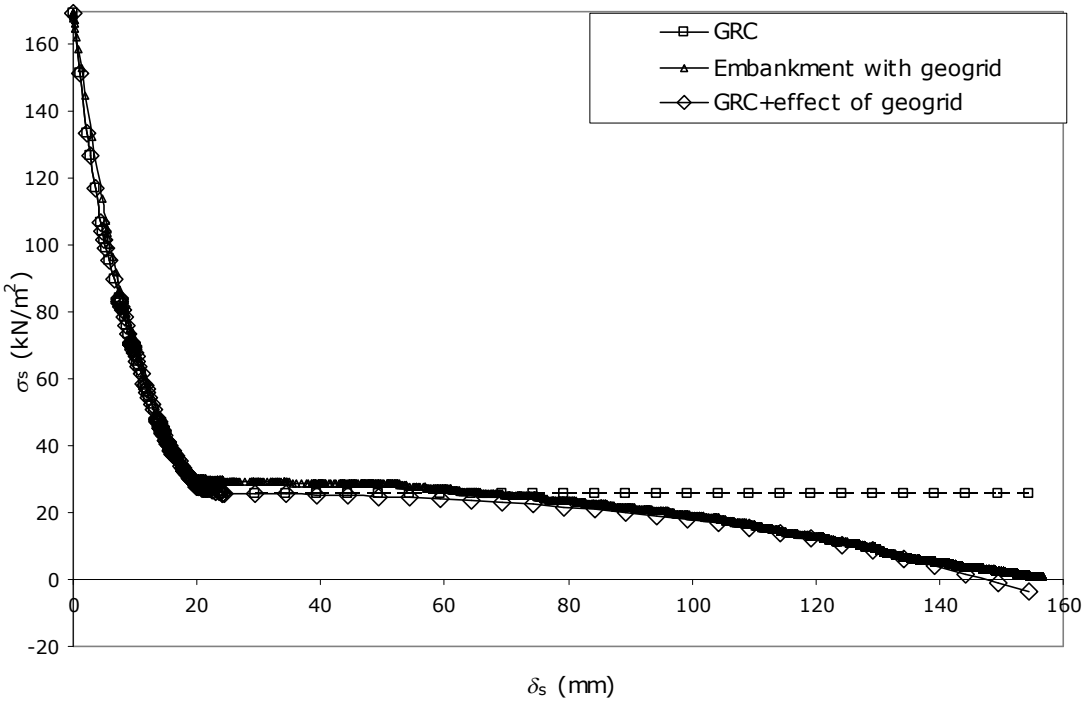

(c) h = 10 m, s = 2.5 m, k = 6 MN/m, δ_i = 0

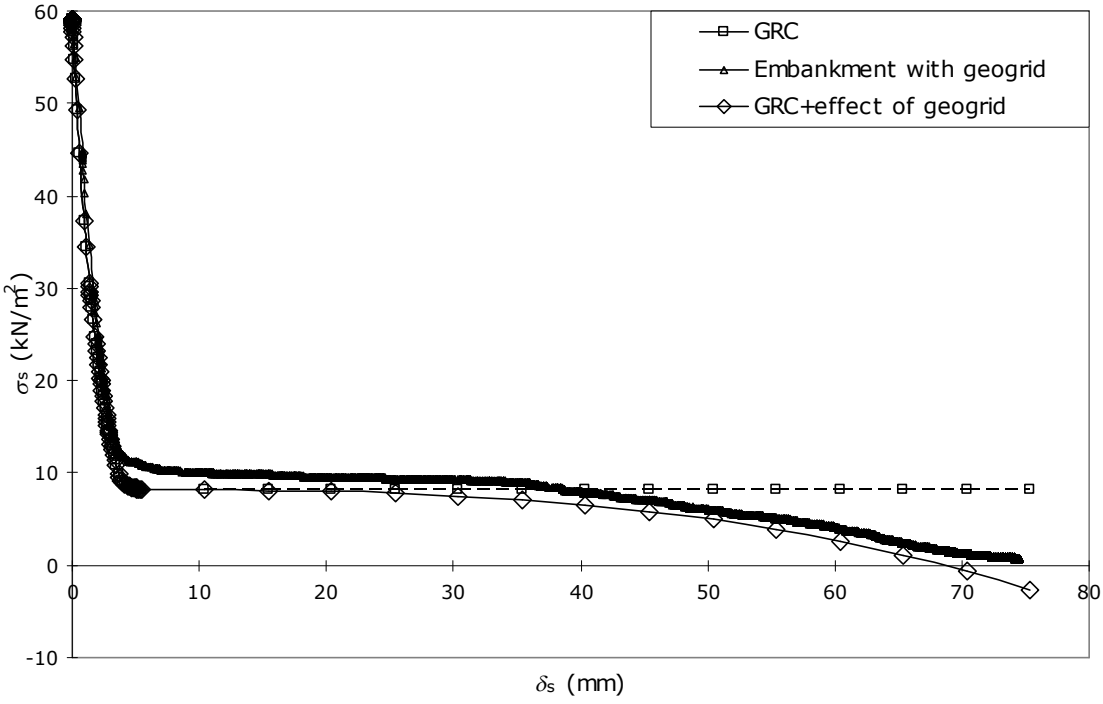

(d) h = 3.5 m, s = 2 m, k = 6 MN/m, δ_i = 0

Figure 4.2 continued on following page

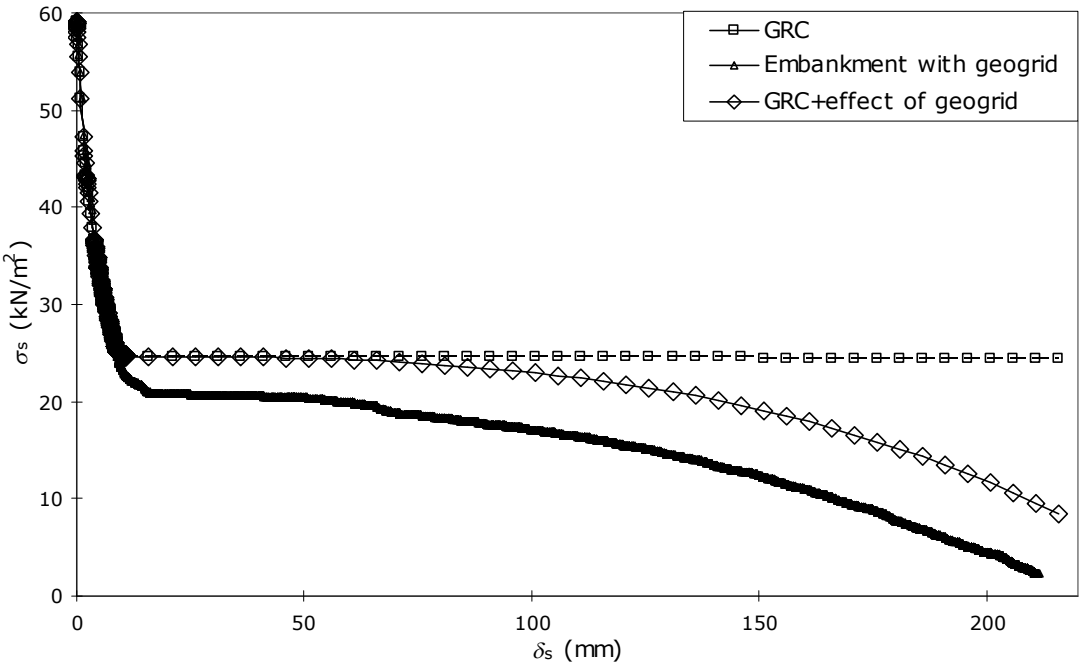

(e) h = 3.5 m, s = 3.5 m, k = 6 MN/m, δ_i = 0

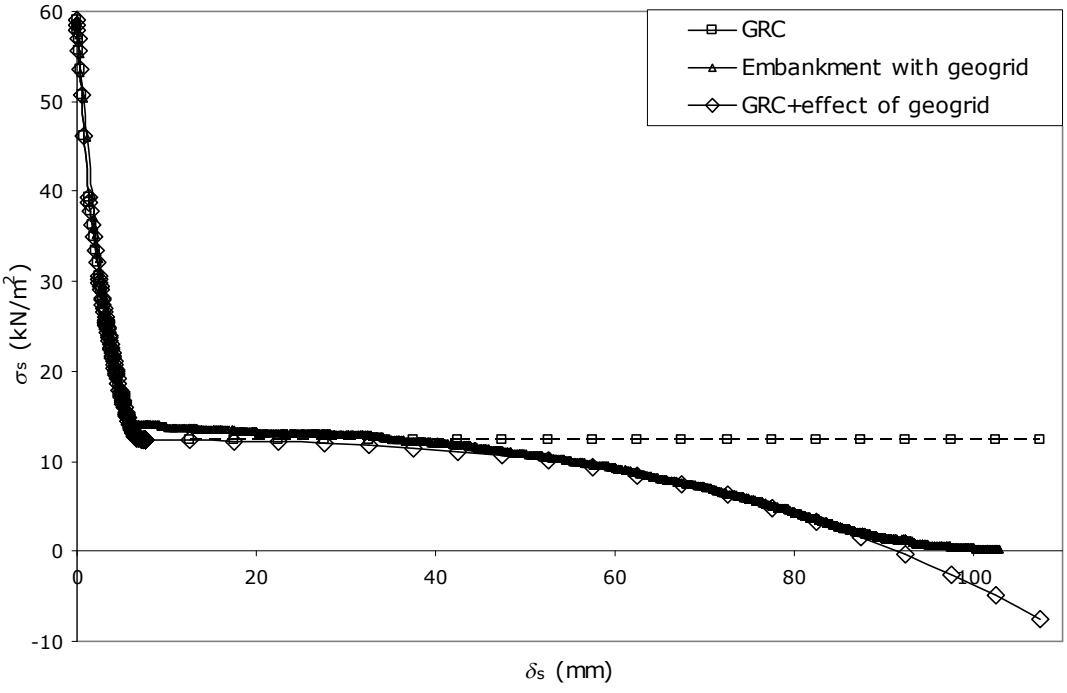

(f) h = 3.5 m, s = 2.5 m, k = 12 MN/m, δ_i = 0

Figure 4.2 continued on following page

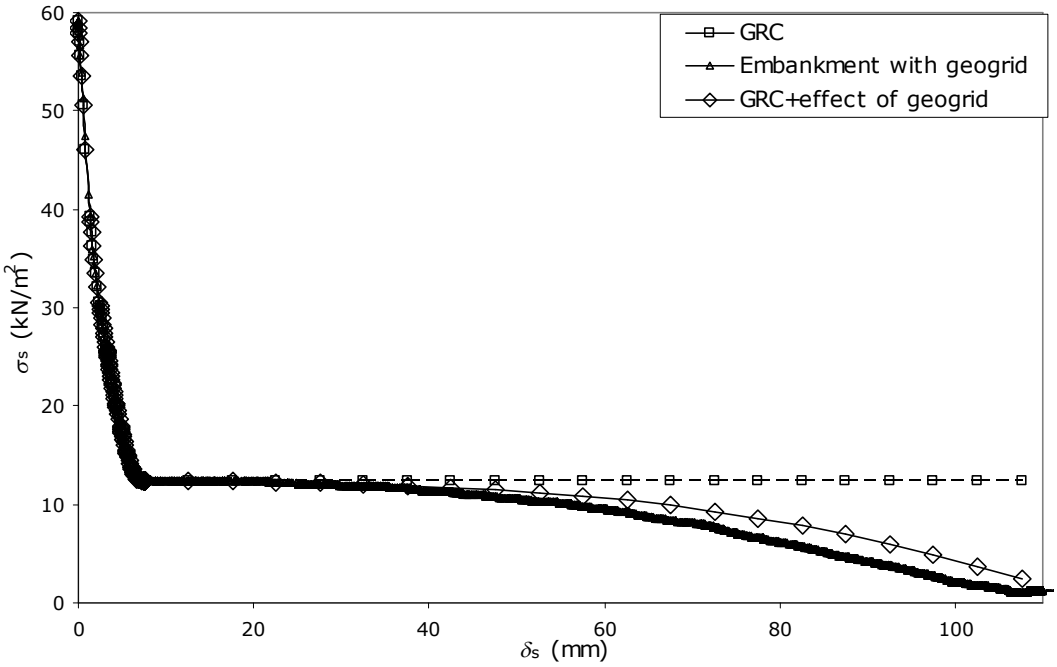

(g) h = 3.5 m, s = 2.5 m, k = 6 MN/m, δ_i = 20 (interface friction angle)

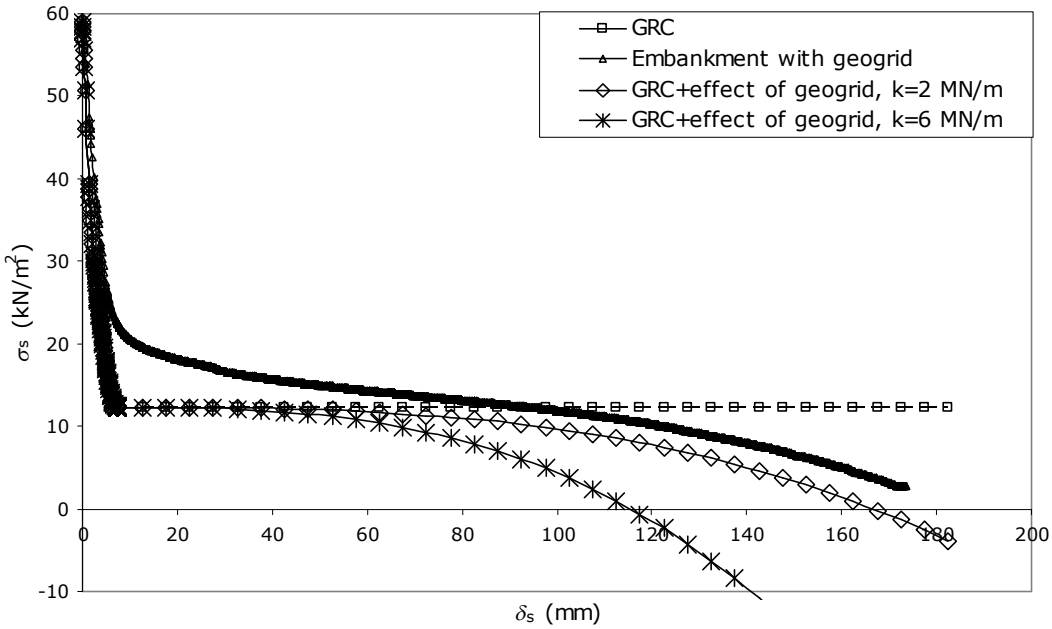

(h) h = 3.5 m, s = 2.5 m, k = 3×2 MN/m, three layers of geogrid with δ_i = 0 (interface friction angle)

Figure 4.2 continued on following page

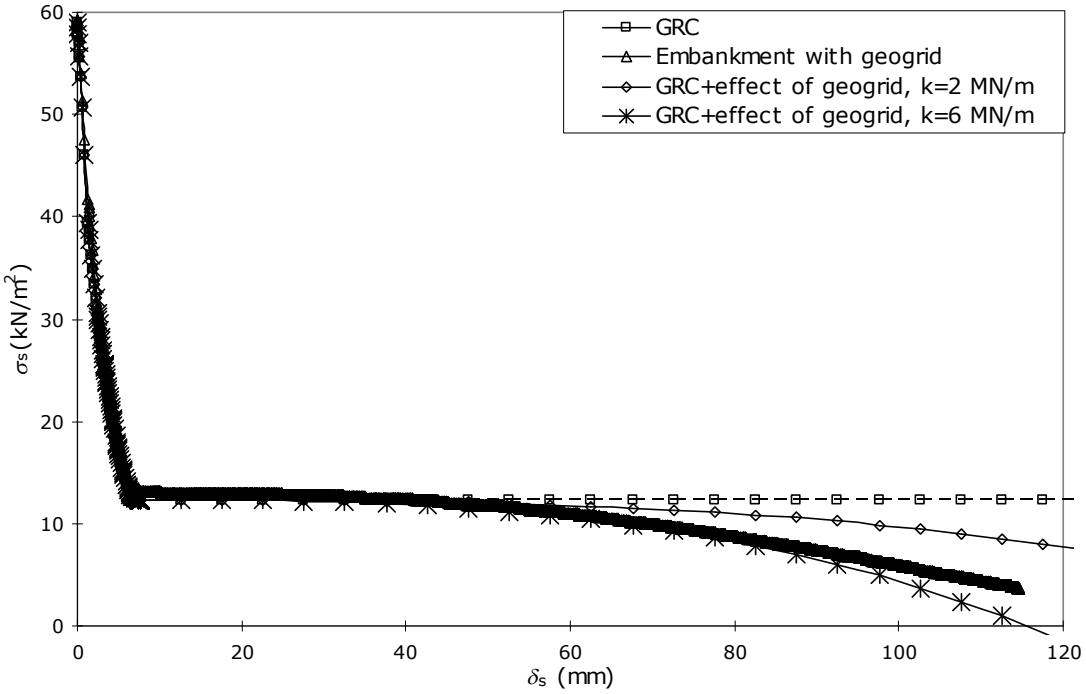

(i) h = 3.5 m, s = 2.5 m, k = 3×2 MN/m, three layers of geogrid with δ_i = 20 (interface friction angle)

Figure 4.2. Variation of subsoil settlement and stress for reinforced piled embankments

4.3.2 Settlement at the subsoil and surface of the reinforced piled embankment

Figure 4.3(a) shows the maximum value of subsoil settlement at the midpoint between piles (see Section 1.1, Figure 1.1) required to reach ultimate conditions: $\sigma_{s,ult} \approx 0$. The value has been normalised by the clear gap between pile caps (s-a) so that it is analogous to δ^* (see Section 2.3, Figure 2.14). Variation with (h/s) is shown (from subplots (a) to (c)) throughout Figure 4.3.

The magnitude of δ^* is between 6 and 11% when $\sigma_{s,ult} \approx 0$ and the normalised displacement to reach this point increases with h/s. These values are considerably larger than the equivalent data for the point of maximum arching, which were approximately between 0 and 1.6% (see Chapter 3, Figure 3.5(a)). This finding can be explained by the significant geogrid sag required to carry the remaining subsoil stress.

As presented in Figure 4.3(b), the ratio of settlement at the top of the embankment at the midpoint between piles (δ_{em}, see Section 1.1, Figure 1.1) to the equivalent value in the subsoil (δ_s) at the point where $\sigma_{s,ult} \approx 0$: $(\delta_{em}/\delta_s)_{ult}$ is in the range 0.4 - 0.9. This is similar to the result reported in Chapter 3 (see Chapter 3, Figure 3.5(b)) for the point of maximum arching on the GRC, and only approaches 1.0 when the embankment is very low and there is no arching. For higher embankments settlement at the surface of the embankment is less than at the subsoil as would be expected.

Figure 4.3(c) shows the ratio of δ_{em} to the equivalent value at the centreline above the pile cap δ_{ec} (see Section 1.1, Figure 1.1) at the point where $\sigma_{s,ult} \approx 0$: $(\delta_{em}/\delta_{ec})_{ult}$, showing variation with (h/s). This is a measure of differential settlement at the surface of the embankment, which shows similar behaviour to the point of maximum arching for the GRC (see Chapter 3, Figure 3.5(c)). For $(h/s) > 1.5$ the ratio is 1.0, which indicates there is no differential settlement at the top of the embankment. However, the differential settlement increases dramatically for the lowest embankment.

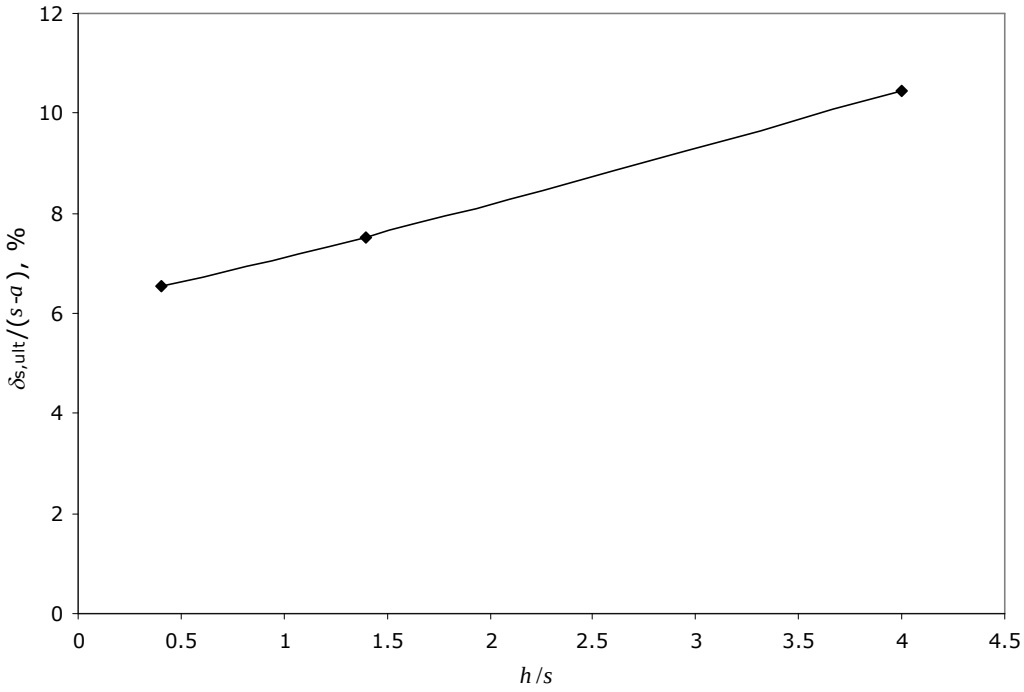

(a) Ultimate settlement of the subsoil at the midpoint between piles ($\delta_{s,ult}$) normalised by the clear gap between pile caps (s-a)

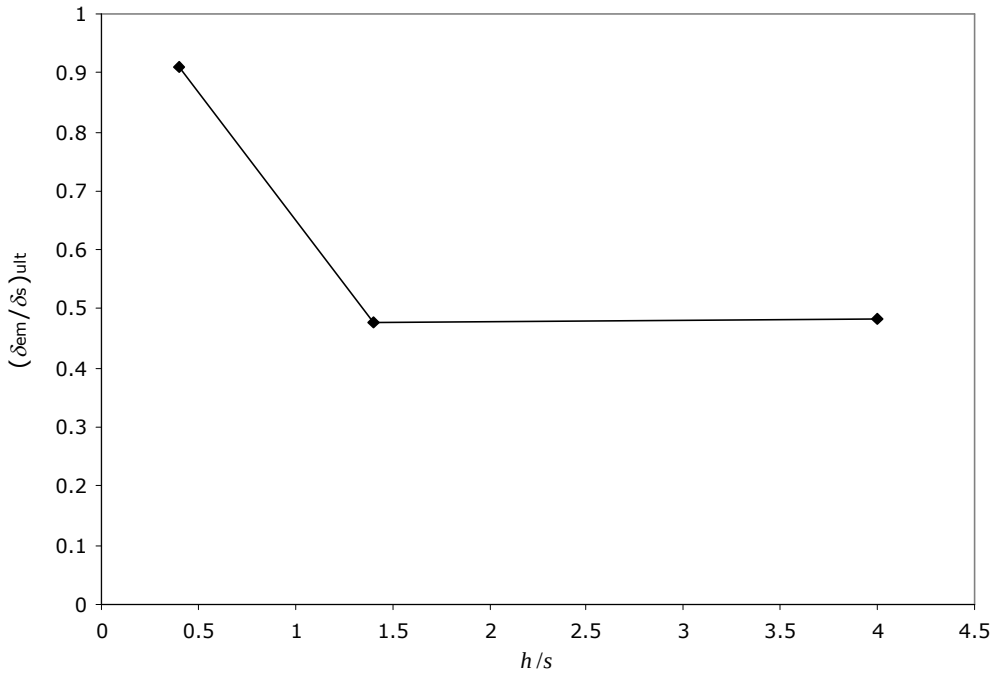

(b) Ratio of the settlement at the top of the embankment at the midpoint between piles (δ_{em}) to the equivalent value at the subsoil ($\delta_{s,ult}$)

Figure 4.3 continued on following page

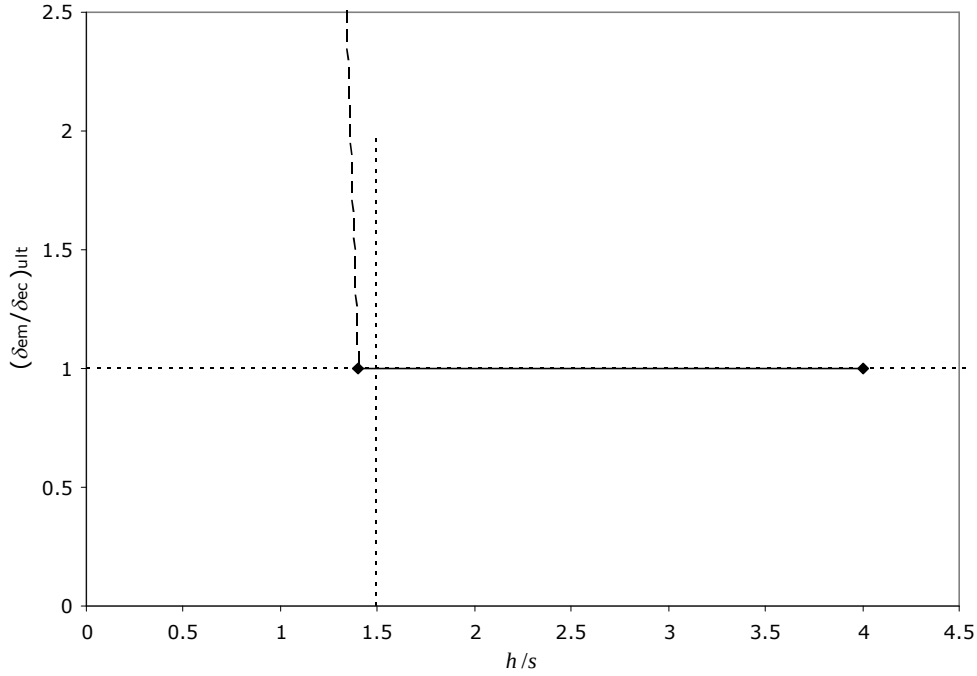

(c) Ratio of the settlement at the top of the embankment at the midpoint between piles (δ_{em}) to the equivalent value at the centreline above the pile cap (δ_{ec})

Figure 4.3. Ultimate ($\sigma_{s,ult} \approx 0$) settlement at the subsoil and surface of the reinforced piled embankment

4.3.3 Behaviour of geogrid in the piled reinforced embankment

Figure 4.4 shows the amount of vertical load which is carried by the geogrid (w), illustrating variation with the maximum sag of the geogrid (subplot (a)), and the tension which this load generates in the geogrid (subplot (b)) respectively. Figure 4.2 shows how these values were established from the plots.

Theoretical comparison lines were derived by combining Equations (2.26), (2.27) and (2.28).

Substituting Equation (2.27) into Equation (2.28) leads to:

$$T = \frac{8}{3}k\left(\frac{\delta_g}{l}\right)^2 \quad (4.1)$$

Re-arranging this equation:

$$\sqrt{\frac{3T}{8k}} = \frac{\delta_g}{l} \quad (4.2)$$

Re-arranging Equation (2.26):

$$\frac{l\,w}{8T} = \frac{\delta_g}{l} \quad (4.3)$$

Combing Equation (4.2) and (4.3),

$$\sqrt{\frac{3T}{8k}} = \frac{l\,w}{8T} \quad (4.4)$$

Thus,

$$T = \left(\frac{1}{24}k\,w^2\,l^2\right)^{(1/3)} \quad (4.5)$$

Equation (2.29) can be re-arranged to give:

$$\delta_g = l\left[\frac{3}{64}\left(\frac{wl}{k}\right)\right]^{(1/3)} \quad (4.6)$$

Equations (4.5) and (4.6) were used to derive the comparison lines in Figure 4.4(b) and (a) respectively with $l = (s - a/2)$. This value was chosen as an average of the unsupported span ($s - a$) and the centre-to-centre spacing s.

Figure 4.4 shows one data point for each of the analyses summarised in Table 4.3. This corresponds to the ultimate point in the analysis, when $\sigma_{s,ult} \approx 0$ and sag of the geogrid has reached its maximum value. The corresponding stress carried by the geogrid w, is taken as the value of σ_s at the point of maximum arching.

Subplot (a) shows stress on the geogrid and the corresponding maximum sag. A total of 4 comparison lines (Equation 4.6) are shown, corresponding to variation of s and k. The comparison line for l = 2 m (s = 2.5 m) and k = 6 MN/m corresponds to cases (a-c) and (g-i) in Table 4.3. Hence the line and corresponding data points are red. The data shows reasonable agreement except for analysis (h) - 3 geogrids with frictionless interface with the soil. Since the sum of stiffness for the 3 grids is 6 MN/m, it can be compared with this line. However, the displacement is somewhat larger than expected, which as previously noted reflects the reduced effectiveness of the upper grids in carrying load.

For l =1.5 m (s = 2.0 m) with k = 6MN/m (pink), comparison with case (d) is good. For l =3 m (s = 3.5 m) with k = 6MN/m (blue), the correct trend of behaviour can be observed, but the comparison line somewhat overestimates the displacement compared to case (e). For l = 2.0 m (s = 2.5 m) with k = 12 MN/m (green), comparison is good with case (f).

In general the results show good comparison with Equation (4.6), confirming that the maximum sag is considerable more affected by the span l than the stiffness k.

Subplot (b) shows that the tension in the reinforcement increases with an increase of the vertical stress carried by the geogrid w. For cases (a-g) the comparison lines are matched with data points from the analyses using the same colours as in Subplot (a). It was observed that tension in the geogrid was approximately constant across the width, including over the pile cap. All the check lines give a slightly conservative estimate of tension compared to the data, but agreement is reasonable.

For the cases with three layers a separate data point is shown for each layer of geogrid, and a new comparison line is shown based on k = 2 MN/m (purple), the stiffness of each geogrid rather than the combined total for all 3 (k = 6 MN/m). It can be seen that the upper two grids carry relatively little tension compared to the bottom layer, presumably implying less sag Equation (4.1) and less effective performance.

In general the results show good comparison with Equation 4.5, confirming that tension is most sensitive to the stress carried by the geogrid and length of the span.

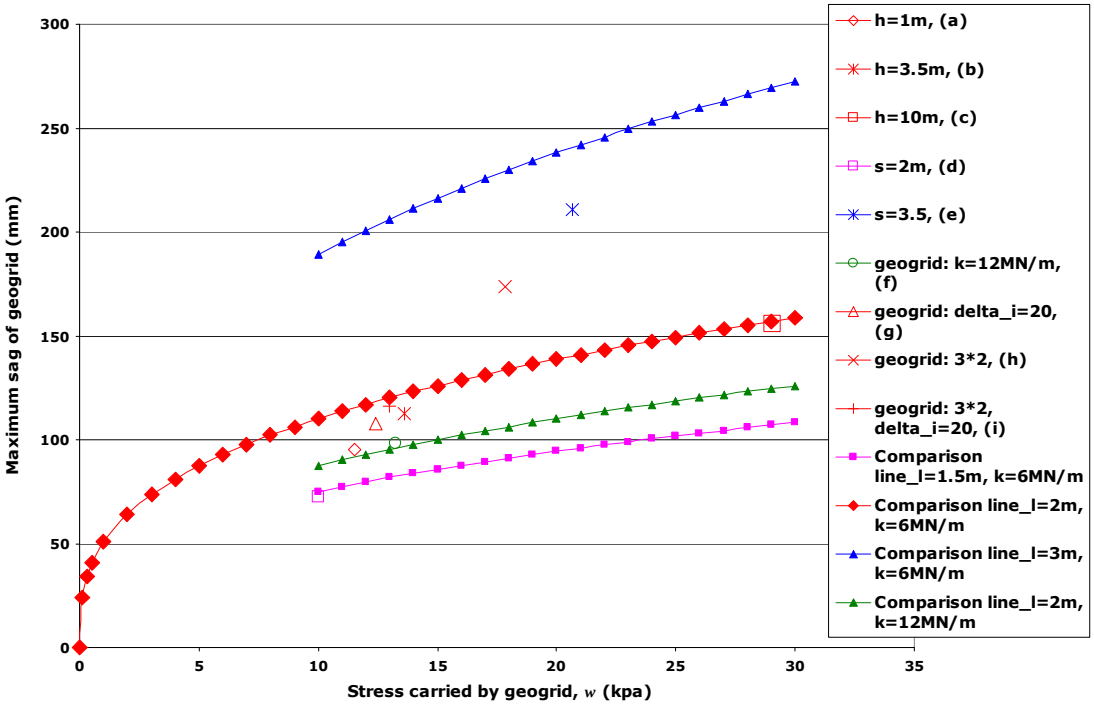

(a) Maximum sag of the geogrid

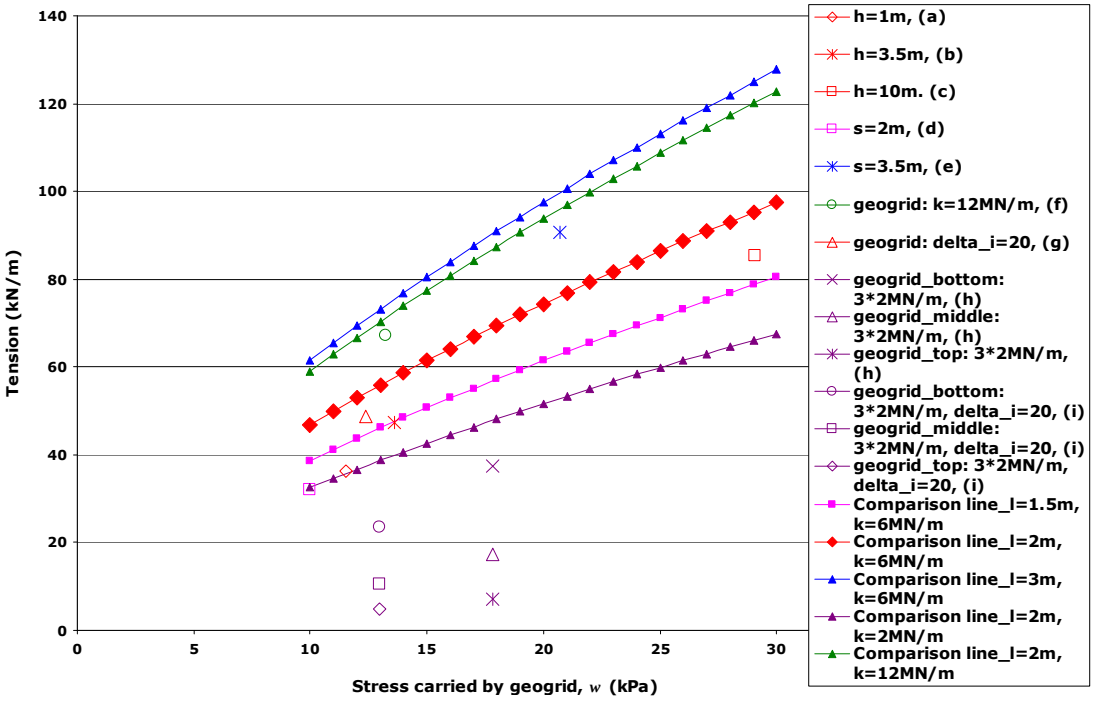

(b) Tension in the geogrid

Figure 4.4. Maximum displacement and tension of geogrid generated by vertical stress carried by the geogrid (w). Specific colours associate results with comparison lines.

4.4 Summary

Chapter 4 has focussed on the role of geogrid reinforcement in addition to the GRC for arching in the embankment previously considered in Chapter 3. The analyses were again conducted in plane strain.

It was found that the geogrid was capable of reducing the ultimate stress on the subsoil to zero. However, this required significant sag of the geogrid. Comparison of the geogrid action with a simple formula (Equation (2.30)) for the sag gave reasonable agreement.

Further development of the formulae indicated that the sag was very sensitive to the span of the geogrid between piles, but relatively insensitive to the stiffness of the geogrid (Equation (4.6)). This observation was supported by the results of the analyses.

For a case with 3 geogrids the upper two grids carried relatively little tension compared to the bottom layer. This finding has been proposed by Jenner et al. (1998) in a field study. They stated that larger grid strains were recorded in the lower grid than the upper gird as anticipated in the design.

CHAPTER 5

REINFORCED PILED EMBANKMENT WITH SUBSOIL IN PLANE STRAIN

5.1 Introduction

The final stage considered here for plane strain analysis is the presence of the soft subsoil beneath a reinforced embankment. The effect of subsoil is normally ignored, as this support may not be reliable in the long-term as consolidation proceeds. The idealised long-term behaviour of the subsoil is investigated here, in conjunction with the ground reaction curve and reinforcement.

5.2 Analyses presented

In this section, the numerical modelling of a geogrid-reinforced embankment with subsoil is again performed using Abaqus Version 6.6. Typical mesh geometry is shown in Figure 5.1 (for h = 3.5 m, s = 2.5 m and subsoil thickness h_s = 5.0 m). There are 1566 eight noded, reduced-integration, two-dimensional, quadratic solid elements (CPE8R) for the embankment, 16 three node quadratic truss elements (T2D3) for the reinforcement, and 1072 eight noded, reduced-integration, two-dimensional, quadratic solid elements (CPE8R) for the subsoil.

The model now consists of reinforced embankment and subsoil. For the top reinforced embankment part, the vertical boundaries represent lines of symmetry at the centreline of a support (pile cap), and the midpoint between supports (see Section 1.1, Figure 1.1) as before with corresponding restraint. The geogrid is again positioned 100 mm above the base of the embankment, with restraint on horizontal movement at both sides. Again there are no boundary conditions imposed at the top embankment surface, and no surcharge is considered to act here.

The embankment is underlain by a half pile cap (width a/2) on the left, and subsoil (width (s-a)/2) at the right. For the subsoil, the vertical boundaries represent the edge of a pile, and the midpoint between piles. There is restraint on horizontal (but not vertical) movement at both boundaries. The bottom boundary represents the base of the soft subsoil, and there is rigid restraint on both vertical and horizontal movement. The subsoil is assumed to be underlain by a relatively stiff layer, and it is assumed that there is no settlement below the soft soil. It is effectively assumed that the pile has the same dimensions as the cap. This would not be the case in practice, but the analysis is somewhat idealised in this respect.

The pile cap is again assumed to provide rigid restraint to the embankment, and a vertical stress supporting the embankment (σ_u) is used to control the analysis. Initially σ_u is equal to the nominal overburden stress from the embankment (and the stress in the subsoil is zero). As σ_u is reduced the embankment material tends to arch and the

reinforcement tends to sag as before. However the subsoil also compresses with corresponding increase in vertical stress. Ultimately σ_u is reduced to zero, at which point the stress in the subsoil equals the stress at the base of the embankment (beneath the reinforcement).

This process is an idealisation, where reduction of σ_u is analogous to the effect of the excess pore water pressure in the subsoil, which initially carries the weight of the embankment, but is finally zero at the end of consolidation. The stress in the subsoil is initially zero, but increases as σ_u reduces, and thus actually represents the increase in vertical effective stress in the subsoil. However, this is sufficient to give a corresponding elastic settlement of the subsoil for one-dimensional conditions. σ_u is used to control the analysis in a similar way to σ_s in Chapters 3 and 4. Now that the subsoil is actually modelled, σ_s is the stress at the top of the subsoil layer in the analysis.

The pile cap width (a) was fixed at 1 m and the centre-to-centre spacing (s) was 2.5 m. The embankment height (h) was 3.5 or 10 m. The thickness of subsoil (h_s) was 5 or 10 m. For the reinforcement installed at the base of the embankment, the distance between the top of the pile cap and the first layer of reinforcement (geogrid) is 0.1 m and the distance between multiple layers is again 0.3 m for three layers of geogrid (a Load Transfer Platform).

Throughout the analyses minimum and maximum element sizes of the embankment and subsoil were approximately 0.0006 and 0.0076 m^3/m. This corresponds to side lengths approximately in the range 30 to 150 mm. The length of truss elements representing the reinforcement was in the range 20 to 100 mm.

The embankment fill was again modelled as a linear elastic material, with a Mohr-Coulomb yield criterion. The parameters are the same as parameters used in Chapter 4 (see Table 4.1). The parameters of the geogrid are also the same as in Chapter 4 (see Table 4.2). The subsoil is considered as a linear elastic material with parameters shown in Table 5.1. The 'ambient' stress level does not affect the behaviour of this material and therefore the self weight was not considered, and as above only the change in effective stress during consolidation was considered, giving a corresponding settlement.

All analyses in this chapter are summarised in Table 5.2, where non-standard values are highlighted in bold. For h = 3.5 m, s = 2.5 m, k = 6MN/m, δ_i =0 with a subsoil thickness h_s = 5 m, the effect of increasing Young's Modulus of subsoil E_s from 2.5 to 10 MN/m^2 was considered in cases (a-c). For h = 3.5 m, s = 2.5 m, δ_i =0 with subsoil thickness h_s = 5 m and E_s = 5 MN/m^2, the effect of increasing k from 6 to 12 MN/m, or using three geogrid layers with k = 2 MN/m was also considered in cases (d) and (e). The influence of increasing the geogrid interface friction angle δ_i to 20° was also considered (f). In cases (g) and

(h) a thicker soft soil layer (E_s = 2.5 MN/m^2 and h_s = 10 m) was considered.

The in-situ stresses were specified for the reinforced embankment (again based on a unit weight of 17 kN/m^3 and a K_0 value of 0.5), with zero stress in the subsoil. Initially σ_u was specified as the nominal vertical stress at the base of the embankment to give equilibrium with the in situ stresses, but this value was then reduced to mimic consolidation of the subsoil as described above.

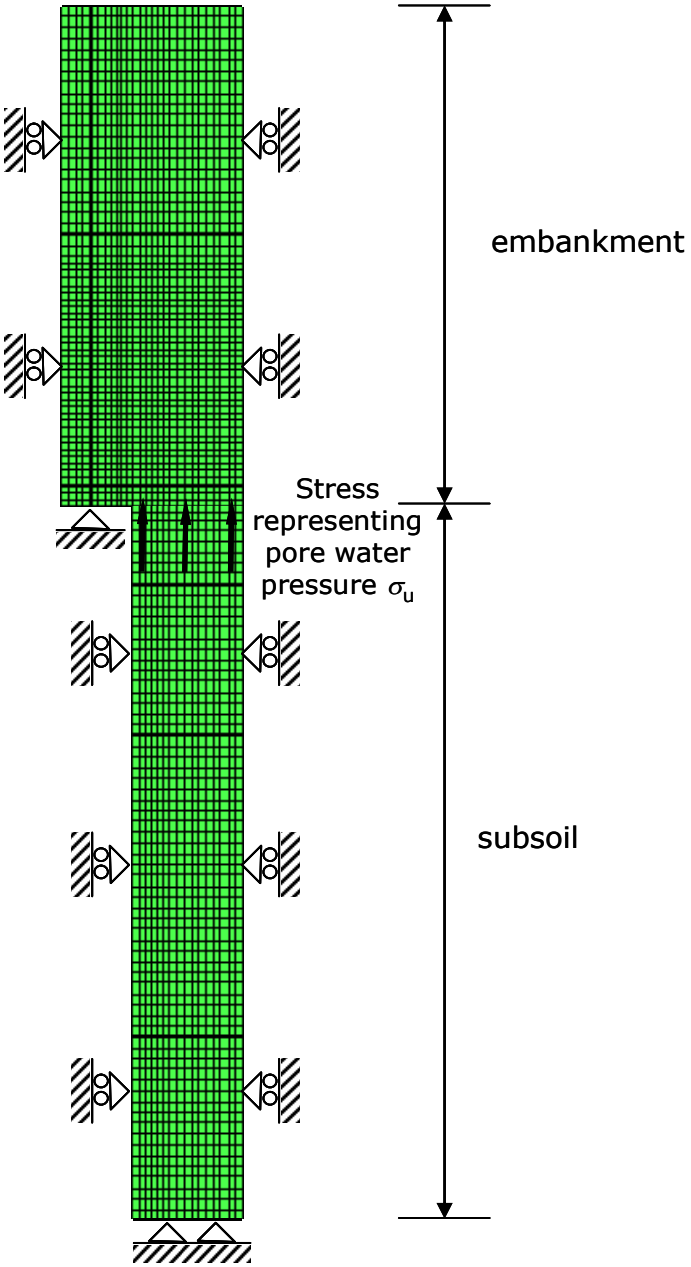

Figure 5.1. Typical finite element mesh (h = 3.5 m, s = 2.5 m, h_s = 5 m) and boundary conditions for reinforced embankment with subsoil

Table 5.1. Material parameters for subsoil

Young's Modulus (MN/m^2)	Poisson's Ratio
5 (or 2.5, or 10)	0.2

Table 5.2. Summary of analyses reported in this Chapter

h (m)	s (m)	k (MN/m)	δ_i	Young's Modulus of subsoil E_s (MN/m^2)	Height of subsoil h_s (m)	subplot
3.5	2.5	6	0	**2.5**	5	(a)
3.5	2.5	6	0	5	5	(b)
3.5	2.5	6	0	**10**	5	(c)
3.5	2.5	**12**	0	5	5	(d)
3.5	2.5	**3×2**	0	5	5	(e)
3.5	2.5	**3×2**	**20**	5	5	(f)
10	2.5	6	0	**2.5**	**10**	(g)
10	2.5	**3×2**	**20**	**2.5**	**10**	(h)

5.3 Results

Figure 5.2 shows the maximum displacement at the midpoint between the pile caps (δ_s) increasing with reduction in the stress at the bottom of reinforced embankment (σ_u).

Three lines are presented in Figure 5.2:

- 'Embankment with geogrid'
- 'Subsoil (analysis)'
- 'Subsoil (comparison)'

The 'embankment with geogrid' data comes from the previous analyses of a reinforced piled embankment (see Figure 4.2), showing the initial data at relatively small settlement. The 'subsoil (analysis)' results are from the analyses presented in this chapter as the stress at the top of the subsoil as σ_u decreases, σ_s increases, and settlement δ_s increases.

The line 'subsoil (comparison)' is simply derived from one-dimensional compression theory. The one-dimensional modulus is given by

$$E_0 = E_y \frac{(1-\mu)}{(1+\mu)(1-2\mu)} \quad (5.1)$$

And then

$$\sigma_s = E_0{}' \frac{\delta_s}{h_s} \quad (5.2)$$

This gives a straight line through the origin on the chart, due to linear elastic response.

As shown in Figure 5.2, the 'subsoil (analysis)' line is steeper than the 'subsoil (comparison)' line; this effect appeared to be related to an additional effect of 'bearing failure' and associated rotation of principal stresses (see Figure 5.3).

At the end of each analysis σ_u had reduced to zero. This logically corresponds to approximate intersection of the 'embankment with geogrid' and 'subsoil (analysis)' lines, since the stress at the base of the embankment is equal to the increase in stress in the subsoil. At this point the displacement is generally relatively small, and the geogrid carries very little load (compared with Chapter 4).

Comparing subplots (a), (b) and (c), the subsoil (analysis) line becomes steeper with increased Young's Modulus of the subsoil, and the settlement δ reduces from approximately 15 to 5 mm when σ_u and the lines intersect.

Comparing subplots (b), (d) and (f) the displacement (δ) at the intersection point is approximately consistent with a value of 7 mm. This is because the geogrid has very little effect at this small displacement (see Figure 4.4(a)).

Subplot (e) shows a slightly larger displacement than the subplot (f). This is because (as noted previously in Chapter 4) the mass strength at the base of the embankment has been reduced by the frictionless interfaces between embankment fill and the 3 geogrids.

For (g) and (h) the load on the geogrid is increased somewhat by increasing the embankment height to 10 m, reducing the subsoil stiffness to 2.5 MN/m^2 and increasing the subsoil thickness to 10 m. The settlement increases to approximately 35 mm, but the stress carried by the geogrid is still implied as small at this displacement (see Figure 4.4(a)). Even in this situation the subsoil is stiffer than the geogrid and hence carries nearly all the remaining load at the point of maximum arching.

The stress carried by the subsoil is up to about 20 kN/m^2, which is higher than the value predicted by the one-dimensional settlement equation. This appears to be related to rotation of the principal stress (Figure 5.3) related to a bearing capacity mechanism. This effect may be limited in a Tresca (rather than elastic) soil due to yielding. However, this is unlikely to have significant impact unless the strength is very low.

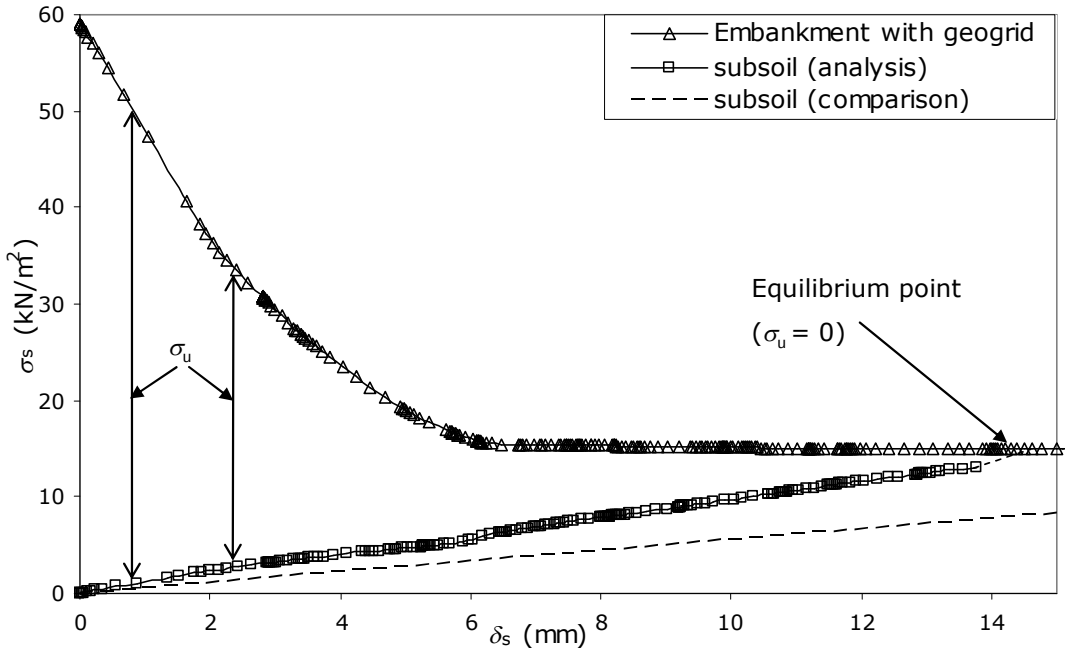

(a) h = 3.5 m, s = 2.5 m, k = 6 MN/m, δ_i = 0, E_s = 2.5 MN/m^2, h_s = 5 m

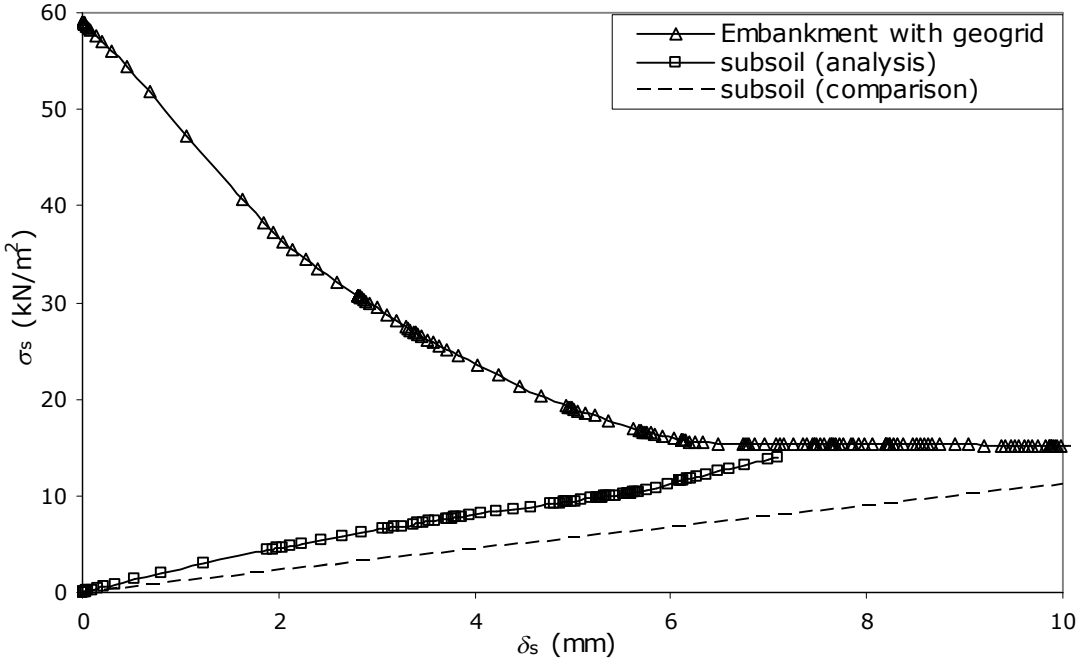

(b) h = 3.5 m, s = 2.5 m, k = 6 MN/m, δ_i = 0, E_s = 5 MN/m^2, h_s = 5 m

Figure 5.2 continued on following page

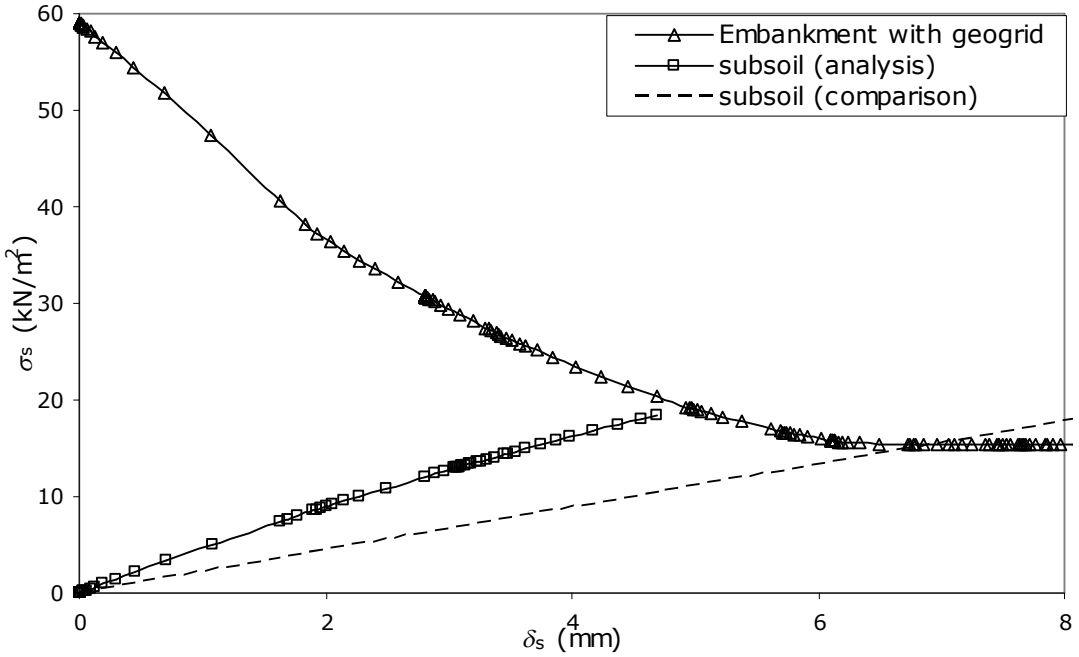

(c) h = 3.5 m, s = 2.5 m, k = 6 MN/m, δ_i = 0, E_s = 10 MN/m^2, h_s = 5 m

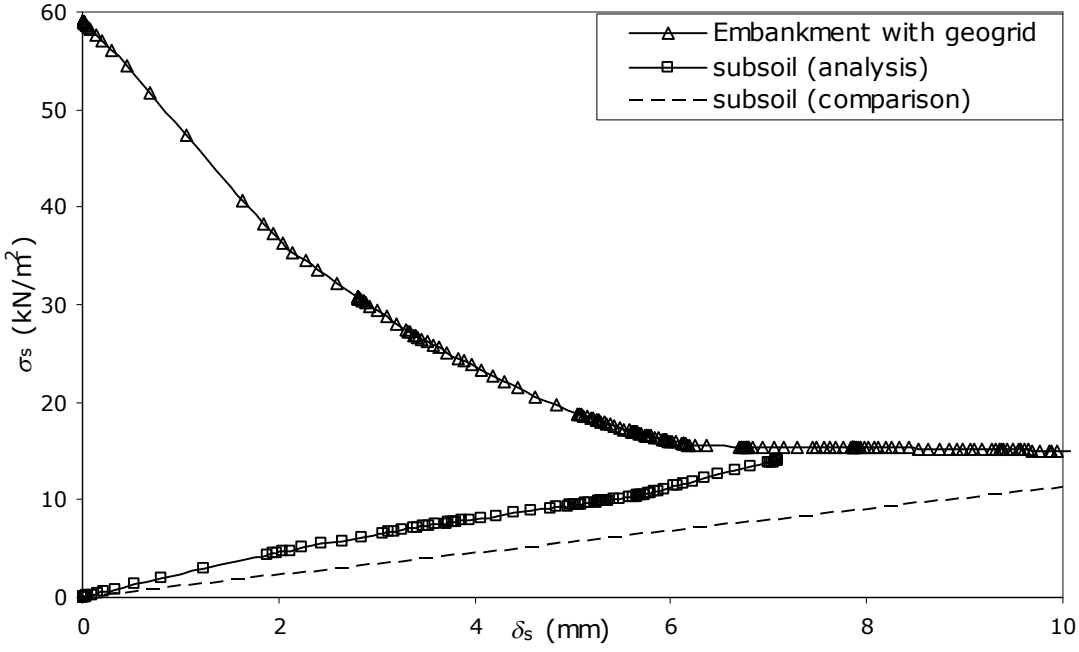

(d) h = 3.5 m, s = 2.5 m, k = 12 MN/m, δ_i = 0, E_s = 5 MN/m^2, h_s = 5 m

Figure 5.2 continued on following page

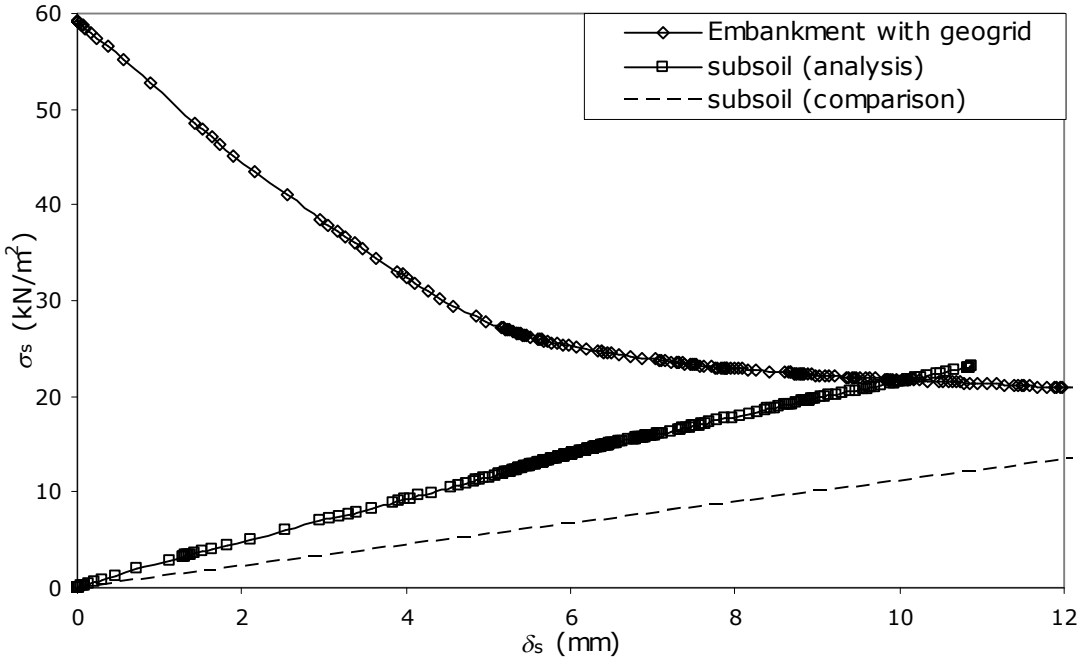

(e) h = 3.5 m, s = 2.5 m, k = 3×2 MN/m with three layers of geogrid, δ_i = 0, E_s = 5 MN/m^2, h_s = 5 m

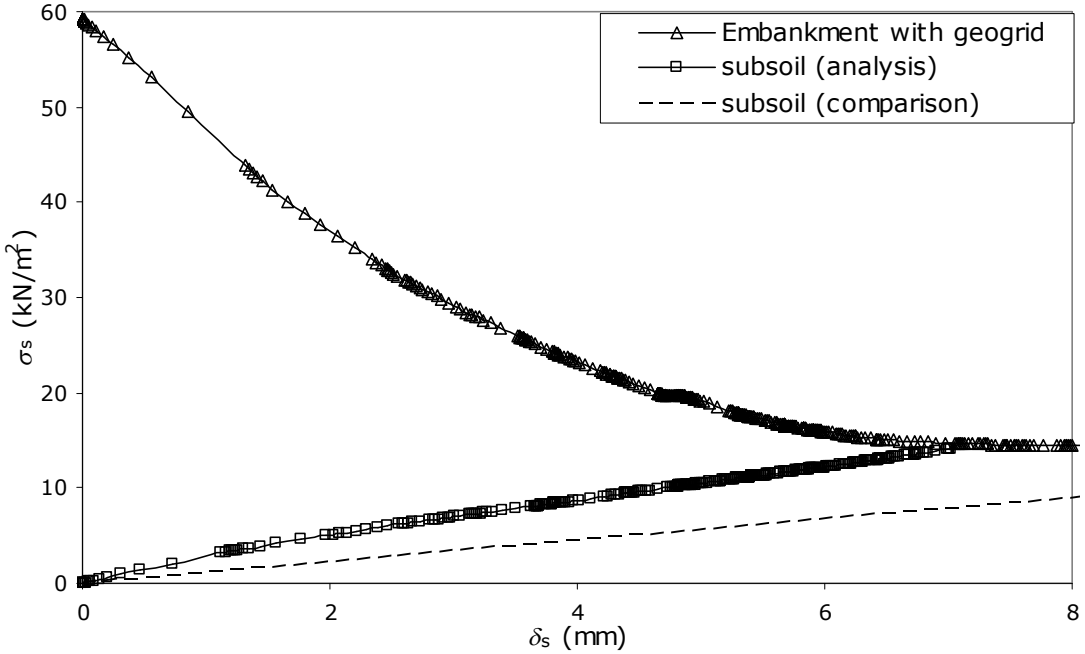

(f) h = 3.5 m, s = 2.5 m, k = 3×2 MN/m with three layers of geogrid, δ_i = 20, E_s = 5 MN/m^2, h_s = 5 m

Figure 5.2 continued on following page

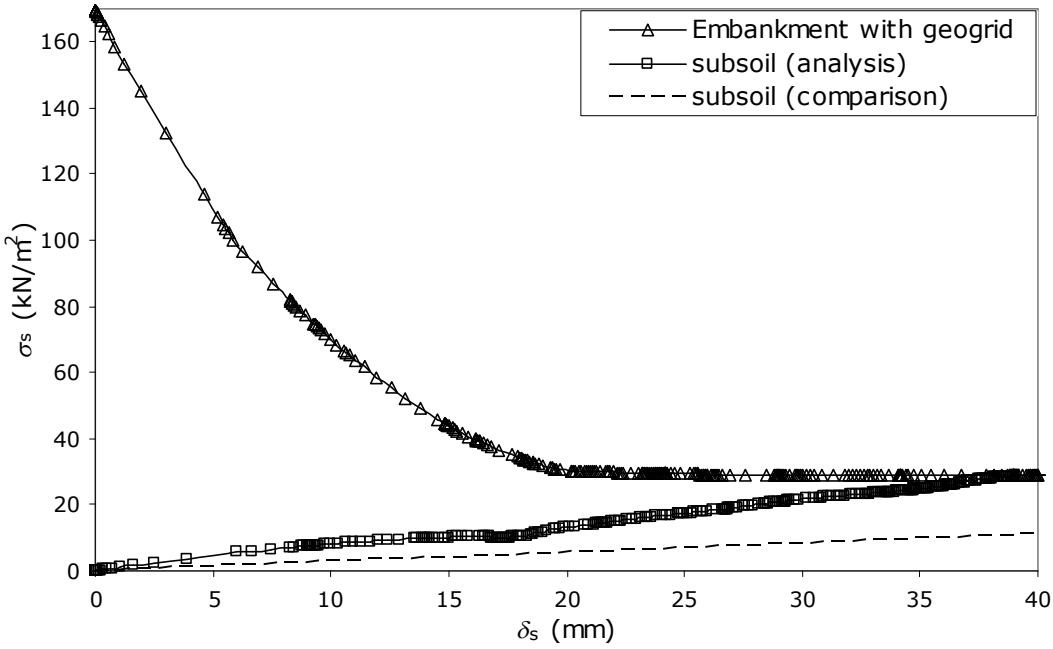

(g) h = 10 m, s = 2.5 m, k = 6 MN/m, δ_i = 0, E_s = 2.5 MN/m^2, h_s = 10 m

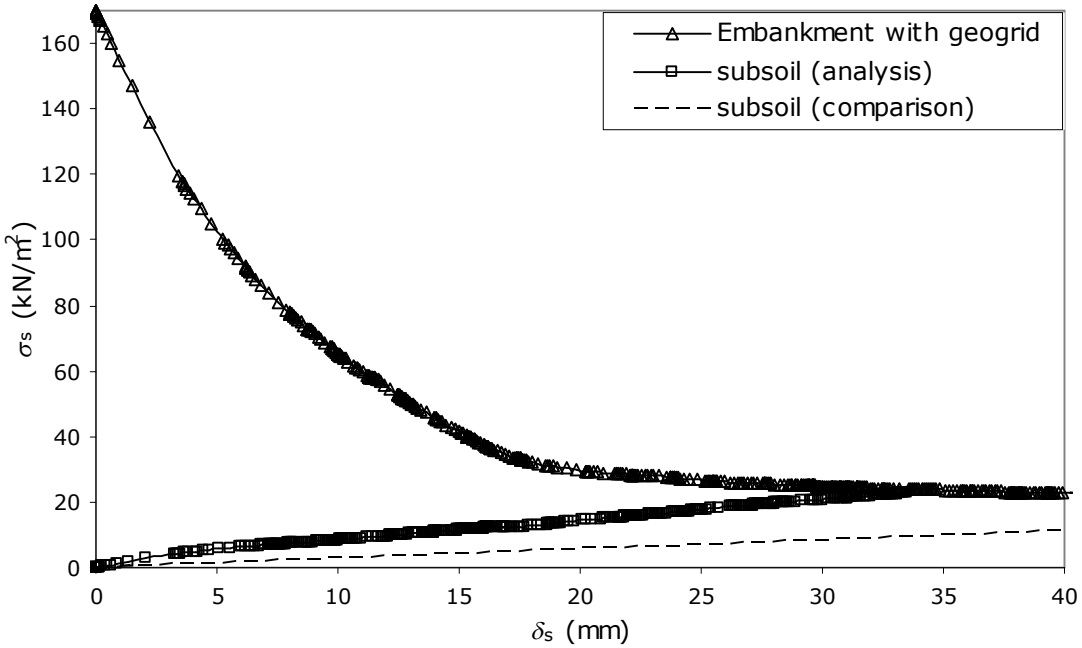

(h) h = 10 m, s = 2.5 m, k = 3×2 MN/m with three layers of geogrid, δ_i = 20, E_s = 2.5 MN/m^2, h_s = 10 m

Figure 5.2. Behaviour of subsoil in different conditions

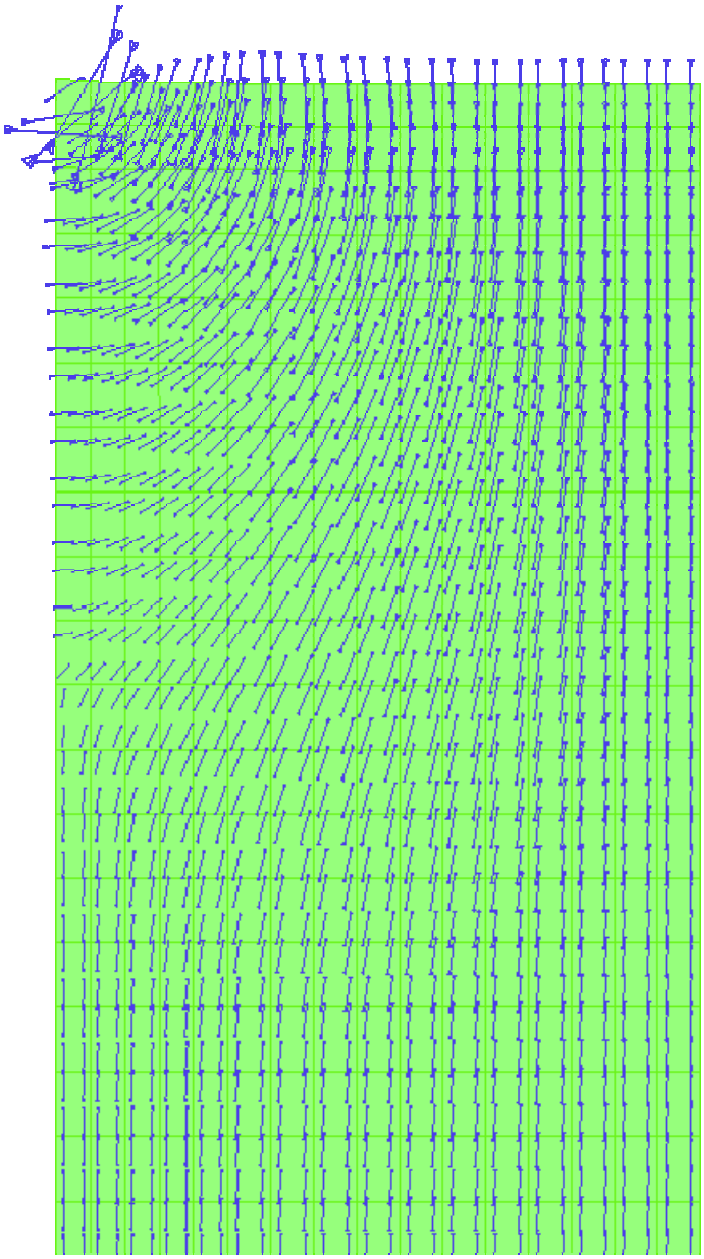

Figure 5.3. Rotation of principal stresses (subsoil)

5.4 Summary

The effect of the subsoil in the analyses was somewhat underestimated by a one-dimensional settlement prediction, due to the additional effect of principal stress rotation.

The analyses indicate that the contribution of vertical equilibrium of the subsoil is considerably more significant than the geogrid. Hence equilibrium of the full system including arching in the embakment, geogrid reinforcement and subsoil is achieved at much lower settlement than the embankment and geogrid alone (Chapter 4).

CHAPTER 6

GROUND REACTION CURVE IN THREE-DIMENSIONS

6.1 Introduction

A three-dimensional model of a piled embankment is reported in this Chapter. This is an extension of the plane strain analyses reported in Chapter 3, where the 'Ground Reaction Curve' (GRC) for arching in the embankment was studied without consideration of reinforcement or subsoil.

There is less support from the pile caps in a three-dimensional situation compared to the plane strain condition. The basic unit is the four pile group shown in Figure 6.1, where the centre-to-centre spacing of the piles in each direction is 's' and the pile caps are assumed to be square with width 'a', and thus the total pile cap area per unit is a^2 and the remaining subsoil area is (s^2-a^2).

As shown in Figure 6.1 the analysis uses lines of symmetry to consider a model which is one quarter of this unit (and one quarter of a pile cap). In fact it would also be possible to bisect this model with a 45° line. However, this would have complicated mesh generation and was not done.

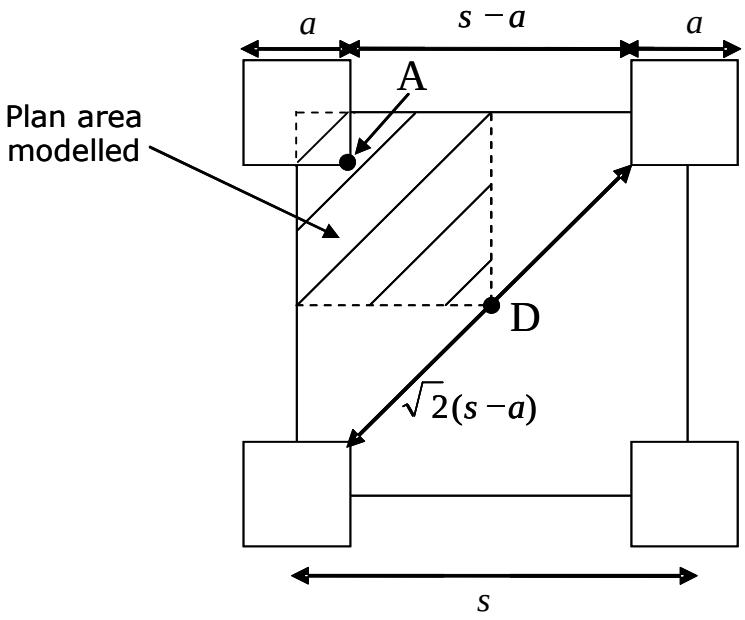

Figure 6.1. Plan view of layout of the pile caps in 3D

6.2 Analyses presented

The analyses presented here were undertaken in 3D using Abaqus Version 6.6. Figure 6.2 shows the mesh for the embankment with h = 3.5 m and s = 2.5 m. There are 5040 twenty noded, reduced-integration, three-dimensional, quadratic brick solid elements (C3D20R).

Table 6.1 and Figure 6.2 present the boundary conditions for the embankment in 3D, whose vertical boundaries represent the planes of symmetry at the central plane of a support (pile cap), and the middle between supports (Figure 6.1). As shown in Table 6.1, there is restraint in the y (but not x or z) direction movement on faces 2, and there is restraint in the x (but not y or z) direction movement on faces 3.

As assumed in the plane strain condition, the top of embankment surface (face 1) can move freely in all directions, and there is no surcharge acting here. Face 4 and face 5 represent the base of the embankment, which is underlain by one quarter of a pile cap (area $a^2/4$) under face 5, and subsoil (area $(s^2-a^2)/4$) under face 4. As assumed in the plane strain condition the pile cap applies rigid restraint in all directions, and vertical stress acting at the interface with the underlying subsoil (σ_s) is used to control the analysis. The subsoil itself was not modelled in the analysis.

The pile cap width (a) was fixed at 1.0 m and the pile spacing (s) was 2.0, 2.5 or 3.5 m. The embankment height (h) was ranged from 1 to 10 m.

Throughout the analyses a typical element volume was approximately $0.001m^3$, corresponding to a typical side length of 100 mm.

The embankment fill was again modelled as a linear elastic material, with a Mohr-Coulomb yield criterion. The parameters are the same as the standard parameters used in the plane strain analyses, see Table 6.2. The effect of increasing the friction angle or kinematic dilation angle was not considered here. All analyses considered in this chapter are summarised in Table 6.3.

The sequence of analysis was the same as the plane strain case. First the in-situ stresses were specified (again based on a unit weight of 17 kN/m^3 and K_0 value of 0.5). Initially σ_s was specified as the nominal vertical stress at the base of the embankment to give equilibrium with the in situ stresses, but this value was then reduced (allowing Abaqus to determine increment size automatically) to mimic loss of support from the subsoil.

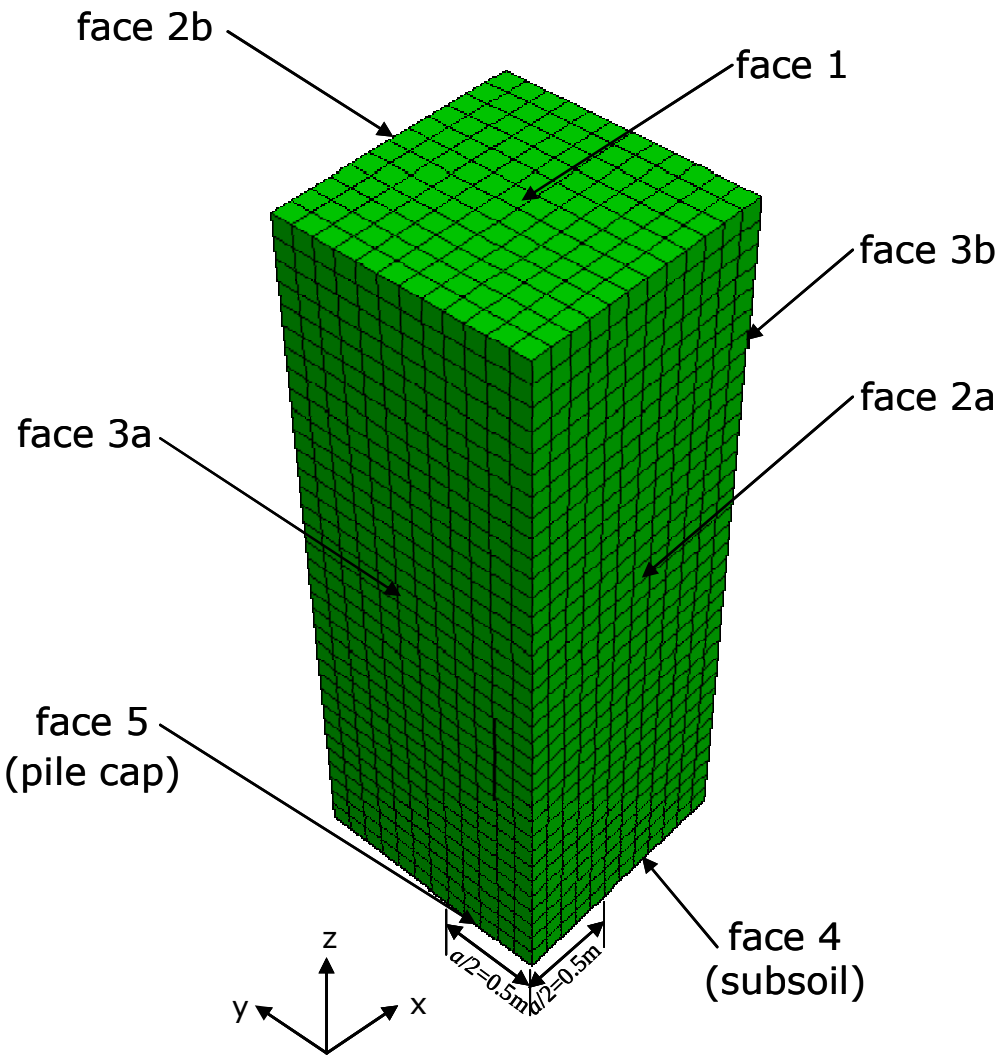

Figure 6.2. Typical finite element mesh (h = 3.5 m, s = 2.5 m)

Table 6.1. Illustrations of boundary conditions as shown in Figure 6.2

Face 1	The top of embankment, there are no boundary conditions (free surface).
Face 2	Restraint on y direction movement, x and z directions are free.
Face 3	Restraint on x direction movement, y and z directions are free.
Face 4	There are no boundary conditions. A vertical stress representing the subsoil beneath the embankment (σ_s) acts here.
Face 5	Pile cap, which is fixed in all directions (x, y and z directions).

Table 6.2. Material parameters for granular embankment fill

Young's Modulus (MN/m^2)	Poisson's Ratio	c' (kN/m^2)	ϕ' (deg)	Kinematic dilation angle (ψ) (deg)
25	0.2	1	30	0

Table 6.3. Summary of analyses reported in this Chapter

h (m)	**s = 2.0 (m)**	s = 2.5 (m)	**s = 3.5 (m)**
	c' = 1kN/m^2, ϕ' = 30°, ψ =0°	c' = 1kN/m^2, ϕ' = 30°, ψ = 0°	c' = 1kN/m^2, ϕ' = 30°, ψ = 0°
subplot	(a)	(b)	(c)
1		√	
1.5	√		
2		√	
2.5	√		√
3.5	√	√	
5		√	√
6.5		√	√
8			
10	√	√	√

6.3 Results

6.3.1 Ground Reaction Curves

Figure 6.3 shows the ground reaction curve for the three-dimensional condition, in which normalised stress ($\sigma_s/\gamma h$) is plotted against normalised displacement at the bottom of the embankment ($\delta_s/(s\text{-}a)$). Here δ_s is taken as the maximum value, occurring at point D (Figure 6.1).

The graphs show the same behaviour as the plane strain results, initially giving a normalised stress of 1.0 before there is any tendency for arching. Then, the normalised displacement increases with a reduction in normalised stress. The GRC curve is again modelled only up to the point of maximum arching, and the automatic incrementation gives smaller changes in stress at the end of the analysis, due to material plasticity.

As shown in Figure 6.3(b), the highest embankment (10 m) requires the largest displacement to reach the point of maximum arching. The value of approximately 4 % is larger than the equivalent value in the plane strain condition (which was around 1 %; see Figure 3.2(b)). Again, this value is directly related to the soil stiffness which has been chosen. This seems reasonable since the supported area is smaller in the 3D case.

As can be seen in Figure 6.3(b) (s = 2.5 m), the ultimate normalised stress is in the range 21 to 28 % for $h \geq 3.5$ m, which is slightly larger

than the equivalent value in the plane strain condition (16 to 20 %). The stress again tends to increase rapidly as h reduces below this value.

Subplots (a) and (c) (s = 2.0 m and 3.5 m respectively) show trends of behaviour which are similar to (b). The normalised stress at the point of maximum arching increases with s, which is consistent with behaviour in the plane strain situation.

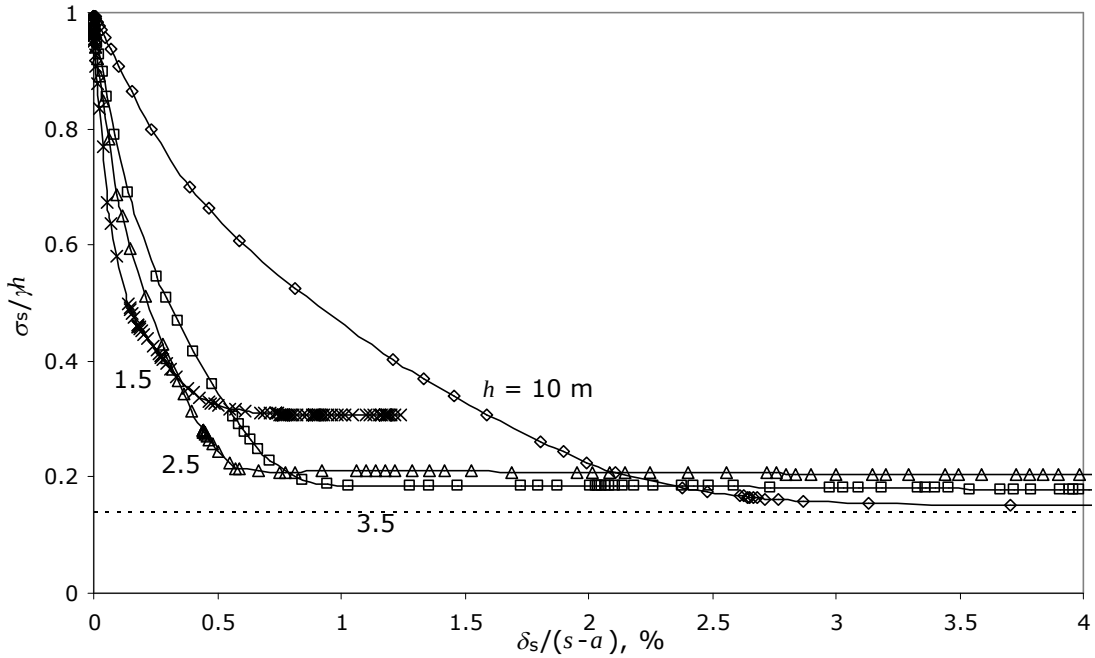

(a) s = 2.0 m

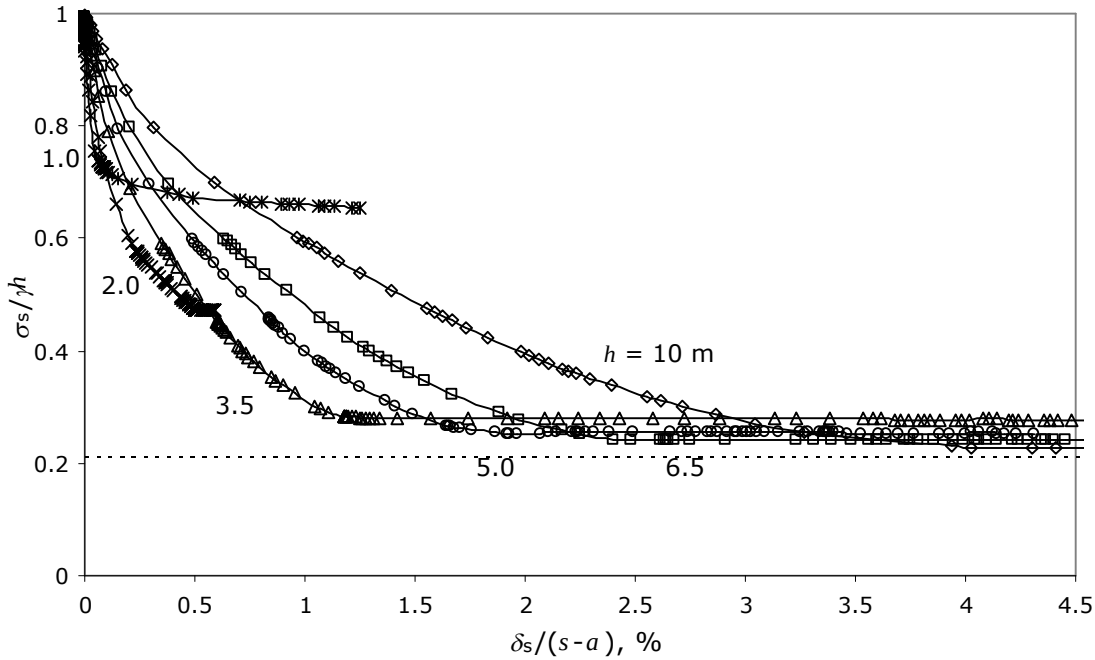

(b) s = 2.5 m

Figure 6.3 continued on following page

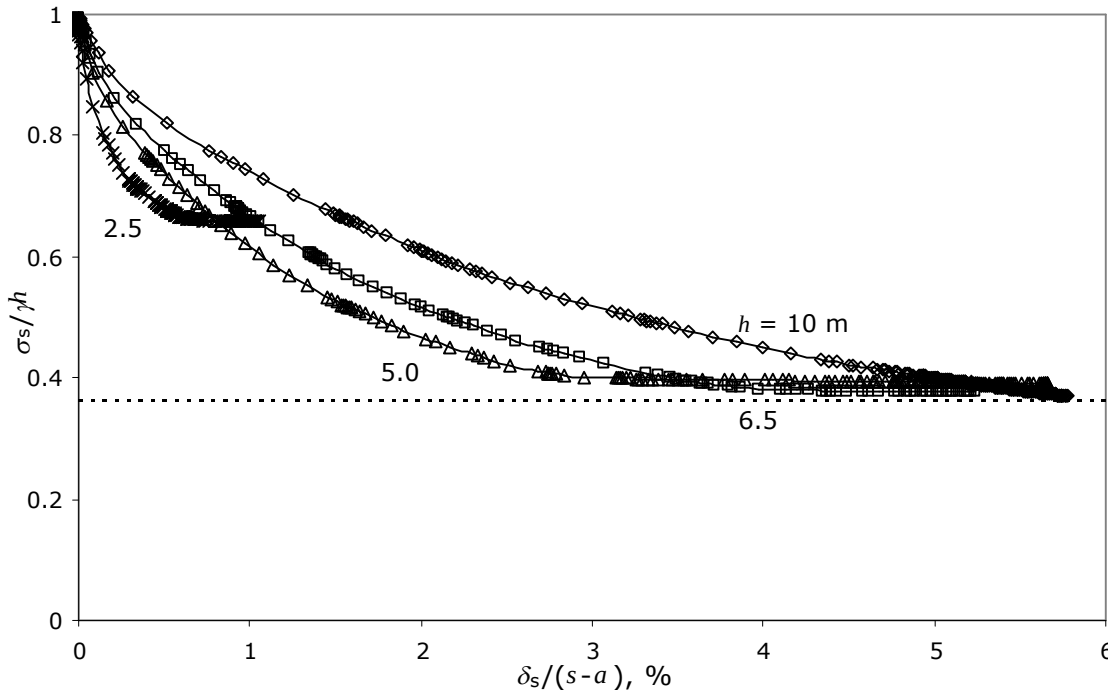

(c) s = 3.5 m

Figure 6.3. Ground Reaction Curves for a variety of embankment heights (h)

6.3.2 Midpoint profile of earth pressure coefficient

Figure 6.4 shows the earth pressure coefficient ($K = \sigma_h'/\sigma_v'$) as a vertical profile at the centre point of the basic unit (D, Figure 6.1). Again, the profiles as plotted do not extend to the top of the embankment for the higher embankments. Values of 0.7(s-a), 0.7s and 1.5s are highlighted on the *z* axis -the geometry of arching in 3D has been modified as shown in Figure 6.5. $K = K_0$ and $K = K_p$ are shown on the K axis. The horizontal stress at D (Figure 6.1) was found to be the same in the x and y directions, with no shear stress. Hence the horizontal stresses (and K) were the same in all directions at this point.

As in the plane strain case, for (z/s) > 1.5, $K = K_0$, and hence has not been modified by the arching. For embankments where (h/s) > 1.5, K increases with depth for z/s < 1.5, reaching K_p when $z \approx 0.7(s\text{-}a)$. Hence the passive limit is reached approximately at the inner radius (and below) the arch. This is consistent with the plane strain condition.

As in plane strain, when (h/s) < 1.5 there is increasing tendency for the highest value of K to occur at the surface of the embankment. This initially gives an 'S-shaped' profile, and then monotonic reduction in K with depth in the embankment for the lowest h. In fact (as in Chapter 3) K_p as indicated on the plots neglects the small cohesion intercept, and thus can be exceeded, particularly when stress is small (e.g. near the surface of the embankment or immediately above the subsoil).

When s increases, there is some reduction in K at z = 0.7(s–a). This reflects the increased tendency for failure of the arch at the pile cap rather than 'crown' (the top of arch), particularly when h is also large. This was also noted in plane strain.

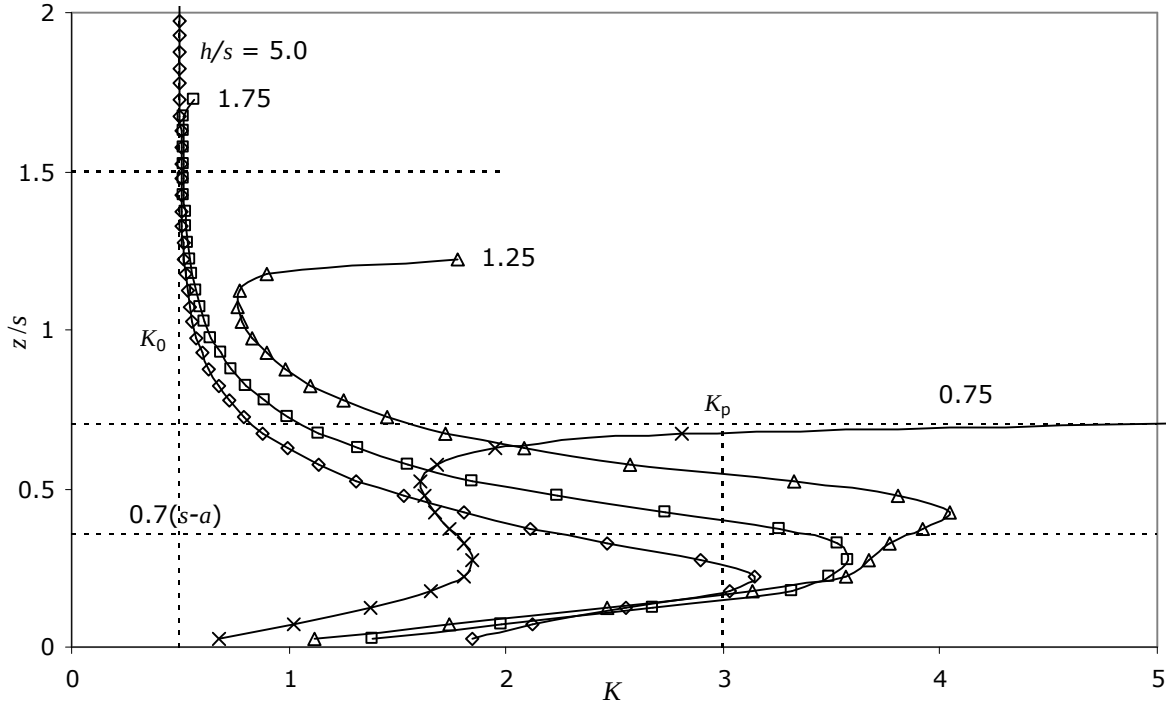

(a) s = 2.0 m

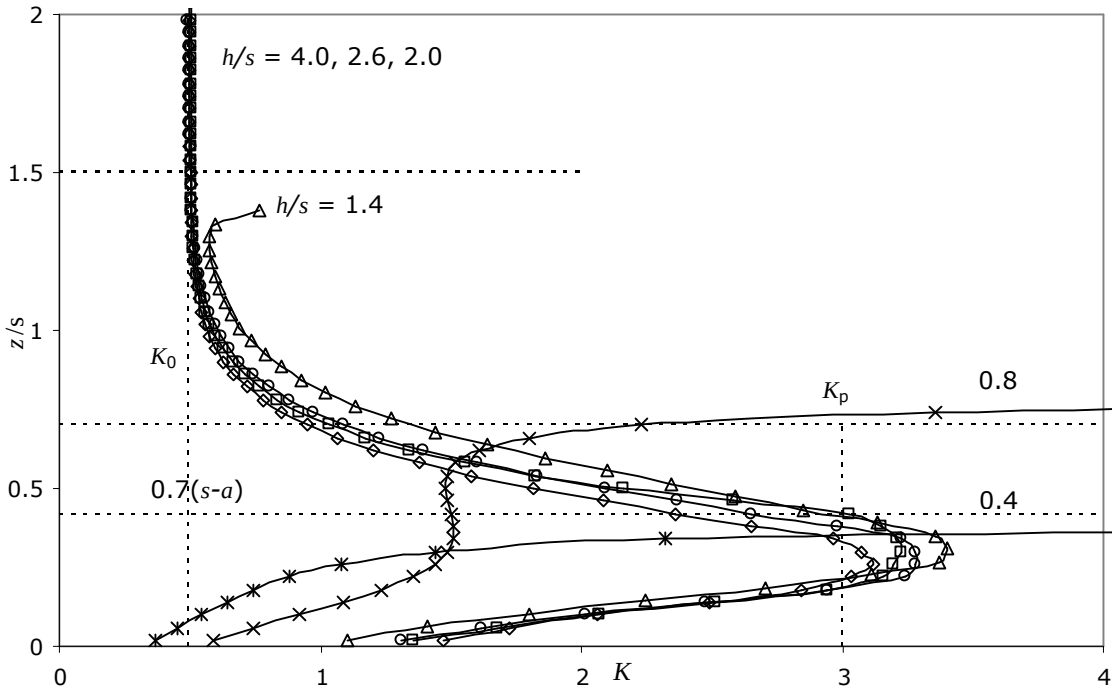

(b) s = 2.5 m

Figure 6.4 continued on following page

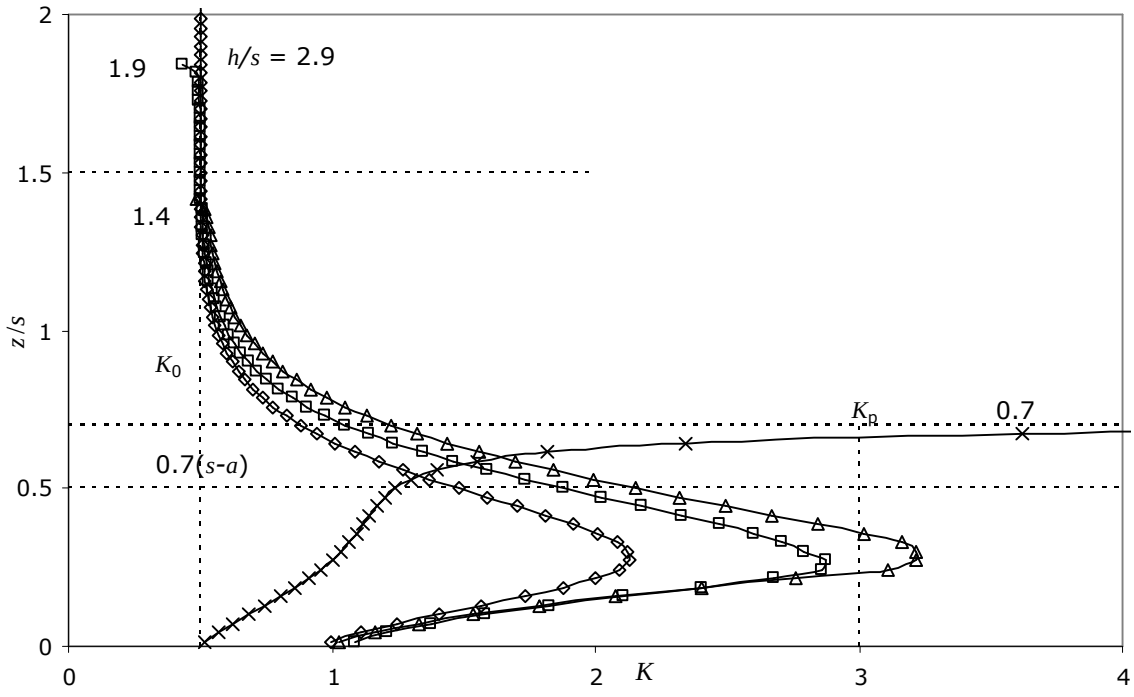

(c) s = 3.5 m

Figure 6.4. Profiles of earth pressure coefficient (K) on a vertical profile at the centre point of the basic unit (D, see Figure 6.1) (z measured upwards from base of the embankment, see Section 1.1, Figure 1.1), showing variety of embankment heights (h)

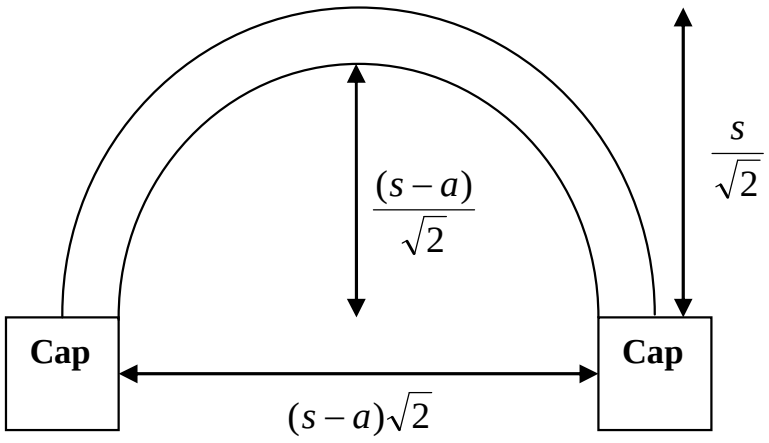

Figure 6.5. Geometry of arching in the three dimensional condition

6.3.3 Ultimate stress on the subsoil

Figure 6.6 shows the ultimate stress on the subsoil ($\sigma_{s,ult}$) at the point of maximum arching normalised by γs, showing variation with (h/s). Again a simplified version of the condition for failure of the arch at the pile cap proposed by Hewlett & Randolph (1988) in shown. The equation of vertical equilibrium for the 3D case, assuming σ_s (subsoil) and σ_c (pile cap) to be constant is:

$$\sigma_c a^2 + \sigma_s \left(s^2 - a^2\right) = \gamma h s^2 \qquad (6.1)$$

It is then assumed (from analogy with bearing capacity) that $\sigma_c = K_p^2 \sigma_s$, to give:

$$\frac{\sigma_s}{\gamma s} = \frac{h}{s} \frac{1}{(a/s)^2 \left(K_p^2 - 1\right) + 1} \qquad (6.2)$$

This result is plotted for the 3 values of s.

The three dotted lines (Equation 6.2) are steeper than the equivalent lines in the plane strain case (Equation 3.2) because the area of the pile cap is smaller – the ratio (a/s) becomes $(a/s)^2$ in the 3D case.

As in plane strain, for small (h/s), ($\sigma_{s,ult}/\gamma s$) is less than 0.5, and when (h/s) ≈ 0.5, the data converge with the 'no arching' line. At larger h Equation (6.2) shows the correct trend of behaviour, but tends to overestimate $\sigma_{s,ult}$, particularly as s reduces.

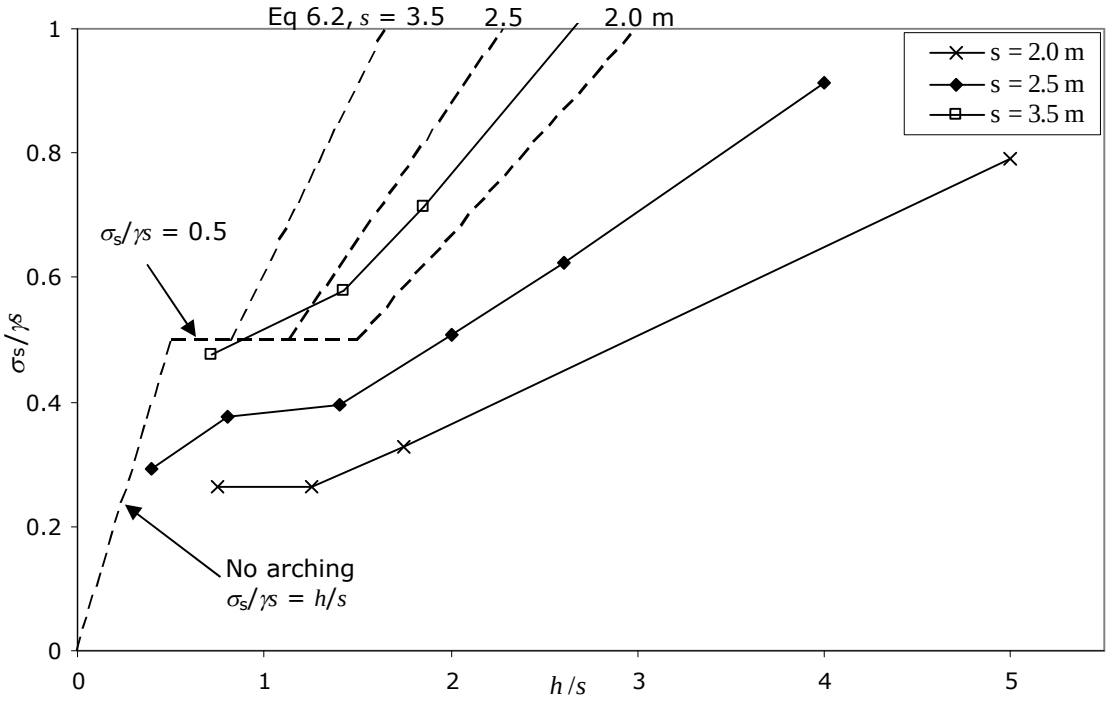

Figure 6.6. Normalised stress on the subsoil at ultimate conditions ($\sigma_{s,ult}$) showing variation with (h/s)

6.3.4 Settlement at the subsoil and surface of the embankment

Figure 6.7(a) shows the maximum value of subsoil settlement at the centre point of the basic unit (D, Figure 6.1), normalised by the clear gap between pile caps (s-a) showing variation with h/s. As in 2D there is a clear trend for the settlement at ultimate conditions to increase with (h/s), tending to zero when (h/s) ≈ 0.5 (corresponding to no arching).

As h increases arching occurs, and the amount of stress redistribution from the subsoil to the pile cap increases, thus it is not surprising that the amount of displacement required to achieve ultimate arching conditions also increases. This observation is also consistent with the variation with s, which indicates more displacement as s increases (for a given h) since this also implies increased redistribution of load from the subsoil to the pile cap.

The absolute magnitude of $\delta_{s,ult}/(s\text{-}a)$ is approximately between 1 and 6 % when (h/s) ≈ 2 to 5, this value is considerably larger than equivalent value in 2D situation (by a factor of about 3). This is because there is less support from the pile caps in the 3D situation, which causes larger displacement at the 'ultimate' condition.

Subplot (b) shows the ratio of settlement at the top of the embankment at the midpoint of the diagonal between piles above point D (δ_{em}, see plane strain graph Figure 1.1, in Section 1.1) to the equivalent value in the

subsoil (δ_s) at the point where ultimate conditions are reached: $(\delta_{em}/\delta_s)_{ult}$, showing variation with (h/s). Values range from 0.75 to 0.95. This is larger than the equivalent value in the 2D situation (0.45 - 0.75). Also the value is largest, tending to 1.0 for increasing s. For low (h/s) the value of 1.0 most likely indicates no arching. At higher (h/s) the relatively high value of this ratio probably again reflects some reduction in the 'effectiveness' of arching in 3D compared to 2D.

Subplot (c) shows the ratio δ_{em} to the equivalent value at the centre above the pile cap (δ_{ec}, see plane strain graph Figure 1.1, in Section 1.1) at the point where ultimate conditions are reached: $(\delta_{em}/\delta_{ec})_{ult}$, showing variation with (h/s). This graph shows a similar trend to the plane strain situation. For (h/s) > 1.5 the value is 1.0, indicating no differential settlement. As (h/s) reduces differential settlement increases, dramatically so for (h/s) less than about 1.4.

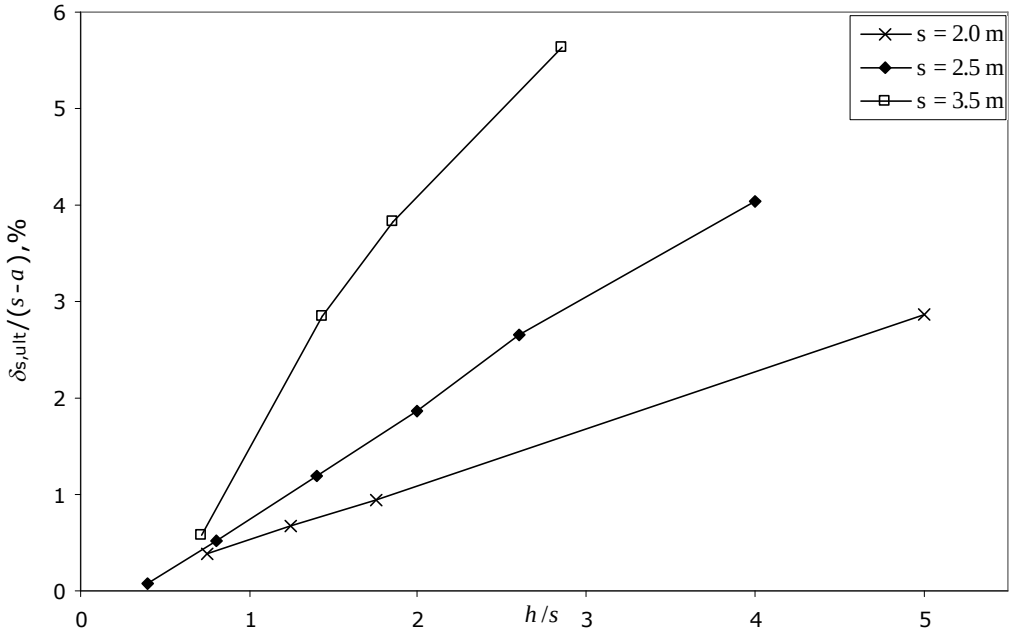

(a) Ultimate settlement of the subsoil at the midpoint of diagonal between piles ($\delta_{s,ult}$) normalised by the clear gap between pile caps (s-a)

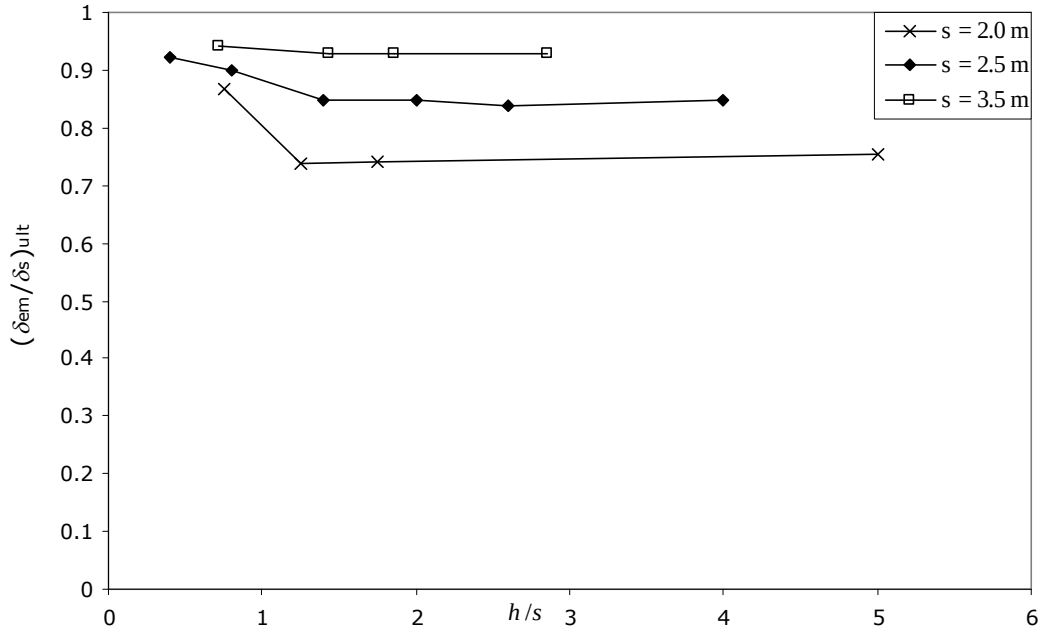

(b) Ratio of the settlement at the top of the embankment at the midpoint of diagonal between piles (δ_{em}) to the equivalent value in the subsoil (δ_s)

Figure 6.7 continued on following page

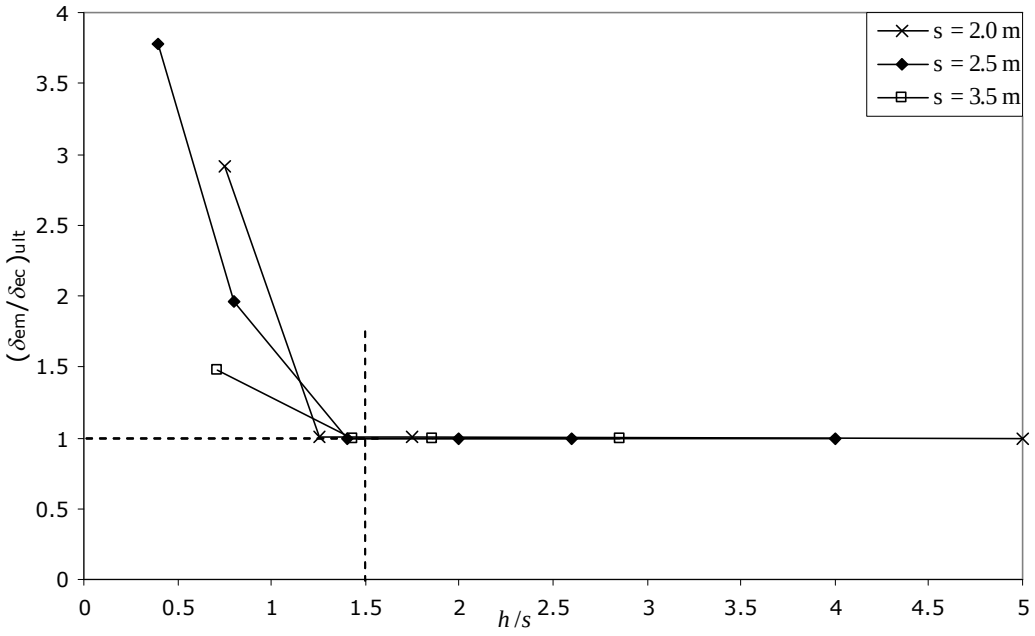

(c) Ratio of the settlement at the top of the embankment at the midpoint of diagonal between piles (δ_{em}) to the equivalent value at the centre above the pile cap (δ_{ec})

Figure 6.7. Settlement results at the subsoil and surface of the embankment

6.4 Summary

The results of a series of linearly elastic-perfectly plastic three-dimensional analyses to investigate the arcing of a granular embankment supported by pile caps have been presented. Like the plane strain analyses already presented the soft subsoil is represented by a decreasing stress which controls the analysis.

Again, the analyses demonstrate that the ratio of the embankment height to the centre-to-centre pile spacing (h/s) is a key parameter:

- (h/s) ≤ 0.5 there is virtually no effect of arching.
- 0.5 ≤ (h/s) ≤ 1.5 there is increasing evidence of arching.
- 1.5 ≤ (h/s) 'full' arching is observed.

Figure 6.6 shows that up to a critical value of (h/s) the stress on the subsoil is less than $0.5\gamma s$, approximately representing the effect of the infill material below the arch. At higher values of (h/s) conditions at the pile cap are critical and Equation (6.2) can be used to conservatively estimate the stress on the subsoil.

It is perhaps surprising that the critical values of (h/s) appear to be so similar in 2D and 3D, since the diagonal unsupported span in 3D is larger by a factor $\sqrt{2}$.

CHAPTER 7

GEOGRID REINFORCED PILED EMBANKMENT IN THREE-DIMENSIONS

7.1 Introduction

A three-dimensional model of a geogrid (or geotextile) reinforced piled embankment will be presented in this chapter. The basic unit is one quarter of the four pile group as used in Chapter 6 (see Figure 6.1). This is an extension of the plane strain analyses reported in Chapter 4, where the effect of the tensile stiffness of geogrid(s) near the base of the embankment was introduced.

7.2 Analyses presented

Figure 7.1 shows a typical mesh for the embankment, with h =3.5 m and s = 2.5 m. There are 5328 eight noded, full-integration, three-dimensional, linear brick solid elements (C3D8) for the embankment and 100 four noded, full-integration, three-dimensional membrane element (M3D4) for the geogrid reinforcement. Membrane elements are surface elements that transmit in-plane forces only (no moments), and have no bending stiffness (Abaqus Analysis User's Manual, Version 6.6). They are used to represent thin surfaces in space that offer strength in the plane of the element but have no bending stiffness (Abaqus Analysis User's Manual, Version 6.6). As described in Chapter 2 'surface to surface' contact model

was used to model the interaction between the reinforcement and embankment.

The vertical boundaries again represent the planes shown in Figure 6.1. The boundary conditions are as previously described in Table 6.1 for the analysis without geogrid. Restraint on horizontal movement of the geogrid at the boundaries was the same as for the soil on the corresponding faces (restraint on horizontal movement normal to the face).

The pile cap is assumed to provide rigid restraint to the embankment, whilst the vertical stress in the subsoil supporting the embankment (σ_s) is again used to control analysis. The geogrid is located at the bottom of embankment, where the thickness of the fill below the reinforcement and above the pile is assumed to be 0.1 m in the model. The subsoil was not modelled.

As in the two-dimensional analyses, the pile cap width (a) was fixed at 1.0 m, the pile spacing (s) was 2.0, 2.5 or 3.5 m and the embankment height (h) was 1.0, 3.5 or 10m. Throughout the analyses minimum and maximum element of embankment sizes were approximately 0.0005 and 0.001 m^3, corresponding to side lengths 50 to 100 mm. The membrane element length and width were 125 mm, and thickness was 1 mm.

The embankment material was again assumed to be granular, and modelled using elastic-perfectly plastic response (E = 25 MN/m^2, ν' = 0.2, c' = 1kN/m^2, ϕ' = 30°, ψ' =0° and γ = 17 KN/m^3).

The geogrid was modelled using three-dimensional membrane elements which can carry tensile force but do not have any bending stiffness. The geogrid is considered as a linear elastic material with E = 6000 MN/m^2, 12000 MN/m^2, or E = 2000 MN/m^2 and ν' = 0.5 (see Table 7.1).

The corresponding geogrid stiffness for nominal 1 mm thickness was 6 MN/m, 12 MN/m, or 2 MN/m with three layers of geogrid. The interface friction angle (δ_i) between the granular material (embankment) and geogrid was 0° or 20°.

All analyses are summarised in Table 7.2. The series of analyses to examine sensitivity to various factors is identical to Chapter 4.
The sequence of analysis was the same as previously described. The in situ stresses were specified. The subsoil stress σ_s was then reduced from the initial value corresponding to the nominal overburden stress to mimic loss of support from the subsoil (allowing Abaqus to determine increment size automatically).

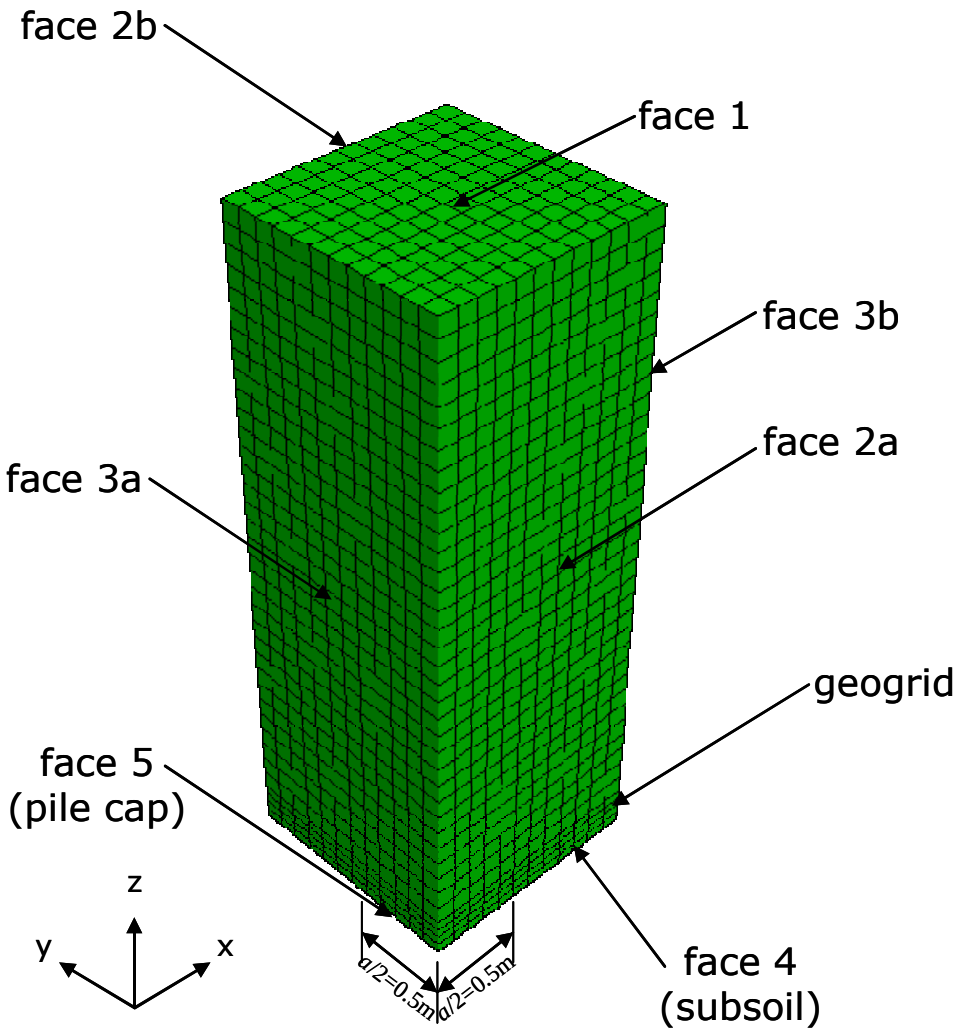

Figure 7.1. Typical finite element mesh (h =3.5 m, s = 2.5 m, one layer of reinforcement) for reinforced embankment

Table 7.1. Material parameters for geogrid

Young's Modulus (MN/m^2)	Poisson's Ratio	Thickness (m)
6,000 (or 12,000 or 2,000 with three layers of geogrid)	0.5	0.001

Table 7.2. Summary of analyses reported in this Chapter

	h (m)	s (m)	k (MN/m)	δ_i	subplot
Effect of h	**1**	2.5	6	0	(a)
	3.5	2.5	6	0	(b)
	10	2.5	6	0	(c)
Effect of s	3.5	**2**	6	0	(d)
	3.5	**3.5**	6	0	(e)
Effect of geogrid: k	3.5	2.5	**12**	0	(f)
Effect of geogrid: δ_i	3.5	2.5	6	**20**	(g)
Effect of geogrid: N	3.5	2.5	**3×2**	0	(h)
Effect of geogrid: N and δ_i	3.5	2.5	**3×2**	**20**	(i)

7.3 Results

7.3.1 Behaviour of reinforced piled embankment

The results in Figure 7.2 are presented in the same format as Chapter 4:

- 'GRC' line (data previously presented in Chapter 6)
- 'Embankment with geogrid' line (data derived in this chapter)
- 'GRC + effect of geogrid' (theoretical comparison)

The theoretical comparison line is again based on Equation (2.30), but here using a span $l = \sqrt{2}\,(s\text{-}a)$, based on the diagonal clear span between pile caps, and accepting that there is some idealisation since the equation is plane strain. The subsoil settlement plotted (δ_s) is the maximum on the diagonal between pile caps (D, Figure 6.1)

The analysis of the 'Embankment with geogrid' is in general similar to the comparison line derived from the GRC combined with Equation (2.30), although agreement is not quite as good as in the plane strain analyses.

For subplots (a), (b) and (c), the subsoil settlement at the midpoint of the diagonal between piles δ_s when $\sigma_s = 0$ increases with the height of the embankment, since the geogrid has to carry more load and deforms more.

Subplots (d), (b) and (e) show the maximum settlement (δ_s) increases with the centre-to-centre pile cap spacing (s).

Again for subplot (f), comparing with subplot (b), δ_s when σ_s = 0 reduces slightly, reflecting the effect of k. Subplot (g) indicates that δ_s for σ_s = 0 reduces slightly as the interface friction angle between the geogrid and subsoil increases, but as shown in plane strain there is not a major impact.

Subplot (h) shows the effect of three layers of low stiffness (k = 2 MN/m) geogrid with a frictionless interface. As shown in plane strain, this causes the point of maximum arching in the analysis for the embankment with geogrid to have slightly higher σ_s than the GRC. This was attributed to the damaging effect of the frictionless interfaces created within the soil. Furthermore, the data ultimately show better correspondence with Equation (2.30) based on k = 2 MN/m rather than the total stiffness of 6 MN/m.

Subplot (i) considers three layers of geogrid (k = 2 MN/m) and the interface friction angle between the geogrid and embankment material is 20°. This improves comparison with the GRC at the point of maximum arching, and the data now lies between the comparison line for k = 2 and 6 MN/m.

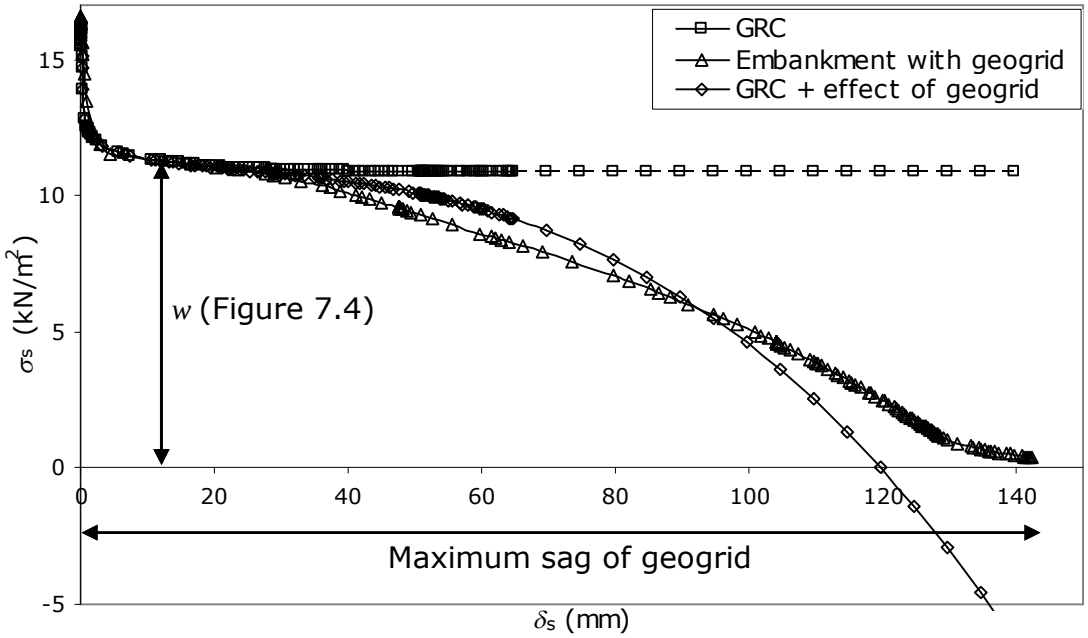

(a) h = 1 m, s = 2.5 m, k = 6 MN/m, δ_i = 0

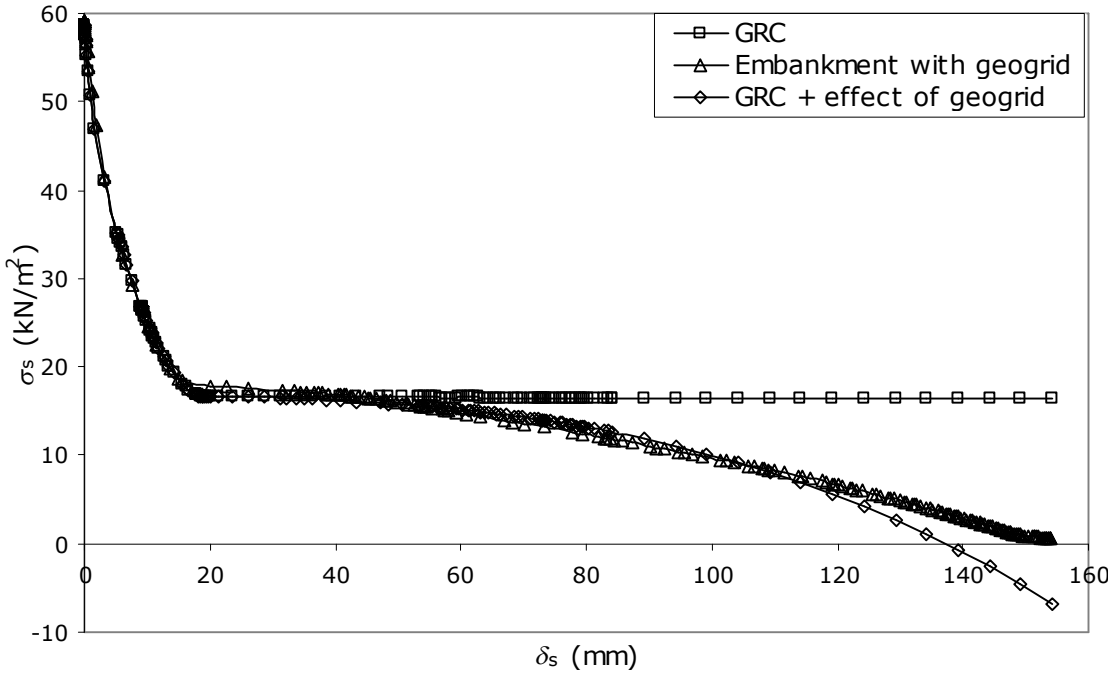

(b) h = 3.5 m, s = 2.5 m, k = 6 MN/m, δ_i = 0

Figure 7.2 continued on following page

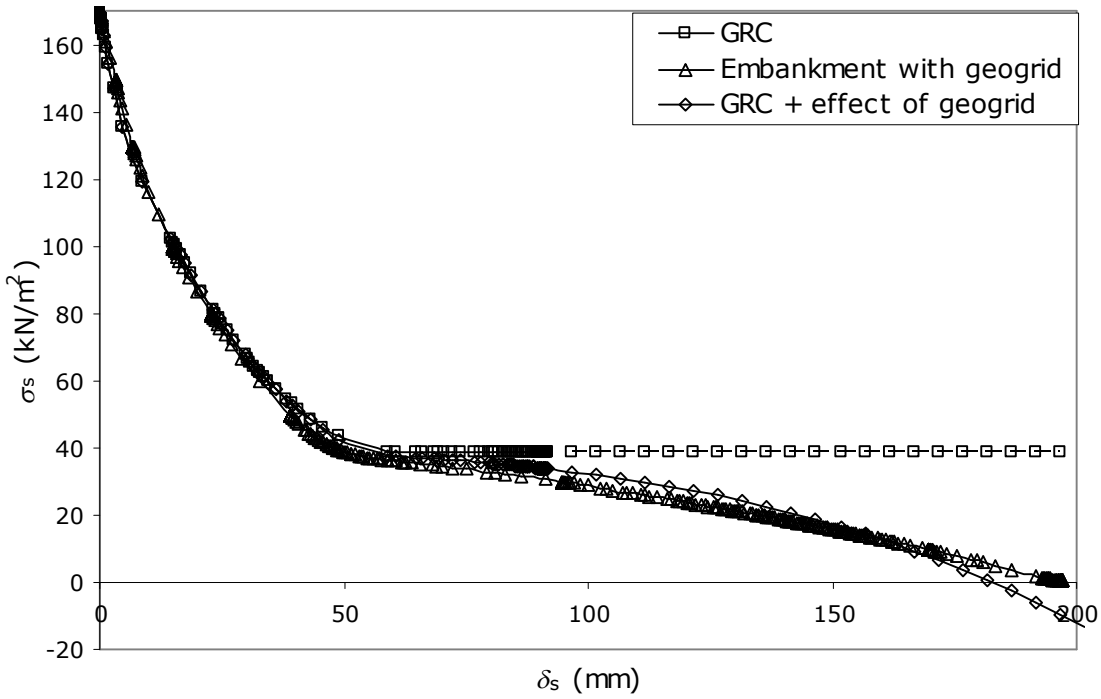

(c) h = 10 m, s = 2.5 m, k = 6 MN/m, δ_i = 0

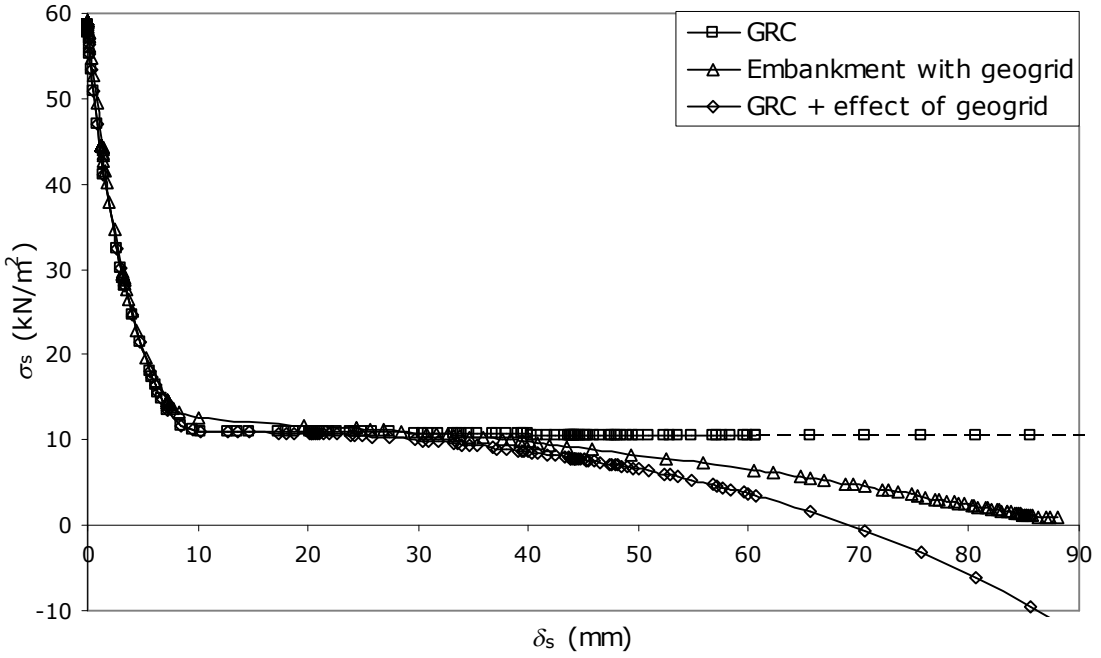

(d) h = 3.5 m, s = 2 m, k = 6 MN/m, δ_i = 0

Figure 7.2 continued on following page

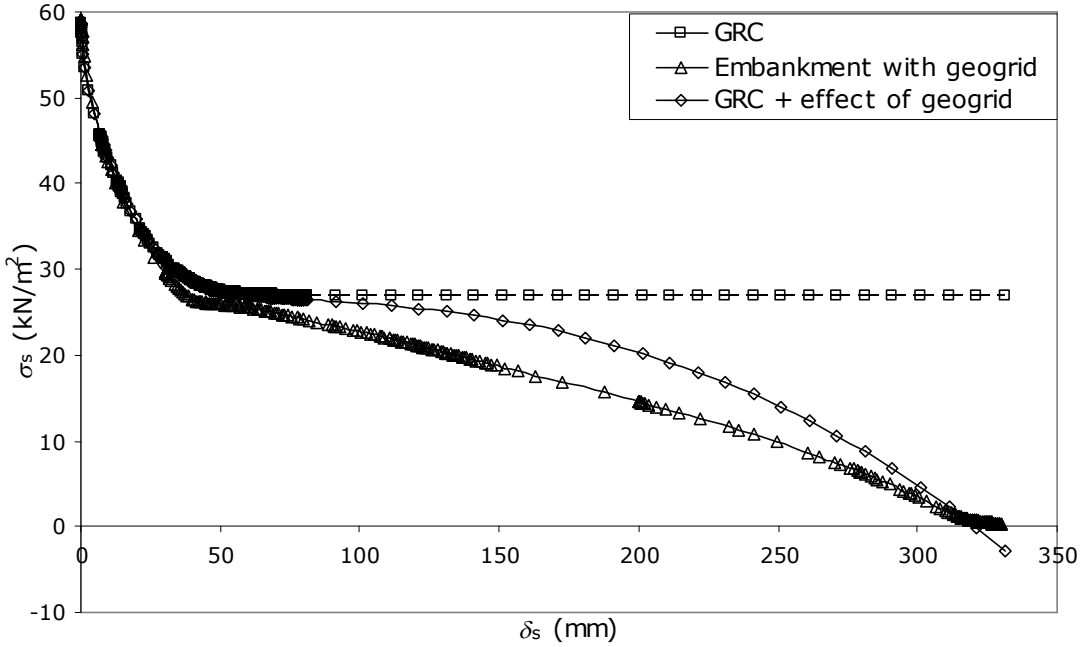

(e) h= 3.5 m, s = 3.5 m, k = 6 MN/m, δ_i = 0

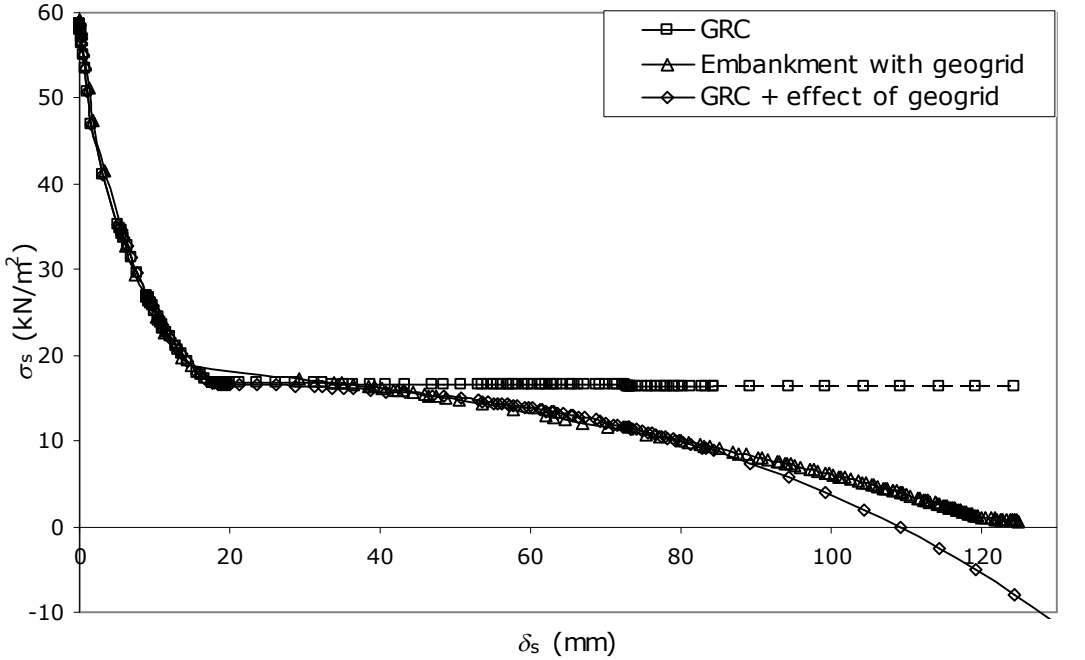

(f) h = 3.5 m, s = 2.5 m, k = 12 MN/m, δ_i = 0

Figure 7.2 continued on following page

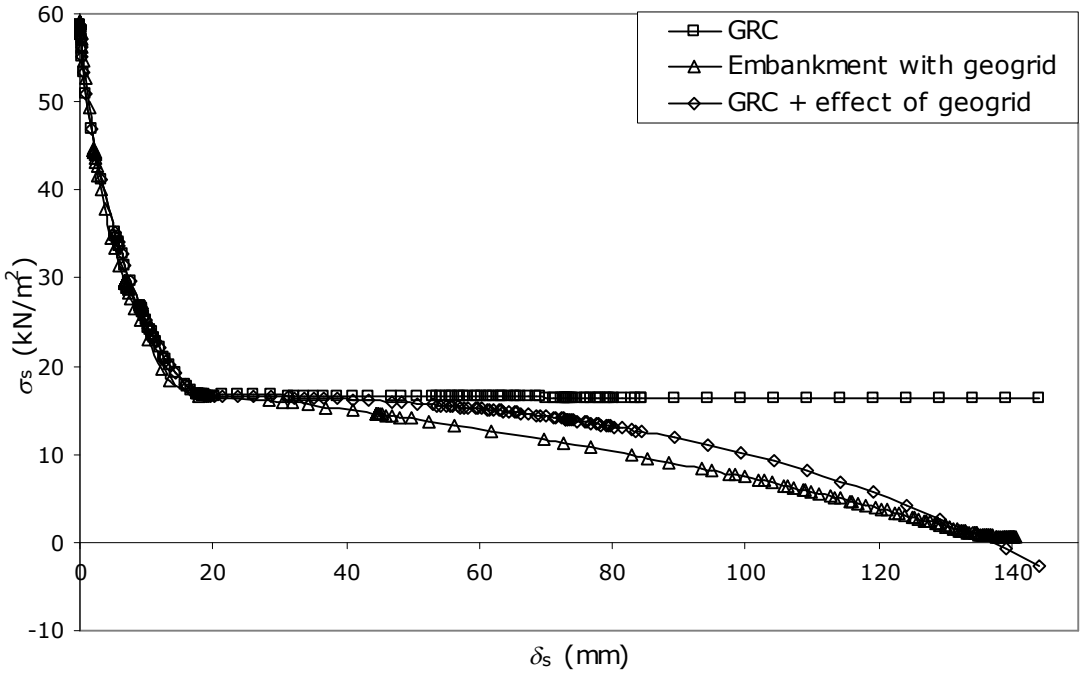

(g) h = 3.5 m, s = 2.5 m, k = 6 MN/m, δ_i = 20 (interface friction angle)

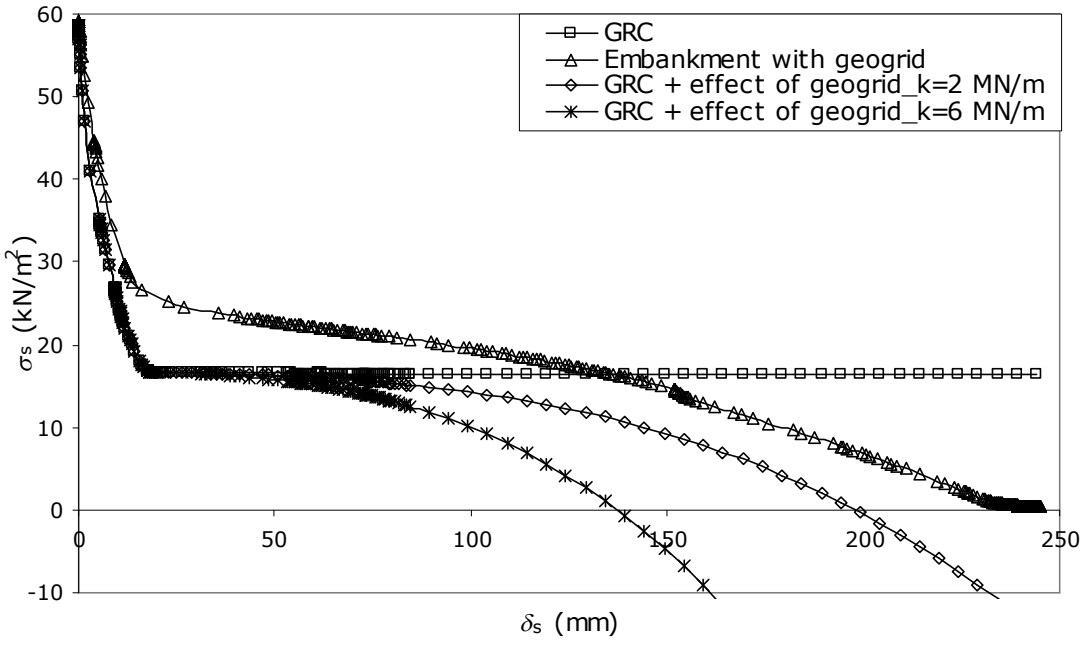

(h) h = 3.5 m, s = 2.5 m, k = 3×2 MN/m, three layers of geogrid with δ_i = 0 (interface friction angle)

Figure 7.2 continued on following page

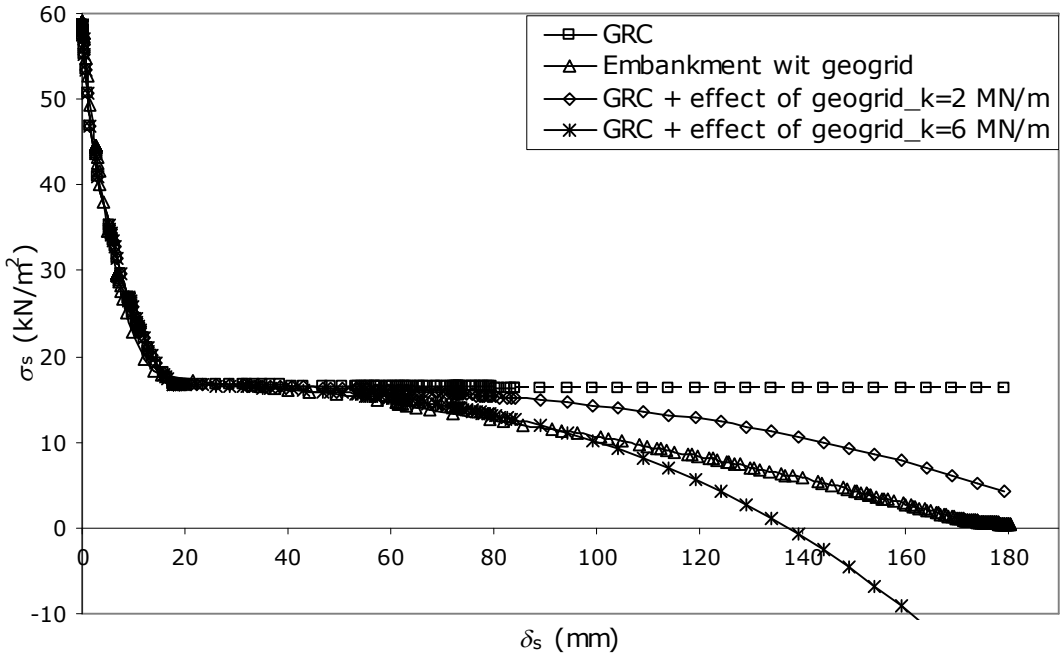

(i) h = 3.5 m, s = 2.5 m, k = 3×2 MN/m, three layers of geogrid with δ_i = 20 (interface friction angle)

Figure 7.2. Variation of subsoil settlement and stress for reinforced piled embankments

7.3.2 Settlement at the subsoil and surface of the reinforced piled embankment

Figure 7.3(a) shows the maximum value of subsoil settlement at the midpoint of the diagonal between piles (D, Figure 6.1) required to reach ultimate conditions: $\sigma_{s,ult} \approx 0$. The value has been normalised by the clear gap between pile caps (s-a) so that it is analogous to δ^* (see Section 2.3, Figure 2.14). Variation with (h/s) is shown (for analyses (a)-(c)).

The absolute magnitude of $\delta_{s,ult}/(s\text{-}a)$ is between 10 and 13% when $\sigma_s \approx 0$. The normalised displacement to reach this point increases slightly with h/s. These values are somewhat larger than the equivalent data in the plane strain analyses (approximately between 6 and 11%). Because the reinforcement span is for the 3D situation, larger displacement is required to reach the point where $\sigma_s \approx 0$.

Subplot (b) shows the ratio of settlement at the top of the embankment at the midpoint of the diagonal between piles (δ_{em}, see plane strain graph Figure 1.1, in Section 1.1) to the equivalent value in the subsoil (δ_s) at the point where $\sigma_s \approx 0$: $(\delta_{em}/\delta_s)_{ult}$. Values are in the range 0.6 - 0.8. This is similar to the plane strain situation, where values were in the range 0.4 - 0.9. The ratio again tends to 1.0 as (h/s) tends to 0.

Subplot (c) shows the ratio of the settlement at the top of the embankment at the midpoint of the diagonal between piles (δ_{em}) to the equivalent value at the centre above the pile cap (δ_{ec}, see plane strain

graph Figure 1.1, in Section 1.1) at the point where $\sigma_s \approx 0$: $(\delta_{em}/\delta_{ec})_{ult}$, showing variation with (h/s). This is a measure of differential settlement at the surface of the embankment, which shows similar behaviour to the plane strain results, and 3D results for an embankment without geogrid.

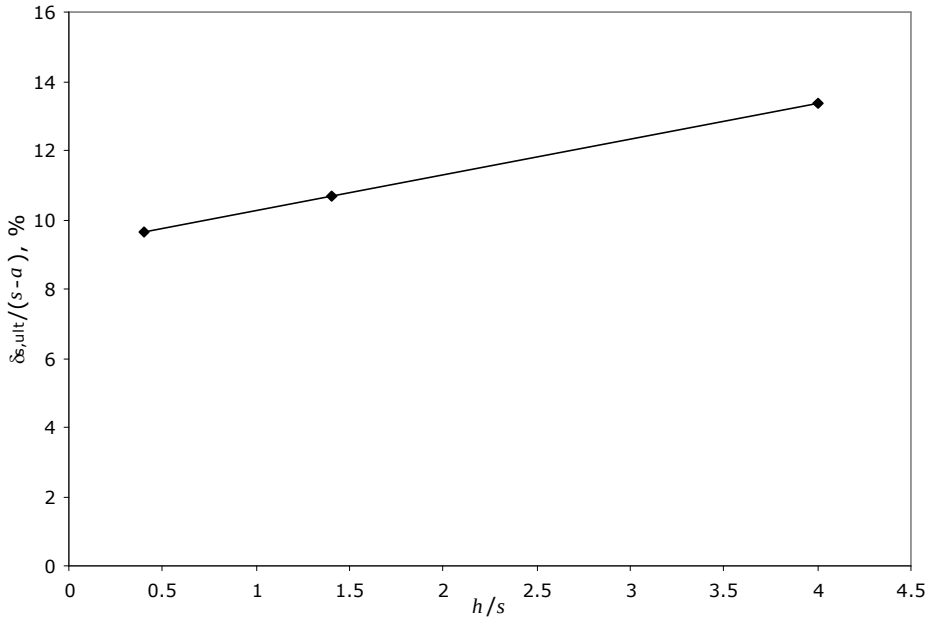

(a) Ultimate settlement of the subsoil at the midpoint of the diagonal between piles ($\delta_{s,ult}$) normalised by the clear gap between pile caps (s-a)

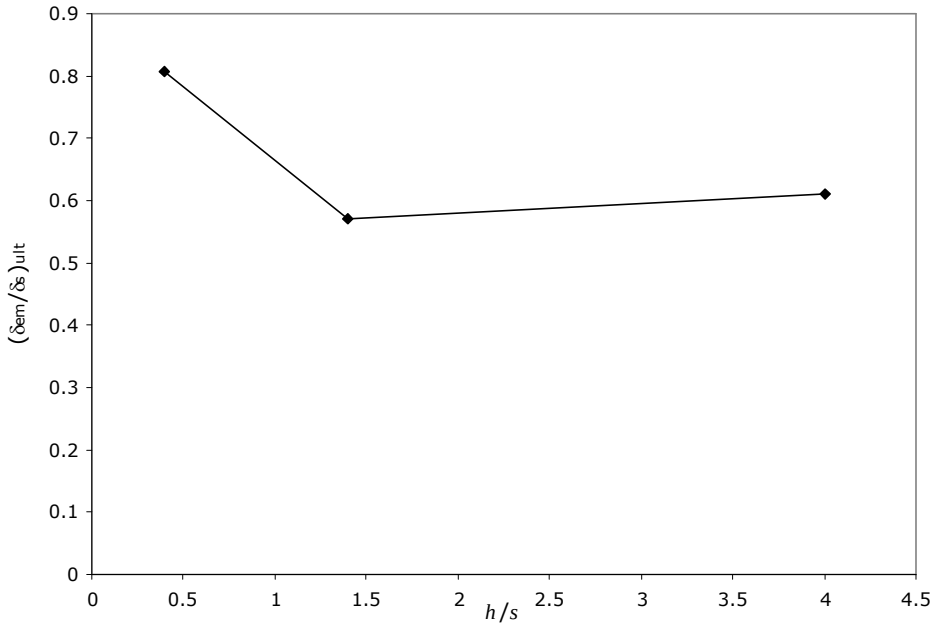

(b) Ratio of the settlement at the top of the embankment at the midpoint of the diagonal between piles (δ_{em}) to the equivalent value at the subsoil ($\delta_{s,ult}$)

Figure 7.3 continued on following page

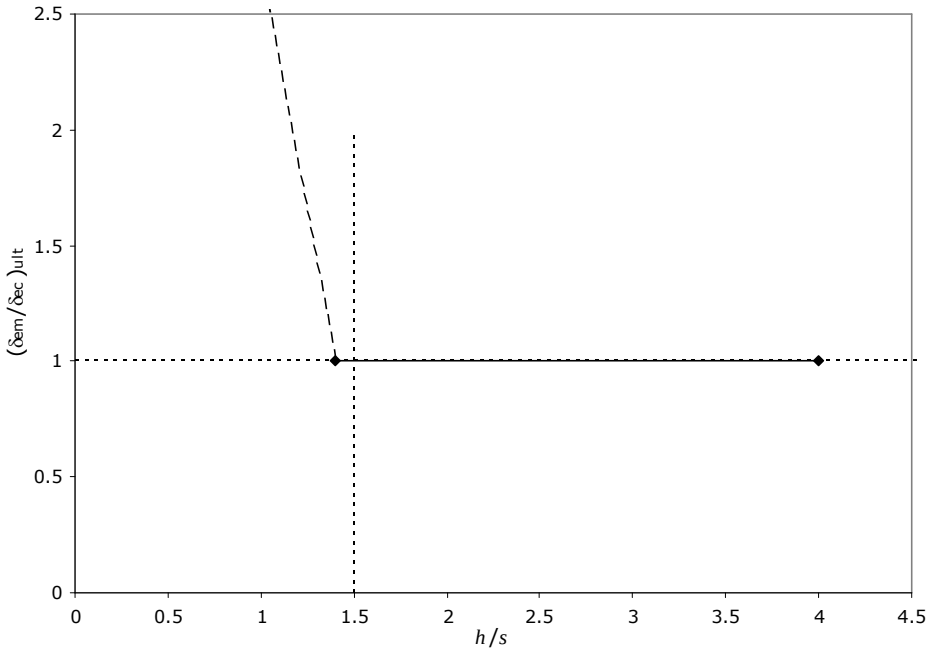

(c) Ratio of the settlement at the top of the embankment at the midpoint of the diagonal between piles (δ_{em}) to the equivalent value at the centre above the pile cap (δ_{ec}) at ultimate conditions

Figure 7.3. Ultimate ($\sigma_{s,ult} \approx 0$) settlement at the subsoil and surface of the reinforced piled embankment

7.3.3 Behaviour of geogrid in the piled reinforced embankment

In Chapter 4 (the equivalent plane strain analyses), equations were derived relating both the maximum sag and tension in the geogrid to the component of vertical stress carried by the geogrid (w). This is the vertical stress at the base of the embankment which 'remains' at the point of maximum arching and is carried by the geogrid when the subsoil stress (σ_s) reaches zero in the analysis. As in Chapter 4 the plots show one data point for each of the analyses. This corresponds to the ultimate point in the analysis, when $\sigma_{s,ult} \approx 0$ and sag of the geogrid has reached its maximum value. As in Chapter 4, the value of w in each case was derived from the GRC at the point of maximum arching.

Figure 7.4(a) shows results for the maximum sag in the geogrid, which occurred at the midpoint of a diagonal between pile caps (point D, Figure 6.1). The four comparison lines were generated using Equation (4.6) with $l = \sqrt{2}(s\text{-}a)$. The factor $\sqrt{2}$ is associated with the change from plane strain to 3D geometry (Figure 6.1). The use of (s-a) rather than (s-a/2) is not strictly consistent with Chapter 4, but was found to give better agreement here.

The use of colours to associate specific data points with each of the comparison lines is the same as Chapter 4. As in Chapter 4 the data shows reasonable agreement except for analysis (h) - 3 geogrids with frictionless interface with the soil. Since the sum of stiffness for the 3

grids is 6 MN/m, it can be compared with this line. However, the displacement is again larger than expected, which as previously noted probably reflects the reduced effectiveness of the upper grids in carrying load.

Figure 7.4(b) shows the tension in the reinforcement at the midpoint of a diagonal between piles, which increases with an increase of the remaining vertical load carried by the geogrid. Comparison lines were generated using Equation (4.5) with $l = \sqrt{2}\,(s\text{-}a)$. However, the comparison lines overestimate the analysis results.

In fact the maximum tension in the geogrid occurred at the corner of a pile cap, and was about 2-3 times higher than the value at the midpoint of the diagonal. Figure 7.5 shows typical contours of this tension in both the orthogonal directions. It has been noted by (Russell & Pierpoint, 1997) that tension will not be maximum at the centre of the span, and this has been confirmed here in 3D (although tension across the span and pile cap was virtually constant in plane strain).

Figure 7.4(c) shows the maximum tension for the various analyses. The tension T predicted by Equation 4.5, is modified by the factor $(s+a)/2a$, and referred to as T^*:

$$T^* = T\,\frac{(s+a)}{2a} \qquad (7.1)$$

This factor was proposed by Love & Milligan (2003) for the increased tension in geogrid between piles where the load is distributed evenly in both orthogonal directions, corresponding to the situation in the analyses. The comparison lines are then generated by Equation (7.1) with l = (s-a/2) in Equation 4.5 to derive T, corresponding to Chapter 4, since a span directly between pile caps rather than a diagonal is considered. The lines in Figure 7.4(c) are therefore the lines in Figure 4.4(b) multiplied by (s+a)/2a.

The data now generally show good agreement with the comparison lines. As in Chapter 4, for the cases with three reinforcement layers a separate data point is shown for each layer of geogrid, and a new comparison line is shown based on k = 2 MN/m (purple), the stiffness of each geogrid rather than the combined total for all 3 (k = 6 MN/m). It can be seen that like in plane strain the upper two grids carry relatively little tension compared to the bottom layer, implying less effective performance. This finding has been proposed by Jenner et al. (1998) for a monitored field case. They stated that larger strains were recorded in the lower grid than the upper grid as anticipated in the design.

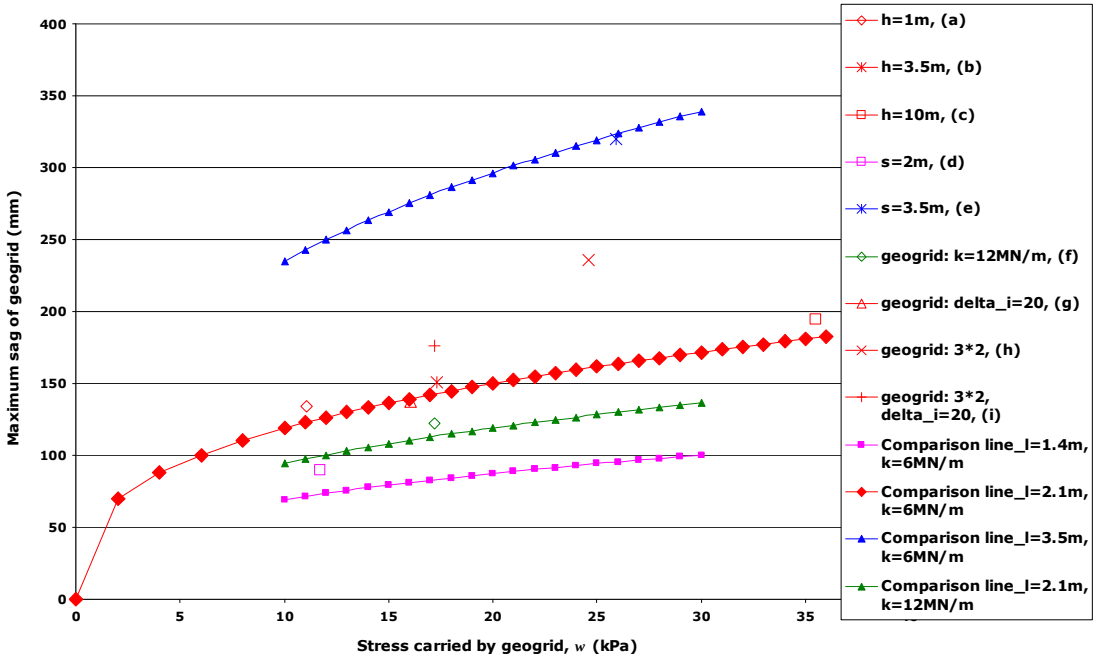

(a) Maximum sag of the geogrid

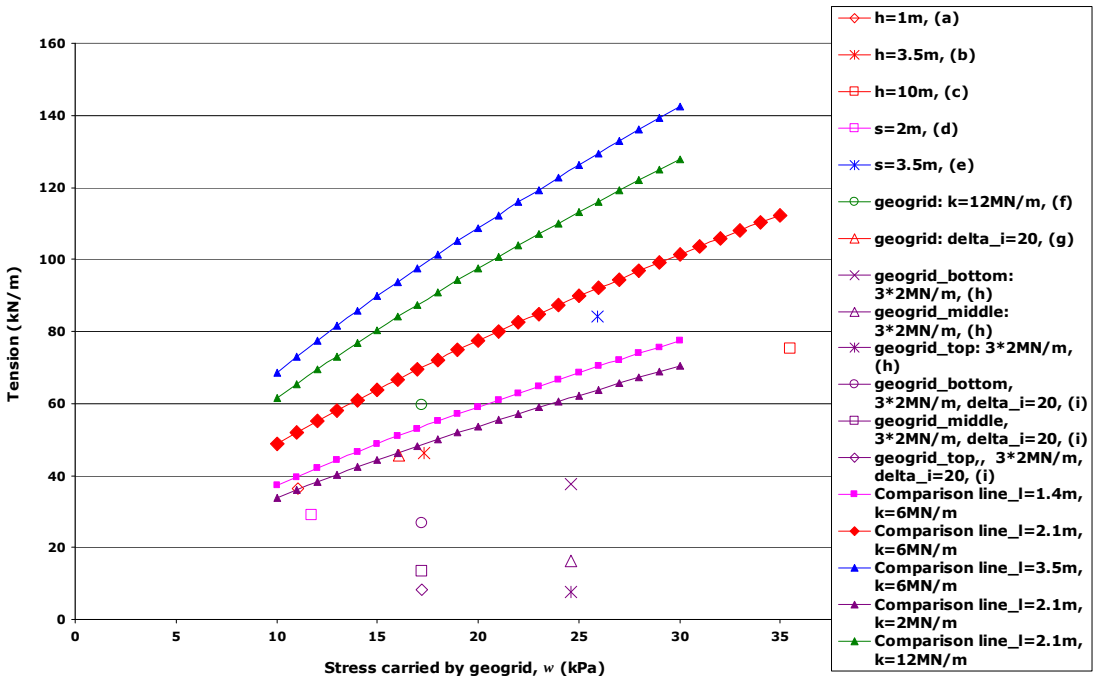

(b) Tension in the geogrid at midpoint of diagonal between piles (D, see Figure 6.1)

Figure 7.4 continued on following page

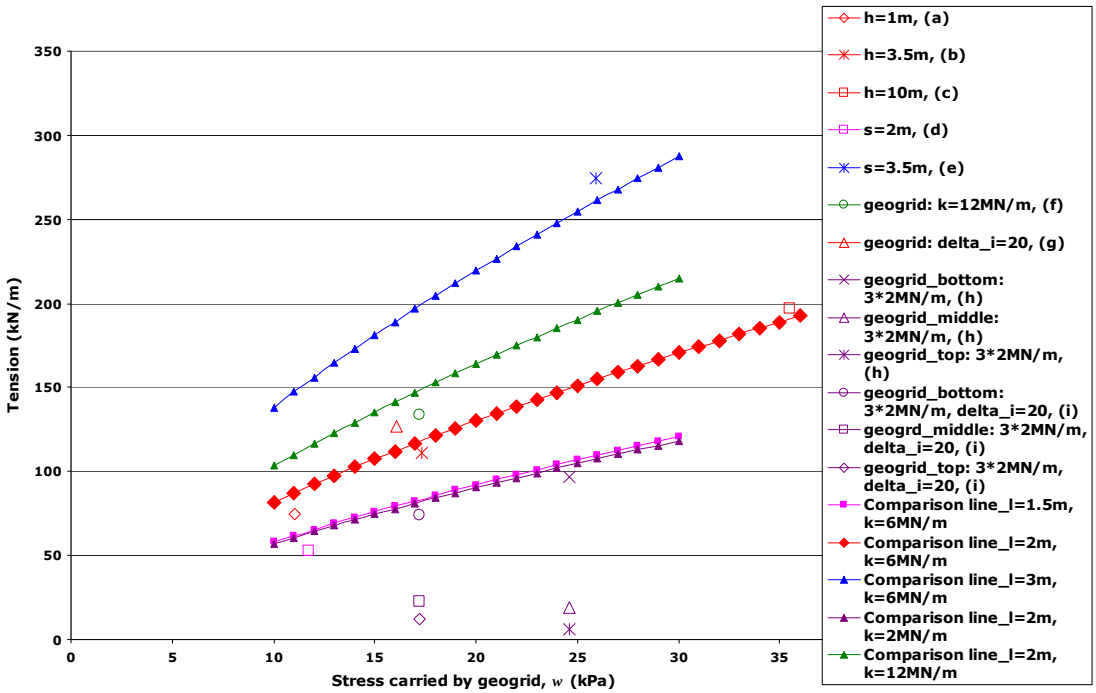

(c) Tension in the geogrid at the corner of the pile cap (A, see Figure 6.1)

Figure 7.4. Maximum displacement and tension of geogrid generated by vertical stress carried by the geogrid (w). Specific colours associate results with comparison lines.

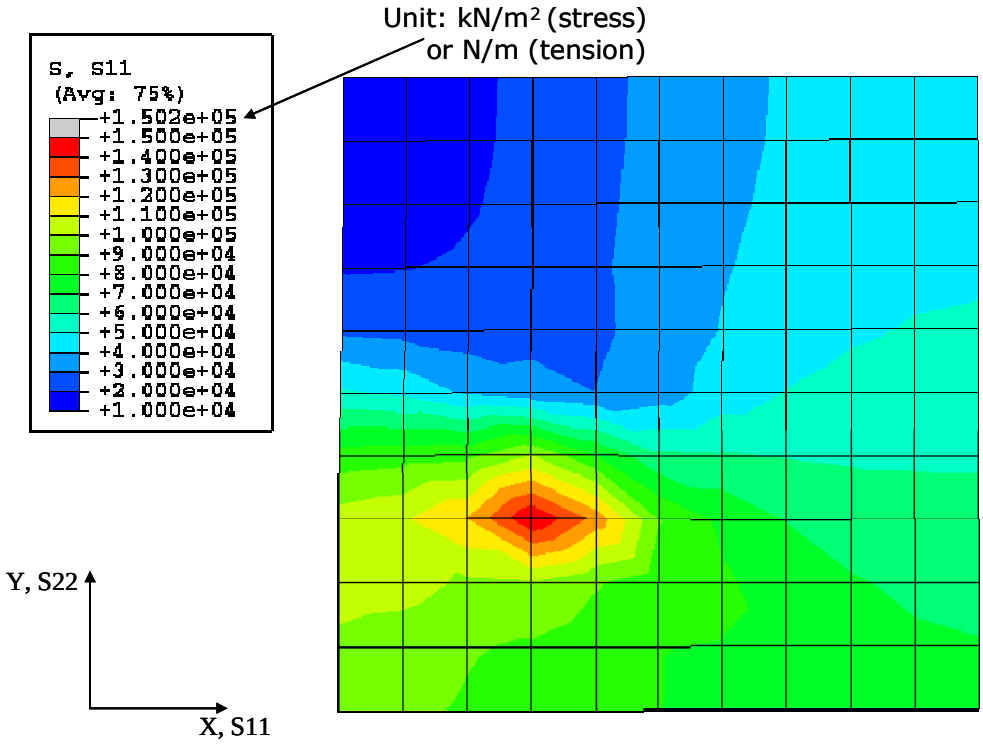

(a) X direction

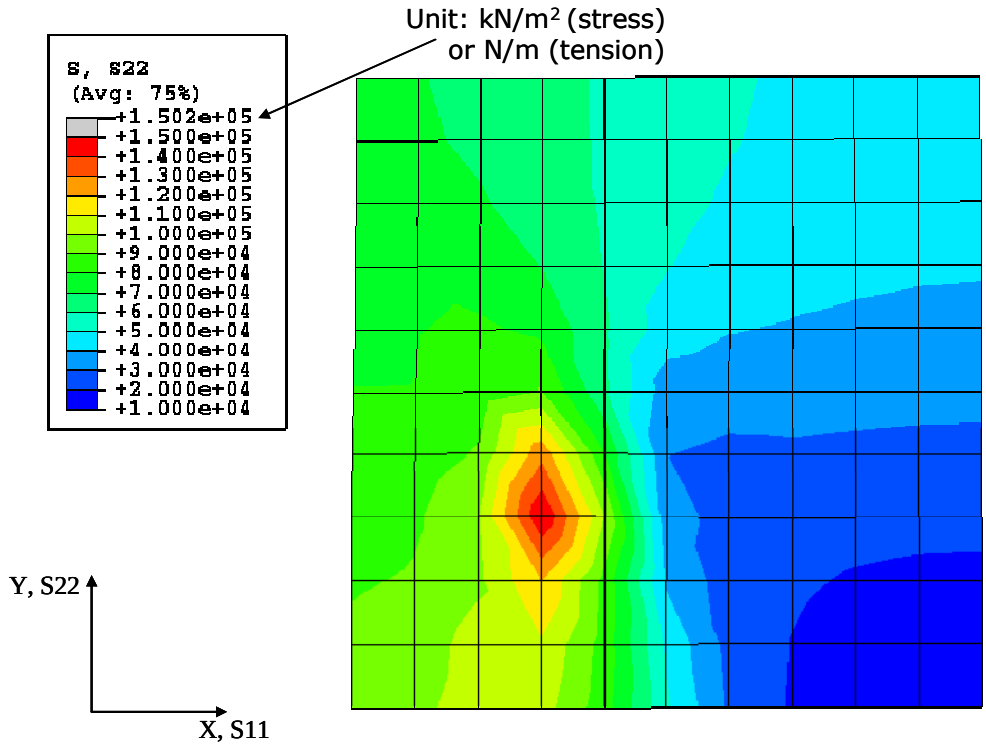

(b) Y direction

Figure 7.5. Tension distribution of geogrid at the maximum sag

7.4 Summary

Chapter 7 has extended the plane strain analyses reported in Chapter 4 to 3D for a square grid of pile caps.

It was again found that the geogrid was capable of reducing the ultimate stress on the subsoil to zero. However, this again required significant sag of the geogrid. Comparison of the geogrid action with a simple formula (Equation (2.30)) for the sag again gave reasonable agreement.

It was found that the maximum tension in the geogrid occurred at the corner of the pile cap, contrasting with the plane strain result where tension was virtually constant across the span and pile cap. The tension on a diagonal between pile caps was about 2-3 times smaller than the maximum and was somewhat overpredicted by the plane strain formula using the diagonal span. However, a version of the formula modified to account for the concentration of load in the geogrid directly between the piles gave reasonable correspondence with the maximum tension at the corner of the pile cap.

CHAPTER 8

REINFORCED PILED EMBANKMENT WITH SUBSOIL IN THREE-DIMENSIONS

8.1 Introduction

Three dimensional analyses for a reinforced embankment including the subsoil are presented in this Chapter. Like plane strain conditions (Chapter 5), only elastic behaviour of the subsoil is considered.

8.2 Analyses presented

In this chapter, three-dimensional numerical modelling of reinforced embankments with subsoil are performed using Abaqus Version 6.6. A typical mesh geometry is shown in Figure 8.1, for embankment height (h) = 3.5 m, subsoil thickness (h_s) = 5.0 m, and pile spacing (s) = 2.5 m. There are 5328 eight noded, full-integration, three-dimensional, linear brick solid elements (C3D8) for the embankment; 100 four noded, full-integration, three-dimensional membrane element (M3D4) for the geogrid reinforcement; and 6069 eight noded, full-integration, three-dimensional, linear brick solid elements (C3D8) for the subsoil.

As in previous Chapters the vertical boundaries represent planes of symmetry passing through the centre of a pile cap and the midpoint between pile caps (Figure 6.1). The restraint on movement at these boundaries is as described in Chapters 6 and 7, with the same restraint on

movement normal to the faces in the subsoil as for the embankment. As in the equivalent plane strain analyses (Chapter 5) for convenience subsoil beneath the pile cap is not modelled. It is effectively assumed that there is a rigid inclusion with plan dimension the same as the pile cap through the full depth of the subsoil. Material beneath the subsoil is assumed to be rigid.

As in previous chapters, the pile cap is assumed to provide rigid restraint to the embankment. Like in Chapter 5, the analysis was controlled by reduction of a stress σ_u applied at the embankment/subsoil interface. The initial value of σ_u was equal to the nominal vertical stress from the embankment, ultimately reducing to zero. Notionally this models the dissipation of excess pore pressure in the subsoil.

The pile cap width (a) was fixed at 1.0 m and the centre-to-centre spacing (s) was 2.5 m. The embankment height (h) was 3.5 or 10 m. The height of subsoil (h_s) was 5 or 10 m. Throughout the analyses the minimum and maximum element size in the embankment and subsoil were approximately 0.0003 and 0.001 m^3. This corresponds to element dimensions of size 30 to 100 mm. The membrane element length and width were 125 mm, and thickness was 1 mm.

The embankment material was again assumed to be granular, and modelled assuming elastic-perfectly plastic response (E = 25 MN/m^2, ν' = 0.2, c' = 1kN/m^2, ϕ' = 30°, ψ' =0° and γ = 17 KN/m^3).

The subsoil was modelled as a linear elastic material, with parameters as summarised in Table 8.1. As in Chapter 5, since a linear elastic approach was used, there was no requirement to model the self-weight of this material, and response of this layer was based on the increase in stress acting on it which occurred during the analysis (see Chapter 5).

The geogrid stiffness was 6 MN/m for a single layer of geogrid, or 2MN/m with three layers of geogrid. The interface friction angle (δ_i) between the granular material (embankment fill) and geogrid was 0° or 20°.

The reinforcement (geogrid) is located at the bottom of embankment, where the thickness of the fill below the reinforcement and above the pile cap is again assumed to be 0.1 m in the model, and two further layers above this are each separated by 0.3 m where three layers were considered. The geogrid is again modelled using three-dimensional membrane elements which can carry tension force but do not have any bending stiffness.

All analyses in this chapter have are summarised in Table 8.2. Two embankment heights were considered. For h = 3.5 m a moderately soft and thick subsoil layer was considered. For h = 10 m a softer and deeper subsoil was considered. For each embankment height either a single smooth layer of geogrid with stiffness 6 MN/m, or 3 layers of geogrid with interface friction angle 20^o and stiffness 2 MN/m were considered.

The sequence of analysis was the same as in Chapter 5. First the in-situ stresses were specified for the reinforced embankment (based on a unit weight of 17 kN/m^3 and a K_0 value of 0.5). Initially σ_u (applied to support the underside of the embankment) was specified as the nominal weight of the embankment, notionally representing the excess pore pressure. This value was then reduced to mimic consolidation and corresponding settlement of the subsoil as effective stress increases.

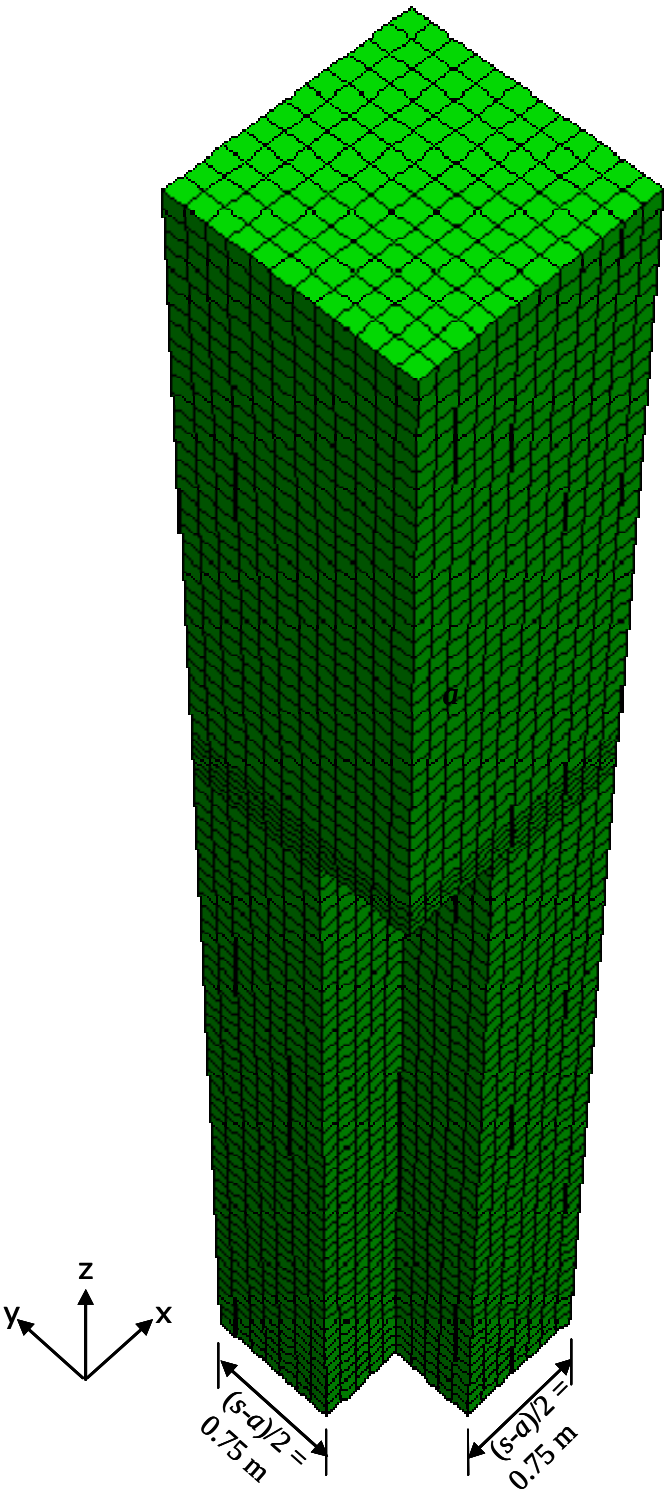

Figure 8.1. Typical finite element mesh (h = 3.5 m, s = 2.5 m, h_s = 5 m) for reinforced embankment with subsoil

Table 8.1. Material parameters for subsoil

Young's Modulus (MN/m^2)	Poisson's Ratio
5 or 2.5	0.2

Table 8.2. Summary of analyses reported in this Chapter

h (m)	s (m)	k (MN/m)	δ_i	Young's Modulus of subsoil E_s (MN/m^2)	Height of subsoil h_s (m)	subplot
3.5	2.5	6	0	5	5	(a)
3.5	2.5	**3×2**	20	5	5	(b)
10	2.5	6	0	**2.5**	**10**	(c)
10	2.5	**3×2**	**20**	**2.5**	**10**	(d)

8.3 Results

Figure 8.2 shows how the maximum displacement of the subsoil at the midpoint between the pile caps (δ_s) increases with a reduction in the stress at the bottom of reinforced embankment (σ_u).

Like in Chapter 5 there are three lines presented in Figure 8.2. They are 'Embankment with geogrid', 'subsoil (analysis)' and 'subsoil (comparison)'. The 'Embankment with geogrid' line comes from previous analyses of reinforced piled embankments (see Figure 7.2). The data for 'subsoil (analysis)' shows results from the analyses presented in this Chapter. As for the plane strain conditions, the line 'subsoil (comparison)' comes from simple consideration of one-dimensional compression.

As in Chapter 5, the 'subsoil (analysis)' line is steeper than the 'subsoil (comparison)' line. For the plane strain analyses this effect appeared to be related to an additional effect of 'bearing failure' and associated rotation of principal stresses (see Figure 5.3).

As in the plane strain analyses, at the end of each analysis σ_u had reduced to zero. This logically corresponds to approximate intersection of the 'embankment with geogrid' and 'subsoil (analysis)' lines, since the stress at the base of the embankment is equal to the increase in stress in the subsoil (σ_s). At this point the displacement is generally relatively small,

and the geogrid carries very little load, even when the subsoil layer is very soft and thick (i.e. very compressible).

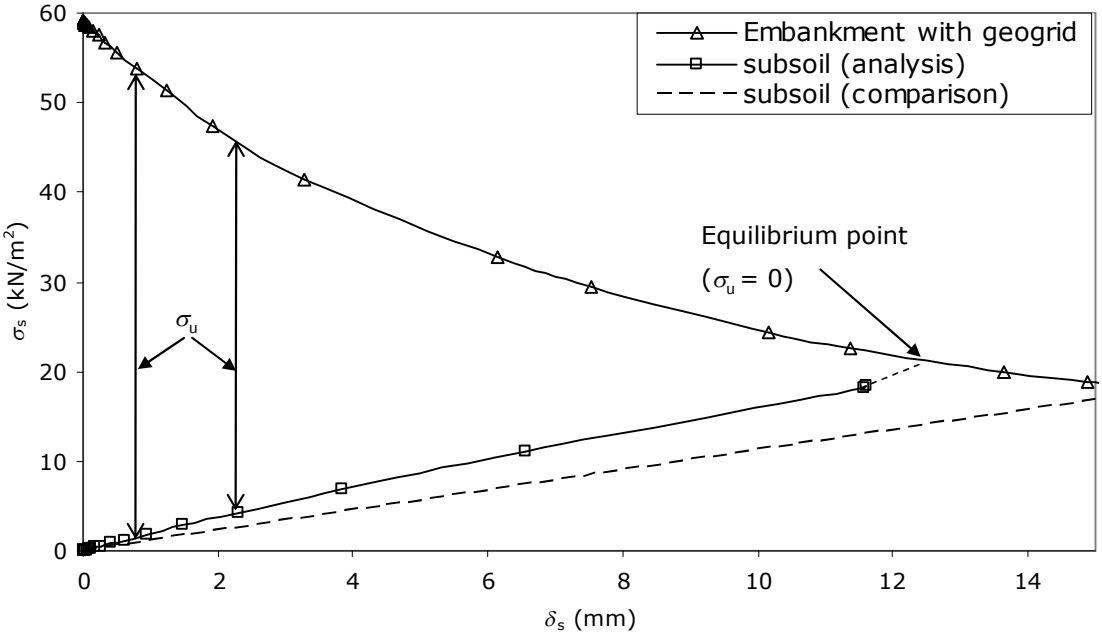

(a) h = 3.5 m, s = 2.5 m, k = 6 MN/m, δ_i = 0, E_s = 5 MN/m^2, h_s =5m

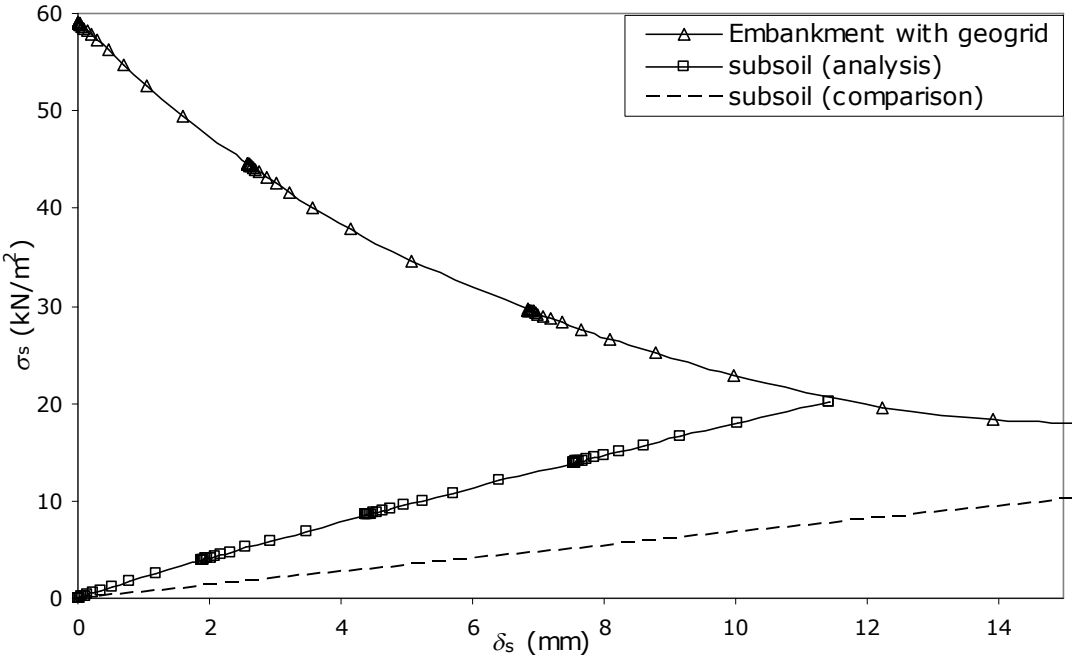

(b) h = 3.5 m, s = 2.5 m, k = 3×2 MN/m with three layers of geogrid, δ_i = 20, E_s = 5 MN/m^2, h_s =5m

Figure 8.2 continued on following page

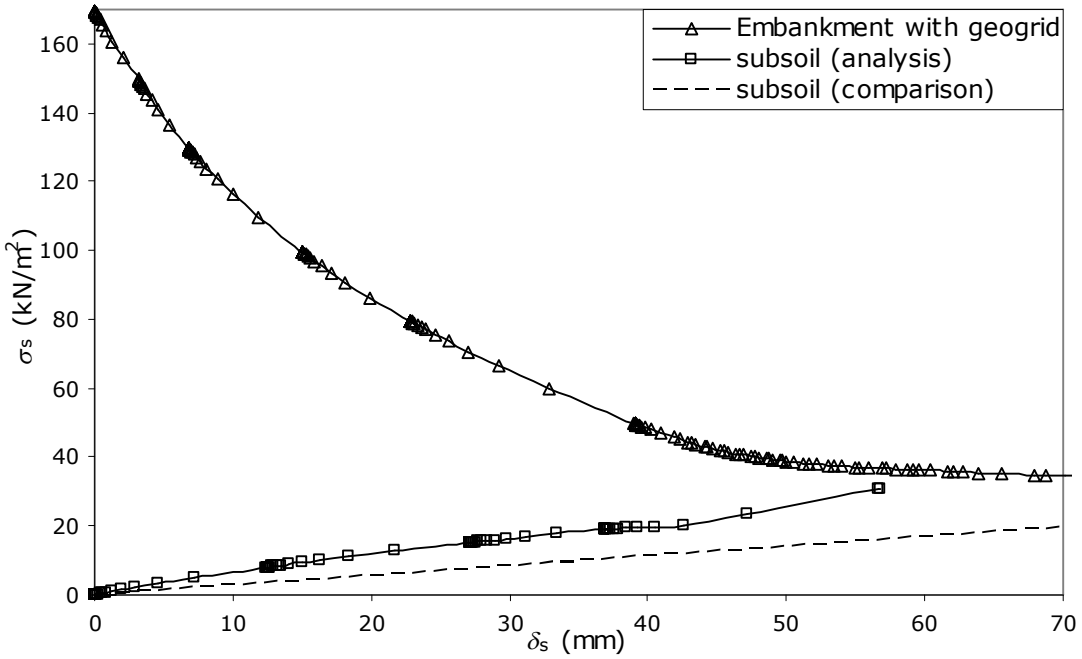

(c) h = 10 m, s = 2.5 m, k = 6 MN/m, δ_i = 0, E_s = 2.5 MN/m^2, h_s =10m

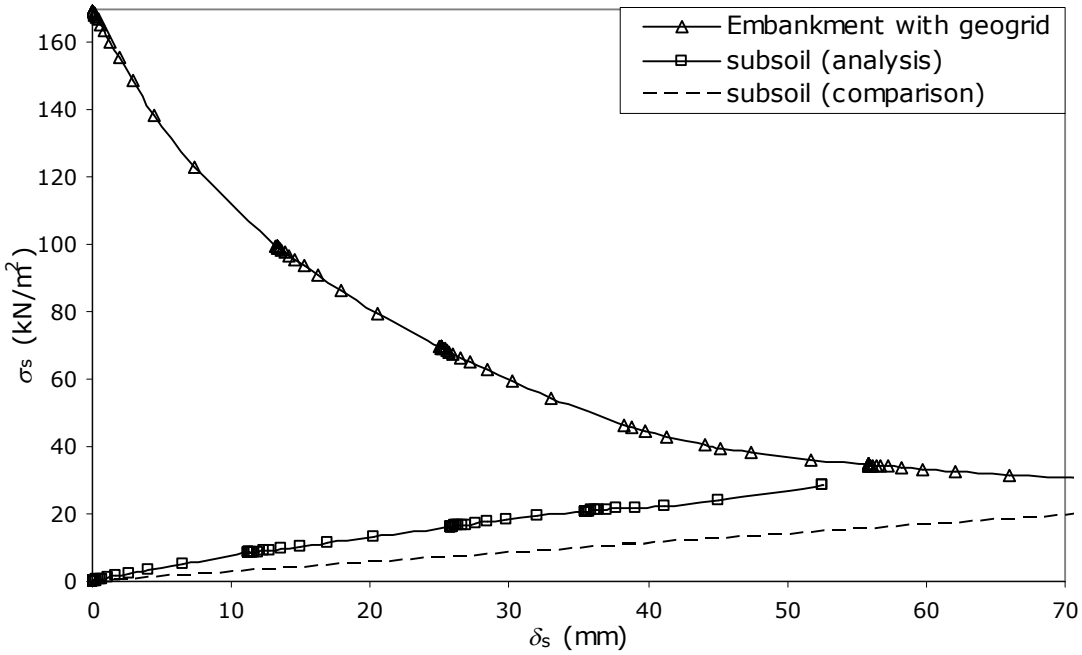

(d) h = 10 m, s = 2.5 m, k = 3×2 MN/m with three layers of geogrid, δ_i = 20, E_s = 2.5 MN/m^2, h_s =10m

Figure 8.2. Behaviour of subsoil in different conditions

8.4 Summary

As in plane strain, the effect of the subsoil in the analyses was somewhat underestimated by a one-dimensional settlement prediction, due to the additional effect of principal stress rotation.

The analyses again indicate that the contribution to vertical equilibrium of the subsoil is considerably more significant than the geogrid. Hence equilibrium of the full system including arching in the embankment, geogrid reinforcement and subsoil is achieved at much lower settlement than the embankment and geogrid alone (Chapter 7).

CHAPTER 9
DISCUSSION OF RESULTS

9.1 Introduction

The aim of this chapter is to summarise the main findings of the finite element analyses, and then present some key comparisons. Finally, four case studies will be introduced.

9.2 Summary of results

9.2.1 Piled embankment

In this research, a series of plane strain and three-dimensional finite element analyses have been undertaken to investigate the behaviour of arching in piled embankments. The subsoil was not modelled, but the 'subsoil stress' at the base of the embankment was used to control the analysis. A parametric study mainly considered variation of the embankment height (h) and centre-to-centre pile spacing (s) with fixed pile cap dimension (a). Some investigation of the embankment soil frictional strength and dilation were also undertaken in plane strain.

The results showed that ratio of the embankment height to the centre-to-centre pile spacing (h/s) is a key parameter.

For embankments with a value of h/s up to about 0.5, there is no evidence of arching based on the stress on the subsoil and there is significant differential settlement. As h/s increases from 0.5 to 1.5, the stress acting on the subsoil reduces compared to the nominal overburden stress from the embankment fill, which implies increasing effect of arching. The differential displacement at the surface of the embankment also reduces. For h/s larger than 1.5, the stress acting on the subsoil is considerably reduced compared to the nominal overburden stress, and there is no differential displacement at the surface of the embankment, i.e. there is 'full arching'.

9.2.2 'Reinforced' piled embankment

The effect of uniform biaxial reinforcement (geogrid or geotextile) in piled embankments was also studied in a series of plane strain and three-dimensional finite element analyses. During the study, the effects of the geogrid stiffness (k), the number of layers, and the interface friction angle were considered. Separate layers of uniaxial grid or 'primary' and 'secondary' reinforcement were not considered.

As expected, the reinforcement was capable of reducing the ultimate stress on the subsoil beneath the embankment (which again controlled the analysis) to zero. The sag of reinforcement could be very large, and was very sensitive to the span of the reinforcement between piles, but relatively insensitive to its stiffness. For the case with three layers of

reinforcement distributed through the bottom metre of the embankment ('a load transfer platform'), the upper two layers carried relatively little tension compared to the bottom layer since they exhibited less sag. This trend of behaviour was also noted by Jenner et al. (1998) in a field case.

In the two-dimensional analyses the tension in the reinforcement was approximately constant across the span. However, in three-dimensional analyses, the results showed that the maximum tension in the geogrid occurred at the corner of the pile cap. Maximum reinforcement tension at the edge of the pile cap has also been noted by Russell & Pierpoint (1997).

9.2.3 'Reinforced' piled embankment with subsoil

The effect of the soft subsoil in the 'reinforced' piled embankment was also presented in a series of plane strain and three-dimensional analyses (rather than just considering the stress acting at the surface of the subsoil). Variation of Young's Modulus and the thickness of the subsoil were considered in the study.

The results showed that the contribution to vertical equilibrium of the subsoil is generally more significant than the reinforcement for the cases considered. It was also found that the subsoil response was somewhat underestimated by consideration of the 1D stiffness since there was also a component of 'bearing' resistance in the soil immediately beneath the embankment.

9.3 Comparison of general trends of behaviour as $h/(s\text{-}a)$ varies

The ratio of the embankment height (h) to the clear spacing between adjacent pile caps (s-a) has been considered as an important parameter for arching behaviour in design.

Aslam (2008) and Ellis & Aslam (2009a and b) investigated the performance of unreinforced piled embankments supported by a square (3D) grid of piles in a series centrifuge tests. Their findings showed that:

- $h/(s\text{-}a) < 0.5$: there is no evidence of arching.
- $0.5 < h/(s\text{-}a) < 2.0$: there is increasing evidence of arching as h increases.
- $2.0 < h/(s\text{-}a)$: there is 'full' arching.

Potts & Zdravkovic (2008b) performed finite element analyses to study the behaviour of geosynthetic reinforced fills overlying voids. They proposed that the development of arching in the fill depends on the ratio H/D (where H is the depth of overlying fill, and D is the width of the void), as well as the geometry of the void and the properties of the soil and geosynthetic. In all cases stable arching behaviour was found to occur when $H/D > 3.0$ for an infinitely long void (plane strain condition). Comparing the gap between piles in a piled embankment with a void H/D, is broadly equivalent to $h/(s\text{-}a)$.

In this work the results have considered the ratio h/s. However, this can be related to $h/(s\text{-}a)$:

$$\frac{h}{s-a} = \frac{h}{s}\frac{s}{(s-a)} \tag{9.1}$$

In this work the ratio (s/a) is in the range 2.0 to 3.5. $s/(s\text{-}a)$ is then in the range 2.0 to 1.4. Thus the critical value of h/s = 1.5 for full arching reported in this work corresponds to $h/(s\text{-}a) \approx$ 2.0-3.0. This is consistent with the values reported by the other authors for physical and numerical modelling.

9.4 Comparison of the value of $\sigma_s/\gamma(s\text{-}a)$ at the point of maximum arching for medium height embankments

Ellis & Aslam (2009a) presented plots of $\sigma_s/\gamma(s\text{-}a)$ against $h/(s\text{-}a)$. The results show that the value of $\sigma_s/\gamma(s\text{-}a)$ at the point of maximum arching is approximately 0.5. However, it was not possible to determine reliably σ_s for high embankments where the efficacy tended to 1.0.

Potts & Zdravkovic (2008b) showed a plot of the magnitude of the vertical stress at the level of the reinforcement (which is equivalent to the subsoil stress, σ_s, in an unreinforced embankment as referred to in this work) against void diameter (D) for circular voids up to 4.0 m wide, Figure 9.1. The results show the gradient of the 'ICFEP' line (from the finite element analyses) σ_s/D is approximately 5 kPa/m. Assuming γ = 16 kN/m^3, then $\sigma_s/\gamma D$ = 0.3. The value D is analogous to $(s\text{-}a)$, and hence this value is approximately consistent with that proposed by Ellis & Aslam (2009a). It is perhaps not that surprising that the value (0.3) is somewhat lower in the axisymmetric case compared to arching over a square grid of piles (0.5).

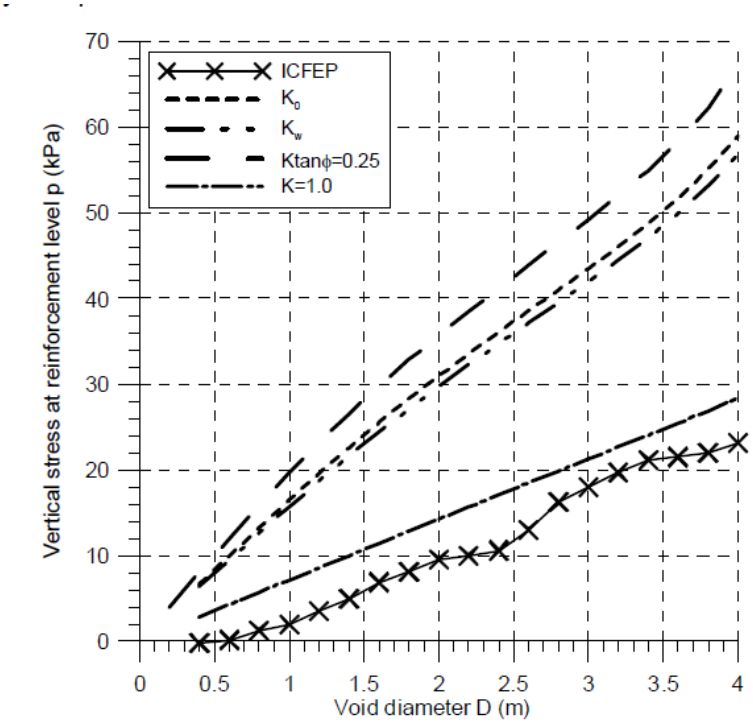

Figure 9.1. Comparison of vertical stresses at the level of the reinforcement (Potts & Zdravkovic, 2008b)

In this research, as shown in Figure 3.4(b) and Figure 6.6, the value of $\sigma_s/\gamma s$ for maximum arching is approximately 0.25 ~ 0.4 except for high s/a in the 3D situation, where punching of the pile caps into the base of the embankment gives higher values of $\sigma_s/\gamma s$.

The results from this study can again be converted from normalisation by s to $(s\text{-}a)$ by multiplication by $s/(s\text{-}a) \approx 1.4$ to 2.0. This gives values of $\sigma_s/\gamma(s\text{-}a)$ in the range 0.4 to 0.8, which is consistent with the other research.

9.5 Equation for equilibrium including arching, reinforcement and subsoil

Aslam (2008) and Ellis & Aslam (2009b) propose an interaction diagram where the combined action of arching in the embankment, reinforcement membrane action and the subsoil give equilibrium at a compatible settlement (δ) – see Figure 2.16 (Section 2.4.3). δ corresponds to the maximum sag of the geogrid, but is considered as a uniform settlement at the surface of the subsoil.

Taking these individual components and writing the equation of equilibrium:

$$E_0 \frac{\delta}{h_s} + 21\frac{k}{l}\left(\frac{\delta}{l}\right)^3 = \sigma_a + \sigma_w \qquad (9.2)$$

Where:

l = (s-a), clear spacing between pile caps (m)

E_0 = the one-dimensional stiffness of the subsoil (kN/m^2)

h_s = the thickness of the subsoil (m)

k = the stiffness of the geogrid (kN/m)

σ_a = the stress at the base of the embankment due to the action of arching alone (i.e. from the Ground Reaction Curve)

σ_w = $\gamma_w h_w$ the stress acting on the subsoil due to the working platform (any imported material below the pile cap level, which is hence not affected by arching)

The first term represents the subsoil response; the second is the geogrid membrane action, whilst σ_a and σ_w are the load that must be carried. In fact the geogrid cannot carry weight from the working platform (which is below it), and hence this term cannot exceed σ_a. Likewise the subsoil term cannot be less than σ_w since the working platform is only supported by the subsoil. At this point a gap would open between the reinforcement and working platform beneath.

It has been shown by Ellis et al. (2009) that this Equation is consistent with a similar but more complex equation proposed by Abusharar et al. (2009). The equation contains four extra terms, but these are shown to be relatively insignificant. The equation is only presented for a plane strain situation by Abusharar et al. (2009).

The span l to be used in the geogrid term has been unclear, particularly for a 3D pile cap layout. However, Chapters 4 and 7 indicate the following values for uniform biaxial reinforcement:

- 2D: $l=(s\text{-}a/2)$
- 3D: $l=\sqrt{2}\,(s\text{-}a)$

Hence for a 3D arrangement

$$E_0 \frac{\delta}{h_s} + 5\frac{k}{s-a}\left(\frac{\delta}{s-a}\right)^3 = \sigma_a + \sigma_w \qquad (9.3)$$

If $\sigma_a = A\gamma(s\text{-}a)$ and the embankment and working platform have the same unit weight then the equation can be written in a non-dimensional form as:

$$\frac{E_0}{\gamma h_s}\frac{\delta}{s-a} + 5\frac{k}{\gamma(s-a)^2}\left(\frac{\delta}{s-a}\right)^3 = A + \frac{h_w}{s-a} \qquad (9.4)$$

9.6 Case studies

9.6.1 Second Severn Crossing

The Second Severn Crossing provides a second motorway link between South Wales and England across the River Severn estuary. The new toll plaza for the Second Severn Crossing was constructed on low lying land adjacent to the estuary. To alleviate the risk of flooding, ground levels were generally raised by between 2.5 and 3.5 m increasing locally to 6m maximum height. The case study of this project has been provided by Maddison et al. (1996).

The ground investigation indicated soft subsoil to depths up to 8 m overlying sands and gravels and Trias sandstone. Table 9.1 summarises the soft subsoil properties.

Ground improvement comprising vibro concrete columns (VCCs) and a 'load transfer platform' (LTP) incorporating relatively low strength geogrids was used to support the embankment. In the design, the VCCs were installed on a triangular grid of 2.7 m maximum spacing founding in the sand and gravel deposits. The load transfer platform at the base of the embankment comprised granular fill incorporating two layers of Tensar SS2 geogrid, in order to promote arching in the granular fill and transfer the embankment loads into the columns. The properties of the geogrid are shown in Table 9.2, which are derived from the short-term quality control strength at approximately 10 % strain as reported by

Maddison et al. The long-term stiffness would be lower than the value derived from the short-term quality control tests (for both cases). A cross section of the design is shown in Figure 9.2. More information can be found in Maddison et al.

Table 9.1. Summary of subsoil properties for the Second Severn Crossing

	Thickness, t (m)	Stiffness, E_0 (kN/m^2)
Desiccated Clay	1-2	5000
Estuarine Clay	2-3	1800
Peat	2-4	500

Table 9.2. Summary of SS2 geogrid properties for the Second Severn Crossing

Property	Transverse direction	Longitudinal direction
Short-term Stiffness (kN/m)	300	150

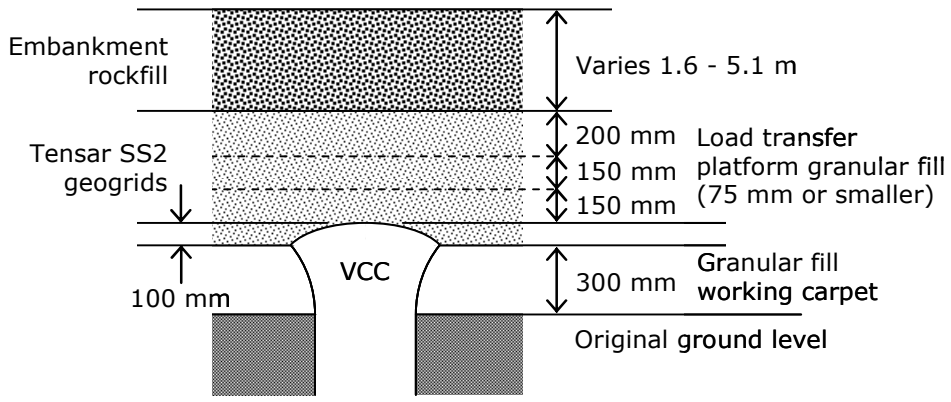

Figure 9.2. Embankment design for the Second Severn Crossing

9.6.2 Construction of apartments on a site bordering River Erne, Northern Ireland

A development of 2 and 3 storey town houses and 4 storey apartment blocks were constructed on a site bordering the River Erne in Enniskillen, Northern Ireland during 1999 and 2000. The details of this project were reported in seminar by Milligan (2006).

Ground investigations showed that the underlying subsoil consisted of made ground over substantial depths of peat and soft alluvial clay of thickness of up to 10 m, and underlying glacial till. A (simplified) schematic of the site is shown in Figure 9.3. A summary of the subsoil properties is shown in Table 9.3. Note that compressibility of the subsoil is very high, for instance compared to the Second Severn Crossing case study.

The site was low-lying and susceptible to flooding so the ground level for the development had to be raised by up to about 3.0 m. Due to the poor ground conditions, a load transfer platform was constructed over the whole area of the site supported by piles into the underlying glacial till (Figures 9.3 and 9.4). The load transfer platform was used to provide the foundation for the buildings, of conventional construction with shallow strip footings, as well as for all the remainder of the site including gardens, roads and parking areas. It should be noted that there was no direct link between the building footings and piles beneath.

The piles were installed in a triangular arrangement at 2.75 m spacing with a pile cap size of 0.75 m. Beneath the pile caps was 0.5 m thickness of working platform (unsupported fill). Three layers of Tensar geogrid were used; SS20 (×1) and SS30 (×2) as shown in Figure 9.4. The short-term properties of the geogrid are shown in Table 9.4, and again long-term values would be lower.

Table 9.3. Summary of subsoil properties for the project in Ireland

	Thickness, t (m)	Stiffness, E_0 (kN/m^2)
Alluvial clay	2.5-10	500
Peat	1-3	200

Table 9.4. Summary of geogrid properties for the project in Ireland

Property	SS20	SS30
Short-term stiffness (kN/m)	280	420

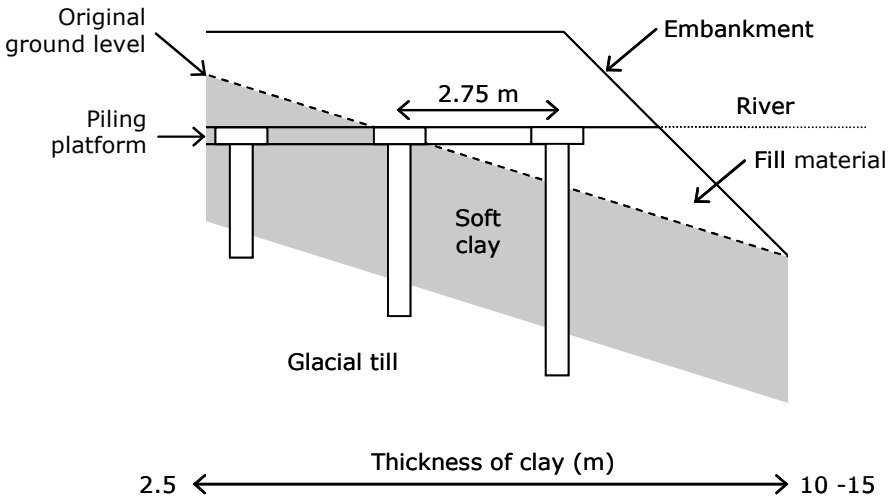

Figure 9.3. Cross section for the project in Ireland

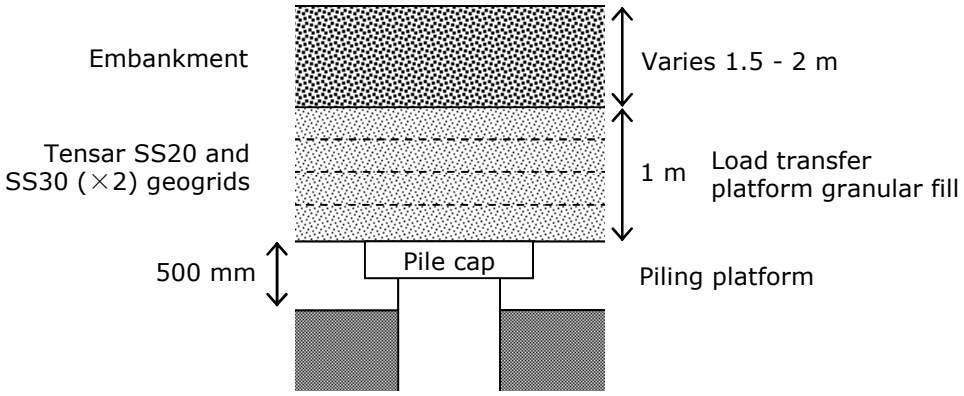

Figure 9.4. Embankment design for the project in Ireland

9.6.3 A650 Bingley Relief Road

The A650, Bingley Relief Road, in West Yorkshire, UK, officially opened to traffic in January 2004. Part of the route involved crossing Bingley North Bog, with soft compressible peat varying in depth up to 11m (and underlain by glacial sands and gravels), adjacent to a sensitive railway. This projected was reported by Gwede & Horgan (2008).

The piled embankment solution adopted across the North Bog involved the construction of approximately 440 m of low height (2.0 m) piled embankment (varying from 1.8 to 2.2 m). The piles were installed on a square 2.5 m grid, with 900 mm wide square precast pile caps bedded onto the piles. A temporary working platform was installed but subsequently removed once the piles were constructed thus minimising the change in the long term stress acting on the peat.

No specific information is provided for the compressibility of the subsoil. However, it is indicated that it is very soft and hence it has been assumed to have a one-dimensional modulus of 200 kN/m^2.

The design for the geosynthetic was provided by two orthogonal (longitudinal and transverse) layers of Stabilenka 600/50. Based on information in Gwede & Horga, the long-term stiffness of the geosynthetic including creep was deduced from a load/ strain plot as 4800 kN/m.

9.6.4 A1/N1 Flurry Bog

A section of the A1/N1 dual carriageway between Dundalk and Newry forming the cross border link between the Republic of Ireland and Northern Ireland has recently been completed (August 2007). This project was reported by Orsmond (2008).

The Flurry Bog is a cutaway bog where the levels had been reduced to groundwater level with poor drainage exacerbated by the adjacent Salmonoid River that is prone to flooding. Ground conditions were typically very weak peat 4 to 6 m deep overlying soft silt 3 to 4 m, then a thin layer of gravel over bedrock.

The embankment height was about 3.0 m over the piles. The pile cap size was 0.8 m and pile spacing was 2.5 m on a square grid. A working platform was constructed, comprising of two layers of geogrid spaced within 600 mm rockfill, which proved sufficient for the intended loads but weak enough for the piles to be driven through it.

Again, no specific information is provided for the compressibility of the subsoil, but again it appears to be very soft, and a one-dimensional modulus of 200 kN/m^2 has been assumed.

The final design incorporated Ployfelt PET woven polyester geosynthetic laid in longitudinal and transverse directions, with strength varying

between 540 and 780 kN/m. Based on manufacturers literature for these products a typical long-term stiffness was taken as 5000 kN/m.

9.6.5 Case study comparison

The project at the Second Severn Crossing has been considered as a successful case, in which the settlement (both absolute and differential) of the embankment have remained within acceptable limits. However, the project in Northern Ireland was not. Within two years of completion, the ground deformations around the buildings constructed on the LTP were becoming noticeable. Some time later, the pile caps 'punched' into the material above, causing significant deformation. According to detailed investigation and assessment of the cause of failure (Milligan, 2006), the problems were caused by excessive and continuing deformation of the load transfer platform.

The A650 and A1/N1 projects have both performed satisfactorily to date, for 5 and 2 years respectively at the time of writing.

Equation (9.4) will be used to consider these four cases, as summarised in Table 9.5.

The pile cap spacing (s) shows relatively little variation between the cases. However, the pile cap size (a) is slightly smaller at the Second Severn Crossing, where enlarged heads on the VCC were used rather than actual

pile caps. The first two case studies consider a triangular grid of piles, but they will be treated as if the grid was square using Equation (9.4).
The height of the embankments (h) are not that significant, generally corresponding to about 1.5 times the clear spacing (s-a). On the A650 h_w is zero since the precaution was taken of removing the working platform.

For various layers of soft subsoil, the total settlement for a given stress can be calculated by:

$$\frac{\delta_s}{\sigma_s} = \frac{h_1}{E_{01}} + \frac{h_2}{E_{02}} + \ldots \frac{h_n}{E_{0n}} \qquad (9.5)$$

Hence for the purposes of defining the variables in Equation (9.4) the subsoil thickness is taken as the sum of thicknesses for all soft layers and then a representative stiffness can be derived as follows:

$$\frac{E_0}{h_s} = \frac{1}{h_1 / E_{01} + h_2 / E_{02} \cdots h_n / E_{0n}} \qquad (9.6)$$

The subsoil thickness for the Second Severn Crossing and apartments in Ireland are based on typical values for the least soft layers, but maximum values for the softest layer, giving a 'worst case scenario'. For the other cases a nominally very low stiffness was used. Notably the derived 'dimensionless subsoil factor' is highest by a significant margin for the Second Severn Crossing.

The equation only considers the reinforcement contribution due to membrane tension, and not any other interaction with the soil. Thus the

effect of multiple layers of biaxial geogrids is incorporated simply by assuming all grids to deform by the same amount and summing the stiffness (k) of the various grids. Where geosynthetics have been laid in orthogonal directions they have effectively been treated as a single biaxial grid with the maximum stiffness in each direction. An approximate long-term stiffness has been assumed throughout.

For the Second Severn Crossing a total biaxial stiffness of 300 kN/m has been assumed, based on two layers of geogrid with short-term stiffness of 150 kN/m and 300 kN/m in orthogonal directions. Thus the long-term value is assumed as two-thirds of the average stiffness (kN/m):
300 = 2×0.67×(300+150)/2.

For the apartments in Ireland where large deformations were known to have occurred the long-term stiffness was taken as half the nominal short-term stiffness at normal working strain, giving a total stiffness of 560 kN/m.

The remaining case studies used two orthogonal layers of geosynthetic, so the biaxial stiffness has been taken as the long-term stiffness of one layer. It is evident that the reinforcement stiffness is much higher in these cases.

The remaining terms in Equation (9.4) are the normalised working platform thickness (as summarised in Table 9.5), and A. Since the embankments are not that high (and punching of the pile caps into the

base of the embankment is unlikely to be an issue) A has been taken as 0.5 (Section 9.4).

Table 9.6 shows the numerical solution of Equation (9.4), with results for the compatible displacement at equilibrium and corresponding reinforcement strain, and the distribution of load between the geogrid and subsoil. Figure 9.5 shows the corresponding interaction diagrams. Note that the point of maximum arching for the Ground Reaction Curve is assumed to extend from 2 % normalised displacement at a constant value. In reality some form of brittle response would be observed (Section 2.3, Figure 2.14), but this is not considered in Equation (9.4). Equilibrium is satisfied when the sum of the subsoil and geogrid response meets the point of maximum arching, $[A+h_w/(s-a)]$.

Table 9.6 shows that the deformation is about twice as large for the Irish apartments as any of the other cases, and the geogrid strain is over 10 %, compared with less than 4 % in the other cases. This is consistent with the observation that failure of the LTP was observed for the Irish apartments. At the Second Severn Crossing, where reinforcement stiffness is low, the subsoil (which is relatively competent) carries most of the load, whereas for the A650 and A1/N1 this situation is reversed.

Solution of the equation does not consider the condition that the geogrid cannot carry a normalised load exceeding A (from the embankment), and likewise that the subsoil must carry the load from the working platform as a minimum. These conditions are most likely to be encountered when the

geogrid is stiff and the subsoil is very compressible. The situation does not arise for the first two case studies (where the geogrid is not that stiff), or the third (where there is no working platform). However, it does occur for the A1/N1. Here the geogrid would carry only the embankment arching load:

$$5\frac{k}{\gamma(s-a)^2}\left(\frac{\delta}{s-a}\right)^3 = A \qquad (9.7)$$

and hence $\delta/(s\text{-}a)$ = $(0.5/509)^{1/3}$ = 9.9 %, with corresponding reinforcement strain 2.6 % - somewhat less than in Table 9.6.

Likewise for the subsoil:

$$\frac{E_s}{\gamma h_s}\frac{\delta}{s-a} = \frac{h_w}{s-a} \qquad (9.8)$$

and hence $\delta/(s\text{-}a)$ = (0.35/1.18) = 30 %.

As anticipated this indicates that the subsoil settles more than the sag in the reinforcement, and hence a gap is formed below the reinforcement. However, it is worth reflecting that the subsoil properties assumed for this case are probably conservative and thus this may not actually happen.

Table 9.5. Summary of input parameters

	Second Severn Crossing			**Construction of apartments, Ireland**		**A650**	**A1/N1**
Piled embankment geometry							
s (m)	2.7			2.75		2.5	2.5
a (m)	0.5			0.75		0.9	0.8
h (m)	3.5			3.0		2.0	3.0
h_w (m)	0.3			0.5		0.0	0.6
Subsoil properties							
E_0 (kN/m^2)	5000	1800	500	500	200	200	200
h_s	1.5	2.5	4	7	3	10	10
Geogrid properties							
k (kN/m)	150	150		140	210	210	4800	5000
Derived parameters							
Clear spacing: (s-a)	2.2			2.0		1.6	1.7
Dimensionless working platform thickness: $h_w/(s\text{-}a)$	0.14			0.25		0	0.35
Dimensionless subsoil factor: $E_0/\gamma h_s$	6.07			2.03		1.18	1.18
Dimensionless geogrid factor: $5k/\gamma(s\text{-}a)^2$	18.23			41.18		551.47	508.85

Table 9.6. Summary of results

	Second Severn Crossing	**Construction of apartments, Ireland**	**A650**	**A1/N1**
Deformation				
$\delta/(s\text{-}a)$ (%)	10.2	20.2	8.9	11.2
δ (mm)	224.4	404.0	142.4	190.4
Geogrid strain ε (%)	2.77	10.88	2.11	3.35
Load distribution				
Total stress (kN/m^2)	23.8	25.5	13.6	24.6
Subsoil stress (kN/m^2)	23	14	2.7	3.8
Geogrid stress (kN/m^2)	0.8	11.5	10.9	20.8

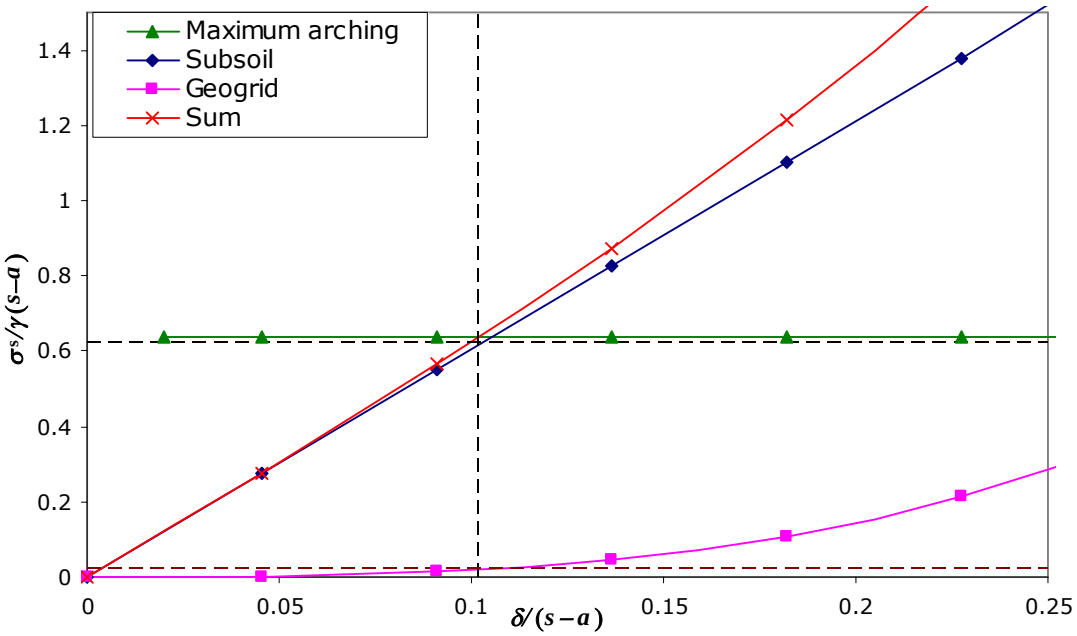

(a) Second Severn Crossing

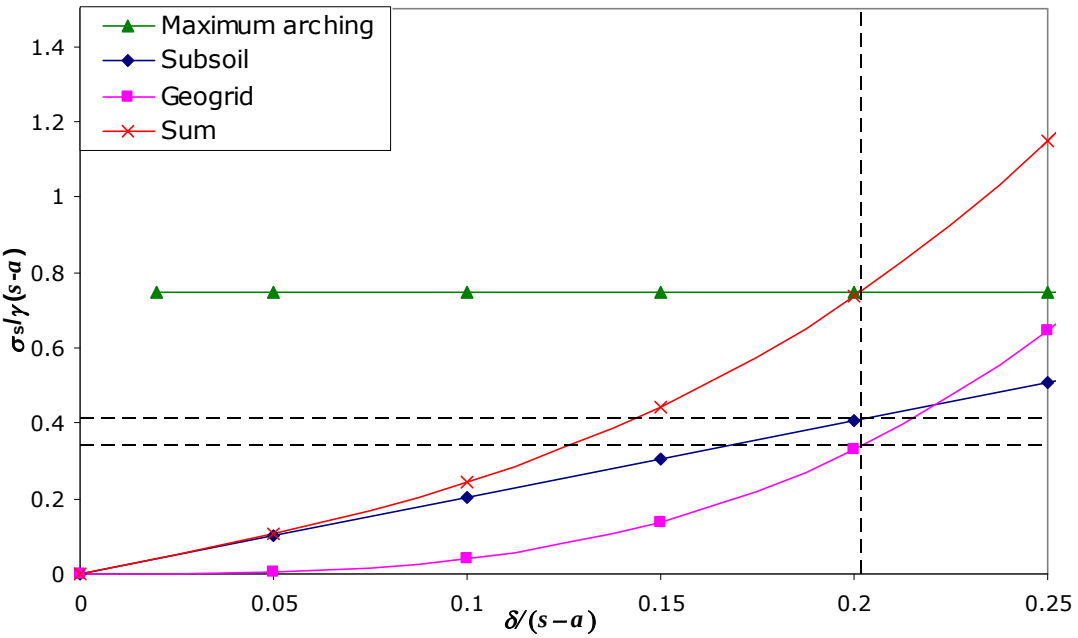

(b) Construction of apartments, Ireland

Figure 9.5 continued on following page

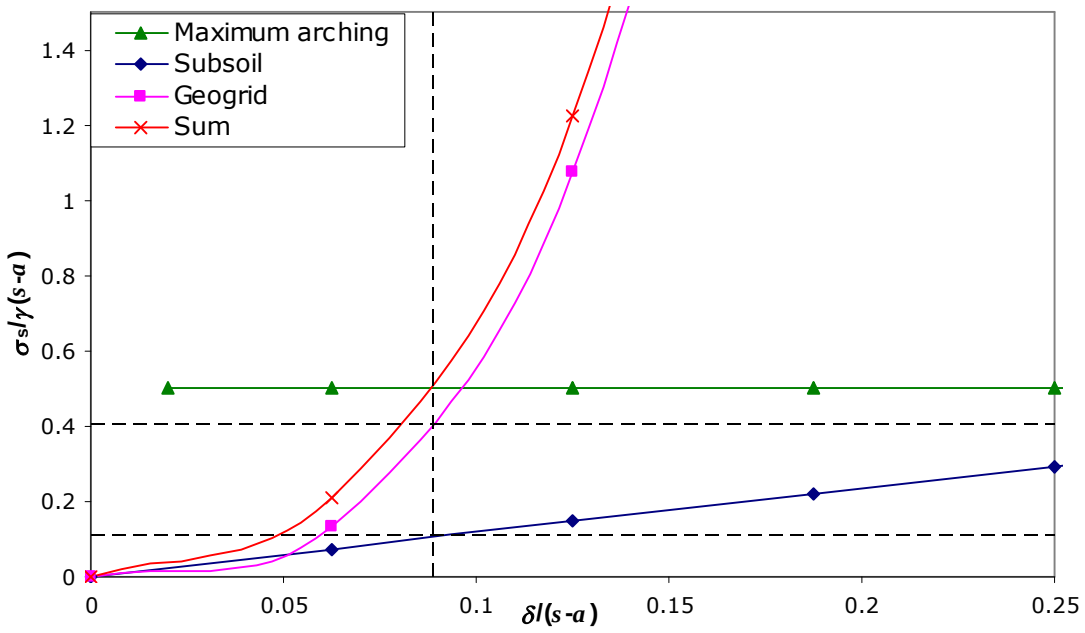

(c) A650

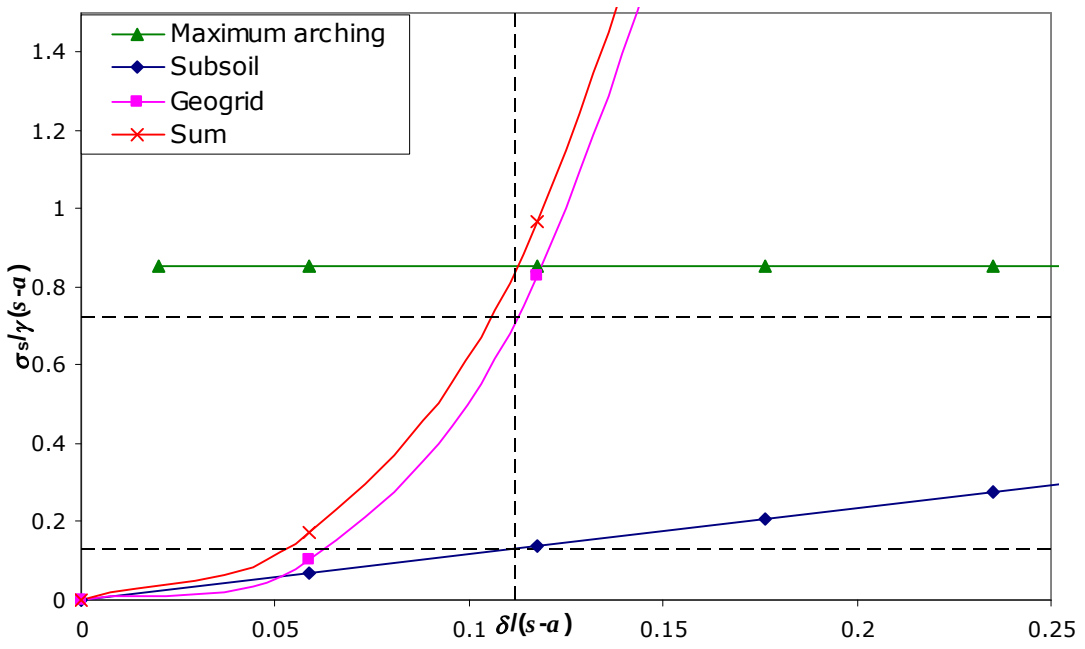

(d) A1/N1

Figure 9.5. Interaction diagrams

9.7 Summary

The ratio $h/(s\text{-}a)$ has been considered as an important parameter for arching behaviour in design. It has been demonstrated that the critical value of h/s = 1.5 for full arching reported in this work corresponds to $h/(s\text{-}a)$ ≈ 2.0-3.0, which was consistent with the values reported by the Aslam (2008), Ellis & Aslam (2009a and b), and Potts & Zdravkovic (2008b).

The value of $\sigma_s/\gamma(s\text{-}a)$ at the point of maximum arching for medium height embankments was between 0.4 and 0.8 in this study, which was again consistent with the values reported by the other authors for physical and numeric modelling.

An interaction diagram has been described (following the concept proposed by Ellis & Aslam, 2009b), where the combined action of arching in the embankment, reinforcement membrane action and the subsoil give equilibrium at a compatible settlement. Equation (9.4) is based on the interaction diagram, using terms for 3D behaviour derived in Chapters 7 and 8.

The interaction diagram and accompanying equation were applied to a number of case studies: two using a 'Load Transfer Platform' (LTP) with multiple layers of low stiffness/strength geogrid, and two with geotextile reinforcement which was approximately 10 times stiffer. Case studies

often contain relatively limited information regarding the subsoil, which is very soft, and has not been extensively considered in the design. In the case studies with relatively stiff reinforcement it was (perhaps conservatively) assumed that the subsoil was very soft. However, the geotextile was able to carry the arching embankment load at a tolerable strain.

In the case studies for the LTPs there was information regarding the subsoil compressibility. In one case the subsoil was soft, but not extremely soft, and here it was found that the subsoil actually carried a significant portion of the arching embankment and working platform load, significantly reducing the load on the geogrid. However, in the other case a combination of very soft subsoil, and geogrid with relatively low stiffness implied intolerable geogrid strain, correctly reflecting an actual failure in the field.

Thus the question regarding design of LTPs with low strength geogrids according to the 'Guido' method still remains. This design method is acknowledged (e.g. Jenner et al. 1998) to fundamentally differ from an approach based on catenary action of the reinforcement. Equation (9.4) is based on catenary action, and has been verified by the FE analyses in this thesis without indication that it is inappropriate.

CHAPTER 10
CONCLUSIONS

10.1 Work reported in the thesis

Numerical modelling of arching in piled embankments has been undertaken. The research has improved generic understanding of arching behaviour, and interaction of the embankment with the subsoil and any layers of geogrid or geosynthetic reinforcement used at the base of the embankment. The work has also supplemented the results of physical modelling recently undertaken at the University of Nottingham. The improved understanding of behaviour highlights the inadequacies in some existing design approaches, and has been used to develop a simple equation for use in design.

The numerical analyses reported in Chapters 3 and 6 were for unreinforced piled embankments without subsoil in 2D and 3D situations respectively. In both cases at $(h/s) \approx 0.5$, there is no evidence of arching based on the stress acting on the subsoil, and there is very large differential settlement at the embankment surface. As (h/s) increases to 1.5 the stress on the subsoil does not increase significantly (and thus there is significant evidence of arching), and differential settlement surface tends to zero. This finding is consistent with the values reported by Aslam (2008) and Ellis & Aslam (2009a and b) and Potts & Zdravkovic (2008b).

The value of $\sigma_s/\gamma s$ for maximum arching is approximately 0.25~0.4 except for high s/a in the 3D situation. This result is consistent with the corresponding findings by Ellis & Aslam (2009a) and Potts & Zdravkovic (2008b). At higher values of (h/s) conditions at the pile cap are critical, and Equation (3.2) and Equation (6.2) can be used to conservatively estimate the stress on the subsoil in two and three dimensional conditions respectively.

Chapters 4 and 7 presented the geogrid reinforced piled embankment for 2D and 3D analyses respectively. The results showed that with the effect of geogrid, the ultimate stress on the subsoil can be reduced to zero. However, this required significant sag of the geogrid reinforcement. The 2D Equation (2.30) (based on a parabola) can be used to predict the geogrid action for both 2D and 3D situations (using an appropriate span).

The 2D and 3D analyses also found that the sag of reinforcement was very sensitive to the span of the reinforcement between piles, but relatively insensitive to its stiffness. For the embankment with three layers of geogrid, the upper two grids showed less settlement compared to bottom layer, and thus less tension. This finding has been proposed by Jenner et al. (1998) in a field study.

It was also found that the tension in the reinforcement was approximately constant across the span in 2D analyses. However, in the 3D situation, the maximum tension in the geogrid occurred at the corner of the pile cap. A similar finding has been noted by Russell & Pierpoint (1997).

Chapters 5 and 8 presented a reinforced piled embankment with subsoil in 2D and 3D situations respectively. The analyses showed that the subsoil could give a major contribution to overall vertical equilibrium. In fact, the contribution from the subsoil exceeded a prediction based on simple 1D settlement, due to the effect of principal stress rotation (effect of bearing) near the top of the subsoil.

A simple equation (or interaction diagram) based on the results has been proposed to allow assessment of the relative contribution of the reinforcement and subsoil to equilibrium, and hence to predict the load and strain in the reinforcement.

10.2 Future work

This work has given considerable insight into the arching behaviour in a piled embankment, and also considered the effects of geogrid or geosynthetic reinforcement and subsoil. However, there is still some work which could be undertaken in the future:

- The post-maximum stage of the Ground Reaction Curve (see Section 2.3, Figure 2.14) was not observed in this research. Presumably the introduction of brittle soil behaviour would rectify this. Physical modelling could also be used to investigate this behaviour.
- This research only considered the behaviour of piled embankments under static loading. The behaviour of piled embankments under cyclic and dynamic loading are not yet fully understood and cannot be predicted. Thus, the numerical and physical modelling could be used to investigate this behaviour further.
- The role of multiple layers of relatively low strength/stiffness geogrid in a Load Transfer Platform may not yet be completely understood. This work has indicated that the response does not significantly exceed that based on prediction by membrane action (and indeed that the higher layers do little work). Based on the case studies presented in Chapter 9 there is some evidence that the use of low strength geogrids actually requires the subsoil to carry a significant proportion of the load at the base of the embankment if it is to be successful.

- The role of 'primary' and 'secondary' reinforcement was not examined, and further research could be undertaken to clarify the strength required for each type of reinforcement, and the effect on settlement of the relative stiffness.

REFERENCES

Abusharar, S.W., Zheng, J.J., Chen, B.G. & Yin, J.H. (2009). A simplified method for analysis of a piled embankment reinforced with geosynthetics. *Geotextiles and Geomembranes*, Vol. 27, February 2009, pp. 39-52.

Almeida, M.S.S., Ehrlich, M., Spotti, A.P. & Marques, M.E.S. (2007). Embankment supported on piles with biaxial geogrids. *Proceedings of the Institution of Civil Engineers*, *Geotechnical Engineering 160*, October 2007 Issue GE4, pp. 185-192.

Aslam, R. & Ellis, E.A. (2008). Centrifuge modelling of piled embankments. *Proc. ISSMGE 1st Int. Conf. on Transportation Geotechnics*, Nottingham, UK, 2008. Taylor & Francis Group, London, ISBN 978-0-415-47590-7, pp. 363-368.

Becker, A. A. (2001). *Understanding non-linear finite element analysis*. NAFEMS, Glasgow, ISBN 1-874376-35-2, 171.

Becker, A. A. (2004). *An introductory guide to finite element analysis*. Professional Engineering Publishing, London, ISBN 1-86058-410-1.

Bell, A.L., Jenner, C., Maddison, J.D. & Vignoles, J. (1994). Embankment support using geogrids with vibro concrete columns. *Fifth international conference on geotextiles, geomembranes and related products*, Singapore, pp. 335-338.

Ellis, E.A., Zhuang, Y., Aslam, R. & Yu, H.S. (2009). Discussion of 'A simplified method for analysis of a piled embankment reinforced with geosynthetics'. *Geotextiles and Geomembranes* 27, pp. 39-52 (under review).

Briancon, L., Faucheux, G. & Andromeda, J. (2008). Full-scale experimental study of an embankment reinforced by geosynthetics and rigid piles over soft soil. *Proceedings of the 4th European Geosynthetics Conference*, Edinburgh, UK, September 2008, Paper number 110.

Britton, E. & Naughton, P. (2008). An experimental investigation of arching in piled embankments. *Proceedings of the 4th European Geosynthetics Conference*, Edinburgh, UK, September 2008, Paper number 106.

BS8006, (1995). *Code of practice for strengthened/reinforced soils and other fills*. British Standards Institution.

Cao, W.P., Chen, Y.M. & Chen, R.P. (2006). An analytical model of piled reinforced embankments based on the principle of minimum potential energy. *Advances in earth structures*, *GeoShanghai 06*, pp. 217-224.

Carlsson B. (1987), Reinforced soil, principles for calculation, Terratema AB, Linköping (in Swedish).

Chen, Y.M., Cao, W.P. & Chen, R.P. (2006a). An experimental investigation of soil arching within basal reinforced and unreinforced piled embankments. *Geotextiles and Geomembranes*, Vol. 26, April 2008, pp. 164-174.

Chen, R.P., Chen, Y.M. & Xu, Z.Z. (2006b). Interaction of rigid pile - supported embankment on soft soil. *Advances in earth structures*, *GeoShanghai 06*, pp. 231-238.

Chen, R.P., Chen, Y.M., Han, J. & Xu, Z.Z (2008). A theoretical solution for pile – supported embankments on soft soils under one – dimensional compression. *Canadian Geotechnical Journal*, Vol. 45, No. 5, May 2008, pp. 611-623.

Chen, C.F. & Yang, Y. (2006). Research on bearing capacity of geosynthetic - reinforced and pile - supported earth platforms over soft soil and analysis of its affecting factors. *Advances in earth structures*, *GeoShanghai 06*, pp. 294-301.

EGBEO (2004): Bewehrte ErdkÖrper auf punkt - und linienfÖrmigen Traggliedern, *Entwurf Kapitel 6.9, 05/16/2004 version*, nonpublished.

Ellis, E.A. & Aslam, R. (2009a). Arching in piled embankments: comparison of centrifuge tests and predictive methods – Part 1 of 2. *Ground engineering*, June 2009, pp. 34-38.

Ellis, E.A. & Aslam, R. (2009b). Arching in piled embankments: comparison of centrifuge tests and predictive methods – Part 2 of 2. *Ground engineering*, July 2009, pp. 28-31.

Fakher, A. & Jones, C.J.F.P. (2001). When the bending stiffness of geosynthetic reinforcement is important. *Geosynthetics International*, Vol. 8, No. 5, pp. 445-460.

Guido, V.A., Knueppel, J.D. & Sweeny, M.A. (1987). Plate loading tests on geogrid - reinforced earth slabs. *Proceedings Geosynthetics 87 Conference*, New Orleans, pp. 216-225.

Gwede, D. & Horgan, G.J. (2008). Design, construction and in – service performance of a low height geosynthetic reinforced piled embankment: A650 Bingley Relief Road. *Proceedings of the 4th European Geosynthetics Conference*, Edinburgh, UK, September 2008, Paper number 256.

Han, J. & Gabr, M.A. (2002). Numerical analysis of Geosynthetic-reinforced and pile-supported earth platforms over soft soil. *Journal of Geotechnical and Geoenvironmental Engineering*, January 2002, pp. 44-53.

Handy, R.L. (1985). The arch in soil arching. ASCE *Journal of Geotechnical Engineering*, Vol. 111, No. 3, pp. 302-318.

He, C., Lou, X.M. & Xiong, J.H. (2006). Arching effect in piled embankments. *Advances in earth structures*, *GeoShanghai 06*, pp. 270-277.

Heitz, C., Lüking, J. & Kempfert, H.G. (2008). Geosynthetic reinforced and pile supported embankments under static and cyclic loading. *Proceedings of the 4th European Geosynthetics Conference*, Edinburgh, UK, September 2008, Paper number 215.

Hewlett, W.J. & Randolph, M.F. (1988). Analysis of piled embankments. *Ground Engineering*, April 1988, pp. 12-18.

Horgan, G.J. & Sarsby, R.W. (2002). The arching effect of soils over voids and piles incorporating geosynthetic reinforcement. Geosynthetics - 7th ICG - Delmas, Gourc & Girard (eds), Swets & Zeitlinger, Lisse ISBN 90 5809 523 1, pp. 373-378.

Iglesia, G.R., Einstein, H.H. & Whitman, R.V. (1999). Determination of vertical loading on underground structures based on an arching evolution concept. *Proceedings 3rd National Conference on Geo-Engineering for Underground Facilities*, pp. 495-506.

Jenck, O., Dias, D. & Kastner, R. (2005). Soft ground improvement by vertical rigid piles two-dimensional physical modelling and comparison with current design methods. *Journal of the Japanese Geotechnical Society of Soils and Foundations*, Vol. 45, No. 6, pp. 15-30.

Jenck, O., Dias, D. & Kastner, R. (2006). Two-dimensional physical modelling of soft ground improvement by vertical rigid piles. *Physical Modelling in Geotechnics* – 6th *ICPMG*, pp. 527-532.

Jenner, C.G., Austin, R.A. & Buckland, D. (1998). Embankment support over piles using geogrids. *Proceedings 6th International Conference on Geosynthetics*, Atlanta, USA, pp. 763-766.

Jones, C.J.F.P., Lawson, C.R. & Ayres, D.J. (1990). Geotextile reinforced piled embankments. *Geotextiles, geomembranes and related products*, Den Hoedt (Ed), 1990, Balkema, Rotterdam, pp. 157-159.

Kempfert, H.G., Göbel, C., Alexiew, D. & Heitz, C. (2004). German recommendations for reinforced embankments on pile - similar elements. *Proceedings of the 3rd European Geosynthetics Conference*, Munich, Germany, pp. 279-284.

Kempfert, H.G., Stadel, M. & Zaeske, D. (1997). Design of geosynthetic – reinforced bearing layers over piles. *Bautechnik 74*, Heft 12, pp. 818-825.

Kempton, G., Russell, D., Pierpoint, N.D. & Jones, C.J.F.P. (1998). Two and three -dimensional numerical analysis of the performance of piled embankments. *Proceedings of the 6th International Conference on Geosynthetics*, Atlanta, GA, USA, pp. 767-772.

Krynine, D.P. (1945). Discussion of "Stability and stiffness of cellular cofferdams," by Karl Terzaghi, *Transactions*, *ASCE*, Vol. 110, pp. 1175-1178.

Love, J. & Milligan, G. (2003). Design methods for basally reinforced pile-supported embankments over soft ground. *Ground Engineering*, March 2003, pp. 39-43.

Low, B.K., Tang, S.K. & Choa, V. (1994). Arching in piled embankments. *ASCE Journal of Geotechnical Engineering*, Vol. 120, No. 11, November, 1994, pp. 1917-1938.

Maddison J.D., Jones D.B., Bell A.L. & Jenner C.G. (1996). Design and performance of an embankment supported using low strength geogrids and vibro concrete columns. *Geosynthetics – Applications, Design and Construction*, De Groot, Den Hoedt & Termaat, pp. 325-332.

McKelvey, J.A. (1994). The anatomy of soil arching. *Geotextiles and Geomembranes* 13, pp. 317-329.

Milligan, G. (2006). Seminar given at the ICE setting out the findings and conclusions from a detailed investigation and assessment of the causes of failure of apartment blocks constructed on a site bordering the River Erne in Enniskillen, Northern Ireland.

Munfakh, G.A., Sarkar, S.K. & Castelli, R.J. (1984). Performance of a test embankment founded on stone columns. *Proceedings of the International Conference on Advances in Pilling and Ground Treatment for Foundations*, Institution of Civil Engineers, London, pp. 259-265.

Naughton, P.J. (2007). The significance of critical height in the design of piled embankments. *Proceedings of Geo-Denver 2007*, Denver, Colorado.

Naughton, P.J. & Kempton, G.T. (2005). Comparison of analytical and numerical analysis design methods for piled embankments. *Contemporary issues in foundation engineering*, GSP 131, ASCE, Geo-Frontiers, Austin, Texas.

Naughton, P., Scotto, M. & Kempton, G. (2008). Piled embankments: past experience and future perspectives. *Proceedings of the 4th European Geosynthetics Conference*, Edinburgh, UK, September 2008, Paper number 184.

Orsmond, W. (2008). A1N1 flurry bog piled embankment design, construction and monitoring. *Proceedings of the 4th European Geosynthetics Conference*, Edinburgh, UK, September 2008, Paper number 290.

Ottosen, N. & Petersson, H. (1992). *Introduction to the finite element method*. Pearson, Prentice Hall, ISBN 0-13-473877-2.

Potts, V.J. & Zdravkovic, L. (2008a). Assessment of BS8006: 1995 design method for reinforced fill layers above voids. *Proceddings of the 4th European Geosynthetics Conference*, Edinburgh, UK, September 2008, Paper number 116.

Potts, V.J. & Zdravkovic, L. (2008b). Finite element analysis of arching behaviour in soils. *The 12th International Conference of International Association for Computer Methods and Advances in Geomechanics (IACMAG)*, Goa, India, October, 2008, pp. 3642-3649.

Raithel, M., Kirchner, A. & Kempfert, H.G. (2008). Pile-supported embankments on soft ground for a high speed railway: Load transfer, distribution and concentration by different construction methods. *Proc. ISSMGE 1st Int. Conf. on Transportation Geotechnics*, Nottingham, UK, 2008. Taylor & Francis Group, London, ISBN 978-0-415-47590-7, pp. 401-407.

Rogbeck, Y., Gustavsson, S., Södergren, I. & Lindquist, D. (1998). Reinforced piled embankments in Sweden-design aspects. *Proceedings of the 6th International Conference on Geosynthetics*, pp. 755-762.

Rowe, R.K. & Li, A.L. (2002). Behaviour of reinforced embankments on soft rate-sensitive soils. *Geotechnique* 52, No. 1, 29-40.

Russell, D., Naughton, P. & Kempton, G. (2003). A new design procedure for piled embankments. *Proceedings of the 56th Canadian Geotechnical Conference and the NAGS Conference*, Winnipeg, MB, pp. 858-865.

Russell, D. & Pierpoint, N. (1997). An assessment of design methods for piled embankments. *Ground Engineering*, November 1997, pp. 39-44.

Slocombe, B.C. & Bell, A.L. (1998). Setting on a dispute: discussion on Russell and Pierpoint paper. *Ground Engineering*, March 1998, pp. 34-36.

Stewart, M.E. & Filz, G.M. (2005). Influence of clay compressibility on geosynthetic loads in bridging layers for column - supported embankments. *Proceedings of GeoFrontiers 2005*, *ASCE*, Austin.

Taechakumthorn, C. & Rowe, R.K. (2008). *The 12th International Conference of International Association for Computer Methods and Advances in Geomechanics (IACMAG)*, Goa, India, October, 2008, pp. 3559-3566.

Terzahgi, K. (1943). *Theoretical Soil Mechanics*. John Wiley and Sons, New York.

Thigpen, L. (1984). *On the mechanics of strata collapse above underground openings*. Lawrence Livermore National Laboratory, U.S. Department of Energy.

Van Eekelen, S.J.M.& Bezuijen, A. (2008). Design of piled embankments considering the basic starting points of the British Standard BS8006. *Proceedings of the 4th European Geosynthetics Conference*, Edinburgh, UK, September 2008, Paper number 315.

Van Eekelen, S.J.M., Bezuijen, A. & Alexiew, D. (2008). Piled embankments in the Netherlands, a full – scale test, comparing 2 years of measurements with design calculations. *Proceedings of the 4th European Geosynthetics Conference*, Edinburgh, UK, September 2008, Paper number 264.

Van Eekelen, S.J.M., Bezuijen, A. & Oung, O. (2003). Arching in piled embankments; experiments and design calculations. *BGA International Conference Foundations: Innovations, observations, design and practice*, Dundee, pp. 889-894.

Wood, H.J. (2003). The design and construction of pile - supported embankments for the A63 Selby bypass. *Foundations: Innovations, observations, deign and practice*, Thomas Telford.

Yan, L., Yang J.S. & Han, J. (2006). Parametric study on geosynthetic-reinforced pile - supported embankments. *Advances in earth structures*, *GeoShanghai 06*, pp. 255-261.